MICHIGAN STATE UNIVERSITY

CYCLOTRON LABORATORY

HIGH ENERGY HEAVY ION COLLISIONS - PROBING THE EQUATION OF STATE OF HIGHLY EXCITED HADRONIC MATTER

HORST STÖCKER and WALTER GREINER

SEPTEMBER 1985

MSUCL-540

MSUCL-540
September 1985

to appear in PHYSICS REPORTS.

HIGH ENERGY HEAVY ION COLLISIONS-

PROBING THE EQUATION OF STATE OF HIGHLY EXCITED HADRONIC MATTER

Horst Stöcker and Walter Greiner

*Institut für Theoretische Physik
Johann Wolfgang Goethe Universität, D-6000 Frankfurt am Main, Germany
and
Department of Physics and Astronomy and
National Superconducting Cyclotron Laboratory
Michigan State University, East Lansing, MI 48824, USA

ABSTRACT

We review the recent progress in extracting the equation of state of hot dense hadronic matter from relativistic heavy ion collisions. At first a discussion of the bulk properties of infinite nuclear matter is presented. Next the theoretical approaches are developed which describe the complicated dynamics and non- equilibrium features in actual high energy nucleus-nucleus collisions: Nuclear fluid dynamics, the intranuclear cascade model, classical equation of motion simulations, the Vlasov Uehling-Uhlenbeck theory and the time dependent Dirac equation with meson field dynamics are exhibited. The recent experimental confirmation of the early hydrodynamic predictions on nuclear shock commpression establishes the key mechanism for creating high nuclear density and temperatures in the laboratory, and thus the key mechanism for investigating the nuclear equation of state. Evidence for a surprisingly stiff nuclear equation of state is presented from a comparison of the distinct theoretical predictions to recent high multiplicity 4π selected data on fragment formation, pion production and collective sidewards flow. We also discuss the possible creation of a deconfined quark gluon plasma at future ultra- relativistic heavy ion facilities.

*Permanent address

TABLE OF CONTENTS

Introduction

Little is known to date about the properties of hadronic matter at finite temperatures and densities other than the nuclear ground state density ρ_0=0.15 fm^{-3}. Hadronic matter may have a rich structure in this hithero unexplored domain of high excitation energies and compression (see Fig. I.1). There are conjectures about a nuclear liquid-vapor phase transition at moderate temperatures T < 20 MeV and $\rho < \rho_0$ and about abnormal nuclear matter (density isomers and pion condensates) at high densities, $\rho \approx 3 - 5\ \rho_0$. Pionization of nuclear matter is predicted for high temperatures, T > 50 MeV and the deconfinement phase transition from hadronic matter into the quark-gluon plasma is expected to happen at high densities, $\rho \approx 5 - 10\ \rho_0$, and/or high temperatures T ≈ 150 - 250 MeV. Such extreme energy densities, temperatures and baryon number densities have probably prevailed during the birth of the universe in the first fractions of a second of the big bang, and during the death of stars in supernova explosions and neutron star formation. However, until recently there was no opportunity to study these extreme conditions in the laboratory. With the recent discovery of nuclear shock compression [Gus84a,b], which had been predicted in classic papers by Scheid and Greiner [Sch68,Sch74a,b], and extended considerably by the Frankfurt school [Ban75,Ho76,Ruc76,Stö78,79,80,81,82,83,Buc80,81,83,84, 85], the key mechanism for high compression and heating of nuclear matter in the laboratory was unambiguously established.

Experimental information about the properties of hot dense strongly interacting systems is now being sought by analyzing high energy collisions of heavy nuclei. If two colliding nuclei can stop each other, high energy densities are achievable for short time spans t ≈ 10^{-22}seconds.

The first exploratory investigations of violent collisions between massive nuclei have been carried out during the last few years at the Berkeley BEVALAC [Gus84a,b], i.e. in the bombarding energy range $E_{lab} \approx$ 100 MeV/nucleon to 2 GeV/nucleon. Fundamental, exciting results have emerged, which have spurred further efforts for relativistic heavy ion facilities.

In this article we shall present a survey of the recent theoretical experimental and developments in the field of high energy heavy ion reactions. First we present the statistical concepts employed in the study of the properties of infinite hadronic systems at high density and finite temperatures, in particular the nuclear matter equation of state and the conjectured phase transitions. In the second section we develop various theoretical approaches to describe the dynamical evolution of the highly excited strongly interacting system in the complicated time dependent situation of an actual heavy ion collision. In the third section the recent 4π experiments on the production of nuclear fragments, pion multiplicities and collective flow (under shock compression) are confronted with theoretical model predictions. In stark contradiction to a decade of reluctance by some people to accept nuclear hydrodynamics [Ber75,Sob75], it is found that this model can well describe the complex processes in relativistic nucleus-nucleus collisions. We also point out the implications of these experiments for the recent attempts to determine the nuclear equation of state. It was particularly R. Stock [Sto82,83] who followed early suggestions [Stö78,81] to investigate the nuclear equation os state via the excitation functions of pions and extracted for the first time valuable information pointing towards a stiff nuclear equation of state. Finally, we turn to the ultrarelativistic domain, $E_{Lab} >> 1$ GeV/N and discuss the deconfinement phase transition from hadron matter into the quark gluon

plasma, with particular emphasis on the available energy densities, the transition parameters and the space time structure of the high energy density regions.

I. Infinite Nuclear Matter in Global Equilibrium
- The Nuclear Equation of State

1. Statistical and Thermodynamical Concepts

Before we start to discuss the properties of systems composed of 'infinite nuclear matter', we have to stress that such systems exist(ed) only in astrophysical events remote in space and time - e.g. in the big bang, supernova explosions, and in the interior of neutron stars. High density matter is formed in nuclear collisions only for brief moments, and global equilibrium can not be reached at high bombarding energies. However, statistical concepts have been successfully applied to nuclear collisions, e.g. in the nuclear fluid dynamical model, which assumes that local (rather than global) equilibrium is closely approached even on rather short time scales. The assumption of statistical equilibrium in nuclear collisions can only be checked via microscopic theories which are able to describe the evolution of the system from the nonequilibrium situation to the locally equilibrated state. These theories and the questions related to the equilibration are discussed in detail in the second part of this article.

Here we want to discuss the general statistical concepts appropriate to describe the near equilibrium situation. The nuclear matter properties can be characterized by two macrocanonical variables, namely by the density ρ and by the temperature T. The discussion of the properties of a piece of hadronic matter at rest then usually starts with the definition of the energy per baryon, W, as a function of the density and the temperature. The energy per nucleon can obviously be related to the center of mass energy in nuclear collisions. It is convenient to divide the total

energy per baryon $W(\rho,T)$ into a thermal and a compression part [Sch74, Bau75, St678-84, Buc80-85]:

$$W(\rho,T) = E_T(\rho,T) + E_C(\rho) + W_o \qquad (1)$$

where

$$E_C(\rho) = W(\rho,T) - W(\rho_o,T=0) = W(\rho,T=0) - W_o \qquad (2)$$

is defined to be the compressional energy and E_T is the thermal excitation energy per nucleon, which is - by definition - zero if the temperature vanishes. $W_0 \approx 923$ MeV is the rest energy of a nucleon at equilibrium density. In order to understand the physical significance of $W(\rho,T)$ let us consider a piece of nuclear matter of volume V. It's energy content is given by $E_V = \int_V \rho\, W(\rho,T)\, dV$, where $e = \rho W$ is the energy density of the matter. We would like to point out that in evaluating this quantity we have excluded the Coulomb energy and the long range part of the Yukawa energy, which lead to divergences if infinite systems are considered. Hence, in this chapter we are concerned with the short range part of the nuclear interaction only. This is the origin of the binding energy of 16 (rather than 8) MeV/nucleon used here - we are at this moment concerned with the volume term of the Bethe- Weizäcker formula only, surface and Coulomb terms are neglected. Once the functional form of W is given, standard thermodynamic relations can be used to calculate the pressure, P, entropy, S, enthalpy, H, etc. of the system at a given density and temperature. For example, the pressure is calculated from the internal energy as

$$P = \rho^2 \left.\frac{\partial E}{\partial \rho}\right|_{S=\text{const}} \qquad (3)$$

and can therefore be separated into two parts, P_c and P_T, accordingly. Similarly, one obtains the entropy of the system from the thermal energy

alone: Because of Nernst's theorem, the T = 0 part of the equation of state does not contribute to the entropy. We will now discuss E_c and E_T in greater detail.

2. A Model Lagrangian for a Relativistic Mean Field Theory

The total energy per baryon can, on the other hand, also be written as an expression involving kinetic and potential terms. This becomes particularly obvious in the mean field approach. The relativistic mean field theory developed by Walecka et al. [Wal74, Ser85] and Boguta et al. [Bog77, Bog83] is of special interest, since one can show that these approaches are strictly relativistically covariant, thermodynamically consistent and - as field theories - renormalizable. The relativistic mean field model discussed here consists of nucleons obeying the time-dependent Dirac equation, of a classical spin zero attractive meson field (sigma) obeying the Klein Gordon equation, of a spin one repulsive meson field (omega) obeying the Proca equation and a meson-baryon interaction between them. The resulting coupled field equations are solved simultaneously in a mean field approximation. The theory is treated in the Hartree approximation which yields an effective Lagrangian. The masses and coupling constants for the mesons are phenomenological and are adjusted to fit static nuclear matter properties.

The model Lagrangian density is

$$\mathcal{L} = -\bar{\psi}(\gamma_\mu \partial/\partial x_\mu + m_N)\psi - \frac{1}{2}(\partial\sigma/\partial x_\mu)^2 - U(\sigma) - \frac{1}{4}F_{\mu\nu}F_{\mu\nu} - \frac{1}{2}m_v^2\omega_\mu\omega_\mu + ig_v\bar{\psi}\gamma_\mu\psi\omega_\mu - g_s\bar{\psi}\psi\sigma, \quad (4)$$

where

$$F_{\mu\nu} = (\partial/\partial x_\nu)\omega_\mu - (\partial/\partial x_\mu)\omega_\nu . \quad (5)$$

The potential function is taken to be a quartic polynomial in the field σ [Bog77, Bog83].

$$U(\sigma) = \frac{1}{2}m_s^2\sigma^2 + \frac{1}{3}b\sigma^3 + \frac{1}{4}c\sigma^4 . \quad (6)$$

The addition of nonlinear terms to the Lagrangian (4) allows for a more realistic fit to other nuclear properties, such as the compressibility and effective nucleon mass.

3. Cold Nuclear Matter

For translationally and rotationally invariant infinite nuclear matter the field equations in the mean field approximation, $\sigma \to \sigma_0$, $\omega_\mu \to i\delta_{\mu 0}\omega_0$ are

$$m_s^2\sigma_0 + b\sigma_0^2 + c\sigma_0^3 = -g_s\rho_s , \quad (7)$$

$$m_v^2\omega_0 = g_v\rho_v , \quad \omega_i = 0,$$

where

$$\rho_v = \frac{2}{3\pi^2}k_F^3$$

is the vector density, referred to throughout the rest of the article as the baryon number density, while the scalar density is given by

$$\rho_s = \frac{4}{(2\pi)^3}\int^{k_F} d^3k \, \frac{m^*}{(k^2+m^{*2})^{1/2}} ,$$

and the effective mass of the nucleon

$$m^* = m_N + g_o\sigma_o . \quad (8)$$

Here we have written down the expressions for zero temperature matter, finite temperatures are discussed e.g. in [Bog81,The83]. The energy density e , pressure P and compressibility constant K at T = 0 are

$$\varepsilon = \frac{1}{2}(g_v/m_v)^2\rho_v^2 + \frac{4}{(2\pi)^3}\int^{k_F} d^3k(k^2+m^{*2})^{1/2} + U(\sigma), \quad (9)$$

$$P = \rho_v^2(d/d\rho_v)(e/\rho_v), \quad (10)$$

$$K = \rho_v^2(d^2/d\rho_v^2)(e/\rho_v), \quad (11)$$

respectively. The energy of a particle moving through matter with momentum k is given by

$$E = g_v\omega_o + (k^2 + m^{*2})^{1/2} \quad (12)$$

$$= (k^2 + m_N^2)^{1/2} + U_{eff},$$

where U_{eff} is the effective nuclear potential

$$U_{eff} = E - [(E-g_v\omega_o)^2 + m_N^2 - m^{*2}]^{1/2}. \quad (13)$$

This model has been applied to dynamical calculations by Cusson et al. and will be discussed in Chapter II. Let us here discuss the equation of state resulting from these relativistic mean field theories for infinite nuclear matter, i.e. neglecting the space- and time derivatives in the equations of motion, and assuming thermal equilibrium. Fig. I.2 shows the compression energy, $E_c(\rho)$ of nuclear matter as calculated in the relativistic field theory [Bog83] with additional nonlinear terms in the Lagrangian (solid lines) and in non-relativistic many-body calculations using the variational method (dots).

It is found that the results of both approaches agree for $\rho < 1.2\ \rho_o$ for any reasonable set of parameters for the incompressibility coefficient K and effective nucleon mass m^* at saturation density ρ_o. However, at higher densities $\rho > 1.2\ \rho_o$ the nuclear equation of state is so sensitive to K and m^* at ρ_o that differences of several hundred percent

arise even if K and m^* are only varied within their present experimental 10-20% uncertainties. These results demonstrate that even a precise determination of the nuclear properties at normal groundstate densities does not enable us to predict the high density behavior of nuclear matter with reasonable accuracy. A theoretical determination of these properties is also very difficult in view of the fact that many body forces can play an essential role, in particular at high densities. Hence experiments which probe the dense nuclear matter directly must reinvigorate the quest for the high density equation of state of strongly interacting matter.

4. A Phenomenologigal Ansatz for the Equation of State

Unfortunately a field theoretical treatment beyond the mean field approximation is not yet developed. To describe the collision dynamics in a time dependent theory, semiclassical approaches must be used which include the nuclear potential, but also the effects of two body collisions (see Chapter II). For these approaches phenomenological equations of state have been developed. In the following we present the equation of state in such a phenomenological theory, and study further simplifying assumptions. The compression energy $E_c(\rho)$ incorporates phenomenologically the nuclear binding energy, the Fermi energy of the nucleons, hard core effects and the exchange part of the nuclear forces. It is often loosely refered to as the "nuclear equation of state". Two commonly used functional forms for $E_c(\rho)$ originate from the extended liquid drop model of Scheid and Greiner [Sch68]:

$$E_c(\rho) = K_l(\rho-\rho_o)^2/18/\rho/\rho_o \quad (14a)$$

$$E_c(\rho) = K_q(\rho-\rho_o)^2/18/\rho_o^2 \quad (14b)$$

the first being refered to as the linear- and the second as the quadratic EOS, respectively, in accord with their asymptotic increase with density.

5. Finite temperatures

The temperature of the system is the second thermodynamic variable of importance for the equation of state. The total energy of the system at finite temperature is being described by the interaction energy plus the kinetic energy of the particles in the system. The latter is given by interacting relativistic Fermi- Dirac and Bose-Einstein distributions, hence the total energy per baryon is given by [Hei79,Hah85]

$$W = U + \sum_{i=1}^{\sigma_b} \left(\rho_{i\circ} m_i c^2/\rho + 4\pi g_i/\rho/(2\pi hc)^3 \int_{m_i c^2} \frac{\varepsilon^2\sqrt{(\varepsilon^2-m_i^2c^4)}}{\exp[\varepsilon/T]-1}\, d\varepsilon \right) +$$

$$+ \sum_{i=\sigma_b+1}^{\sigma} 4\pi g_i/\rho/(2\pi hc)^3 \int_{m_i c^2} \frac{\varepsilon^2\sqrt{(\varepsilon^2-m_i^2c^4)}}{\exp[(\varepsilon+U-\mu))/T]+1}\, d\varepsilon \qquad (15)$$

where the first sum runs over the Bose-degrees of freedom, the pion, the η-meson, and heavier mesons, while the second sum is over all the excited states of the nucleon - the Δ (1232) resonance being the most important resonance in the GeV/nucleon energy region. Here it is assumed that all nucleonic resonances feel the same interaction energy per particle U, which is assumed to depend only on the total baryon density ρ [Hei79,Hah85]. The potential energy must be included into the Fermi- Dirac distribution function in a selfconsistent treatment.

The baryons are assumed to be in chemical and thermal equilibrium and therefore have the same chemical potential μ. Both the chemical potential and the interaction potential for the Bosons are taken to be equal to zero. ρ_i° is the contribution of the Bose ground-state to the density of

the boson-phases. The connection between the baryon density and the chemical potential reads

$$\rho = \sum_{i=\sigma_b+1}^{\sigma} 4\pi g_i/(2\pi hc)^3 \int_{m_i c^2} \frac{\varepsilon\sqrt{(\varepsilon^2-m_i^2c^4)}}{\exp[(\varepsilon+U-\mu)/T]+1}\, d\varepsilon \qquad (16)$$

The number of mesons can be calculated via

$$N_i = g_i/\{\exp(m_i c^2/T)-1\} + 4\pi g_i V/(2\pi hc)^3 \int_{m_i c^2} \frac{\varepsilon\sqrt{(\varepsilon^2-m_i^2c^4)}}{\exp[\varepsilon/T]-1}\, d\varepsilon \qquad (17)$$

We also need the connection between U and the compression energy E_C. For T → 0, eq. (16) becomes

$$(\mu-U)^2 = m^2c^4 + (\rho C/g)^{2/3} \qquad (18)$$

with $C = 6\pi^2(hc)^3$. In the same limit, we get for eq. (15)

$$W(T=0) = 0.75X + U + \frac{m^2c^4}{8}\left\{\frac{3X}{X1^2} - \frac{3m^2c^4}{X1^3}\ln[(X+X1)/mc^2]\right\} \qquad (19)$$

with g = 4, mc^2 = 939 MeV, $X=\sqrt{(m^2c^4 + X1^2)}$, $X1=(\rho C/g)^{1/3}$ assuming that for T=0 only the nucleonic ground state is populated, which should be true for small densities. This point can be questioned, if the nucleon-Δ-interaction is much stronger than the nucleon-nucleon-interaction [Bog81]. Expanding (18) and (19) for small densities, we obtain the well known approximation for the energy

$$\mu - U \approx mc^2 + 1/2\ X1^2/mc^2 + \ldots \qquad (20)$$

$$W \approx U + mc^2 + 0.3\ (\rho/\rho_\circ)^{2/3} h^2/m\ (6\pi^2\rho_\circ/g)^{2/3} + \ldots \qquad (21)$$

The difference between the exact expression (19) and the approximation (21), is about 1 MeV for $\rho/\rho_\circ = 3$. By comparing (1) and (19) we finally get the relation between U and E_C:

$$U(\rho) = E_C + W_o - 0.75\ X - \frac{m^2c^4}{8}\left\{\frac{3X}{X1^2} - \frac{3m^2c^4}{X1^3}\ln[(X+X1)/mc^2]\right\} \qquad (22)$$

For the pressure, we have [Hei79,Hah85]

$$P = -T\sum_{i=1}^{\sigma_b} 4\pi g_i/(2\pi\hbar c)^3 \int_{m_ic^2}^{\infty} \varepsilon\sqrt{(\varepsilon^2-m_i^2c^4)}\ \ln(1-\exp[-\varepsilon/T])d\varepsilon$$

$$+ T\sum_{i=\sigma_b+1}^{\sigma} 4\pi g_i/(2\pi\hbar c)^3 \int_{m_ic^2}^{\infty} \varepsilon\sqrt{(\varepsilon^2-m_i^2c^4)}\ \ln(1+\exp[(\mu-U-\varepsilon)/T])d\varepsilon$$

$$+ \rho^2 \frac{\partial U}{\partial \rho} \qquad (23)$$

and for the entropy per baryon

$$S/N_B = P/\rho/T - \frac{\rho}{T}\frac{\partial U}{\partial \rho} - 1/N_B \sum_{i=1}^{\sigma_b} g_i \ln(1-\exp[-m_ic^2/T])$$

$$+ (W-\mu)/T = -\frac{\partial \Omega}{\partial T/\mu,V} \qquad (24)$$

6. Pionization in Hot Systems - Formation of the Hadron Plasma

These equations have been used in simplified models of heavy ion reactions [Hah85] to extract the temperature from pion multiplicities. The dependence of the number of pions per nucleon on the temperature as calculated with the above approach, which includes all firmly established resonances, the pion and the η meson, are shown in Fig. I.3. Observe that the pion yield increases rapidly with temperature from zero to about one per nucleon at T ≈ 100 MeV, and then flattens out - nuclear matter is gradually transformed into a hadron plasma. This becomes obvious in Fig. I.4, which shows the distribution of pions over the various pion producing channels [Hah85]: At low energy, temperatures of the order of 50 MeV or less, most of the pions reside in the Bose condensed zero momentum state. At higher

temperatures, the pion yield is due to nuclear resonances. The δ-(1232) resonance is of particular importance in the BEVALAC energy regime, $E_{lab} \approx 1$ GeV/nucleon, while the more massive resonances become important at temperatures above T ≈ 100 MeV. Fig. I.3 can be used to extract the temperatures in the moment of pion emission from the observed pion yields [Hah85]. One finds that the temperature rises smoothly with the bombarding energy, reaches about T = 100 MeV at the top BEVALAC energies and can be extrapolated to temperatures exceeding the critical temperature for deconfinement, T ≈ 200 MeV, at energies in the range of relativistic heavy ion facilities presently under construction at CERN and Brookhaven, $E_{lab} > 10$ GeV/nucleon (see Fig. I.5). This equation of state is too complicated to be of practical importance for many three dimensional model calculations. Therefore we will now discuss simpler approximations widely used in practical applications to determine the energy and density dependence of the thermal energy.

The simplest ansatz for the thermal energy is the classical ideal gas $E_T = 3/2\ T$. This is actually the asymptotic value for the full non-interacting non- relativistic Fermi gas, i.e. it neglects the influence of the interactions on the thermal energy, but it contains the Fermi degeneracy energy - this means $E_T = 3/2\ T$ is the full kinetic energy, the degeneracy energy should be subtracted from the compressional energy if this approximation is used [San85]. However, the classical approximation is only reasonable anyhow if the temperatures are considerably larger than the chemical potential, i.e. the Fermi energy at a given density. On the other hand, for temperatures below the Fermi energy, the Fermigas expansion has been used:

$$E_T(\rho,T) = \frac{\beta}{2}\,\rho^{-2/3}\,T^2 = \frac{S^2}{2\beta}\,\rho^{2/3} = E_T(\rho,S) \qquad (25)$$

where

$$T = \left.\frac{\partial W}{\partial S}\right|_\rho = \frac{S}{\beta}\,\rho^{2/3}, \quad \beta = \left(\frac{g\pi}{6}\right)^{2/3}\frac{mc^2}{(\hbar c)}\,,$$

Here S being the nucleon's specific entropy.

At high temperatures, the production of resonances can be treated explicitely using the statistical approach developed above. However, a nice physical insight in the formation of resonances is obtained from the simpler classical gas ansatz for a mixture of resonances [Cha73,Hof76,Sto81]. As practically nothing is known about the N- N^* and N^*- N^* interactions, still assume that the N^* interaction only depends on the total baryon density. Therefore the compression energy $E_C(\rho)$ is unchanged (assuming that the subtraction of the Fermi degeneracy energy discussed above can be neglected). The first interesting quantity is the thermal excitation energy of the isobars. The thermal energy of a free ideal gas of resonances with mass $m_i c^2$ is

$$E_{T_i} = \frac{3}{2}\,T\,. \qquad (26)$$

The resonances can be viewed as excited nucleons (resonance pair production is not important at the above temperatures). A Boltzmann distribution for the excitation probability of the i-th resonance can be assumed at temperatures much above the Fermi energy. Baryon number conservation then yields the partitions [Hof76,Sto81]

$$\lambda_i = \frac{\tau_i e^{E_i/T}}{\sum \tau_k e^{-E_k/T}} \qquad (27)$$

where

$$\tau_i = \frac{g_i\; m_i^{3/2}}{g_n\; m_n^{3/2}} = \frac{(2\ \mathrm{Spin(i)}+1)\cdot(2\ \mathrm{Isospin(i)}+1)\;\; m_i^{3/2}}{4\qquad\qquad\qquad m_n^{3/2}} \qquad (28)$$

is the statistical weight factor of the i-th resonance, and $E_i=(m_i-m_0)c^2$ is the energy necessary for the resonance excitation.

The density of the i-th phase is then given by

$$\rho_i = \lambda_i\,\rho \qquad (29)$$

and the total energy density $e=\rho W$ is given as the sum over the energy densities of all phases

$$e = \sum_i e_i = \sum_i \rho_i W_i\,. \qquad (30)$$

As all baryons are assumed to interact only via $E_c(\rho)$, the energy per resonance i is

$$W_i = m_i c^2 + E_C + E_{T_i} \qquad (31)$$

which corresponds to a mean energy per nucleon

$$W(\rho,T) = m_o c^2 + E_C + \sum_i \lambda_i (E_{T_i} + E_i) \qquad (32)$$

where the mean thermal energy per baryon is

$$E_T = \sum_i \lambda_i E_{T_i} \qquad (33)$$

and

$$\Delta Mc^2 = \sum_i \lambda_i E_i \qquad (34)$$

is the mean additional rest mass due to the occupation of the resonances with $m_i > m_0$. A free pion gas can be included via a polynomial fit [Mek78] to give the pionic energy per baryon

$$E_\pi = 1.85\;\rho_0\;(T/m_\pi)^{9/2}\;m_\pi \qquad (35)$$

That this is of little importance at higher temperatures has been seen above in the evaluation of the relativistic integrals, because most of the pions stem from the decay of the Δ resonance. The direct production of pions due to pion Bremsstrahlung has also been studied, but we will not discuss this here [Vas80,84]

The pressure is evaluated from the relation

$$P = -\left(\frac{\partial E}{\partial V}\right)_S = \rho^2 \left.\frac{\partial W(\rho,T)}{\partial \rho}\right|_S \qquad (36)$$

Taking nucleons only, we immediately obtain

$$P = P_C + P_T = \rho^2 \frac{dE_C}{d\rho} + \rho^2 \left.\frac{\partial E_T(\rho,\sigma)}{\partial \rho}\right|_S . \qquad (37)$$

For the compression energy (14a) we obtain the compression pressure

$$P_C = \frac{K_\rho}{18\rho_o} (\rho^2 - \rho_o^2) . \qquad (38)$$

If the temperatures are small compared to the Fermi energy, the thermal pressure of the Fermi gas is given by

$$P_T = 1/3 \ \beta^{-1} S^2 \rho^{5/3} = \frac{1}{3} \beta \rho^{1/3} T^2 \qquad (39)$$

which leads to the relation

$$P_T = \frac{2}{3} \rho E_T . \qquad (40)$$

This equation is valid not only for the low temperature Fermi gas limit, but in fact it holds, in the nonrelativistic case, for any temperature and is also valid for a classical ideal gas as can be seen directly from $PV=NkT_k$ which is equivalent to $P = \rho \cdot T$ and with $E_T = 3/2\ T$ one has $P_T = 2/3\ \rho\ E_T$.

It is sometimes advantages to use this form for the pressure if resonances are included:

$$P_T = \alpha(\rho,E_T)\ \rho\ E_T . \qquad (40')$$

Here the cooling influence of the resonance is absorbed in the density and temperature dependence of α. Calculations then can be carried out with the usual form of the equation of state, eq. (37), supplemented with the temperature dependent α. Since a significant portion of the "thermal" energy goes into the excitation of hadronic resonances at higher bombarding energies, the relative reduction of the temperature is greatest here. This also reduces P_T, since part of the thermal energy now goes into the additional rest energy, Δm, of the resonances. The coefficient $\alpha(\rho,E_T)$ is almost independent of the density and depends strongly on E_T .

7. The Liquid-Vapour Transition

At intermediate bombarding energies, $E_{lab} \approx$ 100 MeV/nucleon, the temperatures are not high enough (T < 20 MeV) to cause substantial hadronization. However, another interesting phenomenon has been predicted to occur in the late stages of the collisions at these temperatures, namely when the density has dropped below normal nuclear matter density [Dan79]: The pressure diagram P(ρ,T=const) shown in Fig. I.6 [Sto83] exhibits the maximum- minimum structure typical for matter with long range attractions and short range repulsions, i.e. a van der Waals gas. This can be interpreted as a liquid vapour phase transition in low density nuclear matter. The nuclear equation of state exhibits a critical point at $\rho_c \approx 0.4\ \rho_o$ and $T_c \approx$ 18 MeV. It turns out that these values are not too sensitive to the details of the assumed interaction [Kap84,Cse85]. The liquid and the vapour phase can coexist in a well determined density regime once the temperature is less than the critical T_c(the shaded area in Fig. I.6). We

would like to point out that moderate T values are also achieved in the late expansion stage at higher energies due to the adiabatic cooling. The condition for thermodynamic stability of the two phase system is

$$T_{liquid} = T_{gas},$$
$$P_{liquid} = P_{gas}, \qquad (41)$$
$$\mu_{liquid} = \mu_{gas}.$$

At the critical point, $P_c(\rho_c,T_c)$, the isothermal has a saddle point, while for $T > T_c$ the isothermal pressure is monotonous. Then the liquid- vapour phase separation does no longer exist, and this phase is therefore called the fluid phase.

The occurence of a liquid- vapour transition in heavy ion collisions should manifest itself by substantial changes of the mass distributions of light and medium heavy fragments. We would like to point out the importance of the study of finite size effects and time scales and a detailed description of the correlations in the nuclear system in the late break- up stage of the reaction. For a detailed discussion we refer the reader to the excellent review article of Csernai and Kapusta [Cse85].

8. Abnormal Matter

The possible existence of density isomers in nuclear matter has been suggested repeatedly by many authors [Fee46,Bod71,Mig72,Lee74]. Lee and Wick observed that the nonlinear scalar meson self-interaction model - the chiral sigma model - can lead to an abnormal state at high density, $\rho/\rho_0 \approx 3$-5. They found that chiral symmetry is restored in this state - i.e. the nucleons become massless. The binding energy of this state can be enormous, leading to secondary minima in the compressional energy which are several

hundred MeV/nucleon deep. Another mechanism proposed to create secondary minima in $E_C(\rho)$ is the collective excitation of zero frequency spin- isospin modes in nuclear matter which carry the quantum number of the pion, therefore called pion condensation [Mig72,Wei76]. These conjectures have spurred considerable activity. However, it turns out that many of these proposals did either not attempt to describe the nuclear equation of state at other densities or else, as in the case of the linear sigma model, the description of the known properties of nuclear matter was incorrect. Since the existence of isomeric superdense matter is speculative, it is desirable to study this question in models which describe normal nuclear matter in a selfconsistent way. Fig I.7 shows a recent calculation [Bog82] which fulfills this requirement and still predicts abnormal superdense states. The model used is the relativistic mean field theory discussed above, which is well able to describe normal nuclear matter. The abnormal state comes in by introducing the Δ- resonance into the theory. The occurence of abnormal state depends now on the strength of the scalar interactions of the Δ. If the coupling constant for this interaction is only one third larger than the corresponding coupling of the nucleon, secondary minima occur in E_C and the abnormal state is predominantly populated by the resonance rather than the nucleon. A similar mechanism has been discussed at high temperatures, leading to abundant resonance formation above a critical temperature [Hei79,Gar79]. Since the scalar coupling of the Δ is unknown, a possible existence of these baryonic resonance isomers can not be ruled out a priori. Only by doing a careful analysis of high density experiments can this question be settled.

9. Deconfinement and Chiral Transition - Creation of Quark Matter

A transition from the deconfined quark-gluon plasma phase to confined color singlet states has (probably) occured during the rapid expansion of the early universe. Temperatures were very high but the net baryon charge was small. Therefore one can assume zero baryon chemical potentials in calculating the thermodynamic properties of strongly interacting matter in the early universe. It is sought to re-establish these conditions and thus enable a study of quark deconfinement in the laboratory via nuclear collisions at ultrarelativistic energies, $E_{c.m.} > 20$ GeV/N [QM79,QM80,QM82, QM83,QM84; see also the recent review Cle85]. The energy densities attainable in both the central rapidity region, i.e. the nucleus- nucleus center of momentum frame, as well as in the fragmentation regions have been estimated to be 1-2 GeV/fm^3. This range of values coincides with the energy densities at which the deconfinement transition is predicted by SU(N) Yang Mills theory (pure gluon matter) on the lattice [Cle85]. The Monte Carlo data indicate a first order phase transition at temperatures of about T = 190 MeV and zero baryon density, as seen in Fig. I.8 [Eng82].

Unfortunately to date there is only very limited information available about the high density (high chemical potential) region. Lattice QCD calculations of the thermodynamic properties of a plasma with light quarks included are hampered by severe theoretical difficulties: The introduction of fermions on the lattice is at this time only feasible in the quenched approximation, i.e. quarks have to aquire a large mass $m_q >> T_c$ so that the hopping parameter $(1/m_q)$ expansion converges [Cle85]. Detailed nonperturbative calculations for the situation expected to occur in violent nuclear collisions, a plasma of light quarks and antiquarks plus gluons, can

therefore not be studied to date. Furthermore, inclusion of fermions requires that the charge and baryon number assume integer values for color singlet states. These problems have been studied but so far without success.

The behaviour of the confined phase, i.e. hadron matter, can be described by the effective relativistic field theory of strongly interacting matter discussed in section I.2. This approach has been applied successfully to describe known properties of nuclei and nuclear matter. Though developed for normal nuclear systems, this theory may turn out very useful for a phenomenological approach to the phase transition [The83]: A sharp rise is observed for zero chemical potential in the normalized energy density ϵ/T^4. A phase transition occures at a critical temperature T_c = 190 MeV, with quite similar thermodynamic appearance as the one observed for SU(2) and SU(3) Yang Mills theory on the lattice; the order of the phase transition depends on the strength of the coupling constants [The83]. Furthermore, chiral symmetry is restored in this theory just above the critical temperature. The theory does not incorporate deconfinement, though.

Hence, a different approach is necessary if one wants to study deconfinement and the quark- gluon plasma phase at least qualitatively. One can approach the transition region from high temperatures, making use of a perturbative theory of QCD to estimate the thermodynamic properties of a plasma of light quarks and gluons at finite chemical potential μ and temperature T. We would like to emphazise that sizable nonperturbative corrections can be done, but the results should still be taken only as what they are intended to be, namely a qualitative handle on the unsolved nonperturbative treatment [Sto84,Cle85].

For zero temperature, the thermodynamical potential can be written as a perturbative expansion P_{pert} in α with terms up to order $\alpha^2 \ell n \alpha$, a vacuum pressure contribution Λ_{vac} (the Bag constant B in the MIT model [Cho74]) and an instanton term P_{inst} which takes non-perturbative effects partially into account [Shu80]:

$$P = P_{pert} + P_{inst} - \Lambda_{vac} . \tag{42}$$

$$P_{pert} = n_f \frac{\mu^4}{4\pi^2} \left[1 - \frac{2\alpha}{\pi} - \frac{\alpha^2}{\pi^2} \left(n_f \ell n(\alpha n_f) - .74\, n_f + 7.78 \right)\right]$$

$$P_{inst} = \frac{8}{3} C \Lambda_{vac} n_B^{-5/3}$$

where n_f and n_B are the number of quark flavors and baryon density, respectively and C=1000 MeV fm^5. The dilute instanton gas term increases the pressure substantially, which results in a large decrease in the energy per baryon. In fact, the energy per baryon of the quark phase falls below the nucleon mass for a wide range of densities. Therefore this term is often omitted from the calculations.

The thermodynamical potential of a finite temperature plasma at nonzero chemical potential has been calculated up to third order in α [Kap79]:

$$-\Omega = P = \frac{8\pi^2}{45} T^4 + \frac{7\pi^2}{60} n_f T^4$$

$$+ n_f \left(\frac{1}{4\pi^2} \mu^4 + \frac{1}{2} T^2 \mu^2 \right) - g^2 \left(\frac{T^4}{6} + \frac{5 n_f T^4}{72} + \frac{1}{8} n_f \left(\frac{\mu^4}{\pi^4} + \frac{2\mu^2 T^2}{\pi^2} \right) \right)$$

$$+ \frac{2}{3} \frac{g^3}{\pi^4} T (\pi^2 T^2 + \frac{1}{2} \sum_f \int_0^\infty \frac{dp}{E_p} n_p (p^2 + E_p^2))^{3/2} \tag{43}$$

The g^3 term in this expansion corresponds to the plasmon term in Quantum electrodynamics. For small temperatures, it does not converge to the zero temperature perturbation expansion. On the contrary, this term contributes a finite entropy

$$S(T=0) = d\Omega/dT = \text{const} \cdot \mu^2 \tag{44}$$

to the system even at zero temperature. Furthermore, its contribution to the energy per nucleon, which is zero (as it should be) for zero temperature, is large and negative for finite temperatures. In fact, the excitation energy per baryon is decreasing with increasing temperature. Because of this unphysical behavior the plasmon term is also omitted from the further calculations.

Following renormalization group arguments, the running coupling constant α can be written as

$$\alpha = \frac{4\pi}{11 - \frac{2}{3} N_f} \frac{1}{\ell n M^2 / \Lambda^2_{MOM}} \tag{45}$$

where N_f is the number of quark flavors involved, M is the effective momentum scale in the matter and Λ_{MOM} is the scale fixing parameter of QCD. The effective momentum scale is estimated to be [Kap79]

$$M^2 = \frac{4}{3} \sum_i \frac{n_i \langle \vec{p}^2 \rangle_i}{\sum_i n_i} \tag{46}$$

where the sum is over all the constituent species present, each with a number density n_i. $\langle \vec{p}^2 \rangle_i$ is the thermal average of the three momenta of species i. In the case of massless quarks, the above formula reduces to:

$$M^2 = \frac{4/3(16 \int_0^\infty dpp^4 N_p + 6 \sum_f \int_0^\infty dpp^4 n_p}{16 \int_0^\infty dpp^2 N_p + 6 \sum_f \int_0^\infty dpp^2 n_p} \qquad (47)$$

where

$$n_p = \frac{1}{e^{(P+\mu)/T}+1} + \frac{1}{e^{(P+\mu)/T}+1} \quad , \quad N_p = \frac{1}{e^{P/T}-1}$$

The Bose integrals are evaluated using the identity:

$$\int_0^\infty \frac{z^{x-1}}{e^z-1} dz = \Gamma(x)\zeta(x) \quad x \qquad (48)$$

where Γ is the factorial function and ζ the Riemann zeta function. The Fermion integrals for arbitrary chemical potential and temperature yield

$$M^2 = \frac{4}{3} \frac{(16 \cdot 4! \zeta(5) T^5 + 6 \sum_f \int_0^\infty dp P^4 n_p}{(16 \cdot 2 \cdot \zeta(3) T^3 + 6 \sum_f \int_0 dp P^2 n_p)} \qquad (49)$$

They can be solved analytically for the limiting case T=0 and μ=0 only. For T=0

$$M^2 = \frac{4}{5} P_F^2 \qquad (50)$$

For μ=0

$$M^2 = 15.622 T^2. \qquad (51)$$

For finite μ and T the integrals have to be evaluated numerically. It is interesting to note that the numerical result can be approximated by $M^2 \approx 4/5\ \mu^2 + 15.622T^2$. This expression agrees within a few percent with the correct result. The theory therefore has two free parameters, namely the scale fixing parameter Λ_{MOM} and the energy density of the real vacuum , Λ_{VAC} . Λ_{MOM} and Λ_{VAC} can be determined by adjusting the pressure and energy density calculated in this approach at zero chemical potential to SU(N) Yang

Mills Monte Carlo data. One obtains [Cle85] Λ_{MOM}= 100 MeV and Λ_{VAC}= 190 MeV/fm^{-3}. These values are often adopted as reference parameters for simple calculations.

The energy density e, entropy density s, and baryon number ρ of the deconfined quark gluon phase are obtained from the thermodynamical potential via

$$e = -\mu \frac{\partial \Omega}{\partial \mu} - T \frac{\partial \Omega}{\partial T} + \Omega \qquad (52)$$

$$S/V = - \frac{\partial \Omega}{\partial T} \qquad (53)$$

$$\rho = - \frac{1}{3} \frac{\partial \Omega}{\partial \mu} \qquad (54)$$

The pressure P and energy density e of the plasma tend towards $\pm B_{vac}$, respectively for $\mu \to 0$. The running coupling constant exhibits, however, a pole at chemical potentials on the order of 100 MeV, so the curves can not be continued below this value of μ. It is interesting to note that this chemical potential corresponds to zero baryon number density. Hence, the unphysical pole in the coupling constant can be avoided by plotting the thermodynamic variables as a function of the baryon number density ρ.

To do this let us use for simplicity the MIT bag model which describes hadrons and - for this matter - also quark- gluon plasma as a volume in space from which the true vacuum has been expelled - it is filled with color carrying objects, i.e. quarks and gluons, which can not exist in the true vacuum. The bag is a color singlet state, for which a finite energy can be calculated. One can show that this simple bag model fits the mass spectrum of the light hadrons quite convincingly, if the following conditions are fulfilled:

(a) The bag, i.e. the volume in which the quarks move, has a constant positive energy density, $B = \Lambda_{VAC}$, which therefore increases infinitely with the bag volume. This bag energy accounts for the quark confining potential, which does not allow the separation of single quarks from each other.

(b) The zero point motion has to be included for quarks which move within the small volume of a hadron.

(c) The energy of the quarks is included by solving the Dirac equation for a bound quark state inside the bag.

(d) Low-order terms in the quark-gluon coupling constant are additionally included to take into account the mutual interactions more realistically.

For the extended quark gluon plasma the zero point motion can be neglected, as the bag here is supposed to be much larger than a hadron bag. For the kinetic energy of the quarks the Fermigas expression for ultra-relativistic particles yields for zero temperature

$$E_{F_Q} = \frac{3}{4} \left(\frac{6\pi^2}{g_Q}\right)^{1/3} \hbar c \, \rho_Q^{1/3} \, . \qquad (55)$$

From the quark Fermi energy, the Fermi pressure may easily be calculated as

$$P_F = \rho^2 \left.\frac{\partial E}{\partial \rho}\right|_\sigma$$

which yields

$$P_{F_Q} = \frac{1}{4} \left(\frac{6\pi^2}{g_Q}\right)^{1/3} \hbar c \, \rho_Q^{4/3} \, . \qquad (56)$$

Thus, the Fermi energy and -pressure of the quark gas are related via

$$P_{F_Q} = \frac{1}{3} \rho_Q E_Q \, . \qquad (57)$$

The latter relation hold not only for T=0, but is actually valid for all temperatures, if massless particles are considered. The interaction of the quarks can be calculated from the running coupling and leads to an effective rise of the density-dependent Fermi energy [Stö77].

The density-dependent ground state energy of the quark bag is then given by

$$E_{BAG} = \sum_Q \left(\frac{\Lambda_{VAC}}{\rho_Q} + \frac{3}{4} \left(\frac{6\pi^2}{g_Q}\right)^{1/3} \hbar c (1+\alpha_c) \rho_Q^{1/3}\right) = \sum_Q \left(\frac{\Lambda_{VAC}}{\rho_Q} + E_{F_Q}\right). \qquad (58)$$

E_{BAG} is depicted in Fig. I.9. A typical curve for normal nuclear matter is also shown. Observe that near the normal ground state of nuclear matter, with the parameters used by Chodos et al. [Cho74] the quark matter energy is approximately 300 MeV/nucleon above the corresponding nuclear matter curve; here we used $\Lambda_{VAC} = 56$ MeV/fm³ and a constant $\alpha_c = 0.5$. However, for smaller B and α_c values, this difference is much smaller and the Quark energy may be lower than that of nuclear matter at high densities if a rather repulsive interaction is used for the nuclear matter. At moderate densities, however, quark matter is apparently energetically disfavoured compared to ordinary nuclear matter: Other sets of parameters and calculations with running coupling confirm this result [Sto84]; for Λ_{MOM}=100 MeV and Λ_{VAC}=190 MeV/fm³ the minimum energy per baryon of the deconfined phase is about 1.34 GeV, i.e. at an excitation energy per baryon 0.4 GeV higher than the ground state of nuclear matter. Only at high densities would the deconfined state be energetically favorable compared to confined matter at the same density.

The energy density at the crossing of the zero temperature compression energy of the quark matter equation of state with a conventional nuclear compressional energy is (1.4 - 1.8 GeV/N)·(0.6 - 1.2 baryons per

fm^3) = 0.8 - 2.2 GeV/fm^3, hence in the same ball park as the critical energy density obtained from Monte Carlo data at μ=0. The energy per particle depends on the choice of Λ_{VAC} and Λ_{MOM}. The energy gap is 0.9 GeV/N when Λ_{VAC} is increased to 450 MeV/ fm^3. These excitation energies may well be achievable in the fragmentation region of ultrarelativistic nuclear collisions.

Fig. I.10 shows the finite temperature phase equilibrium calculation done with this simple model [Mol84b,Sub85]. Observe the broad phase coexistence region of the quark- gluon plasma with the hadron plasma. A latent heat of about one to two GeV/fm^3 is to be released from the transition from the deconfined phase to the confined phase. This may proof a major handicap for the detection of the quark plasma if it is formed in ultrarelativistic nuclear collisions: Any signal from the interior of the system has to travel through the broad region of the phase coexistence and might be lost by the time it arrives at the surface of the system. This is particularly important for strongly interacting probes like antimatter [Hei84,Sub85] and strangeness [Raf82,Koc83], which will be subject to the complicated hadronic reaction dynamics which has to be tackled on top of the hard problems connected to the confinement problem itself. We will in the next chapter develop the theoretical framework neccessary for the description of the collision dynamics.

II. Many Body Theory of Nuclear Collisions

II.A Microscopic Kinetic Theory

1. Hierarchy of Theories

A comprehensive theory of nuclear collisions at high energies should describe relativistic quantum mechanical wave packets interacting simultaneously with all other wave packets via the correct two nucleon interaction for scattering inside the medium. Although this already neglects correlations, such a quantum mechanical treatment has not yet been attempted, but even the formulation of the interaction itself poses formidable problems. A natural suggestion - and one that has been very successfully employed in the cascade calculations - is to use measured free N-N cross sections as the primary physical input. This is legitimate if only binary N-N interactions occur and the scattered nucleons always reach their asymptotic states before encountering another nucleon; in other words: if the system is dilute. The cascade models and all other models that assume N-N scattering to occur at a point require diluteness.

If one does not want to assume diluteness, the simultaneous interaction of many nucleons has to be allowed. In this case scattering can no longer be described in terms of asymptotic states and cross sections, but an explicit interaction potential is required. The models that use this approach generally describe the nucleon motion in terms of classical trajectories and forces and are therefore often called classical dynamics models. In the relativistic realm there are huge problems even with the formulation of the theory - although it is possible to replace the Dirac equations by relativistic Newton's equations, the meson fields do not obey

classical equations even approximately. The only possibility to obtain a solvable model seems to be to ignore second quantization and treat the meson fields classically. The model which comes closest to solving the many-body aspect exactly are the non-relativistic equations of motion with two body potentials, which are actualy solvable. The major problem associated with this approach is that classical potentials provide only a poor approximation to N-N scattering and to nuclear binding properties. We will start the discussion of dynamical models with this approach.

2. Newtonian Force Model - the Classical Limit

Consider the classical Γ space description of an A body system with fixed degrees of freedom: we have in mind the colliding system of $A = A_P + A_T$ nucleons. Recall that Γ space is a 6A dimensional phase space and the state of the system is represented by one point in this space. Let $\rho(\vec{r}_1,\ldots,\vec{r}_A,\vec{p}_1,\ldots,\vec{p}_A,t)d\Gamma$ be the probability to find the system at the point $(\vec{r}_1,\ldots,\vec{r}_A,\vec{p}_1,\ldots,\vec{p}_A)$ in Γ space at time t: ρ is the A-body distribution function. The classical Liouville equation then follows from considering ρ as a probability fluid:

$$\frac{\partial\rho}{\partial t} + \sum_{i=1}^{A} \left(\frac{\partial}{\partial \vec{r}_i} \cdot (\rho \dot{\vec{r}}_i) + \frac{\partial}{\partial \vec{p}_i} \cdot (\rho \dot{\vec{p}}_i) \right) = 0 \qquad (1)$$

$$= \frac{\partial\rho}{\partial t} + \sum_{i=1}^{A} \left(\dot{\vec{r}}_i \cdot \frac{\partial\rho}{\partial \vec{r}_i} + \dot{\vec{p}}_i \cdot \frac{\partial\rho}{\partial \vec{p}_i} \right) .$$

Hamilton's equations then imply that:

$$\frac{\partial\rho}{\partial t} = \{H,\rho\} \qquad (2)$$

This is the classical Liouville equation which describes a microcanonical ensemble. For equilibrium, we have the condition $\{H,\rho\} = 0$.

The Newtonian Force Model in nuclear physics consists in solving Newton's or Hamilton's equations of motion for the A interacting nucleons. This is a theory for the full non-equilibrium classical situation. The NFM is thus more fundamental than a kinetic equation approach since it solves the Liouville equation.

Of course, there are then no quantum effects in this model. However, one does have information of the A body classical distribution function. One must however use a classical potential to study heavy ion systems. Over the years, nuclear physics has been driven to more and more complicated nucleon-nucleon interactions culminating e.g. in the Paris potential in order to accommodate the spin, isospin, etc. degrees of freedom.

A simple ansatz for a classical central potential that acts between each nucleon and all other A-1 nucleons consists of repulsive and attractive Yukawa terms [Mol 84a]:

$$V = (V_R\, e^{-k_R \cdot r} - V_A\, e^{-k_A \cdot r})/r. \qquad (3)$$

The parameters in the potential are chosen in a compromise between reproducing in a completely classical calculation the n-p differential scattering cross section at large angles $\theta_{CM} \approx 90^\circ$ (which influences the transverse momentum transfer the most) and at the same time giving reasonable binding energies and stable nuclei. Recall that the cross section is calculated classically from:

$$\frac{d\sigma}{d\Omega} = \frac{b}{\sin(\theta)} \frac{db}{d\theta} \quad . \qquad (4)$$

The experimental differential cross section is thus hard to obtain because of the purely quantum mechanical diffraction and exchange effects. A meaningful quantity to fit is the viscosity moment of the scattering cross section:

$$\sigma_v = 2\pi \int \sigma(\theta)\sin^2(\theta)d(\cos(\theta)) \qquad (5)$$

which is related to the viscosity and thermal conductivity in a Boltzmann equation approach [Bod 77].

In the NFM approach [Mol 84a], nuclei are described as an ensemble of protons and neutrons initially distributed randomly throughout a sphere with the nuclear radius $R = 1.2\ A^{1/3}$. Some cutoff on the interparticle positions, say 1.2 fm, must be imposed so that nucleons do not evaporate with large amounts of energy due to the classical potential. The nucleons are also given random Fermi momenta. To numerically simulate a collision process, the nuclei are Galilei boosted with the respective center of mass momenta at given impact parameter. The Newtonian equations of motion are integrated using a fourth order Adams-Moulton predictor-corrector method. Energy conservation to better than 1% is demanded. Then Newton's equations of motion are solved for the $A = A_P + A_T$ interacting nucleons:

$$\vec{F}_i = \frac{d\vec{p}_i}{dt} = -\frac{\partial U}{\partial \vec{r}_i} \qquad (6)$$

where $U(r_i) = \sum_{i<j=1}^{A} V(r_{ij})$.

We show in Fig. II.1 how a Nb + Nb collision at 400 MeV/nucleon evolves in this approach. Note the strong bounce or side-splash of nuclear matter [Mol 84a]. Calculations for many other systems have been done by other authors [Bod 77, Wil 77, Bod 80, Bod 81, Wil 78, Cal 79].

The main problem with this NFM approach is, of course, that classical potentials can provide only a poor approximation to n-n scattering and nuclear binding properties. For example, one finds that in order to simulate nuclear saturation, the two body potential must have a long range repulsive tail, as had been suggested earlier [Wil 78]. However, the NFM do come closest to solving the many-body aspect and probing finite range effects of the repulsive core. And it is of fundamental importance to nuclear physics that such a classical approach can with partial success describe heavy ion interactions in the intermediate energy range. In the relativistic generalization, there are additional complications [Kun 81]. One can write down relativistic Newtonian equations in place of the Dirac equations; but the meson fields do not obey classical equations. One possibility is to ignore second quantization and consider the meson fields as classical radiation fields, thereby studying also retardation effects.

3. N-body density matrix and TDHF

To solve even the quantum non-relativistic A body nuclear physics problem, one has to solve the time dependent Schrödinger equation [Sch 25]:

$$i\hbar \frac{\partial \Psi}{\partial t} = H\Psi \qquad (7)$$

where

$$\Psi = \Psi(1,2,\ldots,A,t) \qquad (8)$$

is the time dependent many-body wave function, A is the total number of nucleons, and H is the many body Hamiltonian. This is in general an impossible task just as the complete relativistic problem is.

Recall that an approach to the static many body problem for atomic electrons is Hartree's theory of the self-consistent field [Har 27]. There one uses a product of single particle wave functions, solves the single

particle wave equation neglecting the interaction, and secondly includes interactions and solves for new single particle wave functions. These two steps are iterated until one achieves consistency between the field and the electron density.

Static Hartree Fock theory differs in the inclusion of an exchange term [Foc 30]. The many body wave function is there approximated as a Slater determinant of single particle wave functions. The Hartree Fock hamiltonian contains the Hartree field and a non-local exchange term. Again one proceeds iteratively to achieve consistency between the field and the density. The HF state is a Fermi sea of particles with a sharp Fermi surface, since in constructing the HF determinant one selects the A lowest energy wavefunctions. Thus one may regard the HF state as the particle hole vacuum $|\ >$. Hole states are occupied single particle states and particle states are unoccupied [Row 70].

Static Hartree Fock theory has had much success in the shell models of electrons and later nucleons. In heavy ion nuclear physics however, one has a time dependent problem of A colliding nucleons. The complete nuclear wave function Ψ contains lots of information - perhaps more than we will ever need or be able to use. One therefore is justified in making some approximations to get a tractable time dependent Hartree Fock theory.

Nucleons are bound together solely by their mutual interaction: there is no external central field as with atomic electrons. The HF method is an approximation for reducing the problem of many interacting particles to one of non-interacting particles in a field. This neglects the residual interaction part of the nucleon-nucleon force. TDHF is used to describe

excited states and to take account of the long range or field part of the residual interaction.

Recall that TDHF can be derived in the formalism of second quantization [KO 75]. Let

$$|abc...\rangle = 1/\sqrt{A!}\sum_{(ab...)}\psi_a\psi_b...\mathrm{sgn}(abc...) \tag{9}$$

be the Slater determinant. The subscripts label space, spin, isospin, etc. Define the particle creation and destruction operators $a_i^\dagger$ and a_i, respectively. Antisymmetry and the Pauli principle yield the anti-commutation relations:

$$\{a_i^\dagger, a_j^\dagger\} = 0 \text{ and } \{a_i^\dagger, a_j\} = \delta_{ij}. \tag{10}$$

The state Ψ of the nucleus is then a linear combination of such Slater determinant kets.

The many body Hamiltonian is

$$H = T + V$$

$$= \sum_{ij} T_{ij} a_i^\dagger a_j + \frac{1}{2}\sum_{ijkl} U_{ijkl}\, a_i^\dagger a_j^\dagger a_l a_k \tag{11}$$

where the kinetic energy is a single particle operator and U is the two body interaction. The one body density matrix is

$$\rho_{ji} = \langle\Psi|a_i^\dagger a_j|\Psi\rangle\ . \tag{12}$$

The von Neumann equation

$$i\hbar\, d\rho/dt = \langle\Psi|[a_i^\dagger a_j, H]|\Psi\rangle \tag{13}$$

follows from the Schrödinger equation and the assumption that H is hermitean After inserting the many body Hamiltonian and considerable algebra, this time dependent density equation will not reduce to a purely one body equation. The two body force couples ρ to $\rho^{(2)}$ the two body density matrix.

This is the BBGKY hierarchy [Koo75]. The TDHF approximation is to assume that

$$\rho^{(2)}_{ijkl} = \rho_{jk}\rho_{il} - \rho_{jl}\rho_{ik} \cdot \tag{14}$$

This terminates the BBGKY hierarchy and yields the TDHF equation

$$i\hbar\, d\rho/dt = [h,\rho] \tag{15}$$

where h is the HF hamiltonian:

$$h = \sum_{ij} (T_{ij} + \sum_{kl} (V_{ikjl} - V_{iklj})\rho_{lk}) \cdot \tag{16}$$

It is not difficult to show that particle number, energy, and Slater-determinantness are conserved in TDHF [Koo75]. Furthermore, each of the single particle orbitals satisfies the time dependent Schrodinger equation with the HF hamiltonian h.

TDHF has been applied with some success at energies up to 10 MeV/nucleon. Fusion, compound nucleus formation, dissipation, strongly damped collisions, shock wave propagation, and fragmentation are all found in TDHF [Bon 76]. Beyond this range, mean field theory is not sufficient because of the lack of two body collisions and that the TDHF model assumes a long mean free path for the nucleons. The mainly potential scattering of TDHF implies only a single particle viscosity so that the nuclei are rather transparent for $E_{CM} > E_F = 38$ MeV. This transparency is illustrated in Fig. II.2 for Kr (85 MeV/nucleon) + Kr [Stö80].

To go beyond TDHF, consider that some perturbing two body interaction causes particles to scatter from their unperturbed orbitals. In first order perturbation theory, the perturbed wave function is:

$$|\Psi\rangle = |\Psi_o\rangle + 1/i\hbar \sum_{klk'l'} \int dt\, e^{i\omega t} V_{k'l'kl} a^\dagger_k, a^\dagger_l, a_l a_k |\Psi_o\rangle$$

$$= |\Psi_o\rangle - \sum_{klk'l'} \frac{e^{i\omega t}-1}{\hbar\omega} V_{k'l'kl} a^\dagger_k, a^\dagger_l, a_l a_k |\Psi\rangle \cdot \tag{17}$$

The density matrix then evolves according to the von Neumann equation:

$$d\rho_{ii}/dt = \frac{1}{i\hbar} \langle\Psi| a^\dagger_i [a_i, V] + [a^\dagger_i, V] a_i |\Psi\rangle. \tag{18}$$

Proceeding from here is complicated by the fact that one has to evaluate octupole Fock space operators. Let us thus consider the one body perturbing interaction as an illustrative example [Ber 84b]. Then the first order perturbed wave function is:

$$|\Psi\rangle = |\Psi_o\rangle - \sum_{kk'} \frac{e^{i\omega t}-1}{\hbar\omega} V_{k'k} a^\dagger_k, a_k |\Psi_o\rangle \cdot \tag{19}$$

In the one body case, it is easily shown using the anti-commutation rules that

$$[a_i, V] = \sum_j V_{ji} a_j \quad \text{and} \quad [a^\dagger_i, V] = -\sum_j V_{ij} a^\dagger_j. \tag{20}$$

With the additional assumption that the one body density matrix is diagonal

$$\rho_{ji} = n_i\, \delta_{ij} \tag{21}$$

we have for the occupation number n_i the equation

$$dn_i/dt = 1/i\hbar \sum_j V_{ij} \langle\Psi| a^\dagger_i a_j - a^\dagger_j a_i |\Psi\rangle. \tag{22}$$

Substituting the bra and ket first order perturbed wave functions, one gets terms of first, second, and third order in V. As Bertsch has noted [BE 84b], the first order terms are already in the mean field and the third order terms may be neglected with respect to the second order ones. A typical second order term is

$$\langle\Psi_o| a^\dagger_i a_j a^\dagger_l, a_l |\Psi_o\rangle = \langle\Psi_o| a^\dagger_i (\delta_{jl'} - a^\dagger_{l'} a_j) a_l |\Psi_o\rangle$$

$$= \rho_{li}\delta_{jl'} - \rho_{ljl'i}$$

$$= \rho_{1i}\delta_{jl'}-\rho_{jl'}\rho_{1i}+\rho_{ji}\rho_{1l'}$$

$$= n_i(1-n_j)\delta_{1i}\delta_{jl'}+ n_i n_1\delta_{ij}\delta_{1l'} . \quad (23)$$

Putting all this together and collecting terms, one finds that

$$dn_i/dt = 1/\hbar^2 \sum_j [2V_{ij} \sin(\omega_{ji}t)/\omega_{ji}][n_j(1-n_i)-n_i(1-n_j)]$$

$$= 2\pi/\hbar \sum_j V_{ij}^2 \delta(E_j - E_i)[n_j(1-n_i)-n_i(1-n_j)]. \quad (24)$$

where in the last step we extend the time limit to infinity and make use of one definition of the delta function. In the two body case, one expects by analogy the corresponding equation:

$$dn_i/dt = 2\pi/\hbar \sum_{ji'j'} V_{ijj'i'}^2 \delta(E_i+E_j-E_i-E_j)$$

$$[n_i n_{j'}(1-n_i)(1-n_j)-n_i n_j(1-n_{i'})(1-n_{j'})]. \quad (25)$$

This then provides some plausible justification for Uehling and Uhlenbeck's original ansatz for a collision term [Ueh33].

4. The Vlasov-Uehling-Uhlenbeck Equation

One way to include two body collisions is thus to couple to the TDHF equation a master equation involving the occupation probabilities of the single particle states n_i. The delta function which we find in the previous derivation is only present at the limit of vanishing single particle widths [Rem84]. We now replace the summation on the discrete single particle levels by continuous integrals over momenta:

$$\sum_{ji'j'} \rightarrow \int d^3p_2 d^3p_1' d^3p_2'/(2\pi\hbar)^3 \quad (26)$$

Furthermore, the continuous analog of the occupation probability is the Wigner function

$$f(\vec{p},\vec{r}) = \int d^3s\, e^{i\vec{p}\cdot\vec{s}/\hbar}\rho_{r+s/2,r-s/2}$$

$$= \int d^3q\, e^{-i\vec{q}\cdot\vec{r}/\hbar}\rho_{p+q/2,p-q/2} \quad (27)$$

which has the properties that

$$\rho(\vec{r}) = \int d^3p\, f(\vec{p},\vec{r})/(2\pi\hbar)^3 \text{ and } \rho(\vec{p}) = \int d^3r\, f(\vec{p},\vec{r})/(2\pi)^3. \quad (28)$$

One can also eliminate the matrix element $\langle \vec{p}_1\vec{p}_2|V|\vec{p}_1'\vec{p}_2'\rangle$ with the Born approximation:

$$\langle p_1p_2|V|p_1'p_2'\rangle^2 = (2\pi\hbar^2/\mu)^2 d\sigma/d\Omega . \quad (29)$$

Then one obtains the Uehling-Uhlenbeck collision term

$$\left(\frac{df}{dt}\right)_{coll} = -\int \frac{d^3p_2 d^3p_1' d^3p_2'}{(2\pi)^6} \sigma v_{12} \times$$

$$[ff_2(1-f_1')(1-f_2')- f_1'f_2'(1-f)(1-f_2)]\delta^3(p+p_2-p_1'-p_2') \quad (30)$$

where we have replaced f_1 by simply f. Finally, we may also write the total derivative as:

$$\frac{df}{dt} = \frac{\partial f}{\partial t} + \vec{v}\cdot\frac{\partial f}{\partial \vec{r}} + \frac{d\vec{p}}{dt}\cdot\frac{\partial f}{\partial \vec{p}} . \quad (31)$$

This last equation set equal to zero is the Vlasov equation. Finally combining these, we get the Vlasov-Uehling-Uhlenbeck equation:

$$\frac{\partial}{\partial t} f + \vec{v}\cdot\frac{\partial}{\partial \vec{r}} f - \nabla U \cdot \frac{\partial}{\partial \vec{p}} f = -\int \frac{d^3p_2 d^3p_1' d^3p_2'}{(2\pi)^6} \sigma v_{12} \times$$

$$[ff_2(1-f_1')(1-f_2')- f_1'f_2'(1-f)(1-f_2)]\delta^3(p+p_2-p_1'-p_2') \quad (32)$$

The main input is now a potential and the free nucleon-nucleon differential cross section. The Fermi-Dirac distribution, which is a solution of the Vlasov equation, is also the equilibrium solution of the collision term.

For the interaction U, a local Skyrme interaction is commonly used. Let us briefly review the Skyrme model. Skyrme's interaction can be written as a potential:

$$V = \sum_{ij} V^{(2)}_{ij} + \sum_{ijk} V^{(3)}_{ijk} \tag{33}$$

with two and three body parts. In configuration space, the two body part is:

$$V^{(2)}(\vec{r}-\vec{r}') = t_0(1 + x_0P_\sigma)\delta(\vec{r}-\vec{r}') + 1/2\ t_1(\vec{k}'^2\delta(\vec{r}-\vec{r}') + \delta(\vec{r}-\vec{r}')\vec{k}^2) +$$

$$t_2\vec{k}'\cdot\delta(\vec{r}-\vec{r}')\vec{k} + iW_0\vec{k}'\cdot\delta(\vec{r}-\vec{r}')\vec{\sigma}\hat{\ }\vec{k} \tag{34}$$

where

$$\vec{k} = (\partial/\partial\vec{r} - \partial/\partial\vec{r}')/2i \quad \text{and} \quad \vec{k}' = \vec{k}^{\dagger} \tag{35}$$

are the relative momentum operators and

$$P_\sigma = 1/2\ (1 + \vec{\sigma}_1\cdot\vec{\sigma}_2) \tag{36}$$

is the spin exchange operator. Also, the three body part is

$$V^{(3)}(\vec{r}_1,\vec{r}_2,\vec{r}_3) = t_3\delta(\vec{r}_1-\vec{r}_2)\delta(\vec{r}_2-\vec{r}_3). \tag{37}$$

The Hartree-Fock method is usually used with this Skyrme interaction, so that the nuclear ground state is represented by a slater determinant of single particle states Ψ. The expectation value of the total energy is then:

$$E = \langle\Psi|T + V|\Psi\rangle$$

$$= \int H(\vec{r})\, d^3r \tag{38}$$

where H is the Hartree Fock functional energy density. For the Skyrme interaction, this energy density is an algebraic function of only three quantities: the nucleon density, kinetic energy density, and spin density:

$$\rho(\vec{r}) = \sum_{i=1}^{A} |\psi_i(\vec{r})|^2\ ,\ \tau(\vec{r}) = \sum |\nabla\psi_i(\vec{r})|^2\ ,\ \vec{J}(\vec{r}) = -i \sum \psi_i^*(\vec{r})\cdot(\vec{\nabla}\psi_i(\vec{r})\hat{\ }\vec{\sigma}). \tag{39}$$

For the case of a symmetric nucleus, N = Z, and if there is no Coulomb field then the densities for neutrons and protons are equal:

$$\rho_n = \rho_p = 1/2\ \rho\ ,\ \tau_n = \tau_p = 1/2\ \tau\ ,\ \vec{J}_n = \vec{J}_p = 1/2\ \vec{J}. \tag{40}$$

Then the energy density simplifies to

$$H(r) = \hbar^2\tau/2m + \frac{3}{8}t_0\rho^2 + \frac{1}{16}\ t_3\rho^3 + \frac{1}{16}\ (3t_1 + 5\ t_2)\rho\tau +$$

$$\frac{1}{64}\ (9t_1 - 5t_2)(\nabla\rho)^2 - \frac{3}{4}\ W_0\rho\nabla\cdot\vec{J}\ . \tag{41}$$

In nuclear matter $\nabla\rho = 0 = \vec{\nabla}\cdot J$, $\rho = \frac{2}{3}\ k_F^3/\pi^2$, and $\tau = 3/5\ k_F^2\rho$. Then the binding energy per particle is

$$E/A = H/\rho = \frac{3}{5}\ E_F + \frac{3}{8}\ t_0\rho + \frac{1}{16}\ t_3\rho^2 + \frac{3}{80}(3t_1+5t_2)\rho k_F^2 \tag{42}$$

and the potential is

$$U(\vec{r}) = \frac{3}{4}\ t_0\rho + \frac{3}{16}\ t_3\rho^2 + \frac{3}{80}(3t_1 + 5\ t_2)\rho k_F^2. \tag{43}$$

Note that the potential and the energy density are related by $U = \left(\frac{\partial H}{\partial\rho}\right)_\tau$.

For colliding relativistic nuclei in the non-ultra-relativistic case, we can to first order neglect the problems of the relativistic field and calculate the potential locally. In the spirit of the Skyrme interaction in nuclear matter, we take the potential in a density expansion $U = a\rho + b\rho^2$ so that the binding energy is $E/A = \frac{3}{5}\ E_F + \frac{1}{2}\ a\rho + \frac{1}{3}\ b\ \rho^2$. The long range Coulomb and Yukawa interaction are neglected here; they become increasingly important at lower bombarding energies and for fragments emitted in the projectile and target rapidity region. We now measure ρ in units of $\rho_o = 0.17/fm^3$. Then we impose the three conditions E/A = - 16 MeV, $\frac{3}{5}\ E_F$ = 23 MeV, and K = 380 MeV. The saturation condition $\frac{\partial(E/A)}{\partial k_F} = 0$ is

equivalent to the zero pressure condition that $\rho^2 \frac{\partial (E/A)}{\partial \rho} = 0$ and the compressibility $K = k_F^2 \frac{\partial^2 (E/A)}{\partial k_F^2}$ may also be written as $K = 9 \rho \frac{\partial p}{\partial \rho}$. These three conditions (two are sufficient) fix the parameters a = -124 and b = 70.5. Similarly, if we take the expansion $U = a\rho + b\rho^{7/6}$ and impose K = 200 MeV, we find a = -356 and b = 303.

In Fig. II.3, we plot these two local Skyrme interactions and compare to the equation of state extracted recently from pion multiplicity data [Sto 82]. Note that the cascade and chemical model analysis, which extract a nuolear EOS from the differences of the calculated pion multiplicities and the observed pion yields, agree more closely with our stiff EOS.

5. Application of the VUU theory -

Study of the Non-Equilibrium and Quantum Effects

The VUU equation is still difficult to solve since it is a highly non-linear differential equation in six dimensional phase space. The close to the classical limit character of this equation does allow one to solve it in terms of quasi-particles whose mean positions are solutions of Newton's equations [Kru 85ab, Ber 84ab, Mol 84b, Mol 85a, Mol 85c]:

$$\vec{p}/m = d\vec{r}/dt \quad \text{and} \quad d\vec{p}/dt = -\partial U/\partial \vec{r} \ . \qquad (44)$$

We actually go beyond the VUU equation in including not only a mean field and Pauli Blocking of the final state, but also relativistic kinematics and particle production.

The stability of the ground state nuclei in this VUU theory is an important issue to address in testing the method [MO 85b]. In Fig. II.4, we show that the ground state nuclei are quite stable up to times of the order of 80 fm/c.

To solve the VUU equation fifteen collision simulations are followed in parallel and the ensemble averaged phase space density in a sphere of radius 2 fm around each particle is computed [KR 85a]. The ensemble averaging results in statistical fluctuations at the 10% level (at normal density) and thus reasonably smooth single particle distribution functions, which are used to determine the mean field and the Pauli blocking probability. About a hundred such parallel ensembles are followed to simulate an actual reaction.

A constant time-step integration routine is used to insure synchronization of the ensembles. The acceleration of the test particles due to the field gradient is calculated prior to each transport step, and is assumed to be constant within a synchronization time-step. The local gradient of the field is computed via a finite difference method between two hemispheres centered around the test particle. This method is analogous to Lagrange's method in fluid dynamics, in contrast to the space-fixed Eulerian mesh.

Protons, neutrons, deltas and pions of different isospin are included separately with their experimental scattering cross sections. The question of double counting of the mean field and the collision term is a basic restriction for the VUU approach. We take the following operational point of view: the phenomenological Skyrme potential incorporates the real part of the potential, i.e. the attractive one meson exchange (the linear term in U) and repulsive mean field interactions, while the two body

scattering accounts for the residual interactions. It should be pointed out that energy and momentum conservation is fulfilled in the present approach for individual two body scatterings and for the ensemble average on the mean (but not within each separate ensemble, because of the coupling between different ensembles --energy conservation problems have been studied for a similar approach by Koehler et al. [Koo80] using the relaxation time ansatz). The free particle cross sections have to be corrected for "in medium" effects, the most important one being the Pauli blocking of collisions. Two particles may undergo s-wave scattering if they approach each other with a minimum distance of less than $(\sigma/\pi)^{1/2}$ and if the final states are not Pauli blocked. The Pauli blocking factor for each nucleon is given by (1-f), and the scattering probability is then reduced by the Uehling-Uhlenbeck factor $(1-f_1)(1-f_2)$. The Pauli blocker has been tested on ground state nuclei and has an efficiency of about 97%.

The Pauli blocking is very important at even intermediate bombarding energies: even at 137 MeV/N, 80% of the attempted collisions are blocked due to lack of available final state configurations (Fig. II.5). Many of these attempted collisions are between nucleons of the same nucleus. The spectra of low energy (E < 80 MeV) nucleons are also influenced by Pauli blocking.

What is the effect of the collision term in the VUU theory? The system Ar + Ca has been studied in the mean field approximation without two body collisions, thus mimicking TDHF by solving the Vlasov equation - as far as we know this is the first time that a solution of the Vlasov equation in three dimensions has been done for nuclear collisions - the lack of two body collisions results in strongly forward peaked angular distributions, in qualitative agreement with 3D TDHF calculations [Sto 80] in this energy

regime. Figure II.6a shows the initial state in momentum space for Ar (137 MeV/N) + Ca; note that at this energy the Fermi spheres of target and projectile nuclei are well separated. The Ar projectile moves in the positive z-direction, while the Ca target moves in the negative z-direction in this center of mass frame. Fig. II.6b,c show the final state of this reaction as obtained in the present theory without and with the Uehling-Uhlenbeck collision term. Note that the momentum space distribution is practically unchanged in the mean field calculation--equilibration of the momenta is not observed--while the inclusion of the Uehling-Uhlenbeck collision term results in strong equilibration--the isotropy in Fig. II.6c is indicative of substantial thermalization. A convenient way to compare the results is to use the ratio of transverse to longitudinal momenta

$$R = 2/\pi \, \Sigma p_{per}/\Sigma p_{par} \qquad (45)$$

where p_{per} and p_{par} are the momenta perpendicular to and parallel to the beam. Comparing the ratio of final to initial R values, one finds 1.08 for the mean field only case and 2.05 for the mean field + collisions approach [Kru85b]. At lower energies, the comparison is not as dramatic; the initial R values are already high since the nuclei overlap more in momentum space--furthermore, most of the collisions are Pauli blocked. But the collision term always leads to increased isotropy. In configuration space, one finds the well known transparency when the Vlasov equation is solved and some stopping when the collision term is included: a substantial degrading of the initial momentum occurs once the collision term is included [Kru 85b, Aic 85].

Figure II.7 shows for C (85 MeV/nucleon) + C at b = 1 fm the time evolution in configuration space in the three dimensional TDHF and Vlasov

equation calculations [Aic85]. There is a very similar behavior in both the quantum mechanical and classical mean field theories: both calculations exhibit transparency and nearly identical small longitudinal and transverse momentum transfers. The lack of two body collisions results in strongly forward peaked angular distributions, in sharp contrast with the data in this energy regime. Both theories predict that for central collisions of C + C the nuclei slip through each other and survive the reaction rather intact. About 85% of the initial longitudinal momentum is conserved in the projectile- and target-like nuclear fragments. Hence the low angular momentum fusion window previously observed in TDHF calculations persists up to energies of 85 MeV/N. The TDHF calculations require more than an order of magnitude more computing time than the Vlasov approach.

The inclusion of the Uehling-Uhlenbeck collision integral into the Vlasov equation changes this drastically (Fig. II.7): each individual reaction can now be separated into two clearly distinct components. First, we observe again the slipped-through projectile- and target-like fragments which, however, now retain only about 40% of the nucleons and less than 20% of the initial longitudinal c.m. momentum. As we see in Fig. II.7, these slipped-through residues contain mostly particles which have not scattered at all.

The second component consists of 60% of the projectile nucleons which underwent at least one nucleon-nucleon scattering and form a non-equilibrated mid-rapidity system, which shows an almost isotropic emission pattern. It is interesting to note that projectile or target residues are not observed in the VUU approach if heavier symmetric systems are studied, e.g. for Ca + Ca at bombarding energies from 40 to 140 MeV/nucleon [KR 85]. At even higher energies, Ar (800 MeV/N) + Pb, complete stopping of the

projectile in the target has been predicted [Mol 85b, 85c]. What is then the reason for the incomplete deceleration of the nuclei in the present study? At these rather low energies we observe that a rather large fraction of the attempted nucleon-nucleon collisions is forbidden by the Pauli blocking of the exit channels. Thus the nucleon's mean free path is effectively longer as a result of the Pauli principle. Furthermore, the system studied above is rather small, hence the chances for a nucleon-nucleon collision to occur is smaller than in a bigger system.

At less central impact parameters, negative angle scattering is observed in both pure mean field approaches, and again the classical and the quantum approach agree remarkably well. The collision term results in less inward scattering. The midrapidity source is much less apparent; two slightly decelerated and excited residues survive the collision. The effect of the collision term is less dramatic at these larger impact parameters due to the smaller geometrical overlap of the nuclei, which reduces the number of nucleon- nucleon collisions even more.

A generalized 6-dimensional coalescence model may be used to find the nucleons bound in clusters, and prevent them from contributing to the proton cross sections [Kru 85b]. This is important at medium energies, where a large fraction of the emitted protons are found to be bound in fragments. In this scheme, a nucleon is part of a cluster if it is within a configuration space distance r_o from any other member of the cluster, and within a momentum space distance p_o from the center-of-momentum of the cluster. The sequential evaporation of protons from residual fragments is not included. The generalized coalescence prescription has been used to calculate inclusive proton spectra from the primordial nucleon distribution. We show the results for r_o=2.2 fm and p_o=200 MeV/c. These parameters are

adjusted to agree with the experimentally observed total cross sections. These values also yield correct clustering at t=0 fm/c: two heavy clusters, namely the ground state nuclei are then obtained. Variation of the coalescence parameters changes the magnitude of the cross sections, but has a negligible effect on the shape of the spectra. It is interesting to point out that the phase space volume spanned by these values is very close to $4\ h,^3$ the volume occupied by a fourfold degenerate Fermion. Our approach gets further support from the agreement of the predicted fragment yields as a function of fragment mass to the experimental data for masses 1 - 14.

Figure II.8 shows the comparison between calculated and measured proton spectra for 42 and 92 MeV/N Ar + Ca. The calculated absolute cross sections and the slopes of the spectra agree reasonably well with the data. In contrast, a simple cascade simulation, though appropriate for high energies, cannot reproduce the medium energy data.

In Fig. II.9 we show the reaction C (85 MeV/N) + C at b = 1 fm in more detail [Aic 85]. We display the initial and the final density profiles in configuration and momentum space. For the display of the final state Aichelin has distinguished between particles which did not undergo any collision ($N_c = 0$) and scattered particles with $N_c > 0$. The projectile-like fragments contain on the average 3-4 unscattered nucleons and about 1-2 scattered nucleons get trapped by the attractive mean field of the projectile-like fragment. The mid-rapidity region contains almost exclusively scattered particles. The high momentum components of the initial momentum space distribution get most effectively depleted by collisions because for them the Pauli blocking is least effective. The projectile-like fragments have densities around $\rho_o/2$. Hence their Fermi energy is lowered. A collective deceleration of these projectile-like

fragments is caused by the mean field. Those particles which have undergone collisions exhibit a nearly isotropic distribution in momentum space, with some forward-backward asymmetry.

The dependence of the nuclear stopping power on the target mass has also been studied [Aic85]. To accomplish this goal, central collisions of ^{12}C (85 MeV/nucleon) projectiles with 6 different targets from ^{12}C to ^{197}Au have been studied. The number of projectile nucleons undergoing at least one collision increases from about 60% for the C target to about 97% for the Au target. These collisions result in a momentum transfer on the target like residue of 44 MeV/c/nucleon (66% of the maximum momentum transfer possible, 67 MeV/c/nucleon) for Ni targets to 18 MeV/c/nucleon (80% of the maximum 22 MeV/c/nucleon) for Au targets. For the heavier targets ($A_T > 50$) this goes hand in hand with an almost complete stopping of the projectile in the target. This result is similar to what has been obtained with the VUU method for $^{40}Ar + ^{197}Au$ at 92, 400 and 800 MeV/nucleon bombarding energy [Mol85b]. The number of projectile nucleons being emitted without having had a collision up to a time t = 160 fm/c is shown in Fig. II.10 as a function of the target diameter D_t for 100 parallel runs each. Observe the exponential fall-off of N_0 with D_t. This fall-off can be reproduced by assuming that the mean free path of the nucleons in heavy ion collisions in this energy region is $\lambda = 2.6$ fm. This value is larger than the mean free path estimated from classical kinetic theory, $\lambda_c = (\sigma\ \rho)^{-1/2} = 1.4$ fm. This discrepancy is mainly due to the effects of the Pauli-principle, which blocks a fraction of the attempted collisions in the VUU approach in accord with the local phase space density. Other effects which

contribute are the density increase in the collision (which decreases λ) and the finite deceleration due to the mean field (which also decreases λ). Please note that for C and Al targets we observe projectile remnants surviving the interaction. Because of residual collisions within these final clusters - after the clusters have separated - we expect N_0 to be smaller than what is expected from the extrapolation from the heavier targets. This is indeed observed.

Let us examine the evolution of the single particle distribution function as obtained from the VUU approach for Ar (770 MeV/N) + Pb collisions. In Figs. II.11 and 12 we display projections of the distribution function into configuration and momentum space for this system. (Note that for ease of viewing, we have flipped both the x and z axis in the configuration space plots and also the p_z axis in the momentum space plots.) The collision term is essential at both intermediate and high energies, as one expects intuitively. Note in Figs. II.11 and 12 that at low impact parameter the Ar projectile is completely consumed by the Pb target as well in configuration as in momentum space. The t=0 configuration space plots show the correct nucleon-nucleon center of momentum frame Lorentz length contraction by a factor $1/\gamma = .85$. In configuration space, for t=10 fm/c, the squashed elliptical to octupole shape is an indication of the high density formed in these collisions. For example, at 1 fm impact parameter, the density within a sphere of radius 2 fm centered at the origin reaches 2.7 ρ_o at 5 fm/c time; then, the density falls very rapidly - by 17 fm/c it is below the ground state value. The directed sidewards flow of nucleons is easily seen in configuration space at b = 3 and 5 fm by the excess of nucleons in the quadrant with $x < 0$ and $z < 0$ (as opposed to $x < 0$ and $z >$

0) as early as t=20 fm/c. Spectator fragments are also observed, namely at 5 fm. The projectile is seen to not just shear off the target; it rather experiences a substantial transverse momentum transfer away from the region of high density - the bounce-off effect predicted earlier on the basis of nuclear fluid dynamics [ST 80, BU 83]. Thus simple geometric models can only be a very rough approximation to the more complicated reaction dynamics illustrated here.

The momentum space evolution of the single particle distribution function displayed in Fig. II.12 exhibits rapid equilibration at low impact parameters: observe that the projectile sphere in momentum space is rapidly depopulated by two body collisions at b = 1 and 3 fm. At t = 5 fm/c substantial filling of the nucleon-nucleon center of momentum region is observable, signaling the formation of a participant zone. At t = 10 fm/c, there are practically no nucleons left in the originally densely populated projectile momentum sphere; almost all of the projectile nucleons have been scattered out of their initial momentum states. At b = 1 fm, this scattering has been with about equal probability into the positive and negative p_x direction. At b = 3 fm, a preference for the positive p_x direction can clearly be observed - this is due to the expansion of the compressed participant matter away from the high density repulsive interaction into the vacuum. At t = 40 fm/c the number of hard nucleon - nucleon collisions has become negligible, the final state in momentum space is closely approached. Observe that secondary, tertiary, etc. collisions of the participants with the target spectator have resulted in a further decrease of the number of fast particles and in a more diffuse momentum distribution in the projectilehemisphere, with a very pronounced sidewards flow visible at b = 3 fm.

At the intermediate impact parameter, b = 5 fm, the situation is even more complicated: since projectile and target exhibit only about half overlap, there are a substantial number of projectile nucleons which do not experience collisions with the target nucleons. Hence the depopulation of the projectile momentum sphere is incomplete, part of the projectile is stopped and forms the participant zone together with the struck nucleons from the target, while the projectile spectators move ahead with nearly their initial longitudinal momentum. The behavior of the participant nucleons is nearly the same as at the lower impact parameters - equilibration is achieved rapidly (t = 10 fm/c) and sidewards flow is observed. The projectile nucleons which have not undergone collisions, and thus the projectile like fragments formed from them, exhibit a finite transverse momentum transfer into the same direction as the directed participant side splash. This bounce-off of the participants is a result of the repulsive interactions felt by the spectators in the vicinity of the compression zone. The simultaneous occurrence of this bounce off and the sidesplash has recently been experimentally observed [Gus 84] in symmetric systems with high statistical confidence. A theoretical analysis of these processes for symmetric systems is presently underway [Mol 85c].

The equilibration at low impact parameter goes hand in hand with nuclear stopping; without the collision term, the nuclei are transparent. As a reference case, we have also solved the Vlasov equation by turning off the collision term; then the final momentum distribution looks very much like the initial one, as is the case also at lower energies. An easily accessible experimental quantity is the longitudinal momentum p_z in the laboratory frame. The multiplicity dependence of this quantity should give information on the nuclear stopping. Note that initially the Ar nuclei

form a bump at the beam momentum whereas the Pb nuclei are at rest. In the final state at the lower impact parameter we see evidence of nuclear stopping: there is no projectile remnant and the Pb target is accelerated. At the higher impact parameter, there is less stopping: one sees some projectile remnants and the target-like fragments are accelerated less [Mol 84b].

6. Intranuclear Cascade simulations and their limitations

The intranuclear cascade model represents the limit of the VUU theory where there is no binding mean field, no sophisticated Pauli blocking. Historically, the intranuclear cascade idea is due to Serber [Ser 47]. His idea was that nuclear reactions at high energies might be understood in terms of a quite simple picture different from the description needed at low energies. Because the collision time between an incident high energy nucleon and a nucleon in the nucleus is short compared to the time between collisions of the nucleons in the nucleus, he inferred that the high energy reaction could be modelled as a cascade process. Collisions occur between the incident particle and those particles which are directly struck in the nucleus. This model was first investigated in two dimensions in 1948 by Goldberger [Gol 48] who performed his calculations by hand for the case of high energy neutrons interacting with heavy nuclei. The first fully three dimensional calculations were done by Metropolis et. al. in 1958 [Met 58] for incident protons and neutrons using the MANIAC computer; they also added a second stage to the cascade calculation during which the excited residual nucleus evaporates particles, as had also been suggested by Serber.

Many others have contributed to the development of the intranuclear cascade model. The two most commonly used versions of the

cascade code in the theory of high energy heavy ion reactions are due to Yariv and Fraenkel [Yar 81] and Cugnon et. al. [Cug 80, Cug 81, Cug 82]. What is the intranuclear cascade model as it is used in these codes? It is a microscopic simulation of a nuclear reaction at high bombarding energies. Nuclear collisions are treated as a superposition of independent two-body nucleon-nucleon collisions. Nucleons move on straight line trajectories (since there is no field) until they collide with a probability given by the free nucleon-nucleon scattering cross section. The creation of deltas, pions, and other particles and the interaction of all these particles occurs according to experimental cross sections. The intranuclear cascade models incorporate relativistic kinematics. Target and projectile nucleons are initialized in configuration and momentum space with random Fermi momenta and then Lorentz boosted to an appropriate frame, where the collision simulation proceeds. Momentum and energy are conserved in the particle-particle interactions and the evolution of the system is followedup to a time where the majority of interactions have ceased. Collisions are only Pauli blocked according to a simple criterion, say if the total center of mass energy is less than the Fermi energy in ground state nuclear matter or if the outgoing particle would scatter into momentum space regions originally occupied by projectile or target.

Both the Yariv-Fraenkel and the Cugnon cascade satisfy the above criteria. They differ in two respects: (1) the particles in the Yariv-Fraenkel simulation sit in a potential well of constant depth V_o; (2) in the original Yariv-Fraenkel approach the incoming particles (projectile nucleons) are cascading independently through a medium (the target) - in the updated version, this scheme has been improved by including the so-called cascade-cascade interactions - for a given cascade particle (a particle

which has undergone at least one collision) the other cascade particles are acting as a medium superimposed on the original target medium.

In the Cugnon cascade, one has the problem that the nucleons are not bound; hence one may get spurious effects due to nuclear instability, see Fig. II.4 [Mol 85b]. It is possible to bind the nucleons by letting each nucleon move only with the beam velocity until it interacts with another nucleon, at which point it 'remembers' it's Fermi momentum. Note however that the bound Cugnon cascade is theoretically not very satisfying either, since in real nuclei, nucleons can travel in all directions.

II.B Nuclear Fluid Dynamics

1. Conservation Laws and the Transition to Local Equilibrium

Just as in the classical case, one can derive from the VUU equation a general transport equation for a function f [Mak85, Mo185]. Assume for simplicity that the external force $\vec{F} = d\vec{p}/dt$ is momentum independent. Let us also re-write the VUU equation in the simple form:

$$\left(\frac{df}{dt}\right)_{coll} = \frac{\partial f}{\partial t} + \vec{v}\cdot\frac{\partial f}{\partial \vec{r}} + \vec{F}\cdot\frac{\partial f}{\partial \vec{p}} \quad . \tag{46}$$

Integration of this equation over p produces:

$$\frac{\partial f}{\partial t} + \nabla\cdot(\rho\vec{u}) = \int d^3p \left(\frac{df}{dt}\right)_{coll} \tag{47}$$

The term containing the external force vanishes by partial integration. Now the collision term describes the net rate of gain of particles at position $\vec{r}$ and with momentum $\vec{p}$. Since the collisions take place at a point and only redistribute particles in momentum space while conserving their number, the integral over all momenta must vanish. Thus we get the first equation of nuclear fluid dynamics, the continuity equation:

$$\frac{\partial f}{\partial t} + \nabla\cdot(\rho\vec{u}) = 0 \quad . \tag{48}$$

To obtain an equation for the momentum density, we integrate the VUU equation with a weight of $\vec{v}$:

$$\frac{\partial}{\partial t}(\rho\vec{u}) + \nabla\cdot\int d^3p \vec{v}\vec{v}f + \sum_j F_j \int \vec{v}\frac{\partial f}{\partial p_j} d^3p = 0 \quad . \tag{49}$$

Again the collision term yields a vanishing contribution, because momentum is conserved in the collisions locally. In the second term on the left, one may separate an average and a fluctuating part:

$$\int d^3p \vec{v}\vec{v}f = \int d^3p \vec{u}\vec{u}f + \int d^3p (\vec{v}-\vec{u})(\vec{v}-\vec{u})f + \int d^3p \vec{u}(\vec{v}-\vec{u})f + \int d^3p (\vec{v}-\vec{u})\vec{u}f \tag{50}$$

The last two terms vanish because the average of $\vec{v} - \vec{u}$ is zero. The fluctuating part defines the kinetic stress tensor:

$$\underline{P}(\vec{r},t) = \int d^3p (\vec{v}-\vec{u})(\vec{v}-\vec{u}) f(\vec{r},\vec{p},t) \quad . \tag{51}$$

Note that the pressure is identically zero only if all the particles have exactly the mean velocity $\vec{u}$. The external force contribution can be rewritten using

$$p_i \frac{\partial f}{\partial p_j} = \frac{\partial}{\partial p_j}(p_i f) - \delta_{ij} f \tag{52}$$

and then the first term on the right hand side vanishes in partial integration. The momentum conservation equation is then:

$$\frac{\partial}{\partial t}(\rho\vec{u}) + \nabla\cdot(\rho\vec{u}\vec{u}) = - \nabla\cdot\underline{P} + \frac{\rho}{m}\vec{F} \quad . \tag{53}$$

Define the energy density as:

$$\rho E = \frac{m}{2}\int d^3p \, v^2 f(\vec{r},\vec{p},t) \quad . \tag{54}$$

Then through the introduction of the average velocity ρE may be split up into a flow kinetic energy and a thermal contribution:

$$\rho E = \frac{m}{2}\rho u^2 + \frac{m}{2}\int (\vec{v}-\vec{u})^2 f(\vec{r},\vec{p},t) d^3p \quad . \tag{55}$$

Integrating the VUU equation with a weight of $mv^2/2$ gives

$$\frac{\partial}{\partial t}(\rho E) + \nabla\cdot\int d^3p \frac{m}{2} v^2\vec{v}f + \vec{F}\cdot\int d^3p \frac{m}{2} v^2 \frac{\partial f}{\partial \vec{p}} = 0 \tag{56}$$

where again the collision term gives no contribution because it conserves kinetic energy of the particles. The second term is split up into a number of parts:

$$\int d^3p \frac{m}{2}\vec{v}v^2 f = \int d^3p \frac{m}{2}(\vec{v}-\vec{u})^2(\vec{v}-\vec{u})f + \int d^3p \, f \frac{m}{2}u^2\vec{u} +$$

$$m \int d^3p \vec{u}\cdot(\vec{v}-\vec{u})(\vec{v}-\vec{u})f + \int d^3p \frac{m}{2}(\vec{v}-\vec{u})^2\vec{u}f$$

$$= \vec{q} \cdot \rho E\vec{u} + \vec{u}\cdot \underline{P} \qquad (57)$$

wherein the first term $\vec{q}$ describes the transport of thermal energy by thermal motion (thermoconductivity). The second and third term are combined to give the transport of total energy by collective flow and the last term describes the work done against the stresses. Finally the external force contribution can be re-written by partial integration [Mol85]:

$$\vec{F}\cdot\int d^3p \frac{1}{2} v^2 \frac{\partial f}{\partial \vec{p}} = -\vec{F}\cdot\int d^3p \vec{v} f = -\rho\vec{u}\cdot\vec{F} \qquad (58)$$

and the conservation of energy equation reads:

$$\frac{\partial}{\partial t}(\rho E) + \nabla\cdot(\rho E\vec{u}) = -\nabla\cdot(\vec{u}\cdot\underline{P}) + \rho\vec{u}\cdot\vec{F} \ . \qquad (59)$$

These then are the equations of nuclear fluid dynamics, which assume a local equilibrium, in contrast to the more general VUU theory which includes non-equilibrium phenomena. These are macroscopic equations which can be solved in three dimensions for two interacting nuclei.

2. Fluid Dynamics and the nucleon's mean free path

For the applicability of the fluid dynamical concepts it has to be ensured that fast equilibration and thermalization of the incident momentum and energy occurs in high energy heavy ion collisions. This is the case if the mean free path λ is small compared to the typical dimension, L, of the system

$$\lambda/L << 1. \qquad (60)$$

The mean free path λ is given by

$$\lambda = \frac{1}{\sigma\cdot\rho}$$

where σ is the total nucleon-nucleon scattering cross section and ρ is the actual nuclear density. For normal nuclear density ρ_o and a free n-n scattering cross section σ_{NN} ~ 30 mb at high energies (E_{Lab}>200 MeV/n), the mean free path is λ ~ 2fm, which is not too small against the nuclear dimensions L~10 fm [Sch68,Sch74a,Sch74b].

High relative momenta between nuclei, signifying no overlap in phase space, as well as the large longitudinal momentum decay length calculated from the free n-n scattering cross section were interpreted as a complete transparency for the two nuclei at high energies and as the death for compression (shock) waves at energies above 1 GeV/n [Sob75]. However, in the "formation flight" of ensembles of nucleons, collective scattering phenomena, namely the enlargement of the cross section due to precritical scattering close to phase transitions [Gyu77,Ruc76] and compression effects cannot be neglected, so that the scattering cross section and the density can be modified drastically leading to a decrease of the mean free path

$$\lambda \approx 1.4 \frac{\sigma_{NN}}{\sigma_{coll}} \cdot \frac{\rho_o}{\rho} \text{ fm} \ . \qquad (61)$$

The precritical scattering of nucleons in the vicinity of a phase transition point is in analogy to the critical opalescence, which is characterized by the great enhancement of the scattering cross section of light near a liquid-gas phase transition, or of the critical scattering of neutrons in ferromagnets near the Curie point [Sta71] or--as a last example--the critical scattering appearing in two colliding plasma beams: When the drift velocity of the two plasmas exceeds a critical value, unstable plasmon modes appear, resulting in a growth of strong electric fields, which greatly reduce the penetration depth of the two plasmon beams in comparison to values estimated from free two-body collisions. Thus the vicinity of a phase

transition--e.g. the onset of pion condensation or gluon condensation is expected to be marked by the occurrence of critical nucleon-nucleon scattering, i.e. a large enhancement (a factor of 2-4 for pion condensation) of the density-dependent n-n cross section [Gyu77,Ruc76).

This would mean that even at bombarding energies above one GeV/n nuclei do not become transparent to each other: On the contrary, very violent collisions can be expected. One should keep in mind, however, that nucleus-nucleus collisions are a quantum mechanical process. Hence--in the sense of quantum mechanical fluctuations--under the same initial conditions process with violent randomization (i.e. the occurrence of pronounced shock waves) may occur as well as processes with less pronounced interaction. It is a formidable experimental task to separate the former from the latter.

Indeed, recent experiments (which we shall discuss later) show that up to lab-energies of 4 GeV/n a considerable part (~30%) of the total cross section is due to violent events with very high multiplicities and large momentum transfer.

3. Nuclear fluid dynamics and quantum mechanics

Immediately after the discovery of quantum mechanics, the formal analogy of quantum mechanics to fluid dynamics had been discovered [Mad26]. One uses the Schrödinger equation

$$-\frac{\hbar^2}{2m}\psi + V(r)\psi = i\hbar\frac{\partial\psi}{\partial t} \tag{62}$$

and the separation of a phase S in the wave function

$$\psi(r,t) = \phi(r,t)\cdot e^{imS(r,t)1\hbar} \tag{63}$$

one gets

$$(-\frac{h^2}{2m}\nabla^2\phi + \frac{m}{2}\phi(\nabla S)^2 - ih\,\nabla\phi\cdot\nabla S - \frac{ih}{2}\phi\nabla^2 S + \nabla\phi)\cdot\exp[imS/h]$$

$$= (ih\frac{\partial\phi}{\partial t} - m\frac{\partial S}{\partial t}\phi)\cdot\exp[imS/h]. \tag{64}$$

Multiplication by $\psi^* = \phi\cdot\exp(-imS/\hbar)$ and separation of real and imaginary part results in

$$\frac{m}{2}\phi(\nabla S)^2 - \frac{h^2}{2m}\nabla^2\phi + V\phi = -m\phi\frac{\partial S}{\partial t} \tag{65}$$

and

$$\phi\frac{\partial\phi}{\partial t} + \phi\nabla\phi\cdot\nabla S + \frac{1}{2}\phi\nabla^2 S = 0\ . \tag{66}$$

respectively. The last equation may be transformed to

$$\frac{\partial}{\partial t}\phi^2 + \nabla\cdot(\phi^2\nabla S) = 0\ . \tag{67}$$

This is nothing else than the well known continuity equation describing the conservation of probability density in quantum mechanics. According to (63) the probability density is

$$\rho(r,t) = \phi^2(r,t) \tag{68}$$

and the probability current is

$$\vec{j}(r,t) = \phi^2(r,t)\cdot\nabla S(r,t) \tag{69}$$

following from the definition

$$\vec{j}(r,t) = \frac{\hbar}{2im}\left[\psi^*\nabla\psi - \psi\nabla\psi^*\right]. \tag{70}$$

From (68) and (69) a velocity field

$$\vec{v}(r,t) = \nabla S(r,t)$$

can be deduced with $\nabla\times\vec{v}=0$. Equation (65) may be treated similarly. After some manipulations and using eq. (67) one finds

$$\frac{\partial}{\partial t}(m\phi^2\nabla S) + \nabla\cdot(m\phi^2\nabla S\nabla S) = -\phi^2\nabla V + \phi^2\nabla\left(\frac{h^2}{2m}\frac{\phi\nabla^2\phi}{\phi^2}\right). \tag{71}$$

and with the definitions of ρ and $\vec{v}$ one finally obtains

$$\frac{\partial}{\partial t}(m\rho\vec{z}) + \nabla\cdot(m\rho\vec{v}\vec{v}) = -\rho\nabla V - \rho\nabla\left(-\frac{h^2}{2m}\frac{\sqrt{\rho\nabla^2\sqrt{\rho}}}{\rho}\right). \qquad (72)$$

that is identical with the conservation equation of the momentum with an external force due to a potential V. Only the last term on the right-hand side is new. It depends solely on density and may be interpreted as an inner pressure caused by quantum mechanical effects. It disappears in the classical limit of $h \to 0$.

Equations (67) and (72) have been obtained for the probability density of one single particle. Thus the conclusion of a quantum mechanical many body system, behaving like interpenetrating fluids with interaction, is obvious. It is important to note that (e.g. in contrast to kinetic theory) each single quantum mechanical particle is a continuum itself. Therefore the problem of granulation of the microscopical density does not occur. However, the main problem will be a reasonable definition for the many particle densities and velocities. An important question will be, whether all quantities entering the equations of motion may be described as functions of these macroscopic variables (and a temperature) or not.

4. Nuclear Fluid Dynamics and TDHF

For many particle systems it is also possible to derive continuity equations. However, the procedure is very lengthy as has been seen above. For reasons of simplicity, we will therefore restrict ourselves to a deviation by analogy of the hydrodynamic equations from the TDHF equations. That is less general but the principal argument [Won 77, Mar 77] is the same as the one used above in Chapter II.A. The TDHF equations are well known:

$$ih\frac{\partial}{\partial t}\psi_\alpha = -\frac{h^2}{2m}\nabla^2\psi_\alpha(r,t) + \psi_\alpha(r,t)\int d^3r'V(r-r')\sum_\beta \psi^*_\beta(r',t)\psi_\beta(r',t)$$

$$-\sum_\beta \psi_\beta(r,t)\int d^3r'V(r-r')\psi^*_\beta(r',t)\psi_\alpha(r',t) \qquad (73)$$

where ψ_α is the single particle wave function and $V(r-r')$ is the two particle interaction. In analogy to the results of the the previous section we define a many particle density and a many particle current density

$$\rho(r,t) = \sum_\alpha \psi^*_\alpha(r,t)\psi_\alpha(r,t) = \sum_\alpha \phi^2_\alpha(r,t) \qquad (74)$$

$$j(r,t) = \sum_\alpha j_\alpha(r,t) = \sum_\alpha \phi^2_\alpha(r,t)\nabla S_\alpha(r,t), \qquad (75)$$

with a separation of the one particle wave function as above.

$$\psi_\alpha(r,t) = \phi_\alpha(r,t)\cdot\exp\left[imS_\alpha(r,t)/h\right]. \qquad (76)$$

In complete analogy to the previous section, we then obtain again a continuity equation with the mean collective velocity being

$$\vec{v}(r,t) = \vec{j}(r,t)/\rho(r,t)$$

$$= \sum_\alpha \phi^2_\alpha(r,t)\nabla S_\alpha(r,t)/\sum_\alpha \phi^2_\alpha(r,t) \qquad (77)$$

$$= \left\{\sum_\alpha \rho_\alpha\vec{v}_\alpha\right\}/\left\{\sum_\alpha \rho_\alpha\right\}.$$

ρ_α and v_α again are the single particle quantities. The collective velocity therefore is the weighted average of the single particle velocities. Due to the average the velocity field $\vec{v}$ is no longer curl-free.

The derivation of the momentum equation again is completely analogous and can be written

$$\frac{\partial}{\partial t}\vec{j}(r,t) + \nabla\cdot\sum_\alpha(\phi_\alpha^2\nabla S_\alpha\nabla S_\alpha) = -\frac{1}{m}\sum_\alpha\phi_\alpha^2\nabla\left\{\frac{\phi_\alpha(-\frac{h^2}{2m}\nabla^2)\phi_\alpha}{\phi_\alpha^2}\right\}$$

$$-\frac{\rho}{m}\nabla\int d^3r'\, V(r-r')\rho(r') \qquad (78)$$

$$+\frac{1}{m}\int d^3r'\,\nabla V(r-r')\Big|\sum_\alpha\psi_\alpha^*(r)\psi_\alpha(r')\Big|^2 .$$

This form is not yet usable for a fluid dynamical description. For the transition to hydrodynamics all one-particle quantities have to be expressed by ρ, j and by a temperature field T.

We will start with the second term of Eq. (78). Introducing the collective velocity $\vec{v}$ (77) we get

$$\nabla\cdot\sum_\alpha(\phi_\alpha^2\nabla S_\alpha\nabla S_\alpha) = \nabla\cdot(\rho\vec{v}\vec{v} + \sum_\alpha\phi_\alpha^2(\nabla S_\alpha-\vec{v})(\nabla S_\alpha-\vec{v}))$$

$$= \nabla\cdot(\rho\vec{v}\vec{v} + \frac{1}{m}\underline{P}) \quad . \qquad (79)$$

with $\underline{P}$ being the (in analogy to kinetic theory) stress tensor

$$\underline{P} = m\sum_\alpha\phi_\alpha^2(\nabla S_\alpha-v)(\nabla S_\alpha-v), \qquad (80)$$

which results from the statistical deviations of the single particle velocities from the mean value v.

In order to reduce the potential terms in Eq. (78) we will use a separation of the n-n force into a short range, density dependent part V_s and into a long range part V_ℓ [Bet68].

$$V(r-r') = V_s(\rho(r))\delta(r'r') + V_\ell(r-r') \quad . \qquad (81)$$

The first (direct) potential term in (78) then becomes

$$\int d^3r'\, V(r-r')\rho(r') = V_s[\rho(r)]\rho(r) + U_\ell(r) \quad . \qquad (82)$$

U_ℓ is the mean potential, stemming from the long range interaction.

$$U_\ell(r) = \int d^3r'\, V_\ell(r-r')\rho(r') \quad . \qquad (83)$$

For the exchange part, the Slater approach is used, yielding [Mar 77]

$$\frac{1}{m}\int d^3r'\,\nabla V(r-r')\Big|\sum_\alpha\psi_\alpha^*(r)\psi_\alpha(r')\Big|^2$$

$$= -\frac{\rho}{m}\nabla\frac{\partial}{\partial\rho}W_x(\rho) + F_{Cx} \quad . \qquad (84)$$

$W_x(\rho)$ stands for a contribution to the exchange force stemming from the binding energy per nucleon at a given density ρ, whereas F_{Cx} reflects the Coulomb part of the exchange force. F_{Cx} cannot be further simplified. Fotunately, it is small in most cases and can be neglected. Particularly in high energy collisions the Coulomb interaction does not play an important role.

The direct short range term as well as the exchange term are not explicitly calculated because they are contained in the effective part of the density dependent binding energy resulting from nuclear matter calculations [Sto79]. That is one way quantum effects can be included effectively in the equation of state.

The Navier- Stokes equations of motion of a viscous fluid, i.e. a fluid with some nonequilibrium properties (thermal conductivity and viscousity, which can be physically associated with finite mean free path effects) can be written as continuity equations for the baryon number ρ, momentum density $\rho\vec{v}$, and energy density ρE with the gradients of the pressure P, the potentials V, and the viscous stress tensor, $\underline{P}$, as source terms,

$$\partial_t\rho + \partial_i(\rho v_i) = 0, \qquad (85)$$

$$\partial_t(\rho v_i)+\partial_j(\rho v_j v_i) = -\frac{1}{m}\partial_i p + \frac{1}{m}\partial_j[\eta(\partial_i v_j+\partial_j v_i - \frac{2}{3}\delta_{ij}\partial_k v_k)+\zeta\delta_{ij}\partial_k v_k] - \frac{\rho}{m}\partial_i V,$$

$$\partial_t(\rho E_T)+\partial_j(\rho E_T v_j)= \kappa\partial_j^2 T+\partial_i v_j\left[-p_T\delta_{ij}+\eta(\partial_i v_j+\partial_j v_i-\frac{2}{3}\delta_{ij}\partial_k v_k)+\zeta\delta_{ij}\partial_k v_k\right],$$

The indices i, j and k are running over the space coordinates and there is a summation for indices occurring twice in one term. The coupled nonlinear equations for the density fields $\rho(r,t)$, momentum density fields $\rho(r,t)$ $\vec{v}(r,t)$ and energy density fields $\rho(r,t)$ $E(r,t)$ are solved simultaneously. The source terms p, V, $\kappa\partial_j^2 T$ and the viscosity part will be discussed below.

5. Relativistic fluid dynamics

We have only discussed the nonrelativistic equations of motion up to now. However, as the bombarding energy is increased, relativistic effects become increasingly important. The range of validity of the non-relativistic formalism is not sharply defined, but at bombarding energies E_{lab}>500 MeV/nucleon, the relative velocity of projectile and target exceeds the speed of light, c, and at best qualitative results may be obtained.

There are two ways in which a system may become relativistic. It may be

(a) macroscopically relativistic in that the flow velocity becomes large or

(b) microscopically relativistic in that the excitation energy is non- negligible in comparison to the rest energy.

Case (a) is reflected by the equations of motion and case (b) by the equation of state.

As in the nonrelativistic case (Eqs. 85), the relativistic equations of motion reflect the conservation of baryon number, momentum and energy, and may be brought into the continuity equation form:

$$\partial_t\rho_L + \partial_k(\rho_L\vec{v}_k) = 0$$

$$\partial_t\vec{M}_i + \partial_k(\vec{M}_i\vec{v}_k) = -\partial_i P$$

$$\partial_t e_L + \partial_k(e_L\vec{v}_k) = -\partial_k(P\vec{v}_k)\ , \qquad (86)$$

where long range potentials and dissipative terms have been dropped.

The quantities ρ_L, M and e_L are the densities for baryon number, momentum and energy respectively as specified in a fixed ("lab") reference frame. These are related to the "proper" or "co-moving" densities in the local rest frame by

$$\rho_L = \gamma\rho$$

$$M_i = \gamma^2(e + p)v_i$$

$$e_L = \gamma^2(e + p) - p \qquad (87)$$

where

$\gamma = (1-v^2)^{-1/2}$ is the usual Lorentz factor,

ρ = the proper baryon number density

$e = \rho(m_o c^2 + E_c(\rho) + E_{th}(\rho,T)$, the proper internal energy density, including the rest energy and

ρ is the pressure.

The proper densities ρ, e and the velocity $\vec{v}$, which are the physically interesting quantities, must be obtained from the lab densities ρ_L, M, e_L by inverting the nonlinear equations (87) with $p=p(\rho,e)$ from the equation of state. This nontrivial technical problem is a complication over the nonrelativistic case, where the velocity can be calculated directly from ρ and ρv.

We show in Figs. II.13 and 14 the relativistic nuclear fluid dynamical model calculations [Gra 84] for the reaction Ar (770 MeV/nucleon) + Pb at b = 0 and 4 fm studied above in the VUU nonequilibrium theory. Note the surprising similarities of the fluid dynamical results with the VUU calculation. Similar results are, however, only obtained when heavy projectile and targets are studied, because only in this case does the VUU approach predict the approach to thermal equilibrium. For light systems like C + C the fluid dynamical model does not apply - there is simply not enough target material in the way of the projectile to result in nuclear stopping.

7. One dimensional shocks

The above equations describe fluid dynamical processes completely. However, it is often advantageous to gain more insight into the physical processes by solving more simplified, schematic models, which can be solved (at least to some extent) analytically. In this case another set of equations is applied in the more schematic treatment of the fluid-dynamical description of high energy heavy ion collisions, namely the shock equations: Shock waves have to be clearly distinguished from sound waves. In contrast to sound waves, shock waves are connected with a strong, density dependent mass flow velocity v_f. The shock front itself propagates with the shock velocity $v_s > v_f$ and also depends strongly on the compression amplitude [Sch74,Bau75]. Shock waves are non-linear phenomena--for large amplitudes $\rho >> \rho_o$ both v_s and v_f tend to the velocity of light (see Fig. II.15), while for small perturbations $\rho \sim \rho_o$ they approach the linear limit of sound waves. Shock waves imply a large entropy production: The matter flow through the shock front is highly irreversible, it is not only connected with strong

compression, but also with large thermal excitation [Hof76;Stö77,Stö77a, Stö78].

The shock calculations have to be viewed as an idealization assuming a zero width of the shock front together with the discontinuous jump of the state variables (e.g. ρ, T, e, p). However, comparison of the nuclear shock wave calculations with the result of the full Navier Stokes calculations [Stö79b] shows that the resulting compression rates and temperatures are very similar, although in the Navier Stokes calculations the compression front is smeared out over 1-2 fm due to the viscosity. Such a width seems to be rather realistic, as the width of a shock front is approximately given by 2-3 mean free path, which can be less than half a fermi in high energy nuclear collisions. For a large nuclear transparency, the shock front width may be of the order of the nuclear radius. However, no indication for transparency has been found in the high energy experiments up to now.

The relativistic Rankine- Hugoniot equations can be derived from the continuity of the

$$\text{particle flux density} \qquad [j^o] = [\rho\, u_x] = 0$$

$$\text{energy flux density} \qquad [T_{ox}] = [i\, u_o u_x] = 0$$

$$\text{and momentum flux density} \quad [T_{xx}] = [i\, u_x^2 + p] = 0 \qquad (88)$$

where [] denotes the jump of the respective variable across the shock front, and x gives the direction normal to the shock front as seen from the shock front's rest frame.

Eliminating the velocities u_x from the continuity equations yields the relativistic shock equation

$$\frac{i_o^2}{\rho_o^2} - \frac{i^2}{\rho^2} + (P-P_o)\left(\frac{i_o}{\rho_o^2} - \frac{i}{\rho^2}\right) = 0 \qquad (89)$$

which gives a unique connection between the free enthalpy i, pressure p, and density ρ within the respective rest frame of the matter (subscript $_o$ stands for the undisturbed matter in front of the shock wave, quantities without subscript refer to matter in the compressed state). When we insert $i=\rho W+p$ and $i_o=\rho_o W_o$ the equation

$$W^2 - W_o^2 + P\left(\frac{W}{\rho} - \frac{W_o}{\rho_o}\right) = 0 \qquad (90)$$

is obtained. This is the Rankine- Hugoniot equation, which determines the temperature T as a function of ρ, i.e. T(ρ). If W is equated with the center of mass kinetic energy one can solve for the density ρ (E_{lab}) and therefore for the bombarding energy dependence of any other thermodynamic quantity. Here W(ρ,T) is the energy per baryon, which characterizes the nuclear equation of state. Neglecting pions and resonances and regarding the pure nucleon fluid only, the relation $P_T=\alpha\rho\ E_T$ obtained above next section can be used to obtain a quadratic equation in E_T, which can be solved in terms of the nucleon density ρ analytically. E_T is the temperature-dependent part of W(ρT).

The shock velocities v_s and v_f can be determined by the continuity of the energy and momentum flux density. From the relative velocities of the matter with respect to the shock front, the relative matter flow velocity v_f is obtained by covariant summation (see Fig. II.12).

$$\frac{v_s}{c} = \left\{ \frac{PW\rho}{(W\rho-W_o\rho_o)(W_o\rho_o+P)} \right\}^{1/2}$$

$$\frac{v_f}{c} = \left\{ \frac{P(\rho W-\rho_o W_o)}{\rho W(P+\rho_o W_o)} \right\} \qquad (91)$$

A simple illustration model can be constructed to calculate the shock compression and temperature in the central collision of two heavy

nuclei as a function of the bombarding energy [Bau75; St678]. This model assumed the compressed fluid to be at rest in the center-of-momentum system (equal velocity frame). Three-dimensional fluid dynamical calculations show that this requirement is fulfilled fairly well for nonperipheral collisions of heavy nuclei near the collision axis: A sort of stationary compression stage develops. That means, that practically all of the incident kinetic energy is transformed into internal energy (compression and excitation). As v_f denotes the flow velocity of the shocked matter , which is at rest in the c.m. frame, relative to the target matter, we can calculate the laboratory bombarding energy via

$$E_{LAB} = \left[\left(1 - \left(\frac{v_p}{c}\right)^2\right)^{-1/2} - 1\right] W_o \qquad (92)$$

where $v_f = \frac{2v_f}{1+(v_{f/c})^2}$ is the projectile velocity.

Though this model will, due to the lack of kinetic energy of the compressed matter and due to the outflow of matter perpendicular to the collision axis (as compared to three dimensional calculations), give too large values for compression and temperatures as function of the bombarding energy, it is sufficiently good to give a rather quantitative overview about the expected compression and thermal excitation. The influence of the beam energy and the nuclear equation of state (e.g. different compressibility constants) and the importance of resonance and pion production in the collision dynamics can be studied nearly analytically.

III. Confrontation of the Theory with Experimental Data - Extraction of the Nuclear Equation of State

III.A Expansion, Fragment Formation and the Entropy Puzzle

1. Compression and expansion

In the preceding chapter the fluid dynamical model has been introduced. Historically fluid dynamics has been the first approach to be applied to high energy nuclear collisions. This model is most intuitive in that it refers directly to the thermodynamical concepts developed in Chapter I. Therefore the underlying physics of high compression and excitation can be discussed in a macroscopic language. The spatial and temporal distributions of the density, velocity, temperature, etc. as obtained from this approach are in the following analyzed. The dependence of the thermodynamic variables on the impact parameter, bombarding energy, and projectile- target combination is studied. The fluid dynamical model is the only of the above discussed approaches for which the nuclear equation of state serves as immediate input - the VUU approach also includes the compression energy, but since it is a nonequilibrium theory the statistical variables temperature, thermal pressure, etc. are not easily accessible. We use the fluid dynamical model in the following as a reference case - not only to compare to the data, but also to the microscopic theories.

The fluid dynamical development of a heavy ion collision typically proceeds in the following way (Fig. III.1): When the two nuclei collide at high energy the overlap zones are stopped and a strong nonlinear shock wave is formed. High density, pressure and temperature are created in this region. This stage is described by the "compression" line in Fig. III.1.

The numbers on that line indicate the energies in GeV/n at which the corresponding maximum values for ρ/ρ_0 and T are reached. At E_{lab}=200 MeV/n, for example, a maximum compression of three times equilibrium density and a temperature of about 40 MeV can be obtained. During that stage the entropy of the system rises up to a certain saturation value which depends on the nuclear equation of state, the bombarding energy and the viscosity in the system.

Subsequent to this compression phase the temperature drops during the hydrodynamic (quasi-adiabatic) expansion while the entropy S stays nearly constant at the asymptotic value reached at the point of highest compression. A three dimensional calculation of the entropy is shown in Fig. III.2 [Buc85] - observe that the entropy is increased somewhat due to viscous effects [Cse80, Stö84, Buc 84]. The system expands due to it's large internal pressure and at densities ρ-0.5-0.7 ρ_0 the collisions between the particles cease: the hydrodynamic description loses its validity and the nuclear fluid breaks up into light fragments π, p, n, d, He, ... The fragments formed in this late stage of the reaction are the only messengers from the reaction which are actually observed experimentally. Fragment formation is a topic of great current interest because of their possible relation to the entropy and also in connection with speculations about the discovery of the nuclear liquid gas phase transition [Stö83, Cse85].

In the fluid dynamical model the fragment formation is usually treated in the quantum- statistical approach presented below. The fragments carry the only available information from the initial dense state of the system. However, they have gone through the much later freeze out stage which follows the hydrodynamical expansion of the reaction. This freezeout starts when the the density in the fluid becomes so low that the particles

in the fluid cease to interact - then the fluid breaks apart into single fragments. The quantum statistical model used to obtain the fragment yields and the spectra is described in the next paragraph.

2. Quantum statistical model of break-up and fragment formation

We will in the following concentrate on the formation of light and medium mass fragments in the freeze-out stage of the collision. There are two important questions: What is the "chemical" composition of the reaction products, i.e. how abundantly and where are the different nuclei, π etc. produced? What is their distribution in momentum space, i.e. how do the experimentally observed spectra look like? These two points are discussed in the following section.

To simulate the transition from the interacting nucleon fluid to the free gas of nuclear fragments traveling towards the detectors the hydrodynamic calculation is halted when the average density is $\approx 0.5\rho_o$. Then the light fragment composition is calculated from a quantum statistical model by assuming that the baryon number and energy per particle of the interacting nucleon fluid is conserved. The quantum statistical model [Gos78, Sub81,Sto83,Han85] used to calculate the fragment yields assumes that chemical equilibrium between the different fragments produced (p, n, d, t, ^{3}He and α's ...) is established towards this late stage of the collisions. This assumption is supported by rate calculation for the appropriate densities and temperatures [Mek78].

The model can be recapitulated as follows [Sub81]: Baryon number and charge conservation are enforced via

$$\bar{Z} = \sum_{i=1}^{N} n_i((Z_i,N_i)\cdot Z_i \qquad (1)$$

$$\bar{N} = \sum_{i=1}^{N} n_i(Z_i,N_i)\cdot N_i \qquad (2)$$

where n_i is the number of particles of species i with Z_i protons and N_i neutrons. The equilibrium is established in a volume V_{ext} (or at a density ρ) and at a temperature T. Every particle moves freely in the volume V left over from the external volume V_{ext} after subtracting the volume occupied by each particle,

$$V = V_{ext} - \sum_i N_i V_i \qquad \rho = (\tilde{N} + \tilde{Z})/V_{ext} \qquad (3)$$

where V_i is the ith particle's volume. So the point-like particles move freely in a reduced volume V with the Density determining the chemical equilibrium of $\rho_{pt}=(\tilde{N}+\tilde{Z})V$. For fermions we have

$$\lambda_i^3 N_i/g_i V = (2/\pi^{1/2})F_{FD}(v_i) \qquad i = p,n,^3He,t... \qquad (4)$$

where

$$\lambda_i = h/(2\pi m_i kT)^{1/2} \qquad (5)$$

is the thermal wavelength of the ith particle with mass m_i. The spin degeneracy factor $g_i=2S_i+1$. The chemical potential of the ith particle is μ_i,

$$v_i = \beta\mu_i = \mu_i/kT \qquad (6)$$

and

$$F_{FD}(v) = \int_o^\infty dx\ x^{1/2}/(\exp(x-v)+1). \qquad (7)$$

The function $F_{FD}(v)$ is tabulated in the literature [Sub81]. For bosons we have

$$N_i = 1/(\exp(\alpha_i)-1)+(g_i V/\lambda_i^3)F_{BE}(\alpha_i) \qquad i = d,^4He... \qquad (8)$$

where $\alpha_i=-\beta\mu_i$, the final term gives the number of condensed particles, and

$$F_{BE}(\alpha) = \sum_{n=1}^{\infty} \exp(-n\alpha)/n^{3/2}. \qquad (9)$$

The constraint of chemical equilibrium implies that the chemical potential

$$\mu_i = Z_i\mu_p + N_i\mu_n + E_i \qquad (10)$$

where

$$E_i = Z_i m_p c^2 + N_i m_n c^2 - m_i c^2 \qquad (11)$$

is the binding energy of the cluster (Z_i, N_i).

3. Thermal fragment emission

The particle cross sections are calculated by transforming the internal thermal momentum distribution for each particle density in every fluid element to the laboratory system with the corresponding flow velocity [Cse80,Buc81,Cse83]. The inclusive cross sections are obtained by a weighted average over the impact parameter.

The thermal momentum distribution of the nucleons inside a fluid cell is described by relativistic Fermi distributions. To obtain the momentum distribution of all fragments in the laboratory frame the distributions are Lorentz transformed to this frame by the relativistic boost velocity β_j of the cell j arising from the collective flow [Cse80, Buc81]:

$$f_j^{lab}(\vec{P})d^3\vec{P} = \frac{w(\vec{P})}{W} f_j[\vec{P}(\vec{P})]d^3\vec{P}. \qquad (12)$$

Here $(\frac{w}{p})$ and $(\frac{W}{p})$ are the four-momenta in the cell and lab systems, respectively. From Eq. 12 we obtain the double differential cross section of the emitted fragments via

$$\frac{d^2\sigma}{dWd\Omega} = \sum_j \frac{4V_j\sigma_o}{(2\pi\hbar)^3} \frac{A_j(W^2-m^2)^{1/2}}{\exp[(A_j-\mu_j)/T]+1} \; N_{particle} \qquad (13)$$

where V_j is the volume of the corresponding fluid cell, σ_o is the geometrical cross section of the reaction, and

$$A_j = \gamma_j(W - \vec{\beta}_j\vec{P}_j) . \qquad (14)$$

$N_{particle}$ is the fraction of the corresponding particle species calculated in the chemical equilibrium model from above. The momentum vector p of the observed particle depends on the observation energy E and angles θ and ϕ:

$$\vec{p} = (W^2 - m^2)^{1/2} \begin{Bmatrix} \sin\theta\cos\phi \\ \sin\theta\sin\phi \\ \cos\theta \end{Bmatrix} , \qquad (15)$$

where W=m+E. This method is applied below to calculate fragment spectra and angular distributions from the fluid dynamical model.

4. Light Fragments and the Entropy Puzzle

Since - as seen in Fig. III.2 - for a perfect fluid the entropy saturates at it's asymptotic value already in the moment of highest compression and stays constant during the expansion from this compressed state, a method that would allow to determine the entropy from experiment could yield important insight into the state of the matter in the moment of highest compression and excitation of the collision.

It has been suggested [Sie79] to measure the entropy S via the observed proton-to-deuteron ratio R_{dp}: In chemical equilibrium

$$S = 3.95 - \ln R_{dp} \quad [\text{for } \langle p\rangle_{equil.} >> \langle d\rangle_{equil.}] \qquad (16)$$

This formula has been used to extract entropy values from the inclusive fragment data [Nag81]. The resulting entropy values are plotted in Fig. III.3 as a function of the bombarding energy. Also shown are the entropy values obtained from the hydrodynamical model [Stö84].

The experimental values of S seem to be much larger than the calculated entropy values, in particular for $E_{LAB} \leq 400$ MeV/n, even after the effects of viscosity are considered. However, the proton to deuteron ratios calculated from the fluid dynamical model, $R_{dp} < 0.35$, agree well with the experimental data over the whole range of bombarding energies considered [Nag81] (see Fig. III.4). This paradox is resolved [Stö84] as being due to the decay of the particle unstable excited nuclei,

$$A^* \rightarrow (A-1) + p, \qquad (17)$$

which become increasingly important at intermediate and low energies [Stö84]. In fact, the resonance decay products dominate the chemical equilibrium contribution for $E_{LAB} < 400$ MeV/n. Hence the relation between the entropy and the observables is not given by the simple formula given above. It turns out, however, that the entropy can be related to the d to p ratios discussed above in a quantum statistical model whence the decay of particle instable states is explicitely included. The relation to the entropy is then not given via the simple equation (16), but has to be determined from a full numerical calculation of the quantum statistical model with several hundreds of stable and instable nuclides (see Fig. III.5). Recent data from the GSI/LBL Plastic Ball collaboration have made clear, though, that the d to p ratio depends strongly on the multiplicity of the event in which the particles are emitted: in peripheral collisions, which dominate the inclusive particle spectra, the ratio is much smaller than in central collisions with high multiplicity (see Fig. III.6) [Gus85]. The quantum statistical model has been used to extract the entropy from the asymptotic (infinite miultiplicity) 'data' [Dos85]. The results are shown in Fig. III.7 in comparison with the entropy values calculated in the fluid dynamical model with a stiff nuclear equation of state [Stö81] and with a simple fireball calculation which neglects compression effects entirely. We want to emphazise that the data are in strong disagreement with the fireball calculations - they seem to indicate strong compression effects and point towards a stiff nuclear equation of state.

5. Temperatures and single particle spectra

The temperatures T as calculated in the hydrodynamical model [Sto81] are compared in Fig. III.8 to the experimentally determined slope factors T_o [Nag81] of protons and pions emitted from violent nuclear collisions at various bombarding energies. The data seem to rule out a pure nucleon Fermigas (dashed curve) at energies $E_{LAB} > 800$ MeV/n. A mixture of noninteracting gases of the different hadrons with an exponentially increasing hadronic mass specrum (solid curves) seem to be in much better agreement with the data.

However, it has to be pointed out that the finally observed slope factors do not give a direct measure of the initial temperature: Due to the expansion the temperature drops substantially [Sie78,Sto81]]. This is compensated by an increase in the collective flow velocity. It is interesting that those effects roughly balance each other because of energy conservation and the finally obtained slopes of the spectra do not deviate too strongly from the initial temperature.

III.B Pion Production and the Nuclear Compression Energy

The nuclear fluid dynamical model can also be used to predict pion yields and study their dependence on the nuclear equation of state [Stö78, Dan79, Hah85]. Figure III.9 shows the original calculation of Stöcker, Scheid and Greiner, who first proposed to measure the stiffness of the nuclear compression energy via the pion multiplicities. The first exclusive measurements of the pion multiplicities as a function of the participant multiplicity is shown in Fig. III.10 [San80]. It has been used recently to extract the compressional energy via the method proposed [Stö78,Har85, Hah85,see Fig. III.11] and via a substraction procedure, which used the

cascade model - which does not employ any compressional energy - as input [Sto82]. It turns out that the data can only be explained if a very stiff compression potential is assumed [see Fig. II.3]. The assumption of immediate freeze-out in the high density stage in this procedure could overestimate the pion multiplicities, which would drop during an isentropic expansion of the system before freeze-out [Stö 81c, 84c] (see Fig. III.10). However, cascade calculations show that the pion degree of freedom decouples from the baryonic 'heat bath' very early in the collision, namely in the high density stage [Cug80,Sto82].

To study pion production on the microscopic level the VUU theory can be employed [Kru85, Mol85]. Pions of different isospin are produced in this model via a delta resonance mechanism in elementary nucleon-nucleon collisions: thus both production and absorption mechanisms are treated microscopically. The VUU approach has first been tested by turning off the Pauli blocking and mean potential field. Then the parallel ensembles decouple and the test particles move on straight line trajectories until they scatter the intranuclear cascade model is recovered. The pion yields calculated with the VUU method in the cascade mode agree quantitatively with results obtained with the conventional cascade, e.g. of Cugnon et al. and Yariv et al. [Cug80, Yar81]. Both results differ substantially from the data. If the nuclear compression energy and the Pauli blocking are employed in the VUU- method, the pion multiplicities change dramatically, as shown in Fig. III.12 [Kru85]: Take the 360 MeV/nucleon case, for instance. The π^- yield is 1.05 in the cascade mode, but drops to 0.56 if the compression energy is included; the suggested large difference due to the nuclear matter EOS is observed. The pion yield drops further to 0.46 when the VUU Pauli blocking is applied. These results differ by factors of three from results

published elsewhere [Ber 84a]; a revised version of that program [Aic85b] now reproduces the results presented here.

The pion multiplicities as calculated with the full VUU theory are shown in Fig. III.12 as a function of the bombarding energy for the Ar + KCl system. The VUU theory with stiff EOS plus phase space Pauli blocker compares well with the data whereas the cascade mode overestimates the data by factors > 2 at energies up to 1 GeV/nucleon, just like the intra-nuclear cascade calculations.

The required drop in the predicted pion yield is found to be due to the transformation of kinetic energy into potential energy during the high density phase of the reaction as well as due to Pauli blocking. To check the sensitivity of the pion yields to the EOS the calculations have been repeated with the medium potential. At 772 MeV/nucleon we find n_{π^-} = 2.45 and 2.13 with the medium and the stiff EOS respectively. At lower energies, statistical error bars of 10% preclude an accurate assessment of the effect of the potential. At all other energies, where the error bars are 3%, the yields are systematically higher by about 10% with the medium EOS. The stiff equation of state which reproduces the pion yields best is shown in Fig. II.3 together with the medium EOS. We will confront these equations of state with other data on nuclear flow below. We want to anounce here already that we will find further support for the stiff equation of state also from this completely independent comparisons.

The time dependence of the total pion multiplicity as calculated from the VUU approach for Nb (1050 MeV/nucleon) + Nb collisions at b = 3 fm is shown in Fig. III.13a [Mol85]. Note that the pion number rises rapidly to a maximum value at 10 fm/c and then drops to a stable final value by 20 fm/c. There is a small but significant effect due to re-absorption until

the pions escape the hot interaction zone. We want to emphazise that in this theory - as in the previously discussed cascade calculations - the pion yield approaches it's asymptotic value at a time which nearly coincides with the moment of highest compression (Fig. III.13b) and 'temperature', thus demonstrating one more time that information on the high density stage can be attained.

The bombarding energy dependence of the total pion multiplicity at b = 3 fm for Nb + Nb collisions is shown in Fig. III.14a. For the system Au + Au, the pion multiplicity for b = 3 fm collisions is shown in Fig. III.14b for the different isospin channels in the final state. Note that the VUU theory predicts a distinct difference of the pion multiplicity with a charged pion ratio $\pi^- / \pi^+ \approx 2$.

The VUU approach has also been used to study pion production in asymmetric nucleus-nucleus collisions [Mol85b]. It is observed that in Ar (770 MeV/nucleon) + Pb collisions the pions tend to escape into the backward hemisphere at low impact parameters. At intermediate impact parameters the pion emission pattern is directed sidewards away from the high density zone. The total average pion multiplicities vary from 10.6 at b = 1 fm to 3.7 at b= 7 fm. About 25-30% more pions are created when the Pauli blocking is turned off. This is understood physically: with the Pauli principle turned off, the final state phase space in the intermediate rapidity region is more strongly occupied; equivalently, with the Pauli principle turned on, many collisions that would otherwise produce pions are forbidden by Pauli blocking.

III.C Collective Sidewards Flow - Evidence for Shock Compression and a Hard Equation of State

1. Inclusive Fragment Spectra

Spectra obtained from the hydrodynamical model by the freeze-out procedure described in paragraphs III.2-5 can be compared directly with the experimental observations at various input energies. We would like to point out that little information about the details of the reaction mechanism can be extracted from comparison of the inclusive data and impact parameter averaged calculations. For example, in spite of it's obvious presence at small impact parameters, no signatures of the collective sidewards flow predicted by the fluid dynamical calculations for central impact parameters seems to be visible even in the calculated inclusive cross sections [Ams75, Ams77, Buc83]: only by triggering for nearly central collisions, i.e., high multiplicity selected events, can the sensitivity of the experiments be improved. Furthermore, since the proton production probability is largest in hot regions [Sub81] the effect of the collective flow is smeared out by the thermal motion, which makes the proton cross sections almost isotropic. This phenomenon has been observed at high energies [Sto80] and seems in agreement with previous three dimensional nonviscous calculations [Stö81b,82].

A better experimental testing ground for flow effects is therefore provided by particles heavier than the proton, e.g. t, ^{3}He, α (or also Li, Be, C) cross sections. These particles are produced in colder regions of the system [Stö 81b,82]. Hence, they tend to exhibit the signatures of the collective flow more strongly. In Fig. III.15 we compare the calculations [Buc84a,85] with recent measurements of B.V. Jacak, G.D. Westfall et al. [Jac 83] for ^{40}Ar+^{197}Au at 137 MeV/N. The left frame shows the inclusive double differential ^{3}He cross section, the right frame compares the results for tritons. In both cases a reasonable agreement can be seen between the

calculation (full lines) and the data. Especially the tendency of the ^{3}He spectrum to decrease with decreasing energy and the opposite behavior of the triton spectrum is reproduced fairly well. This systematic behavior is due to the neutron rich Au-target, preferring neutron-rich particle production at low energies.

The Ar+Au spectra at lower energies seem to indicate a transition to a different reaction mechanism - whereas the 92 MeV/N data still show a reasonable agreement with the fluid dynamical calculations, there is a clear misalignment for E_{LAB}=42 MeV/N. Especially at forward angles the data are totally missed by the fluid dynamical calculation, thus indicating that the stopping power of nuclear matter decreases drastically at these low energies.

2. High Multiplicity Selected Inclusive Data

First fingerprints for collective flow have been found in high multiplicity selected early particle track detector experiments [Bau75], which exhibit sidewards maxima in the angular distribution of He - nuclei emitted in very asymmetric reactions, e.g. C + Ag. Also in the double differential cross sections of light fragments (p,d,t) emitted from high multiplicity selected reactions of Ne + U exhibit sidewards maxima, in accord with the longstanding predictions of the nuclear fluid dynamical model [Sch74, Stö80], while the intranuclear cascade model exhibits forward peaking [Stö81]. The angular distributions of protons emitted in central collisions of Ne (393 MeV/N) on U exhibit broad sidewards maxima (middle left frame of Fig. III.16). The numbers in the figure indicate the proton kinetic energies. Cascade calculations [Stö81b,82] yield forward-peaked angular distributions, even if central collisons are selected (upper and

lower left frame). Hydrodynamic calculations without thermal breakup yield sidewards peaks which are too narrow (lower right frame) [Stö81b,82]. The simplified two component and firestreak models (upper right frame) give similar results as the complex three dimensional cascade calculations, but since they are also forward peaked, they also disagree with the data. On the other hand, the fluid dynamical model with final breakup included [Stö81b,82] (middle right frame) gives a reasonable description of the observed forward suppression and also reproduces qualitatively the forward shift of the position of the sidewards maxima with proton energy.

However, as the bombarding energy is increased, relativistic effects become increasingly important. The range of validity of the non-relativistic formalism is not sharply defined, but at bombarding energies E_{LAB}>500 MeV/N, the relative velocity of projectile and target exceeds the speed of light, c, and at best qualitative results may be obtained. In fact, this can already be seen at 400 MeV/N, where the relativistic treatment has a substantial influence on the spectra [Stö80] of protons, deuterons and tritons emitted from central collisions of Ne+U. Fig. III.17 shows the comparison of the relativistic calculations [Gra84] with the data [Sto80]. Observe that the agreement with the experimental data is much improved as compared to the nonrelativistic calculations presented earlier (Fig. III.16). Therefore, the relativistic formulation of the hydrodynamic model is always used in the rest of the article at higher energies, E_{LAB}>0.4 GeV/N. However, the forward emission of particles is still strongly suppressed exhibiting sidewards maxima. It is important to point out that these sidewards maxima are predicted to be even more pronounced for the summed charges than for protons. In fact, such behavior has been found in experiments with α-particle detectors [Bau75]. Also, the high multiplicity

selected angular distributions of ^{2}H and ^{3}H [Sto80] show sharper sidewards peaking than the protons.

The qualitative features of the ϕ-averaged distributions calculated in the fluid model, however, do not change dramatically with impact parameter, once violent collisions with $b \lesssim 4$ fm are selected. This means, unfortunately, that ϕ-averaged double differential cross sections are of limited value for obtaining information on details of the reaction dynamics and on the nuclear equation of state [Ber78,Stö80b]. Therefore, we next consider whether the azimuthal dependence of the differential cross sections, to be obtained from 4π exclusive experiments with single event analysis [Gus84,84b;Ren84, Mey80], can provide more specific dynamical information.

3. Event by Event Analysis - Triple Differential Cross Sections

Figure III.18 shows the triple differential cross sections [Stö82a] $d^3\sigma/d\cos\theta d\phi dE$ in the scattering plane, i.e., the $y_{||}/p_T$ plane at $\phi=0°/180°$, for the reaction ^{20}Ne (393 MeV/nucleon)+^{238}U at various impact parameters b. For head-on collisions, b=0 fm, the two maxima at $p_T/m \approx 0.1$-0.2 indicate the azimuthally symmetric large angle sidewards emission of cold (T<10 MeV) matter [Stö80b]. At intermediate impact parameters, a considerable azimuthal asymmetry appears. A strong maximum at small transverse and longitudinal velocities indicates the presence of a large chunk of cold, slowly moving matter, namely the target residue at $\phi=180°$. A flat local maximum in the projectile hemisphere ($\phi=0°$) at larger p_T and $y_{||}$ reflects some sidewards deflected fragments of the beam particles. The spread of the maxima in ϕ depends strongly on b; for intermediate b it is on the order of $\Delta\phi \sim 40°$. The apparent large collective transverse and

longitudinal mmomentum transfer (the bounce-off process [Stö80b,Mey80,Ren84]) results from the high pressure in the "participant" head shock zone, pushing the nuclear residues apart to opposite directions ($\Delta\phi=180°$). This process is of great importance, as it intimately connects the momentum transfer to be observed in bounce-off events with the quantity of central interest, namely, the nuclear equation of state $E(\rho,T)$ [Stö81]. At large impact parameters (b>6 fm) the invariant cross sections peak more closely to the initial projectile and target momenta. Maxima at finite p_T are found even in the azimuthally averaged particle cross sections.

4. Azimuthal Resolution of Reaction Products

The measurement of the triple differential cross section can yield, however, considerably more information about the collision dynamics: The distance between the jet maxima, i.e., the mean momentum along the jet axis, may serve as a measure of the transport properties of the matter: For example, a large viscosity slows down the collective fluid motion in the jet direction. There are many other features of the reaction dynamics which are only accessible by detailed inspection of the triple differential cross sections: For head-on collisions of equal nuclei, the compression in the shock zone is maximized, and most of the matter participates in the strong compression. The two-jet patterns give way to an azimuthally symmetric disk of nuclear matter, expanding towards 90° in the c.m. system [Sch74]. It eventually results in doughnut-shaped (toroidal) triple differential cross sections symmetric around the beam axis. The strong collective transverse matter flow [Sch74] with large mean velocity, $p_T/m \approx 0.4$ is caused by the high pressure in the shock region, in analogy to the intermediate impact parameters. Remnants from the squeezeout can still be seen at small, but

finite impact parameters, b~2 fm, thus, giving rise to additional out-of-plan jet structures--four-jet-events--at $\theta_{c.m.}$=90°, ϕ=90°, as the outflow of the compressed matter perpendicular to the scattering plane is not hindered by "spectator" matter. These predictions, however, do not take into account into account the limitations (e.g., considerable fluctuations) of Eulerian fluid dynamics when applied to light systems: microscopic calculations [Sch81,Ber74,Hal81,Bon76,Ams77,Gud79,Yar79,Cug80,Bod77,Kit78,Bod81] for C+C and Ne+Ne indicate large nonequilibrium contributions. However, while the cascade calculations [Hal81,Yar79,Cug80]--based on free n-n collisons--do not show a considerable transverse momentum transfer even for heavy nuclei, many body calculations with realistic n-n interactions [Bod77,Kit78,Mol84] predict hydrodynamic features such as the 90° sideways peaking for systems with $A_T,T_P>40$. We have shown that the experimentally observed cross sections are in good agreement with fluid dynamical calculations. However, triple differential particle cross sections offer a unique tool for the investigation of the complicated reaction dynamics in high energy heavy ion collisions. The combination of the jet analysis with the composition analysis in 4π exclusive experiments, with special emphasis on production and correlations of the different nuclei emitted, can provide snapshots of bulk motion, mass, and temperature distributions, as well as energy and momentum flux in violent nuclear collisions. One problem to be solved in order to obtain triple differential cross section is the necessity to know the experimental reaction plane where ϕ=0°, 180°, respectively.

Via the principal axis transformation of the flow tensor discussed below, the azimuthal angle ϕ of the reaction plane may be determined experimentally. Thus, the reaction plane for <u>each</u> event is known giving us the opportunity to obtain the <u>triple</u> differential cross sections.

5. 90° Out-of-Plane Spectra

When a fluid element has been stopped and compressed in the hydrodynamical model calculation, it tries to escape and to expand under a finite angle to the beam axis. In the reaction plane, this angle depends on the impact parameter b. For b=0, the matter flow is perpendicular to the beam axis, for b=6 fm there is a flow angle of θ=10°.

Perpendicular to the reaction plane, however, there is always a squeezeout under 90° in the c.m. system (Fig. III.19). In that direction the matter can escape freely from the compression zone without being hindered by the target or by projectile mass. Additionally, the cross section of this out-of-plane matter is not distorted by any spectator material or by corona effects, i.e. it reflects the pure hydrodynamical part of the reaction. The 90° out-of-plane spectrum is therefore very well suited to study the fluid dynamical behavior of colliding matter. Fig. III.20 shows this spectrum for Nb+Nb, 400 MeV/nucleon. In the data of Gutbrod et al. [Gus84] (triangles) high multiplicity events had been selected. The fluid dynamical calculation for b=2 fm reproduces these data very well, as long as an equation of state is chosen which fits the data of Stock et al. (see Chapter III.B) [Sto82]. The results of this calculation are indicated by crosses. An equation of state having a compressibility of K=200 MeV and an extrapolation being linear in ρ for $\rho>>\rho_0$ is much too soft (circles) and results in a too "cold" 90° out-of-plane spectrum. This soft calculation reflects more or less the data for the lighter Ca+Ca system which indeed is colder [Buc84,85;Gus84].

As the results seem to depend strongly upon the nuclear equation of state (EOS), the EOS could be determined by taking an excitation function of the high multiplicity selected 90° out-of-plane temperature which can be

directly read from the corresponding spectra. The corresponding experimental analysis is currently under way [Gut84].

6. Transverse Momentum Distributions versus Rapidity

Once the reaction plane is determined, it is possible to analyze the inplane and the out-of-plane momentum components. We will present such an analysis for the fluid dynamical calculation of an Nb+Nb, 400 MeV/N collision.

We will concentrate first on the temporal development of the momentum components perpendicular to the beam axis. Fig. III.21 shows the results for $\vec{p}_{perp}$ in the scattering plane (right column) and out of plane (left column) at b=3 fm (upper line) and b=6 fm (lower line) for various times. In all cases the high momentum tail of the distribution has its largest contribution in the early stage of the compression. Here the highest temperatures appear, leading to a considerable amount of fast particles (full lines). At the end of the compression phase (t=25 fm/c, broken lines) a lot of matter has already started to expand and to cool, reducing the amount of fast particles. This effect continues when the expansion of the system goes on (t=34 fm/c, dots) [Buc84,85].

It is also very instructive to look at the average p_{perp} component projected into the reaction plane depending on the rapidity Y. Fig. III.22 shows the time dependence of this quantity for a b=3 fm collision the average p_{perp} dives to higher values during the collision as the flow direction settles at about 30° after the compression phase. The flow tensor therefore is not symmetric to the beam axis (direction of Y), thus yielding finite values for the amount of $\langle\vec{p}_{perp}\rangle$. $|\langle p_{perp}\rangle|$ increases with increasing amount of Y until it reaches a maximum at $|Y|=0.5$.

However, depending on the impact parameter there has to be a maximum of $\langle\vec{p}_{perp}\rangle$: At high impact parameters, there is little creation of sidewards flow resulting in $\langle\vec{p}_{perp}\rangle_{max}=0$. At central collisions, on the other hand, there is azimuthal symmetry in the momentum distribution, and the various $\vec{p}_{perp}$ contributions average out to zero. This can be seen in Fig. III.23, where in part (a) the $\langle\vec{p}_{perp}\rangle(Y)$ distribution for b=2, 4 and 6 fm is shown. Here the distribution becomes flatter with <u>increasing</u> impact parameter. In part (b) the results for b=0, 1, 2 and 3 fm are shown, and the distribution flattens with <u>decreasing</u> impact parameter. This effect may offer a unique opportunity to select <u>very</u> central events: One quantity for that is the charged particle multiplicity $\langle M_c\rangle$, which allows for a selection of $0\leq b\leq 3$ fm (see above). When this large $\langle M_c\rangle$ selection is correlated with a low $\langle\vec{p}_{perp}\rangle$ trigger, the remaining events must originate from small impact parameter $b\leq 1$ fm. In consequence, these events should have flow angles much larger than 30°.

7. Macroscopic, Fluid Dynamical Analysis of the Kinetic Energy Flow - Evidence for Nuclear Stopping and Shock Compression

With the cross sections discussed above we have investigated the "classical" observable of nuclear collisions. However, this observable describes more or less the <u>final</u> state features of the reaction, i.e. the situation after the freezeout of different matter clusters. Different models like the fireball [Gos 78] or the cascade [Yar79,Cug80] reproduce at least some (i.e. inclusive) of the experimental results fairly well, but one of the important parameters of the different models is always the breakup mechanism which had been used to obtain the spectra. We have seen above that in this context the fluid dynamical model plus chemical equilibrium is

a powerful tool to describe the experimental data. However, the principal difference between hydrodynamics and other models (i.e. stopping, compression, sidewards emission, bounce-off) cannot be seen in the double differential inclusive spectra. High multiplicity selection helps a little, but still more information is needed.

It would be very important if we could find more measurable quantities which are influenced in the compression phase only. Then we could decide whether the matter had been stopped and compressed or not. We will discuss such quantities and their interpretation during this section.

The first step in order to find messengers from the compression phase is to look for the quantitities which are integrated in the equations of motion.

Such a quantity is the density, for example. However, we have already learned that the density rises and falls off during the reaction i.e. it has no saturation value. Therefore it cannot carry detailed information from the compression phase. A density distribution is not even observable in experiments. The strong sidewards emission of matter observed in Fig. III.24-26, on the other hand, should be seen experimentally if matter principally behaves like a fluid.

The same seems to be true for the momentum: the various momentum components have very different histories during the collisions. P_z starts with a high value and is decreased, whereas p_y and p_x are built up. On first glance it again seems that only the direction of $\vec{p}$ could be an interesting quantity. In the experiment there is only a distinction between $p_{||}$ and $p_{\perp}$ possible, reducing the outcome of information. However, we will see later that more detailed information can be obtained by the momentum flow analysis:

As discussed in III.A, another quantity of interest is the entropy. Entropy is generated during the first half of the reaction when the nuclear matter is stopped, compressed and heated. Fig. III.2a describes the situation for a Nb+Nb collision at 400 MeV/n and an impact parameter of b=3 fm in detail: Entropy is created during the first ≈20 fm/c of the collision (full line). During that time the various zones of the two nuclei are stopped and compressed. When the maximum density of the system starts to drop (broken line after ≈20 fm/c) the entropy has reached its saturation value of about 2.6. As the subsequent expansion phase is isentropic, this value of S/A is maintained during the rest of the calculation. The entropy even saturates when a large sheer viscosity η is present in the Navier Stokes equations. In Fig. III.2(b) it can be seen that for η=20 MeV/fm²c and for η=60 MeV/fm²c the absolute value of the entropy rises from 2.66 (nonviscous) over 2.96 (η=20 MeV/fm²c) to 3.17 (η=60 MeV/fm²c) whereas the asymptotic constancy of these values remains unaltered.

That is due to the fact that in the expansion phase no more sheer-flow is present: Either the matter has a collective flow or it expands isotropically. However, the situation changes completely when bulk viscosity ζ is allowed for because then all expanding matter is affected. This has not so much influence on the reaction dynamics (see also ref. [Buc81]) but mainly on the expansion phase. There is a substantial entropy production also at late times, (Fig. III.2b), and a saturation does not occur.

We conclude that entropy is a very interesting quantity, but it is very hard to handle. When bulk viscosity is present, entropy is also generated during the expansion phase of the system and there is little chance of getting "pure" information from the compression phase only. If

there is no bulk viscosity the problem of experimental determination of S/A remains. We have seen above (Section III.A) that certain assumptions on the decay of the system are necessary. We will therefore concentrate on other interesting quantities.

Fig. III.27 shows the average values of total (full line), cold internal (point-dotted), kinetic (dotted) and thermal (broken) energy obtained during a fluid dynamical simulation of a central Nb+Nb collision at 400 MeV/n in the cm system. In principle, the total energy contained in the system should stay constant. The small energy loss (about 1% of the lab energy) in Fig. III.27 is due to numerical reasons and will be neglected in the further discussion.

When the two nuclei touch each other after about 5 fm/c the matter in the contacting zones is stopped, thus reducing the average kinetic energy in the whole system. Due to the supersonic incident velocity a shock front is created resulting in heat production. As the matter is compressed, the cold internal energy smoothly raises form its minimum at W_o=-16 MeV into larger values. During the next ≈15 fm/c, more and more matter undergoes the process described above. However, the matter which had been stopped first, already starts to expand again (see e.g. Fig. III.28). Therefore the mean kinetic energy does not reach zero, i.e. the system is never stopped in total. The expanding matter cools, resulting in a drop of the mean thermal energy. However, the cold internal energy still rises because the density now drops below the equilibrium value of ρ_o=0.17 fm^{-3}.

Finally, after roughly 30 fm/c, the mean kinetic energy of the expanding sytem seems to saturate at about 80 MeV/n in the cm system. Obviously, $E_{kin}=p^2/2m$ is a quantity saturating once the compression phase is over. However, the scalar E_{kin} contains only limited information. It would

be important to know, if more general quantities as, for example, quadratic combinations of the momentum components $p_i p_j$ have these saturation features too. The idea and the results of such a "global momentum tensor analysis" (flow analysis) will be discussed in this paragraph.

The collective flow, predicted by fluid dynamical calculations [Stö79-84, Bu80-84] could be observed directly by the global momentum tensor analysis: This analysis can be done experimentally with 4π detector systems such as emulsion, streamer chamber, or the plastic ball. The basic idea is to measure event-by-event the momenta of all (charged) particles. Once this information is available, one can transform all the physical quantitites into the center-of-momentum frame and determine the direction of maximum momentum and energy flow by performing a principal axis transformation. The various concepts which have been proposed to analyze nuclear collisions are thrust [Kap81, Cug82], sphericity [Cug82,Guy82,Stö82], kinetic energy flow [Guy82,Stö82,Buc83d]. The first two concepts have been adapted from high energy physics, but they have the disadvantage of being either nonanalytic (thrust) or of not properly taking into account the emission of composite particles (sphericity). The kinetic energy flow tensor [Guy82, Stö82, Buc84d],

$$F_{ij} = \sum \frac{p_i(\nu)p_j(\nu)}{2m_\nu} , \qquad (18)$$

where the sum runs over all fragments ν with mass and center of mass momentum $\vec{p}(\nu)$, is a generalization of the sphericity concept. The factor $(2m_\nu)^{-1}$ ensures that composite fragments contribute to the matter flow tensor with the correct weight relative to nucleons.

By comparing the results of the cascade and the hydrodynamic calculation, we want to determine the sensitivity of the global variables to the collision dynamics. In cascade calculations, $m_\nu = m_N$ and the $\vec{p}(\nu)$ are the final momenta of all nucleons. In hydrodynamic calculations the reaction volume is divided into cells ν characterized by a mean flow velocity, $\vec{p}(\nu)/m_N$, a local temperature $T(\nu)$, and a local baryon number $N(\nu)$. The baryon density in a cell contributes an amount $\bar{p}_i\bar{p}_j/2m+\delta_{ij}T/2$ to the flow tensor. Thus, for hydrodynamics F_{ij} is the sum of a collective flow energy $\bar{F}_{ij}$ and a thermal energy $\delta_{ij}E_T/3$,

$$F_{ij} = \sum_\nu \frac{\bar{p}_i(\nu)\bar{p}_j(\nu)}{2m_N} + \delta_{ij}\frac{1}{2}T(\nu) = \bar{F}_{ij} + \delta_{ij}E_T/3 \ . \qquad (19)$$

Observe that the eigenvalues of F are then $\lambda_n=\bar{\lambda}_n+E_T/3$, where $\bar{\lambda}_n$ are the eigenvalues of $\bar{F}$. However, the eigenvectors, $\hat{e}_n$, are identical to those of F. Thus, while the aspect ratio, $R_{13}=\lambda_1/\lambda_3$ $(\lambda_1>\lambda_2>\lambda_3)$ is brought closer to unity by thermal smearing, the flow angle $\theta_F=\cos^{-1}(\hat{e}_1\cdot\hat{2})$ is unaffected by temperature. Experimentally, this procedure can always be done, and there will be a distinguished average value for R_{13} and θ_F. In the fluid dynamical model, there is a saturation for R_{13} and θ_F once the compression phase is over. This value then is conserved to the asymptotic times. Fig. III.29 shows the temproral development of R_{13} and θ_F for a central Nb(400 MeV/n)+Nb collision [Buc84,85]. First, when the two nuclei approach each other, we have a very stretched tensor. Subsequently the matter is stopped and the flow ratio is reduced (nearly to (12 to 18 fm/c). During that time the main flow proceeds parallel to the beam axis, i.e. θ_F is zero. After $\simeq$ 18 fm/c the expansion of the system is the dominating component of the

kinetic flow. The main contribution now stems from matter flowing perpendicular to the beam axis. As the λ_i are ordered by magnitude, there is a sudden flip in the flow angle θ_F from 0° to 90° when the $p_\perp$ contribution starts to be larger than $p_{||}$. After about 23 fm/c, i.e. when the compression phase is just over (see contour plot in Fig. III.30), the flow ratio R_{13} saturates at $R_{13}=2$. This is much earlier than the saturation of E_{kin} in Fig III.27.

In Fig. III.31 we plot the flow angle $\theta_{flow}^{c.m.}$, i.e., the angle of the largest principle axis of the flow tensor to the beam axis, versus the aspect ratio R_{13} for the reaction U(400 MeV/nucleon)+U [Buc83a,b]. Note that $R_{13}>>1$ reflects events stretched in momentum space, while $R_{13}=1$ indicates a spherical momentum distribution. The ridge in the (θ_{flow},R_{13}) plane resulting from the cascade calculations depends on the total mass of the systems. The cascade calculations [Cug82, Guy82] show that substantial flow angles should only be expected for very heavy systems $A_1=A_2>100$.

Furthermore, there are substantial finite number distortions [Dan84] of the flow characteristics for A<100. Also shown are the results of the fluid dynamical calculation for the same system. Larger deflection angles and aspect ratios R_{13} indicate that the matter flux is apparently more strongly correlated for the hydrodynamical model. The impact parameter dependence of the flow angle, θ_F, aspect ratio R_{13}, sphericity $S=\frac{3}{2}(\lambda_1+\lambda_2)$, and coplanarity (or flatness) $C=\frac{3}{2}(\lambda_2-\lambda_1)$ with $\lambda_1<\lambda_2<\lambda_3$ the principal values [normalized by $(TrF_{ij})^{-1}$] is shown in Fig. III.32 from the hydrodynamic model calculation for the system ^{40}Ca(400 MeV/nucleon)+^{40}Ca. Observe the greater sensitivity of θ_F, R_{13} to impact parameter than that of S and D. Also note that $R_{13}=1.7$ at b=0 is remarkably close to the value computed via cascade for this reaction in [Guy82]. However, this coincidence is due only

to finite number distortion effects in cascade calculations. As shown in [Dan84], a sphere sampled randomly by M particles results in $R_{13}=1+3/\sqrt{M}+22/M=1.6$ for M=80. In hydrodynamics, the limit $M\to\infty$ is taken. Therefore $R_{13}=1.7$ in hydrodynamics represents true collective flow, while in cascade this value is consistent with an isotropic sphere sampled by 80 particles.

The general behavior of the flow pattern in the fluid dynamical model is as follows: The flow angle rises smoothly from 0° at large impact parameters to 90° at b=0, while sphericity and coplanarity rise from 0 to 0.9 and 0.2, respectively. Since the matter flow reflects the longitudinal, $p_{||}$, and transverse $p_{\perp}$, momentum transfer in a collision, it can be used to directly measure the pressure built up in the high density stage of the reaction [Stö81d]

$$p_{\perp}' = \int_t\int_f P(\rho,S)df\,dt, \qquad (20)$$

where df represents a surface element between the participant and the spectator matters and the total pressure $P(\rho,S)$ is the sum of an interaction pressure $P_c(\rho,S=)$ and a kinetic term $P_T(\rho,S=0)$

$$P(\rho,S) = P_c(\rho,S=0)+P_T(\rho,S>0) \qquad (21)$$

The bombarding energy dependence of $(P_c+P_T)/P_T$, i.e., the ratio of the total pressure to the Fermi-gas term, has been calculated in [Stö81a] see Fig. III.33a. The results show that there is a strong bombarding energy dependence of $P/P_T(E_{LAB})$. The kinetic term P_T dominates at high energies, $E_{LAB}>1$ MeV/nucleon, while the interaction term P_c far exceeds P_T at intermediate energies, $\lesssim$200 MeV/nucleon. Second, the total pressure is most

sensitive to the stiffness of the nuclear equation of state at energies $\lesssim$200 MeV/nucleon. Since the flow charateristics depend directly on the pressure, we can expect a dependence of the flow pattern on the stiffness of the equation of state. To check this idea we have investigated in Fig. III.33b the bombarding energy dependence of the kinetic flow ratio R_{13} for central collisions of U+U using both the fluid and cascade model [Buc83a,b].

Figure III.33b shows an important result: We find a strong energy dependence of $R_{13}(E_{LAB})$ in the fluid dynamical calculation, which indeed closely reflects the energy dependence of $P/P_T(E_{LAB})$ discussed above. This is in strong contrast to the cascade results (shaded area in Fig. III.33b) that show no appreciable indications for a dependence of R_{13} on the bombarding energy, even for the heavy system U+U. The values $R_{13}^{cascade} \lesssim 1.5$ reflect only a globally thermalized "fireball" momentum distribution. In particular, finite number effects [Dan84] map $R_{13}=1.0$ into $R_{13}\sim1.2$ for M=476. The strong collective flow, as observed in the hydrodynamical calculations is not seen. At high energies, $E_{LAB}>1$ GeV, both approaches yield similar values $R_{13}<1.5$. In hydrodynamics R_{13} approaches unity because the random thermal flow $\delta_{ij}E_T/3$ dominates the flow $\bar{F}_{ij}$ in Eq. (19) at high energies.

Again, for finite impact parameters, there is the same behavior. The curves are only shifted by a constant. The dependence of $R_{13}(E_{LAB})$ on the nuclear compressibility is of particular interest. Figure III.33b shows $R_{13}(E_{LAB})$ for three different equations of state. As with the dependence of P/P_T on the compressibility, R_{13} increases (at a given bombarding energy) if the compressibility [and hence $P_c(\rho)$] is increased. This finding shows that global event analysis as a function of beam energy can indeed provide information on the stiffness of the equation of state. The measurement of

$R_{13}(E_{LAB})$ can also allow for an experimental search for abnormal superdense states (pion condensates, density isomers, in general bends and secondary minima in the interaction pressure), which would reveal themselves by a threshold decrease of R_{13} at the critical bombarding energy E_{LAB}^{crit} sufficient for a transition into an abnormal state to occur. The decrease of the interaction pressure P_c may even lead to metastable density isomeric states. Just above the barrier to such a hypothetical abnormal state, P_c would be negative and inhibit an immediate decay of this state [Stö79]. The consideration of such abnormal states is speculative. However, our point is that $R_{13}(E_{LAB})$ is a sensitive probe to exotic phenomena as well.

To compare with actual experiments, the ideal hydrodynamic model predictions will have to be corrected for the contribution to F due to nucleons that suffer too few collisions to evolve hydrodynamically. First, there are spectator nucleons that do not suffer any large momentum transfer collisions in the first place. Second, there are knockout nucleons which suffer only on NN collision. Finally, there are intermediate collision nucleons that suffer 2-3 collisions. These nucleons will be distributed approximately isotropically in the c.m. frame [Sch81].

To incorporate such nonhydrodynamical background, we decompose F according to the number of collisions made by nucleons [Buc83a,b]

$$F = \sum_{n=0}^{\infty} P(n)F(n), \tag{22}$$

where P(n), with $\sum P(n)=1$, is the relative weight of the contribution of nucleons, which collided n times, to F, and F(n) is the flow tensor associated with the final distribution of such n collision nucleons in momentum space. We normalize F to unit trace in Eq. (22) by requiring

TrF(n)=1 for all n. At best, the flow tensor calculated in hydrodynamics can approximate F(n) for n>>1. To gain insight into the effect of small n contributions, we divide Eq. (22) into three main terms,

$$F = p_0F_0+p_1F_1+(1-p_0-p_1)\bar{F}, \tag{23}$$

where $\bar{F}$ is given by Eq. (19), $p_0=P(0)+P(1)$ is the weight of spectator and direct knockout nucleons, and p_1 is the fraction of nucleons suffering an intermediate number of collisions with N_c~2-3. The spectator plus knockout contribution F_0 is approximated by

$$F_0 = \mathrm{diag}(0,0,1), \tag{24}$$

since the spectator nucleons and--due to the forward-backward peaking of the N-N cross section--also the knockout nucleons are concentrated around ± the incident c.m. momentum per nucleon. For simplicity, we approximate the intermediate collision contribution, N_c=2-3, by an isotropic momentum distribution for which

$$F_1 = \mathrm{diag}(\tfrac{1}{3}, \tfrac{1}{3}, \tfrac{1}{3}) \tag{25}$$

Finally, for central collisions, for which $\bar{F}$ in Eq. (19) is diagonal,

$$\bar{F} = \frac{1}{2-r_h}\,\mathrm{diag}(1,1,r_h) \tag{26}$$

the full tensor has the diagonal form

$$F = \frac{1}{2+r}\,\mathrm{diag}(1,1,r). \qquad (27)$$

Note, for example, from Fig. III.33 that $r_h \sim 0.5$ for the U+U collision at 400 MeV/nucleon. For $0<r<1$, F in Eq. (27) describes a pancake shape with aspect ratio $R_{13}=1/r$ and flow angle $\theta_F=90°$. For $r>1$, F describes a cigar shape with $R_{13}=r$ and $\theta_F=0°$.

The effect of adding F_0 and F_1 to F in Eq. (23) is to replace the hydrodynamic value, r_h, by r given by [Buc83a,b]

$$\frac{r}{r+2} = p_0 + p_1 + (1-p_0-p_1)\,\frac{r_h}{2+r_h}\,. \qquad (28)$$

For example, for $r_h=\frac{1}{2}$, i.e., $R_{13}=2$, the measured r exceeds 1 if the fraction of spectator nucleons p_0 exceeds $\frac{1}{6}$. With $p_1=\frac{1}{4}$, $r>1$ when $p_0>\frac{1}{8}$.

Equation ( ) shows that the magnitude of R_{13} in Fig. III.33b can be significantly reduced as a result of the nonhydrodynamic background contributions. Only a 5% spectator contribution is required to lower R_{13} from 4 at 300 MeV/nucleon in Fig. III.33b to 2.7. Alternately, a 25% intermediate isotropic background is sufficient to reduce R_{13} to 2.5 from 4. Therefore, in comparing data to the hydrodynamic predictions in Fig. III.33b, the substantial modification of R_{13} due to the background must be taken into account. The presence of the nucleons with $N_c \leq 3$ also means that the hydrodynamic calculation should only be started after the few collision initial stage with densities depleted to the value $\rho_0(1-p_0-p_1)$ instead of using all the nucleons. However, due to the scaling of the hydrodynamic equations with the nucleon number A (i.e., since the results of the calculations are practically independent of A), we do not anticipate a qualitative change of these results.

A simple way to eliminate the spectator and knockout contributions is to remove nucleons with momenta in a shell of radius $p_{c.m.}$ and thickness $\Delta \sim 100$ MeV/c from the sum of Eq. (23). However, it is not so simple to remove the approximate isotropic background F_1. One possibiity is to estimate that component via an intranuclear cascade calculation.

We will now report a detailed analysis of the reaction Nb(400Mev/N)+Nb based on nuclear fluid dynamics and intranuclear cascade simulations. The theory is compared to recent experimental data of Ritter et al. [Rit84], who studied this system with the "Plastic Ball" 4π electronic detector system.

The general behavior of the flow pattern in the fluid dynamical model is as follows: The flow angle θ_f rises smoothly from 0° at large impact parameters to 90° at b=0. Since the contribution of zero impact parameters to the actual experiment is negligible, the theory has to sample over a range of finite impact parameters before it can be compared to the data.

The major cause of concern for a direct comparison of the data to the hydrodynamical predictions is, however, the finite multiplicity, $M<50$, of emitted fragments: There are substantial finite-number distortions [Dan84] to the kinetic-energy-flow analysis for multiplicities $M<100$. Therefore, a direct comparison of the conventional "infinite-particle-number" hydrodynamics with the "raw" finite-multiplicity experimental data is inhibited. Only for very massive systems such as uranium on uranium could the finite-particle-number distortions be considered reasonably small. There are two ways out of this dilemma: The first is to correct for the finite-multiplicity distortions in the experimental data via an unfolding procedure, which extrapolates the data to the thermodynamic limit, i.e.,

towards infinite particle number. The second method, applied in this work, incorporates the finite-multiplicity effects via a Monte Carlo procedure into the theory. This is done by random sampling of a given fragment multiplicity from the momentum-space distribution of the flow tensor as obtained from the fluid dynamical calculation. This procedure has the distinct advantage that the detector efficiencies can be folded into the theoretical analysis, thus allowing for an unbiased, direct comparison of theory and data. In particular, the restriction to light fragments $Z \leq 2$, the low-energy cutoff ($E^{cut}/A < 25$ MeV), and the backward-angle acceptance hole of the Plastic Ball ($\theta_{lab}^{cut} > 160°$) have been taken into account in the present analysis [Buc84].

Figure III.34 shows the distribution of flow angles, $dN/d\cos\theta_F$, thus obtained in comparison with the experimental data and the intranuclear cascade calculation [Gus84, Yar79]. The fragment yield calculation performed after the breakup of the fluid yields average multiplicities from M=35 at b=6 fm to M=46 at b=0. The dispersion of multiplicities around these values has not been taken into account. The theoretically obtained high-multiplicity triggered events, corresponding to the small impact parameters (b=0 to 3 fm), compare favorably with the high-multiplicity selected experimental data. Both exhibit average sidewards flow angles of $\theta_F = 30°$, whereas the high-multiplicity selected events of the cascade calculation [Gus84,Yar79] exhibit strongly forward-peaked distributions. This observation of collective sidewards flow represents the first unambiguous evidence for the formation of high density matter, which has been predicted on the basis of nuclear fluid dynamics a decade ago [Sch74]. Thus the key mechanism for the investigation of the nuclear equation of state has been experimentally established. It is surprising that the

predicted 90° flow [Sch74,Hof76,St678] can be observed neither in the data nor in the fluid calculation. This is due to the rapid falloff of θ_F for b>0: $dN/d\cos\theta$ is dominated by contributions from b≈2-3 fm. Only for much heavier sytems, e.g., U+U, would this range of b values reveal flow angles $\theta_F \geq 60°$. The intermediate multiplicities (30<M<40) correspond to larger impact parameters, b<6 fm in the hydrodynamical plus statistical breakup calculation. The experimentally observed decrease of the average flow angle ($\theta_F = 15°$) is well reproduced by the fluid dynamical calculation. The lowest interval of multiplicities, M<20, corresponds to large impact parameters, where the projectile and target remnants cause the strong 0° peak in $dN/d\cos\theta_F$.

The asymmetric system Ar+Pb at 800 MeV/N is the heaviest system to date for which 4π-data exist at relativistic energies. The streamer chamber measurements by the GSI-LBL-Heidelberg collaboration [Str83] indicate consistently larger flow angles and more isotropic aspect ratios than are predicted by the cascade code of Cugnon et al. [Cug82]. This may be taken as evidence for a fluid dynamical behavior of this system. The details of the analysis, however, make a quantitative comparison with fluid dynamical calculations difficult.

We present the results of a 3-dimensional relativistic fluid dynamical calculation for Ar+Pb coupled with a generalized flow analysis using relativistic kinematics [Gra84]. The center of momentum frame used to construct the flow tensor,

$$F_{ij} = \Sigma_\nu w(\nu) p_i(\nu) p_j(\nu)) \qquad (29)$$

is determined by the "participants", defined in the experiment [Str83] as all particles with transverse momentum $p_t > 270$ MeV/c. In contrast to a symmetric system, the velocity of this participant CM is not constant, but ranges from the compound nucleus limit for central collisions to the nucleon-nucleon limit (and beyond) for peripheral collisions (Fig. III.35).

The experimental analysis is restricted to charged particles in the forward hemisphere of the participant CM. The transverse energy E_t of these particles, defined as

$$E_t = \Sigma_\nu \{[p_t(\nu)^2 + m(\nu)^2]^{\frac{1}{2}} - m(\nu)\} \qquad (30)$$

is found to decrease with increasing impact parameter b in the cascade and hydrodynamical models and is used experimentally as a measure for b. The flow tensor F_{ij} is diagonalized with the weight function $w(\nu) = 1/|p(\nu)|$. This has properties similar to the kinetic flow tensor (Eq. 19)), with $w(\nu) = 1/2m_\nu$, but does not show collective effects as clearly. This is seen in Fig. III.36 which shows the aspect ratio R_{12} (largest eigenvalue of F_{ij} to second) as a function of E_t for the weights

$$w(\nu) = 1/(2m(\nu)),\ 1/(|p(\nu)|),\ 1/(|p(\nu)|)^2. \qquad (31)$$

The choice at R_{12} and the $1/|p|$ weighting, instead of R_{13} and $1/2m$ as in other analyses presented here, has been introduced by the experimentalists to facilitate the analysis of the streamer chamber data. We would like to point out that $R_{12} \to 1$, does not necessarily imply isotropy but would also emerge from oblate shapes of F_{ij}. The flow angle θ_F is essentially independent of $w(\nu)$ but R_{12} and hence the sensitivity of the

flow analysis to dynamical effects decreases for increasing powers of $1/|p|$ and tends towards a constant value of 1 independent of E_t. Figs. III.37 and III.38 show the R_{12} and θ_F values as a function of E_t as determined by hydrodynamics (solid curve). The values corrected for finite multiplicities [Dan84] of 30 (dashed line) are also shown. In addition, the cascade and experimental values are shown [Str83]. With increasing E_t, i.e. decreasing b, the flow angle increases, i.e. shows more sidewards flow, and R_{12} decreases, which in this case indicates more isotropy. Hydrodynamics exhibits the largest flow angles, while the experimental data lie between the hydro and cascade results. The flow angle distribution for data, cascade and fluid dynamics are compared in Fig. III.39.

A further indication of hydrodynamical behavior can be seen in Fig. III.40 which shows the mean longitudinal versus mean transverse momentum per event. Events which lie on the dotted line may indicate isotropy. However, events with a collective flow may also exhibit the same transverse as longitudinal momenta and hence lie on the dotted diagonal line. The only direct signature for strong transverse flow in this plot is due to events which lie above this line. This is the case for central collisions, $b<4$ fm, in the hydrodynamic calculation. Also the experimental data [Str83] lie above this line once high-E_t events are selected. However, it is not clear if this is an indication for strong transverse flow or only the result of a bias due to the high E_t sampling [Str83]. The high-E_t cascade events [Str83] only approach the diagonal, which in this case still means a forward peaking because of the sampling bias.

Unfortunately an improved quantitative comparison is not possible at this stage. On the one hand, the finite particle effects are only treated approximately in the hydrodynamical calculations. On the other

hand, the varying participant CM velocity of this asymmetric system, particularly in combination with the restriction to the forward hemisphere, leads to problems with the specification such quantitites as E_t and the flow tensor.

A small change in the CM velocity, which is experimentally determined for each event, results in a dramatic displacement of the event in the $p_\perp$, $p_{||}$ plane. A small increase of β_{CM} for example, causes particles with essentially transverse momenta to be displaced from the forward hemisphere. Thus the effective E_t of the event is reduced. In addition, the longitudinal momentum components of the remaining forward particles are reduced which in turn changes both flow angle and aspect ratio. Thus both axes of the corresponding figures are distorted. This effect is demonstrated in Fig. III.41 where the variation of θ_F--(about a factor of 2!) with a ±20% change in β_{cm} is depicted.

The best solution we see is to perform such experiments for a symmetric system where the cm is well defined.

8. Microscopic Analysis of Collective Flow

- Indication for a Stiff E.O.S.

The quantitative confirmation of the longstanding predictions of the collective sidewards flow [Sch74;St880] discussed in the previous section establishes clearly the formation of highly compressed nuclear matter.

On the other hand, although the key mechanism for the investigation of the properties of high density matter has been identified, the problem remains to extract the nuclear equation of state, in particular the compression energy, from the flow data. This can in principle be

accomplished via a detailed comparison with the hydrodynamic model predictions for different equations of state and different transport coefficients. However, we have seen in the previous section that there is a substantial non-equilibrium contamination of the data, i.e. direct (knock-out) nucleon-nucleon scattering, etc. It has been shown that it is not entirely clear how to subtract this contamination from the data. Therefore, in order to perform a quantitative extraction of the compression energy from the data, we will in the following return to the microscopic approaches discussed and applied above, in particular the Newtonian Force Model and the VUU-approach [Mol85].

In the Newtonian Force Model the computations are stopped after t = 30 fm/c, after which the flow results are constant. The evolution of a collision at b = 3 fm impact parameter is shown in Fig II.1. The resulting sidewards flow can clearly be seen. Note that the average deflection angle of the center of mass of projectile and target nucleons, respectively, is approximately equal to the average calculated flow angle. This associates a simple meaning to the flow concept. The demonstrated strong correlation between configuration space and momentum space can be attributed to the repulsive short range component of the nucleon-nucleon potential.

The individual collisions are analyzed by diagonalizing the kinetic energy flow tensor [Gyu 82]

$$F_{ij} = \sum_\nu p_i(\nu)p_j(\nu)/2m(\nu) \qquad (32)$$

where the sum is over all charged particles in a given event. By diagonalizing this tensor, the flow angle θ_F is obtained for each event. The distribution of flow angles $dN/d\cos\theta_F$ is presented in Fig. III.42 for various impact parameter intervals. The qualitative behavior of the flow

pattern in the NFM model is as follows: the flow angle θ_F rises smoothly from 0° at large impact parameters to 90° at b=0 fm. However, the contribution of zero impact parameter collisions to the observable cross sections is negligible. Thus a finite range of impact parameters is sampled to compute the angular distributions of the flow angles, $dN/d\cos\theta_F$, which is to be compared to the experimental data of the GSI/LBL collaboration.

The distribution of flow angles was computed taking into account the formation of fragments via a generalized coalescence model discussedabove. We have found that one obtains roughly the same flow distribution by doing the flow analysis with protons only (no clustering), with clustering (protons only), or by counting all particles obtained with the coalescence model.

Fig. III.34 shows the experimental data for the Nb(400 MeV/N)+Nb case discussed above, together with the predictions of the intranuclear cascade, and fluid dynamical calculations. The data exhibit nonzero average flow angles once high multiplicity, i.e. small impact parameter collisions, are selected. This is in contrast to the intranuclear cascade calculation (using the Yariv Frankel and Cugnon approaches), which yields zero flow angles even at the highest multiplicities (also see Fig. III.43).

The present microscopic NFM model, on the other hand, predicts peaks in the angular distributions of the flow angles. The peak shifts to larger angles with increasing multiplicity. This is in qualitative agreement with the experimental data. The physical difference between the INC model and the NFM approach, which leads to such distinct predictions can be traced back to the different treatments of the nn collision process. The INC applies a stochastic 4π scattering at the point of closest approach of straight line trajectories; this allows for substantial transparency. In

contrast, the repulsive short range component in the NN potential used for the NFM approach is a hard core and thus effectively results in an excluded volume effect. The nuclei are not as transparent and easily compressible as in the INC. This causes incident nucleons to be deflected away from zones of high density, i.e. small interparticle separations, towards sidewards angles.

Let us now return to the VUU theory, which also predicts finite flow angles [Kru85a,Mol84,85]. We study the flow angle as a function of time. For example, in Nb (1050 MeV/nucleon) + Nb, at b = 3 fm, the flow angle reaches a maximum at t = 14 fm/c (see Fig. III.44). The compression or density of nuclear matter reaches its maximum value at 5 fm/c (Fig. III.45): it takes a finite amount of time for the equilibration of the momentum distribution to occur.

As a function of energy, the density probed in heavy ion collisions is very similar in Au + Au (see Fig. III.46), Nb + Nb, or Ar + KCl collisions. What is important for the maximum density probed is not the atomic number, but the EOS: higher densities are achieved with softer equation of states. Notice that the densities probed with the VUU theory are much less than those reached with the less realistic intranuclear cascade model.

The density probed is related to the flow angle for a given system via the EOS. A softer equation of state results in lower peak flow angles (Fig. III.47). Hence, the flow data indicate again a stiff EOS [Kru85a].

How does the peak flow angle vary as a function of the bombarding energy? At fixed impact parameter (b = 3 fm), the flow angle reaches a maximum value at 400 MeV/nucleon and then does not change further as the collision energy increases (Fig. III.48). There is however a very strong

effect due to the atomic number (Fig. III.49) at fixed energy E = 400 MeV/nucleon. This is easily understood: even though these different symmetric systems probe the same densities, there are much more collisions for the higher atomic numbers. The collective flow thus comes about as an interplay between the collision term and the EOS in the VUU theory. We find similar results for the peak flow angle in Au + Au versus energy (Fig. III.50) at b = 3 fm except that the maximum flow angle is now twice as large than for Nb + Nb (Fig. III.48) [Mol85].

Asymmetric collisions present results entirely consistent with but somewhat different from the above. One sees from Fig. II.12 that in order to detect the collective sidewards flow of nuclear matter one needs to look at the projectile hemisphere $p_z < 0$ in momentum space. An asymmetry here is evidence of collective flow; this is easily observed at the intermediate impact parameter b = 5 fm in Fig. II.12. Observe that the flow of nucleons in momentum space is correlated with a flow in configuration space, as is the case also for symmetric systems.

Let us compare the predictions of the VUU approach to the data of the GSI-LBL streamer chamber group. The experimentalists analyzed their data using the momentum flow tensor:

$$P_{ij}=\Sigma_\nu[p_i(\nu)p_j(\nu)/\mathrm{abs}(p(\nu))]/\Sigma_\nu \mathrm{abs}(p(\nu)) \qquad (33)$$

The data analysis proceeds on an event by event basis in a rather non-trivial way. First, only charged particles are used. Then the center of mass velocity for each event is computed from the momenta of all charged particles with transverse momenta per nucleon greater than the Fermi momentum. Then only the forward hemisphere of this participant center of

mass frame is analyzed. Their results are shown in Fig. III.51a. We compare in Fig. III.51b the corresponding predictions of the Vlasov-Uehling-Uhlenbeck theory. Both in theory and experiment a broad bump is observed in the angular distribution of flow angles for near central collisions, while a rather sharp peak occurs at 15-30 degrees for the medium impact parameters, i.e. intermediate multiplicity events. This contrasts strongly with the results of intranuclear cascade calculations, which exhibit forward peaked angular distributions independent of impact parameter as well for asymmetric as for symmetric collisions.

The flow analysis has also been done in the more rigidly defined nucleon-nucleon center of momentum system with the coalescence invariant kinetic energy flow tensor.The analysis is also restricted to the projectile momentum hemisphere $p_z < 0$ since this will avoid the distortion of the event shape by the large number of target spectators at rather small momenta and thus best reflect the flow of the participant nucleons. We see in figure III.51c that the flow distribution changes it's characteristics in particular for the high multiplicity events. One now sees a distribution skewed towards 90° for the small impact parameters, while the peak remains near 20° degrees for the intermediate impact parameters. This is similar to the results for symmetric systems; the peak of the flow angle distribution decreases with increasing impact parameter.

In Fig. III.52 the standard kinetic energy flow distributions are compared for individual impact parameters to the novel transverse momentum analysis of Danielewicz and Odyniec [Dan84] that provides a sensitive test for collective flow and it's dependence on the nuclear equation of state in light systems [Mol85a]. The transverse momentum spectrum $p_x(y)$ is analyzed here

$$y=1/2 \ln (E+p_{par})/(E-p_{par}) \quad (35)$$

is the rapidity, E is the total energy of the fragment, and p_{par} is the momentum in the beam z-direction. Note that in the simulations shown here the projectile has $p_{par} = p_z > 0$; in the configuration and momentum space plots shown above the axis have been flipped for ease of viewing. This technique has also been used to predict the presence of collective flow for ^{16}O (600 MeV/A) + ^{16}O within the time dependent Dirac equation approach [Cus85].

As is evident from Fig. II.12, the flow angle approaches it's asymptotic value rather rapidly; indeed at b= 3 fm, the final flow angle distribution is established in less than 20 fm/c. At b = 1 fm, the flow angle distribution is skewed to 90°, i.e., the projectile momentum hemisphere exhibits sidewards peaking as is evident from Fig. III.52; a significant number of particles are thrust to the side perpendicular to the beam axis. A broad peak around 55° is observed at b = 3 fm; the flow angle begins to become well defined. For b = 5 fm, there is a clear peak at 20-30 degrees. Thus it is only at the intermediate impact parameters that the flow is evident by a sharp peak in such asymmetric systems. Part of the reason why the peak is not so pronounced at lower impact parameters is statistical: the projectile hemisphere contains substantially fewer fragments in the final state in an Ar + Pb collision than in a Nb + Nb collision.

In the transverse momentum plots, much the same behavior is seen. However, here the analysis is not restricted to the forward hemisphere in momentum space. Summation over p_x and division by the number of protons in each rapidity bin shows very little flow effects in the target rapidity region, which is dominated by target spectator matter. At b = 1 fm, p_x/N is

about 50 MeV/c/N at projectile rapidity, $y_p = 0.60$, whereas at target rapidity, $y_T = -.60$, p_x amounts to only 25 MeV/c/N. The flow at b = 3 fm is particularly pronounced in this method of analysis: $p_x(y_p) = 150$ MeV/c/N whereas $p_x(y_T) = 40$ MeV/c/N. At b = 5 fm, we have much the same result as at b = 3 fm. Note that in the massive system studied here the transverse momentum transfer (bounce-off effect) is larger than in lighter systems at higher energies - 100 MeV/c/N have been observed for the system Ar (1.8 GeV/N) + KCl (Fig. III.55).

Effects of the nuclear equation of state have also been looked for by varying the compressibility from K=380 MeV to K=200 MeV at b=1,3 and 5 fm. At the lower impact parameter, the broad distribution prevents any statistically significant difference from being seen. At the intermediate impact parameter, one sees a small shifting of the flow angle peak to the smaller angles as the compressibility decreases; this is consistent with but less dramatic than what we have found for symmetric systems. Note that one sees a great difference if K=0 MeV, i.e., the cascade model is used; then the distributions are peaked at zero degrees for all impact parameters. An equation of state with compressional energy seems essential to qualitatively reproduce the data; but asymmetric systems appear to be less sensitive to the details of the equation of state than symmetric collisions. Furthermore, one can look for quantal effects by turning off the Pauli principle at b= 3 and 5 fm. No strong effects are seen. This is somewhat of a surprise in view of the strong effect we see in the symmetric case and the fact that about 50% of the collisions are Pauli blocked even at this high energy. However, this may perhaps be understood by the fact that many of the blocked collisions are between nucleons in the same nucleus, not between nucleons in the compression zone.

Let us also studied the same system at a lower energy 400 MeV/N (see Fig. III.52). The kinetic energy flow angle distribution becomes more forward peaked at fixed impact parameter b = 5 fm. The transverse momentum transfer $p_x(y_p)$ decreases to 100 MeV/c/N. The similar system Ar (92 MeV/N) + Au shows what happens in an event by event analysis as the energy is decreased further: the flow distributions at b= 2, 3, and 4 fm impact parameter become very broad; the transverse momentum at beam and target rapidities is zero to within 10 MeV/c/N. At still lower energies, the transverse momenta spectra are inverted as the attractive part of the nuclear potential becomes dominant: the bounce-off caused by the short range repulsion at high density is converted into the negative angle deflection known from TDHF calculations in this energy region and from experimental data.

The transverse momentum for symmetric systems Nb + Nb (Fig. III.53) and Au + Au (Fig. III.54) is a strong function of energy. At b = 3 fm the transverse momentum $p_x(y_p)$ rises from negative or zero values for E < 100 MeV/nucleon to 140 to 160 MeV/c/nucleon at 1050 MeV/nucleon for Nb and Au systems, respectively. The bounce-off increases dramatically with energy but only slightly with atomic number.

9. More Evidence for a Stiff Nuclear Equation of State from the Transverse Momentum Analysis

For light systems and high energies flow effects are not observed when the standard kinetic energy flow analysis is used. In fact, the experimental flow angular distributions for the reaction Ar(1800 MeV/nucleon, b<2.4fm) + KCl are peaked at zero degrees as the cascade model predicts. But also the present Vlasov-Uehling-Uhlenbeck approach, which

does predict finite flow angles for heavier systems at lower energies, does not yield any observable sidewards maxima in the flow angle distributions ; even less so can we distinguish between hard and medium equations of state when the standard kinetic energy flow tensor analysis is used: all flow angle distributions are peaked at zero degrees [Mol 85a]. Therefore, one might be tempted to hastily conclude that flow effects do not occur for light systems.

However, Danielewicz and Odyniec have recently proposed a novel transverse momentum analysis technique that provides a much more sensitive test for collective flow. They analyze the transverse momentum spectrum $p_x(y)$ where

$$y=1/2 \ln (E+p_{par})/(E-p_{par}) \qquad (35)$$

is the rapidity, E is the total energy of the fragment, p_{par} is the momentum in the beam (here the z-) direction, and p_x is the projection of the transverse momenta into the scattering plane. Danielewicz and Odyniec have been able to determine the scattering plane in the experimental data by controlling the finite multiplicity distortions carefully. They have tested their method by subjecting events generated via the intranuclear cascade model, i.e. events where the actual reaction plane has been given, to their procedure for determining the reaction plane from data and find good agreement. In the following we compare the data in the extracted scattering plane to the theoretical results in the given (x-z) scattering plane.

Danielewicz and Odyniec detected collective flow effects in the streamer chamber data for Ar(1800 MeV/nucleon)+ KCl using this technique (see Fig. III.55). There is a transverse momentum accumulation at both the projectile and target rapidities y = ±0.86 in the center of momentum frame. They report that the collective flow effects are weaker than in the

hydrodynamic model, but much stronger than in the cascade (see Fig. III.55). It is important to point out that the intranuclear cascade model fails to reproduce the data, even though it appeared to be consistent when the kinetic energy flow analysis had been applied. The highly increased sensitivity of this new technique has more recently been used to predict the presence of collective flow for O (600 MeV/nucleon) + O within the context of the time dependent Dirac equation with relativistic mean field dynamics, see Fig. III.56 and III.57 [Cus85].

The transverse momentum analysis technique has been applied to the Vlasov-Uehling-Uhlenbeck results for the reaction Ar(1800 MeV/nucleon, b < 2.4 fm) + KCl studied experimentally. One finds that the peak in the transverse momentum spectrum $p_x(y)$ depends linearly on the nuclear equation of state: the cascade model predicts $p_x^{max} \approx 25$ MeV/c/nucleon (Fig. III.55), the medium equation of state in the Vlasov-Uehling-Uhlenbeck approach predicts $p_x^{max} \approx 50$ MeV/c/nucleon (Fig. III.55d), and the stiff equation of state yields $p_x^{max} \approx 100$ MeV/c/nucleon (Fig. III.55c). Only the latter is in agreement with the data. This result is supported by the fact that the stiff equation of state reproduces best the pion yields observed in the streamer chamber at this energy (1800 MeV/nucleon) and also at lower energies, down to 360 MeV/nucleon (Fig. III.12). It is most important to point out that this equation of state agrees rather well with the one extracted phenomenologically from the pion data, thus offering the fourth independent clue on the stiffness of the nuclear matter equation of state [Mol85].

IV. Creation of the Quark Gluon Plasma at Ultrarelativistic Energies

Space-Time evolution of the high energy density region

The possibility of creating an entirely new form of matter, the deconfined quark-gluon plasma, in the laboratory has spurred a tremendous activity, both theoretical and experimental, in the high energy and nuclear community during the last few years [QM79, QM80, QM82, QM83, QM84]. We have developed some of the statistical concepts frequently used in the theoretical description of this state in Chapter I.

Here we will not consider the transition itself, but we will discuss the space-time evolution of the high energy density matter in ultrarelativistic heavy ion collisions, where the relativistic fluid description is used as a dynamical model. The foregoing chapters have presented evidence for hydrodynamical behavior at energies up to $E_{LAB} = 4$ GeV/N. In the following we assume [Stö80c] that hydrodynamics is also valid at higher energies, $E_{LAb} > 4$ GeV/N. This extrapolation is questionable at very high energies, $E_{LAB} > 100$ GeV/N, because of the longitudinal growth which may lead to the "transparency" predicted by the inside out cascade [Nik81, Pok75, Gyu83]. The minimal requirements on beam energy and -mass are discussed in the following section.

Energy densities on the order of 1-2 GeV/fm^3 are predicted to be necessary for the deconfinement transition to occur. This number is derived from SU(N) Yang Mills theory (pure gluon matter) on the lattice [Eng82]. However, the idealized configuration of a zero net baryon number (zero chemical potential) plasma may be different to attain, even in the mid-rapidity region of collisions with $E_{LAB} > 100$ GeV/N, since nuclei seem to be

not as transparent as once thought [Bus83,Kaj83]. Thus it probably is necessary to study a baryon rich plasma. This may, in fact, prove very interesting, since it may be reachable at considerably lower energies [Stö84].

Whence the plasma is created, there is the additional problem of detecting it experimentally. Possible signatures of a quark-gluon plasma include enhanced production of lepton pairs [Dom81, Kaj81,Kaj82], influences on the photon spectrum [Kaj81,82], and the relative abundance of strange particles [Raf82,Koc83,Elz84,Ka83,Bir82,Rat82]. Recently antinuclei have been proposed as a signature for the phase transition [Hei84,Mol84,Sub85]: The abundance of antiquarks in the quark gluon plasma can favor the formation of antinuclei as compared to the - energetically less favorable - formation in the normal hadronic phase.

Let us first look at the simplified one-dimensional hydrodynamical model with subsequent isentropic expansion. It can be used to study the maximum density and temperature obtained at a given energy [Stö80]. Results on the time evolution of the system are obtained using full 3-dimensional hydrodynamics.

Figure IV.1 shows the result of a simplified 1-D hydrodynamic calculations of the energy densities attainable in central collisions of heavy nuclei. Observe that the energy density obtained depends on the equation of state (EOS) used in calculation. The different types of EOS include a Hagedorn hadron gas with an exponentially increasing mass spectrum and a deconfined quark gluon plasma. The different EOS lead to prediction of a regime of bombarding energies at which the "critical" energy densities e=1-2 GeV/fm^3, may be reached: E_{LAB}^{crit}=4-7 GeV/N, values surprisingly modest compared to the values E_{LAB}>100 GeV/N generally believed to be necessary to

form the baryon free plasma. The one dimensional calculations give only the initial energy densities in the collisions. The system will subsequently expand as a result of the high pressure buildup. Hence the matter is accelerated, the density diminished and, because of energy conservation, the internal energy and temperature drop.

The dynamical path of a collision in the ρ-T plane, the phase diagram of hadronic matter, is depicted in Fig. IV.2. The initial stage of high compression and excitation is followed by the isentropic expansion of the system. The matter cools only modestly during the dense stage where baryon densities exceed normal nuclear density. At densities below normal density, the system is cooled much more rapidly due to the formation of pions. Also shown in the figure are contours of constant energy densities of 1 and 1.5 GeV/fm^3 of the deconfined phase. Observe that according to this simplified calculation bombarding energies E_{LAB}> 2-4 GeV/N should be sufficient for deconfinement to occur in stopping collisions. If deconfinement actually would occur at these rather modest energies, the energy gap between confined and deconfined matter would result in temperatures and entropies substantially lower than those calculated under the assumption that confinement does not happen. The nuclear matter entropy exceeds 4 at E_{LAB}>2 GeV/N. The plasma entropy, on the other hand, is zero at the critical energy , E_{crit}=2.2 and 4.2 GeV/N for B_{VAC}=190 and 450 MeV/fm^3, respectively, necessary to overcome the energy gap between the hadron and the quark-gluon phase (see Fig IV.3). This mechanism of "cold" plasma production has been emphasized before [Stö80c,Guy83,Bir83,Stö84].

It should be noted that none of the discussed possible experimental signatures for the deconfinement transition (dilepton [Dom81], photon [Kaj81] and strangeness [Koc83] production) would necessarily make

sense in this baryon rich region: These signatures rely on the very high temperatures predicted for the baryon free plasma, while the temperatures in the baryon rich plasma are much lower, even at the same energy density.

Let us now study the question of timescales and spatial size of the region of high energy density. Three-dimensional relativistic hydrodynamical calculations have been done at high energies by Graebner et al. [Gra84]. The system Ne + Pb at energies of 5, 10 and 15 GeV/N is of particular interest as it will be studied in the near future (1986-87) at the upgraded alternating gradient synchroton (AGS) at BNL, Brookhaven and at the SPS at CERN.

Two equations of state have been considered in the fluid calculations, namely the linear and quadratic cases discussed in Chapters I and III. The "harder" quadratic EOS corresponds to the form deduced by Stock et al. [Sto82] from the excess pions produced in cascade calculations. In both cases the hadron gas thermal energy discussed in Chapter I is used to describe the thermal behavior.

Fig. IV.4 shows the number of nucleons contained in an energy density regime above a given threshold value, e_{crit}, as a function of the proper time in the rest system of the high energy density matter. The dependence of the bombarding energy (E_{LAB}=5, 10, 15 GeV/N) and on the (linear and quadratic) EOS are shown. For example, there are >30 nucleons above the critical energy density e_{crit}=2 GeV/fm³ for a period of ca. 4 fm/c at 15 GeV with the linear EOS (Fig. IV.4, right).

Fig. IV.5 indicates the reduction of $A(e_{crit})$ with impact parameter for e_{crit}=2 GeV/fm³. The stiffer quadratic EOS shown on the left of Fig. IV.4 results in a more rapid evolution: here a significant number of nucleons is in the e > 2 GeV/fm³ region for only ca. 2 fm/c.

Note that we have not examined the transition per se to the deconfined quark-gluon phase, but only the necessary condition for its occurrence: a large volume filled with high energy density matter. The time scale for establishing the deconfinement transition itself to occur must be obtained from other considerations and then compared with the time for which the high energy zone exists. Only then can one decide if the phase transition can actually take place. Should the phase transition develop rapidly enough, it may exert an influence on the dynamics of the collision itself. This remains to be investigated.

Very important information is the dependence of the energy density attainable on the mass of the projectile: Fig. IV.6 shows the energy density attained in a collision of two very massive nuclei, Pb+Pb at 5 and 15 GeV/N. We want to highlight the following points:

(a) First, the maximum energy density achievable is doubled by going to the heavy system: Energy densities above 5 GeV fm^{-3} are attainable for a large number of nucleons (A > 200!) and a considerably prolonged time span, $\tau \approx 3$ fm/c.

(b) The total number of baryons in the high energy density regime increases dramatically: 200-300 baryons rather than 30-50 are at $e>e_{crit}$.

(c) Energy densities E>2 GeV fm^{-3} can be obtained for a large number of baryons and for a rather long period, $\tau \approx 5$ fm/c at much lower bombarding energies, $E_{LAB}<5$ GeV/N, with the lead projectile, while there are no baryons in the high energy density regime, if the light neon projectile is used.

Therefore, it seems to be extremely promising to study collisions of massive nuclei at comparatively moderate bombarding energies (e.g. Pb + Pb at $E_{LAB} \approx 5$ GeV/N) rather than reactions at higher energies, but with

light projectiles (e.g. Ne+Pb at 15 GeV/N). This should be considered for the plans of future experimental facilities: It is easier to compress a fluid with a piston than with a pin.

Conclusions

We have reviewed the exciting recent progress made in the understanding of the fundamental physics of relativistic heavy ion collisions. A wealth of new phenomena related to the bulk properties of nuclei and nuclear matter is being investigated. Heating of nuclear matter and shock compression, the key mechanisms for investigations of bulk properties of nuclear matter, have been observed, as predicted in 1974 [Sch74]. In particular one seems to have extracted first information on the equation of state of hot dense hadronic matter from recent data.

We presented the statistical concepts employed in the study of the properties of infinite hadronic systems at high density and finite temperatures, the equation of state and the conjectured phase transitions. The formalisms appropriate to describe the dynamical evolution of the highly excited strongly interacting system - nuclear fluid dynamics, the intranuclear cascade model, classical equation of motion simulations and the Vlasov Uehling-Uhlenbeck theory - have been derived.

Recent 4π experiments on fragment formation, pion production and collective flow have been presented. Evidence for the same surprisingly stiff nuclear compression energy has been obtained independently from the the distinct data sets by comparison to both macroscopic and microscopic theories.

We also discussed the possible creation of a deconfined quark gluon plasma at future ultra-relativistic heavy ion facilities. Relativistic fluid dynamical calculations have been presented, which indicate that energy densities as high as several GeV/fm^3 may be attainable for considerable time spans in the bombarding energy range E_{LAB}=5-15 GeV/N. Thus it may indeed be

possible to produce quark-gluon matter in the future BNL and CERN experiments. Uncertainties remain, however, in the transition mechanism and the possible detection of the quark qluon plasma. The calculations suggest that massive projectiles can be used to explore the behavior of matter under extreme temperatures and densities that prevailed in the big bang, in neutron stars and in supernova explosions.

References:

Aic 85 J. Aichelin, H. Stöcker, MSU-CL505, Phys. Lett. B, in print.

Ald 57 B.J. Alder and T.E. Wainwright, J. Chem. Phys. 27, 1208, 1957.

Ams 75 A.A. Amsden, G.F. Bertsch, F.H. Harlow, and J.R. Nix, Phys. Rev. Lett. 35, 905, 1975.

Ams 77a A.A. Amsden, F.H. Harlow and J.F. Nix, Phys. Rev. C15, 2059, 1977.

Ams 77b A.A. Amsden, J.N. Ginocchio, F.H. Harlow, J.R. Nix, M. Danos, E.C. Halbert and R.K. Smith,Jr., Phys. Rev. Lett. 38, 1055, 1977.

Ani 80 R. Anishetty, P. Koehler, and L. McLerran, Phys. Rev. D22, 2293, 1980.

Awe 81 T.C. Awes, G. Poggi, S. Saini, C.K. Gelbke, L. Legrain, G.D. Westfall, Phys. Lett. 103B, 417, 1981.

Bau 75 H.G. Baumgardt, J.U. Schott, Y. Sakamoto, E. Schopper, H. Stöcker, J. Hofmann, W. Scheid, W. Greiner, Z. Phys. A273, 359, 1975.

Bau 79 H.G. Baumgardt and E. Schopper, J. Phys. G5, L231, 1979.

Bay 76 G. Baym and S.A. Chin, Phys. Lett. 62B, 241, 1976.

Ber 74 H.H. Bertini, T.A. Gabriel and R.T. Santoro, Phys. Rev. C9, 522 1974.

Ber 75 G.F. Bertsch, Phys. Rev. Lett. 34, 697, (1975).

Ber 78 G.F. Bertsch and A. Amsden, Phys. Rev. C18, 1293, 1978.

Ber 84a G.F. Bertsch, H. Kruse and S. das Gupta, Phys. Rev. C29, 673, 1984.

Ber 84b G.F. Bertsch, Erice School in Nuclear Physics 1984.

Bet 68 H.A. Bethe, Phys. Rev. 167, 879, 1968.

Bir 82 T.S. Biro and J. Zimanyi, Phys. Lett. 113B, 6, 1982.

Bir 83 T.S. Biro and J. Zimanyi, Nucl. Phys. A395, 25, 1983.

Bjo 83 J.D. Bjorken, Phys. Rev. D27 , 140, 1983.

Bod 71 A.R. Bodmer, Phys. Rev. D4, 1601, 1971.

Bod 77 A.R. Bodmer and C.N. Panos, Phys. Rev. C15, 1342, 1977.

Bod 80 A.R. Bodmer, C.N. Panos and A.D. Mackellar, Phys. Rev. C22, 1025, 1980.

Bod 81 A.R. Bodmer and C.N. Panos, Nucl. Phys. A356, 517, 1981.

Bog 77 J. Boguta and A.R. Bodmer, Nucl. Phys. A292, 413, 1977.

Bog 82 J. Boguta, Phys. Lett. 109B, 251, 1982.

Bog 83 J. Boguta and H. Stöcker, Phys. Lett. 120B, 289, 1983

Bon 76a J. Bondorf, H.T. Feldmeier, S. Garpman and E.C. Halbert, Phys.Lett. 65B, 217, 1976.

Bon 76b P. Bonche, S. Koonin and J.W. Negele, Phys. Rev. C13, 1226, 1976.

Bon 79 J.P. Bondorf, Proc. of the Topical Conf. on "Large Amplitude Collective Nuclear Motions", Lake Balaton, 1979, p. 482.

Buc 80 G. Buchwald, Diploma Thesis Universität Frankfurt, 1980.

Buc 81a G. Buchwald, L.P. Csernai, J.A. Maruhn, W. Greiner, and H. Stöcker, Phys. Rev. C24, 135, 1981.

Buc 81b G. Buchwald, C.P. Csernai, G. Graebner, J.A. Maruhn, W. Greiner and H. Stöcker, Z. Phys. A303, 111, 1981.

Buc 83a G. Buchwald, G. Graebner, J. Theis, J.A. Maruhn, W. Greiner and H. Stöcker, Phys. Rev. C28, 1119, 1983.

Buc 83b G. Buchwald, G. Graebner, J. Theis, J. Maruhn, W. Greiner, H. Stöcker, K. Frankel and M. Gyulassy, Phys. Rev. C28, 2349, 1983.

Buc 84a G. Buchwald, Ph.D. thesis, Universität Frankfurt, 1984.

Buc 84b G. Buchwald, G. Gräbner, J. Theis, J. Maruhn, W. Greiner, and H. Stöcker, Phys. Rev. Lett. 52, 1594, 1984.

Buc 84c G. Buchwald, G. Graebner, D. Barthel, J.A. Maruhn, H. Stöcker, and W. Greiner, Springer Tracts of Physics, 1985

Buc 85 G. Buchwald and H. Stöcker, Reports on Progress in Physics, to be published (1985).

Bus 83 W. Busza and A.S. Goldhaber, preprint (1983).

Byc 73 E. Byckling and K. Kajantie, Particle Kinematics, Wiley, New York, 1973.

Cal 79 D.J.E. Callaway, L. Wilets and Y. Yariv, Nucl. Phys. A327, 250, 1979.

Cha 73 G.F. Chapline, M.H. Johnson, E. Teller and M.S. Weiss, Phys. Rev. D8, 4302, 1973.

Chi 78 S.A. Chin, Phys. Lett. 78B, 552, 1978.

Cho 74 A. Chodos, R.L. Jaffe, K. Johnson, C.B. Thorn, and V. Weisskopf, Phys. Rev. D9, 3471, 1974.

Cle 85 J. Cleymans, R.V. Gavai and E. Suhonen, to be published in Phys. Rep.

Col 75 J.C. Collins and M.J. Perry, Phys. Rev. Lett 34, 1353, 1975.

Col 80 M.T. Collins and J.J. Griffin, Nucl. Phys. A348, 63, 1980.

Cse 80 L.P. Csernai, B. Lukacs and J. Zimanyi, Nuovo Cimento Lett. 27, 111, 1980.

Cse 81 L.P. Csernai and H.W. Barz, Z. Phys. A296, 173, 1981.

Cse 82 L.P. Csernai and H. Stöcker, Phys. Rev. C25, 3208, 1982.

Cse 85 L.P. Csernai and J.I. Kapusta, to be published in Phys.Rep.

Cug 80 J. Cugnon, Phys. Rev. C22, 1885, 1980.

Cug 81 J. Cugnon, T. Mizutani, and J. Van der Meulen, Nucl. Phys. A352, 505, 1981.

Cug 82 J. Cugnon, D. Kinet and J. Vandermeulen, Nucl. Phys. A379, 553, 1982

Cug 84 J. Cugnon, D. L'Hote, Phys. Lett. 149B, 35, 1984.

Cus 85 R.Y. Cusson, P.G. Reinhard, H. Stöcker, M.R. Strayer and W. Greiner, MSUCL-497, Phys. Rev. Lett., in print.

Dal 76 R.H. Dalitz, Fundamentals of Quark Models, 17th Scottish Universities Summer School in Physics, St. Andrews (ed. J.M. Barbour and A.T. Davis) 1976.

Dan 79 P. Danielewicz, Nucl. Phys. A314, 465, 1979.

Dan 84a P. Danielewicz and G. Odyniec, Phys. Lett., in print.

Dan 84b P. Danielewicz, Phys. Lett. 146B, 168, 1984.

Dom 81 G. Domokos and J. Goldman, Phys. Rev. D23, 203, 1981.

Dos 85 K.G.R. Doss, H.-Å. Gustafsson, H.H. Gutbrod, B. Kolb, H. Löhner, B. Ludewigt, A.M Poskanzer, T. Renner, H. Riedesel, H.G. Ritter, A. Warwick, and H. Wieman, Phys. Rev. C32, 116 (1985).

Elz 84 T. Elze, Thesis, University of Frankfurt, 1984; and T. Elze, W. Greiner, and J. Rafelski, to be published.

Eng 82 J. Engels, F. Karsch, H. Satz and I. Montvay, Nucl. Phys. B205 [FS5], 545, 1982.

Fee 46 E. Feenberg and H. Primakoff, Phys. Rev. 70, 980, 1946.

Foc 30 V. Fock, Zeit. für Phys. 61, 126, 1930.

Fra 84 Z. Fraenkel, Nucl. Phys. A428, 373c, 1984.

Fre 77 B.A. Freedman and L.D. McLerran, Phys. Rev. D16, 1169, 1977.

Fre 78 B. Freedman and L. McLerran, Phys. Rev. D17, 1109, 1978.

Fri 81 B. Friedman and V.R. Pandharipande, Nucl. Phys. A361, 502, 1981.

Gar 79 S.I.A. Garpman, N.K. Glendenning and Y.J. Karant, Nucl. Phys. A322, 382, 1979

Gel 82 C.K. Gelbke, Nucl. Phys. A387, 79c, 1982.

Gel 85 C.K. Gelbke, N. Trautmann, private communication.

Gla 83 R. Glasow, G. Gaul, B. Ludewigt, R. Santo, H. Ho, W. Kühn, U. Lynen, and W.F. Müller, Phys. Lett. 120B, 71, 1983.

Gol 48 M.L. Goldberger, Phys. Rev. 74, 1269, 1948.

Gos 78 J. Gosset, J. Kapusta, and G. Westfall, Phys. Rev. C18, 844, 1978.

Gra 84 G. Graebner, Ph.D. Thesis, Universität Frankfurt, 1984, unpublished.

Gud 78 K.K. Gudima and V.D. Toneev, Phys. Lett. 73B, 293, 1978

Gud 79 K.K. Gudima, H. Iwe, and V.D. Toneev, J. Phys. G5, 229, 1979

Gus 84a H.A. Gustafsson, H.H. Gutbrod, B. Kolb, H. Löhner, B. Ludewigt, A.M. Poskanzer, T. Renner, H. Riedesel, H.G. Ritter, A. Warwick, F. Weik, H. Wieman, Phys. Rev. Lett. 52, 1590, 1984.

Gus 84b H.A. Gustafsson, H.H. Gutbrod, B. Kolb, H. Löhner, B. Ludewigt, A.M. Poskanzer, T. Renner, H. Riedesel, H.G. Ritter, A. Warwick and H. Wieman, Phys. Lett. 142B, 141, 1984.

Gut 80 H.H. Gutbrod, LBL report 11123 1980.

Gut 84 H.H. Gutbrod, private discussion.

Gyu 77 M. Gyulassy and W. Greiner, Ann. Phys. 109, 485, 1977.

Gyu 82 M. Gyulassy, K.A. Frankel, H. Stöcker, Phys. Lett. 110B, 185, 1982.

Gyu 83 M. Gyulassy, LBL preprint 16292 1983.

Hah 85a D. Hahn and H. Stöcker, MSUCL-535 (1985).

Hah 85b D. Hahn and H. Stöcker, MSUCL-506 (1985).

Hal 81 E.C. Halbert, Phys. Rev. C23, 295, 1981.

Har 27 D. Hartree, Proc. Camb. Phil. Soc. 24, 111, 1927.

Har 85 J.W. Harris, R. Stock, R. Bock, R. Brockman, A. Sandoval, H. Ströbele, G. Odyniec, H.G. Pugh, L.S. Schröder, R.E. Renfordt, D. Schall, D. Bangert, W. Rauch and K.L. Wolf, Phys. Lett. in print

Hei 79 U. Heinz, W. Greiner and W. Scheid, J.Phys. G5, 1383, 1979.

Hei 84 U. Heinz, P.R. Subramanian, and W. Greiner, Zeit. f. Physik A316, 341, 1984

Hof 76 J. Hofmann, H. Stöcker, U. Heinz, W. Scheid and W. Greiner, Phys.Rev. Lett. 36, 88, 1976.

Jac 83 B.V. Jacak, G.D. Westfall, C.K. Gelbke, L.H. Harwood, W.G. Lynch, D.K. Scott, H. Stöcker, M.B. Tsang and T.J.M.Symons, Phys. Rev.

Lett. 51, 1846, 1983; and B.V. Jacak and G.D. Westfall, private communication.

Jak 81 B. Jakobsson, L. Carlen, P. Kristiansson, J. Krumlinde, A. Oskarsson, I. Otterlund, B. Schröder, H.-A. Gustafsson, T. Johansson, H. Ryde, G. Tibell, J.P. Bondorf, G. Fai, A.O.T. Karvinnen, O.-B. Nielsen, M. Buenerd, J. Cole, D. Lebrun, J.M. Loiseaux, P. Martin, R. Ost, P. de Saintignon, C. Guet, E. Monnand, J. Mougey, H. Nifenecker, P. Perrin, J. Pinston, C. Ristori and F. Schussler, Phys. Lett. 102B, 121, 1981.

Jak 82 B. Jakobsson, University of Lund Report LUIP 8208, 1982.

Kaj 81 K. Kajantie and H.I. Mietinnen, Z. Phys. C9, 341, 1981.

Kaj 82 K. Kajantie and H.I. Mietinnen, Z. Phys. C14, 357, 1982.

Kaj 83 K. Kajantie, P. Raitio, and P.V. Ruuskanen, Nucl. Phys. B222, 152 1983.

Kap 79 J.I. Kapusta, Nucl. Phys. B148, 461, 1979.

Kap 81a J.I. Kapusta, Phys. Rev. C24, 245, 1981.

Kap 81b J.I. Kapusta and D. Strottman, Phys. Lett. 103B, 269, 1981.

Kap 84 J.I. Kapusta, Nucl.Phys. A418, 573c, 1984.

Kei 76 B.D. Keister and L.S. Kisslinger, Phys. Lett. 64B, 117, 1976.

Kit 78 Y. Kitazoe, M. Sano, and K. Yamamoto, J. Phys. Soc. Jpn. Suppl. 44, 386, 1978.

Kno 79 J. Knoll and J. Randrup, Nucl. Phys. A324, 445, 1979.

Koc 83 P. Koch, J. Rafelski, and W. Greiner, Phys. Lett. 123B, 151, 1983.

Koe 80 H.S. Koehler, Nucl. Phys. A343, 315, 1980.

Kog 83 J. Kogut, M. Matsuoka, M. Stone, H.W. Wyld, J.H. Shenker, J. Shigemitsu and D.K. Sinclair, Nucl. Phys. B225, 93, 1983.

Koo 75 S. Koonin, PhD Thesis, MIT 1975.

Kru 85a H. Kruse, B.V. Jacak and H. Stöcker, Phys. Rev. Lett. 54, 289 1985.

Kru 85b H. Kruse, B.V. Jacak, J.J. Molitoris, G.D. Westfall and H. Stöcker, Phys. Rev. C31, 1770, 1985.

Kun 81 J. Kunz, R. Babinet, L. Wilets and U. Mosel, Nucl. Phys. A367, 459, 1981.

Lee 74 T.D. Lee and G.C. Wick, Phys. Rev. D9, 2291, 1974

Mad 26 E. Madelung, Z. Phys. 40, 332, 1926.

Mar 77 J.A. Maruhn, Proc. Topical Conf. on Heavy Ion Collisions,

Pikeville, TN 1977 p. 156.

Mar 80 J.A. Maruhn, GSI-Report 5-80.

Mar 85 J.A. Maruhn and W. Greiner, Heavy Ion Science, D.A. Bromley (ed.) (Addison Wesley, 1985).

Mek 78a A. Mekjian, Phys. Rev. C17, 1051, 1978.

Mek 78b A. Mekjian, Nukl.Phys. A312, 491, 1978.

Met 58 N. Metropolis, R. Bivins, M. Storm, A. Turkevitch, J.M. Miller and G. Friedlander, Phys. Rev. 110, 185, 1958.

Mey 80 W.G. Meyer, H.H. Gutbrod, Ch. Lukner, and A. Sandoval, Phys. Rev. C22, 179, 1980.

Mey 81 H.O. Meyer and P. Schwandt, Phys. Lett. 107B, 353, 1981.

Mig 72 A.B. Migdal, JETP 34, 1184

Mis 80 I.M. Mishustin, F. Myhrer, and P.J. Siemens, Phys. Lett. 95B, 361, 1980.

Mol 84a J.J. Molitoris, J.B. Hoffer, H. Kruse, H. Stöcker, Phys. Rev. Lett. 53, 899, 1984.

Mol 84b J.J. Molitoris and H. Stöcker, Fundamental Problems in Heavy Ion Collisions, N. Cindro, R. Caplar, W. Greiner (eds.), World Scientific (1985); MSUCL-504; Phys. Lett. B (1985).

Mol 85a J.J. Molitoris and H. Stöcker, Phys. Rev. C32, 346 (1985).

Mol 85b J.J. Molitoris, H. Stöcker, H.A. Gustafsson, J. Cugnon and D. L'Hote, Phys. Rev. C33, (1985).

Mol 85c J.J. Molitoris, D. Hahn, and H. Stöcker, MSUCL-530, invited lectures at the Erice School on Heavy ion Collisions from the Coulomb Barrier to the Quark Gluon Plasma, A. Faessler (ed.), Prog. Part. Nucl. Phys. (1985);
J.J. Molitoris and H. Stöcker, to be published;
J.J. Molitoris, MSU PhD thesis 1985.

Mon 82 I. Montvay and E. Pietarinen, Phys. Lett. 110B, 148, 1982.

Nag 81 S. Nagamiya, M.-C. Lemaire, E. Moeller, S. Schnetzer, G. Shapiro, H. Steiner and I. Tanihata, Phys. Rev. C24, 971, 1981.

Neg 81 J.W. Negele and K. Yazai, Phys. Rev. Lett. 47, 71, 1981.

Nik 81 N.N. Nikolaev, Sov. J. Part. Nucl. 12, 63, 1981.

Nix 79 J.R. Nix, Prog. Part. Nucl. Phys. 2, 1237, 1979.

Pok 75 S. Pokorski and L. Van Hove, Nucl. Phys. B86, 243, 1975.

QM 79 First Workshop on Ultra-Relativistic Nuclear Collisions, Lawrence

Berkeley Laboratory report LBL 8957 (1979).

QM 80 Proceedings of an International Symposium in Bielefeld, August 1980 Statistical Mechanics of Quarks and Hadrons, edited by H. Satz North-Holland Publishing Company, Amsterdam 1980

QM 82 Proceedings of the Bielefeld Workshop, May 1982 Quark Matter Formation and Heavy Ion Collisions, edited by M. Jacob and H. Satz, World Scientific Publishing Co, Singapore 1982

QM 83 Proceedings of the Third International Conference on Ultra-Relativistic Nucleus-Nucleus Collisions, Brookhaven National Laboratory September 1983, Nucl. Phys. A418, 1984

QM 84 Proceedings of the Fourth International Conference on Ultra-Relativistic Nucleus-Nucleus Collisions, Helsinki, June 1984 edited by J. Maalampi, Springer Verlag, Berlin, in press

Raf 82 J. Rafelski and B. Müller, Phys. Rev. Lett. 48, 1066, 1982.

Ran 79 J. Randrup, Nucl. Phys. A316, 509, 1979.

Rem 84 B. Remaud, F. Sebille, C. Gregoire and F. Scheuter, Nucl. Phys. A428, 101c, 1984.

Ren 84 R. E. Renfordt, D. Schall, R. Bock, R. Brockmann, J.W. Harris, A. Sandoval, R. Stock, H. Ströbele, D. Bangert, W. Rauch, G. Odyniec, H.G. Pugh, L.S. Schroeder, Phys. Rev. Lett. 53, 763, 1984.

Ren 85 T. Rentzsch, to be published.

Ric 79 J.L. Richardson, Phys. Lett. 82B, 272, 1979.

Rit 83 H.G. Ritter, H.A. Gustafsson, H.H. Gutbrod, B. Kolb, H. Löhner, B. Ludewigt, A.M. Poskanzer, T. Renner, H. Riedesel, A. Warwick, F. Weik, H. Weiman, Lawrence Berkeley Laboratory preprint 16110 1983 and Proceedings of the International Conference on High Energy Nuclear Physics, p. 275

Row 70 D. Rowe, Nuclear Collective Motion, Methuen and Co., London, 1970.

Ruc 76 V. Ruck, M. Gyulassy and W. Greiner, Z. Phys. A277, 391, 1976.

San 80 A. Sandoval, R. Stock, H.E. Stelzer, R.E. Renfordt, J.W. Harris, J.P. Brannigian, J.V. Geaga, L.J. Rosenberg, L.S. Schroeder and K.L. Wolf, Phys. Rev. Lett. 45, 874, 1980.

San 83 R. Santo, private communication.

San 85 M. Sano, M. Guylassy, M. Wakai and Y. Kitazoe, Phys.Lett., in print

Sat 81 H. Satz, ed., Statistical Mechanics of Quarks and Hadrons, North-Holland Publ., Amsterdam, 1981.

Sat 82 H. Satz, Bielefeld preprint 1982.

Sch 25 E. Schrödinger, Ann. Phys. (4) 79, 361 and 489 1925.

Sch 68 W. Scheid, R. Ligensa and W. Greiner, Phys. Rev. Lett. 21, 1479 1968.

Sch 74a W. Scheid, H. Müller and W. Greiner, Phys. Rev. Lett. 32, 741, 1974.

Sch 74b W. Scheid, J. Hofmann,, and W. Greiner, Proc. High Energy Heavy Ion Summer Study, Berkeley, 1974.

Sch 80 J.P. Schiffer, Nucl. Phys. A335, 339, 1980.

Sch 81 B. Schürmann, M. Hartmann and H.J. Pirner, Nucl. Phys. 360, 435, 1981.

Sco 82 D.K. Scott, Nucl. Phys. A354, 375c, 1981.

Ser 47 R. Serber, Phys. Rev. 72, 1114, 1947.

Ser 85 B. Serot and J.D. Walecka, Advance in nuclear physics, Plenum 1985

Shu 80 E.V. Shuryak, Phys. Rep. 61, 71, 1980.

Sie 79 P.J. Siemens and J.I. Kapusta, Phys. Rev. Lett. 43, 1486, 1979.

Sie 80 A.J. Sierk and J.R. Nix, Phys. Rev. C22, 1920, 1980.

Sob 75 M.I. Sobel, P.J. Siemens, J.P. Bondorf and H.A. Bethe, Nucl. Phys. A251, 502, 1975.

Sta 71 H.E. Stanley, Introduction to Phase Transitions and Critical Phenomena, Clarendon Press, Oxford 1971.

Sto 80 R. Stock, H.H. Gutbrod, W.G. Meyer, A.M. Poskanzer, A. Sandoval, J. Gosset, J.H. King, Ch. Lukner, Van Sen, Nguyen, G.D. Westfall and K.L. Wolf, Phys. Rev. Lett. 44, 1243, 1980.

Sto 82 R. Stock, R. Bock, R. Brockman, J.W. Harris, A. Sandoval, H. Stroebele, K.E. Wolf, H.G. Pugh, L.S. Schröder, M. Maier R.E. Renfordt, A. Dacal and M.E. Ortiz, Phys. Rev. Lett. 49, 1236, 1982.

Sto 83 R. Stock, R. Bock, R. Brockmann, A. Dacal, J.W. Harris, M. Maier, M.E. Ortiz, H.G. Pugh, R.E. Renfordt, A. Sandoval, L.S. Schröder, H. Stöbele and K.L. Wolf, Physica Scripta T5, 130, 1983

Stö 77a H. Stöcker, W. Scheid and W. Greiner, Proc. of the Topical Conf. on Heavy Ion Collisions, Fall Creek Falls State Park, Oak Ridge, TN 1977.

Stö 77b H. Stöcker, J. Hofmann, W. Scheid, and W. Greiner, Conf. on Nuclear Collisions, Bled, Yugoslavia, Fizika 9, Supp. 4, 1977a, p. 671.

Stö 78 H. Stöcker, W. Greiner and W. Scheid, Z. Phys. A286, 121, 1978

Stö 79a H. Stöcker, J. Maruhn and W. Greiner, Z. Phys. A290, 297, 1979.

Stö 79b H. Stöcker, J.A. Maruhn and W. Greiner, Phys. Lett. 81B, 303, 1979.

Stö 80a H. Stöcker, R.Y. Cusson, J. Maruhn and W. Greiner, Z. Phys. A294, 125, 1980.

Stö 80b H. Stöcker, J.A. Maruhn and W. Greiner, Phys. Rev. Lett. 44, 725, 1980.

Stö 80c H. Stöcker, G.F. Graebner, J.A. Maruhn and W. Greiner, Phys. Lett. 95B, 1982, 1980.

Stö 81a H. Stöcker, M. Gyulassy and J. Boguta, Phys. Lett. 103B, 269, 1981.

Stö 81b H. Stöcker, C. Riedel, Y. Yariv, L.P. Csernai, G. Buchwald, G. Graebner, J.A. Maruhn, W. Greiner, K. Frankel, M. Guylassy, B. Schürmann, G. Westfall, J.D. Stevenson, J.R. Nix and D. Strottmann, Phys. Rev. Lett. 47, 1844, 1981.

Stö 81c H. Stöcker, A.A. Ogloblin and W. Greiner, Z. Phys. A303, 253, 1981.

Stö 81d H. Stöcker, R.Y. Cusson, J.A. Maruhn and W. Greiner, Phys. Lett. 101B, 379 (1981).

Stö 82a H. Stöcker, L.P. Csernai, G. Graebner, G. Buchwald, H. Kruse, R.Y. Cusson, J.A. Maruhn, W. Greiner, Phys. Rev. C25, 1873, 1982.

Stö 82b H. Stöcker, G. Buchwald, G. Graebner, J. Theis, J.A. Maruhn and W. Greiner, Nucl. Phys. A387, 205 (1982), and Nucl. Phys A400, 63, 1983.

Stö 83 H. Stöcker, G. Buchwald, G. Gräbner, P. Subramanian, J.A. Maruhn, W. Greiner, B.V. Jacak and G.D. Westfall, Nucl.Phys. A400, 63,1983.

Stö 84a H. Stöcker, J. Physics G5, L111, 1984.

Stö 84b H. Stöcker, Nuclear Physics A418, 587c, 1984

Stö 85 H. Stöcker and W. Greiner, Scientific American, January 1985.

Str 83 H. Stroebele, R. Brockmann, J.W. Harris, F. Riess, A. Sandoval, R. Stock, K.L. Wolf, H.G. Pugh, L.S. Schröder, R.E. Renfordt, K. Tittel and M. Maier, Phys. Rev. C27, 1349, 1983.

Sub 81 P.R. Subramanian, L.P. Csernai, H. Stöcker, J.A. Maruhn, W. Greiner and H. Kruse, J. Phys. G7, 241, 1981.

Sub 85 P.R. Subramanian, W. Greiner, D. Hahn, H. Stöcker and U. Heinz, to be published

Tan 80 H.H.K. Tang and C.Y. Wong, Phys. Rev. C21, 1846, 1980.

Tan 82 H.H.K. Tang and C.Y. Wong, Phys. Rev. C26, 284, 1982.

The 83 J. Theis, G.F. Graebner, G. Buchwald, J.A. Maruhn, W. Greiner, H. Stöcker and J. Polonyi, Phys. Rev. D28, 2286, 1983.

Ueh 33 E.A. Uehling and G.E. Uhlenbeck, Phys. Rev. 43, 552, 1933.

Uhl 84 M. Uhlig, Ph.D thesis, Universität Frankfurt 1984

Vas 80a D. Vasak, H. Stöcker, B. Müller and W. Greiner, Phys. Lett. 93B 243, 1980.

Vas 80b D. Vasak, B. Müller and W. Greiner, Physica Scripta 22, 25, 1980.

Vas 84 D. Vasak, W. Greiner, B. Müller, Th. Stahl and M. Uhlig, Nucl.Phys. A428, 291c, 1984.

Vau 72 D. Vautherin and D.M. Brink, Phys. Rev. C5, 626, 1972.

Wal 74 J.D. Walecka, Ann. Phys. 83 491, 1974.

Wal 75 J.D. Walecka, Phys. Lett. 59B (1975) 109;

Wei 76 W. Weise and G.E. Brown, Phys. Rep. 27C, 1, 1976

Wes 76 G.D. Westfall, J. Gosset, P.J. Johansen, A.M. Poskanzer, W.G. Meyer, H.H. Gutbrod, A. Sandoval and R. Stock, Phys. Rev. Lett. 37, 1202, 1976.

Wes 81 G.D. Westfall, B.V. Jacak, N. Anantaraman, M.W. Curtin, G.M. Crawley, C.K. Gelbke, B. Hasselquist, W.G. Lynch, D.K. Scott, B.M. Tsang, M.J. Murphy, T.J.M. Symons, R. Legrain and T.J. Majors, Phys. Lett. 116B, 118, 1981.

Wil 77 L. Wilets, E.M. Henley, M. Kraft and A.D. Mackellar, Nucl. Phys. A282, 341, 1977.

Wil 78 L. Wilets, Y. Yariv and R. Chestnut, Nucl. Phys. A301, 359, 1978;

Won 77 C.Y. Wong, J.A. Maruhn and T. Welton, Phys. Lett. 66B, 1, 1977.

Yar 79 Y. Yariv and Z. Fraenkel, Phys. Rev. C20, 2227, 1979.

Yar 81 Y. Yariv and Z. Fraenkel, Phys. Rev. C24, 488, 1981.

Figure Captions

Fig. I.1 Phase diagram of nuclear matter shows the fundamentally different states that have been conjectured. Experimentally, only the point $(\rho_0,0)$ is known [Stö85].

Fig. I.2 Energy per baryon of cold nuclear matter as calculated in thermodynamically consistent relativistic mean field theory [Bog83] with different parameter sets compatible with known ground state properties of nuclei.

Fig. I.3 Pion multiplicities versus the temperature for baryon densities two times (solid line) and four times (dashed line) normal nuclear matter density. The curves describe the properties of a hot and dense piece of nuclear matter [Hah85].

Fig. I.4 Various contributions to the pion yields for a C + C reaction. Dotted line: delta resonance; Dashed line: free pion gas; solid line: Bose condensed pions; dashed-dotted: heavy resonances [Hah 85].

Fig. I.5 The freeze out temperature of the pions calculated from the pion multiplicity data per nucleon. For $E_{lab}<400$ MeV/nucleon, a freeze-out occurs for $\rho_0 < \rho < 3\rho_0$, for higher energies between two and five ρ_0.[Hah85]

Fig. I.6 The liquid gas phase transition in nuclear matter in the pressure density plane [Stö83].

Fig. I.7 Possible abnormal states with bends or secondary minima in $E_c(\rho)$ caused by the delta resonance coupling, as predicted by the relativistic mean field theory [Bog82], which is in agreement with known nuclear properties at ground state density.

Fig. I.8 Normalized energy density versus inverse strong coupling constant as obtained with lattice QCD calculations using Monte Carlo methods [Eng82]. The crosses are the pure Yang Mills theory, the open circles include effects of dynamical fermions. A rapid change to a deconfined state is predicted at a temperature of about 200 MeV for zero chemical potential.

Fig. I.9 Energy per baryon of cold quark matter (solid lines) as compared to nuclear matter (short dashed). The contributions of volume bag energy (dashed-dotted) and kinetic Fermi energy (long-dashed) are shown for various strong coupling constants α_c [Stö77b,80c].

Fig. I.10 Phase coexistence region of the Quark Gluon Plasma and the Hadron Plasma in a simple two phase model [Mol84b,Sub85] is shown in the energy density-chemical potential plane. The dynamical path as obtained in the fluid model is sketched by the line with arrowheads.

Fig. II.1 Nb(400 MeV/nucleon) + Nb as a function of time in the Newtonian Force Model: strong collective flow is caused by the short range repulsive nuclear force [Mol85a].

Fig. II.2 Contour plots of the baryon density in the scattering plane for a TDHF-calculation of Kr + Kr at b=0 fm and 100 MeV/nucleon incident energy (left) and the corresponding system at E_{LAB}=400 MeV/nucleon as calculated in the fluid dynamical model [Stö80a].

Fig. II.3 The Skyrme equations of state with K=200 MeV and K=380 MeV as used in the VUU theory [Kru85] are compared with values extracted from pion yields [Sto82].

Fig. II.4 The stability of nuclei in the VUU approach versus a corresponding instability in the Cugnon cascade for Nb (0 MeV/nucleon) + Nb [Mol85].

Fig. II.5 Fraction of Pauli-blocked collisions in the VUU theory versus energy for the Nb + Nb system at b=3 fm [Mol85].

Fig. II.6 The evolution in momentum space in the VUU theory of Ar (137 MeV/nucleon) + Ca at b=0 fm. The results from several parallel ensembles are superposed in order to represent the distribution function. The collision term results in substantial equilibration [Kru85b].

Fig. II.7 Time evolution in configuration and momentum space for C (85 MeV/nucleon) + C at b=1 fm for TDHF, the Vlasov equation,and the Vlasov-Uehling-Uhlenbeck theory. Transparency occurs in both cases with a mean field only [Aic85].

Fig. II.8 Single particle inclusive proton spectra experimentally and theoretically (histograms) in the VUU theory for the Ar + Ca system [Kru85b].

Fig. II.9 Initial and final states in configuration and momentum space in the VUU theory for C (85 MeV/nucleon) + C at b=1 fm [Aic85].

Fig. II.10 The number of uncollided projectile nucleons in the VUU model emitted for C (85 MeV/nucleon) induced reactions is used to extract a mean free path [Aic85].

Fig. II.11 The time evolution of the single particle distribution function as obtained in the VUU-theory for Ar (770 MeV/nucleon) + Pb is shown after projection into configuration space at b=1, 3, and 5 fm [Mol85].

Fig. II.12 The time development of the same system after projection in momentum space [Mol85]. The rapid (t=10 fm/c) equilibration is obvious for near central collisions.

Fig. II.13 Collision of Ar (770 MeV/nucleon) + Pb at b=0 fm in the Nuclear Fluid Dynamic model. Note the remarkable similarity to the VUU theory [Gra84].

Fig. II.14 The same system at b=4 fm in the Nuclear Fluid Dynamic model [Gra84].

Fig. II.15 The dependence of the velocity of the shock front and the matter flow velocity on the density. Dashed lines: influence of hadronic

resonances; short dashes: influence of a density isomer at $\rho \approx 3\rho_0$ [Hof76,Stö77].

Fig. III.1 Path of the dynamics of nuclear collisions in the ρ-T phase diagram showing the compression Hugoniot adiabat and isentropic expansion stage. The influence of the compressional energy is depicted by the solid line (linear e.o.s.) and thd dashed line (quadratic E.O.S.) - clearly the compression achievable depends quite strongly on the repulsive short range interactions [Stö84a].

Fig. III.2 Shows the time dependence of the entropy production as obtained with the three dimensional viscous fluid dynamical approach [Buc85] for the reaction Nb (400 MeV/nucleon) + Nb at b=3 fm

(a) compares the maximum density with the entropy: entropy is produced during the high density stage of the reaction. The entropy stays constant during the expansion, therefore the entropy can be used as a messenger from the high density stage.

(b) inclusion of viscous effects modifies the entropy: shear viscosity only (dashed line) raises the total entropy, bulk viscosity (dotted line) destroys the saturation of S/A(t) observed in the other cases.

Fig. III.3 Dependence of the entropy per baryon on the bombarding energy S_s (dashed line): result of a one dimensional shock calculation; S_η (solid line): entropy production with viscous effects included; "data": estimate of the entropy production obtained from the simple relation (Eq. III.16) given by Siemens and Kapusta [Sie79], and prediction of fluid dynamics with attached quantum statistical model of fragment production [Stö84a].

Fig. III.4 Bombarding energy dependence of the d/p ratios as obtained from inclusive measurements and various theoretical approaches. The calculations of Bertsch and Cugnon, as well as Siemens and Kapusta grossly overestimate the data [Nag81].

Fig. III.5 Quantum statistical model prediction of the dependence of the d/p ratio on the entropy. The primordial d/p ratio (upper line) is strongly distorted by the decay of particle unstable nuclear and hadronic resonances [Stö83].

Fig. III.6 Multiplicity dependence of the d/p ratio as observed in the Plastic Ball 4π electronic spectrometer system [Gus84b]. This result indicates that inclusive measurements are not suitable for an extraction of the entropy--the thermodynamic lines can only be approached for very high multiplicities, i.e. very massive colliding nuclei.

Fig. III.7 Extraction of the entropy from the high multiplicity Plastic Ball data for heavy systems [Gus84b,Dos85]. A surprisingly low entropy is obtained if the quantum statistical model is applied [Hah85a]. The data are compared to fluid dynamical calculations which use different relativistic mean field theories as input for the equation of state [Stö81a].

Fig. III.8 Bombarding energy dependence of the temperature calculated in the shock model using different equations of state: nucleon Fermi gas (dashed line) and hadron plasma with a Hagedorn mass spectrum [Stö81c]. The

data are extracted from fits to the 90° c.m. slopes of the spectra of protons (and pions) [Nag81].

Fig. III.9 Early predictions on the bombarding energy dependence of the pion multiplicities and their dependence on the nuclear compressional energy [Stö78]. The upper frame shows the influence of the compression constant, using the linear $E_c(\rho)$ ansatz. The middle frame shows the influence of a hypothetical abnormal density isomeric state; threshold increase of pion production is predicted at a critical energy. Lowest frame: influence of the E.O.S. on the temperature achieved in shock compression.

Fig. III.10 The observed pion multiplicities [San80] are compared to fireball calculations (short dashed line) and nonviscous fluid dynamics with late freeze-out (long dashed line). The influence of the viscosity is shown by the lines labeled η [Stö84a].

Fig. III.11 Pion multiplicities per nucleon versus bombarding energy calculated with the shock model with the quadratic EOS and K_q=250 (solid) and 500 (dashed) MeV, respectively [Hah85b].

Fig. III.12 π^--multiplicity versus energy for the system Ar + KCl in the cascade approach [Cug80] and VUU theory [Kru85a] as compared to the experimental data [San80].

Fig. III.13a The total pion multiplicity versus time in the VUU approach for Nb (1050 MeV/nucleon) + Nb at b=3 fm; note the small but significant effect of reabsorption [Mol85].

Fig. III.13b The corresponding figure for the maximum density achievable: pions can serve as signals from the high density stage [Mol85].

Fig. III.14a Total pion multiplicity versus bombarding energy for Nb + Nb at b=3 fm in the VUU theory [Mol85].

Fig. III.14b VUU predictions for pion multiplicities versus energy for Au + Au at b=3 fm. Note the strong influence of isospin [Mol85].

Fig. III.15 Inclusive ^{3}He (left) and triton (right) cross sections from the reaction Ar 137 MeV/n + Au as obtained from nuclear fluid dynamics with the attached quantum statistical model [Buc85] compare well with the data of Jacak et al [Jac83].

Fig. III.16 Inclusive, but high multiplicity selected proton cross sections from Ne (400 MeV/nucleon) + U exhibit broad sidewards maxima [Sto81] (data: middle left frame). Cascade calculations of Stevenson (lower left) and Yariv and Frankel (upper left) result in strongly forward peaked angular distributions, in agreement with thermal model calculations of Westfall and Schürmann (upper right), but in sharp contrast to the data. Fluid dynamics predicts sharp sidewards maxima [Stö80a,Nix82] if the thermal breakup is not included (lower right frame); the incorporation of thermal evaporation yields qualitative agreement of the nonrelativistic fluid model with the data [Stö81].

Fig. III.17 High multiplicity selected p, d, and t angular distributions as measured by the GSI-LBL collaboration [Sto81] are compared to the relativistic fluid dynamical calculations of the Frankfurt school, which include the quantum statistical calculation of fragment formation plus thermal evaporation of the various ejectiles [Gra85]. The relativistic treatment and the fragment formation prove essential for a quantitative reproduction of the data as compared to the previous qualitative agreement obtained with the earlier nonrelativistic calculation [Stö81].

Fig. III.18 The triple differential cross section of emitted nucleons is shown for the reaction Ne (400 MeV/nucleon) + U in the scattering plane as obtained in the fluid dynamical model as a function of impact parameter [Stö82]. A pronounced off-beam axis peak has been predicted as the result of the collective bounce-off effect [Stö80], which has been recently confirmed experimentally [Rit84,Gus84].

Fig. III.19 Pictorial representation of the in-plane bounce-off and the out-of-plane squeeze-out of participant matter predicted by fluid dynamics [Stö82,Buc85].

Fig. III.20 Invariant 90° out-of-plane spectra of protons calculated in the fluid dynamical model [Buc84] with two different equations of state: The soft E.O.S. grossly underpredicts the data, while the stiff E.O.S. agrees well with the recent data of the GSI-LBL Plastic-Ball collaboration [Rit84,Gut84].

Fig. III.21 The change of the 90° transverse momentum distribution $d\sigma/dp$ with time for the reaction Nb (400 MeV/nucleon) + Nb is shown for various impact parameters [Buc85].

Fig. III.22 The time dependence of the transverse momentum per nucleon projected in the scattering plane versus rapidity is shown for the system Nb (400 MeV/nucleon) + Nb [Buc85].

Fig. III.23 The rapidity dependence of the transverse momenta projected into the scattering plane $\langle p_\perp \rangle$ is shown as a function of impact parameter ((a) b=2,4,6 fm; (b) b=0,1,2,3 fm) for the system Nb (400 MeV/nucleon) + Nb [Buc85]. Observe that $\langle p_\perp \rangle$ (y) is remarkably similar at b=1 fm and b=6 fm. The maximum $\langle p_\perp \rangle$ is observed at b=3 fm. We would like to point out that for exactly central collisions, b=0 fm, $\langle p_\perp \rangle$ is zero everywhere for symmetry reasons. Therefore one must conclude that the novel transverse momentum analysis proposed by Danielewicz and Odyniec provides valuable information about the momentum transer only for intermediate impact parameters [Dan85].

Fig. III.24 Density contour plots as obtained with the nonrelativistic nuclear fluid dynamical model [Stö80] for the reaction Ne (400 MeV/nucleon) + U at b=0 fm as a function of time. Observe the directed sidewards flow as a result of the shock wave formation (high density of contour lines).

Fig. III.25 Final state of the reaction Ne (400 MeV/nucleon) + U at b=6 fm shown as contour plot in the scattering plane. The recently observed [Rit84,Gus84] strong bounce-off effect predicted by nuclear fluid dynamics (left, [Stö80]) is not reproduced by the microscopic cascade model of Gudima

and Toneev (right, [Ton83]), which neglects the repulsive nuclear interactions at high density, i.e. the nuclear compression energy.

Fig. III.26 Time dependence of baryon density contours [Buc84b,Buc85] for the reaction U (100 MeV/nucleon) + U as calculated by the fluid dynamical model shows clearly the formation of an ellipsoidal compression zone and sideward squeeze-out of matter predicted in earlier schematic approaches of the Frankfurt school [Sch74a,b].

Fig. III.27 Division of the total energy into various channels as a function of time in the reaction Nb (400 MeV/nucleon) + Nb. The fluid dynamical model predicts that with the soft equation of state, the transformation of the incident kinetic energy proceeds predominantly into random thermal motion E_{th}. Observe that substantial collective macroscopic motion is present at all times; total collective stopping of all regions of the projectile and target at the same instant of time does not occur. This is due to the beginning of the collective sidewards expansion, which yields transformation of random microscopic motion into collective flow, before all parts of the initial nuclei have participated in the reaction [Buc85].

Fig. III.28 The fluid dynamical predictions for the impact parameter dependence of the baryon density contours as a function of time for the system Ar (400 MeV/nucleon) + Ca [Stö80]. Observe the transition from the bounce-off dominated intermediate impact parameters to the 90° squeeze-out at b=0 fm.

Fig. III.29 Time dependence of the aspect ratio R_{13} and the flow angle θ_F as obtained from the fluid dynamical calculation for the reaction Nb (400 MeV/nucleon) + Nb at b=0 fm. We would like to point out that both R_{13} and θ saturate at the point of highest density and are conserved during the expansion. Therefore, both R_{13} and θ can serve as messengers for the high density stage of the reaction [Buc84,Buc85].

Fig. III.30 The change of the flow angle with impact parameter (upper row: b=3 fm, lower row: b=6 fm) becomes obvious in these density contour plots for the system Nb (400 MeV/nucleon) + Nb obtained with the fluid dynamical model [Buc84].

Fig. III.31 Kinetic energy flow analysis for U(400 MeV/nucleon) + U is shown in the R_{13}-θ plane for the cascade model calculation (the shaded area) and the fluid dynamical calculation (solid line). The numbers indicate the impact parameter in fm's [Buc83].

Fig. III.32 The impact parameter dependence of R_{13}, θ_{flow}, sphericity, and coplanarity is shown as calculated for the reaction ^{40}Ca(400 MeV/nucleon) + ^{40}Ca in the fluid dynamical model [Stö82].

Fig. III.33 The bombarding energy dependence of (a) the ratio of compression-to-thermal pressure for various compression constants [Stö81] and (b) the aspect ratio R_{13} is shown for central collisions of uranium on uranium. The dashed area in (b) indicates the results of the cascade calculation; the solid lines in (b) represent the results of the fluid dynamical model for different equations of state [Buc83].

Fig. III.34 Distributions of flow angles $dN/cos\theta_F$ for the reaction ^{93}Nb(400A MeV) + ^{93}Nb. (a) Result for the hydrodynamical calculation [Buc84a]. The finite-multiplicity distortions are taken into account. The given impact-parameter ranges correspond to the multiplicity cuts indicated at the experimental curves below [(b)]. (b) Plastic Ball data [Rit84,Gus84] for various multiplicity cuts given at the curves. (c) Result of the cascade simulation after multiplicity selection [Gus84].

Fig. III.35 The impact parameter dependence of the velocity of the participant center-of-mass system as calculated in the relativistic fluid dynamical model for the reaction Ar (0.8 GeV/nucleon) + Pb [Gra84].

Fig. III.36 Dependence of the aspect ratio R_{13} vs. the transverse energy E_t on the various weights $w(v)$ used in the flow analysis.

Fig. III.37 Comparison of R_{13} vs. E_t (see previous figure) as obtained from fluid dynamics with and without finite multiplicity distortions [Gra84] for the reaction Ar (0.8 GeV/nucleon) + Pb with the data [Str83].

Fig. III.38 Flow angle vs. transverse energy as obtained from the relativistic fluid dynamical model [Gra84] with and without finite multiplicity distortions as compared to the data and cascade calculations [Str83] for the reaction Ar (0.8 GeV/nucleon) + Pb.

Fig. III.39 Comparison of the flow angular distribution obtained experimentally for the reaction Ar(0.8 GeV/nucleon) + Pb and the cascade predictions [Ren84] to the predictions of the relativistic one fluid model [Gra84].

Fig. III.40 Average cm momentum calculated with the relativistic one fluid model for the reaction Ar (0.8 GeV/nucleon) + Pb [Gra84] as a function of impact parameter b given in the figure (corresponding to the squares from left to right).

Fig. III.41 Influence of a rather slight shift of β_{cm} on the resulting flow angles. The relativistic fluid dynamical calculations [Gra84] are compared to the experimental data [Str83]. This ambiguity for asymmetric systems is best avoided by analysis in a prescribed Lorentz frame, say the nucleon-nucleon center of mass [Mol85].

Fig. III.42 Kinetic energy flow angle distributions for Nb (400 MeV/nucleon) + Nb in the Newtonian Force Model compared to the experimental data [Mol84a].

Fig. III.43 The bound and unbound Cugnon cascade compared to the experimental data for Nb (400 MeV/nucleon) + Nb in various multiplicity bins [Mol85].

Fig. III.44 The average flow angle for Nb (1050 MeV/nucleon) + Nb at b=3 fm versus time in the VUU approach [Mol85].

Fig. III.45 The corresponding time dependence of the compression for Nb (1050 MeV/nucleon) + Nb at b=3 fm in a central region of radius 2 fm shows

that the flow angle can yield information about the high density stage [Mol85].

Fig. III.46 Maximum density in the center-of-mass frame for Au + Au collisions at b=3 fm in the VUU approach [Mol85].

Fig. III.47 Effect of the compressibility on the flow angle distribution for Nb (400 MeV/nucleon) + Nb at b=1 fm in the VUU approach [Kru85a]: the flow angle indicates a stiff nuclear equation of state.

Fig. III.48 Peak flow angle versus bombarding energy from a VUU calculation for Nb + Nb at b=3 fm [Mol85].

Fig. III.49 Peak flow angle in the VUU model for E=400 MeV/nucleon at b=3 fm strongly depends on atomic number due to the increased number of collisions [Mol85].

Fig. III.50 Peak flow angle versus energy for Au + Au at b=3 fm from the VUU approach [Mol85].

Fig. III.51 Flow angle distributions for Ar (770 MeV/nucleon) + Pb for (a) the experimental data with high and low multiplicity cuts using the momentum flow tensor; [Ren84] (b) corresponding predictions of the VUU theory; and (c) a standard kinetic energy flow analysis done in the nucleon-nucleon center of momentum frame using only the projectile momentum hemisphere [Mol85].

Fig. III.52 VUU predictions for two different methods of detecting collective flow are shown for Ar + Pb: (a) the standard kinetic energy flow analysis in the NN center of momentum frame is done on the forward hemisphere for b=1, 3, and 5 fm and (b) the transverse momentum analysis is shown at the same impact parameters [Mol85].

Fig. III.53 Transverse momentum spectra for Nb + Nb at b=3 fm versus energy in the VUU theory [Mol85].

Fig. III.54 Transverse momentum at projectile rapidity for Au + Au at b=3 fm versus energy in the VUU theory [Mol85].

Fig. III.55 Transverse momentum spectra for Ar (1800 MeV/nucleon) + KCl for the experimental data (a), intranuclear cascade (b), and the VUU approach with hard (c) and soft (d) equations of state. The data again indicate a stiff nuclear equation of state [Mol85].

Fig. III.56 Momentum space density contours for the reaction ^{16}O (600 MeV/nucleon) + ^{16}O as obtained as a function of time from the solution of the time dependent Dirac equation (TDDE). The buildup of transverse momentum transfer is observed at t>7 fm/c [Cus85].

Fig. III.57 Projection of the in-plane transverse momentum per nucleon, k_y, versus the longitudinal momentum, k_z, as obtained from the TDDE-approach [Cus85]. The results agree qualitatively with the data obtained by the GSI-LBL streamer chamber collaboration at higher energies and with more massive nuclei [Dan85].

Fig. IV.1 The energy density obtained from the simplified 1-D hydrodynamical model is shown vs. the bombarding energy. Three different equations of state are used: Hagedorn gas, K=100 MeV (upper curve), nucleon Fermi gas, K=300 MeV (lower curve), and deconfined plasma of quarks and gluons (dash-dotted) [Stö84].

Fig. IV.2 Dynamical path of nuclear collisions in the ρ-T diagram as obtained in the hydrodynamical model. Arrows indicate compression (towards right) and subsequent expansion (to left) at E_{LAB}=1,2,4 and 8 GeV/N for hadron matter. Critical energy density contours (e=1 and 1.5 Gev fm^{-3}) of the plasma phase are also shown, indicating that the latent heat necessary for deconfinement may be achievable in the high baryon density region at laboratory bombarding energies in the 10 GeV/nucleon range [Stö84].

Fig. IV.3 The excitation energy per baryon needed to form the deconfined phase is plotted versus the baryon density ρ/ρ_o for Λ_{VAC}=190 MeV fm^{-3} and Λ_{MOM}=100 MeV and T=0, 100, 150 MeV. The dotted line gives the $O(\alpha^2 \ell n \alpha)$ result for T=0. The dashed line indicates normal nuclear matter. The lines labelled R and L represent the result of a combustion [Stö84] and fireball calculation of quark matter formation, respectively. The incident energy for these is given on the top of the figure [Stö84].

Fig. IV.4 The number of baryons in the region of high energy densities exceeding 1 (dotted line), 2 (solid line) and 3 GeV fm^{-3} (dashed line) as calculated for the system Ne + Pb with the relativistic fluid dynamical model is shown for various bombarding energies for a soft (right) and a stiff (left) nucelear equation of state [Gra84].

Fig. IV.5 The impact parameter dependence of the number of baryons in the high energy density region (e>2 GeV fm^{-3}) for the reaction Ne (15 GeV/nucleon) + Pb as obtained in the relativistic one fluid model [Gra84] with the soft E.O.S.

Fig. IV.6 Same as Fig. IV, but for the system Pb + Pb. Observe the order of magnitude increase in A(e>2 GeV fm^{-3}), even at E_{LAB}=5 GeV/nucleon . Also the duration of the stage of high energy density as well as the absolute magnitude of e^{max} are greatly enhanced whence the massive Pb projectile is used instead of the light Ne nucleus [Gra84].

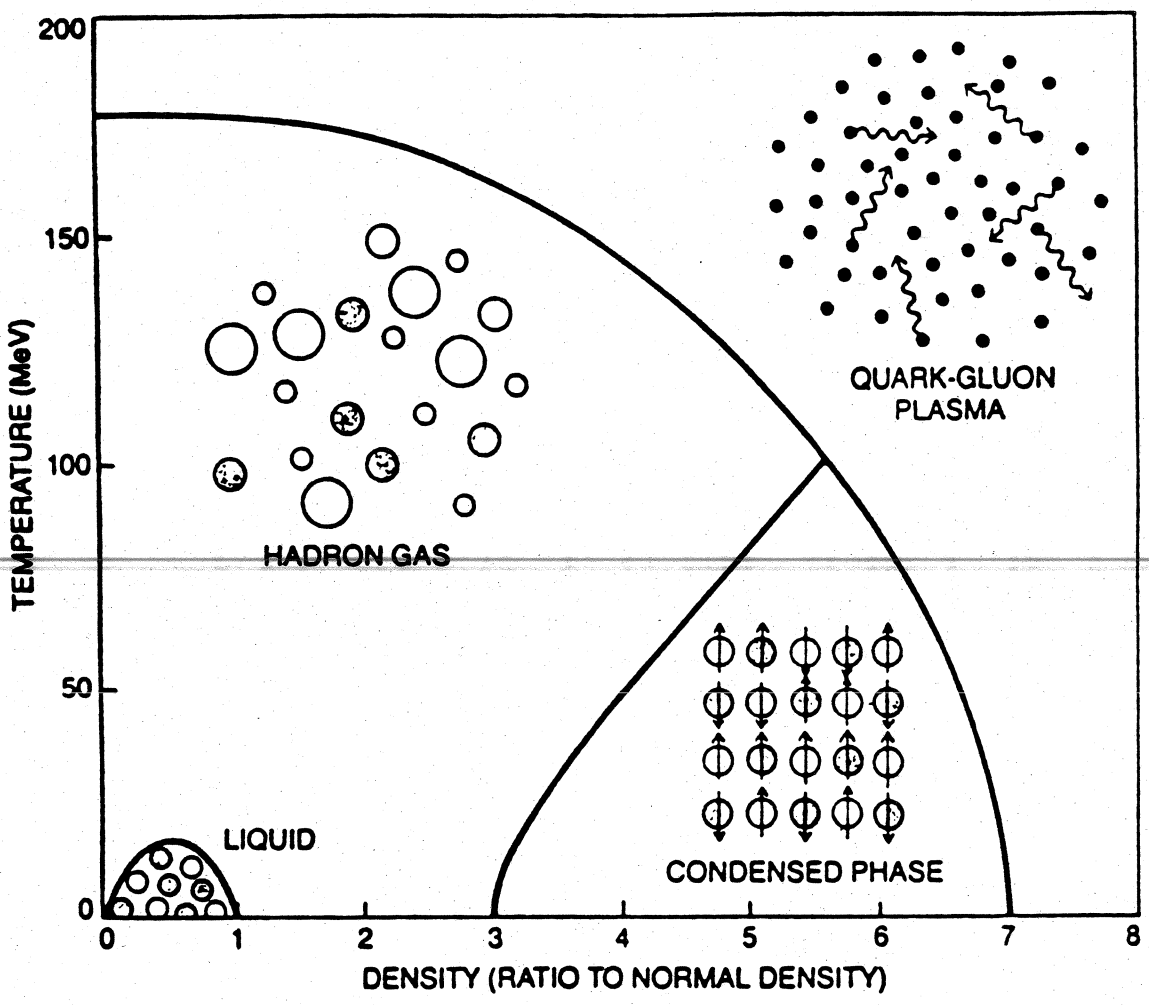
200
150
100
50
0
TEMPERATURE (MeV)
HADRON GAS
QUARK-GLUON
PLASMA
LIQUID
CONDENSED PHASE
0
1
2
3
4
5
6
7
8
DENSITY (RATIO TO NORMAL DENSITY)

FIGURE I.1

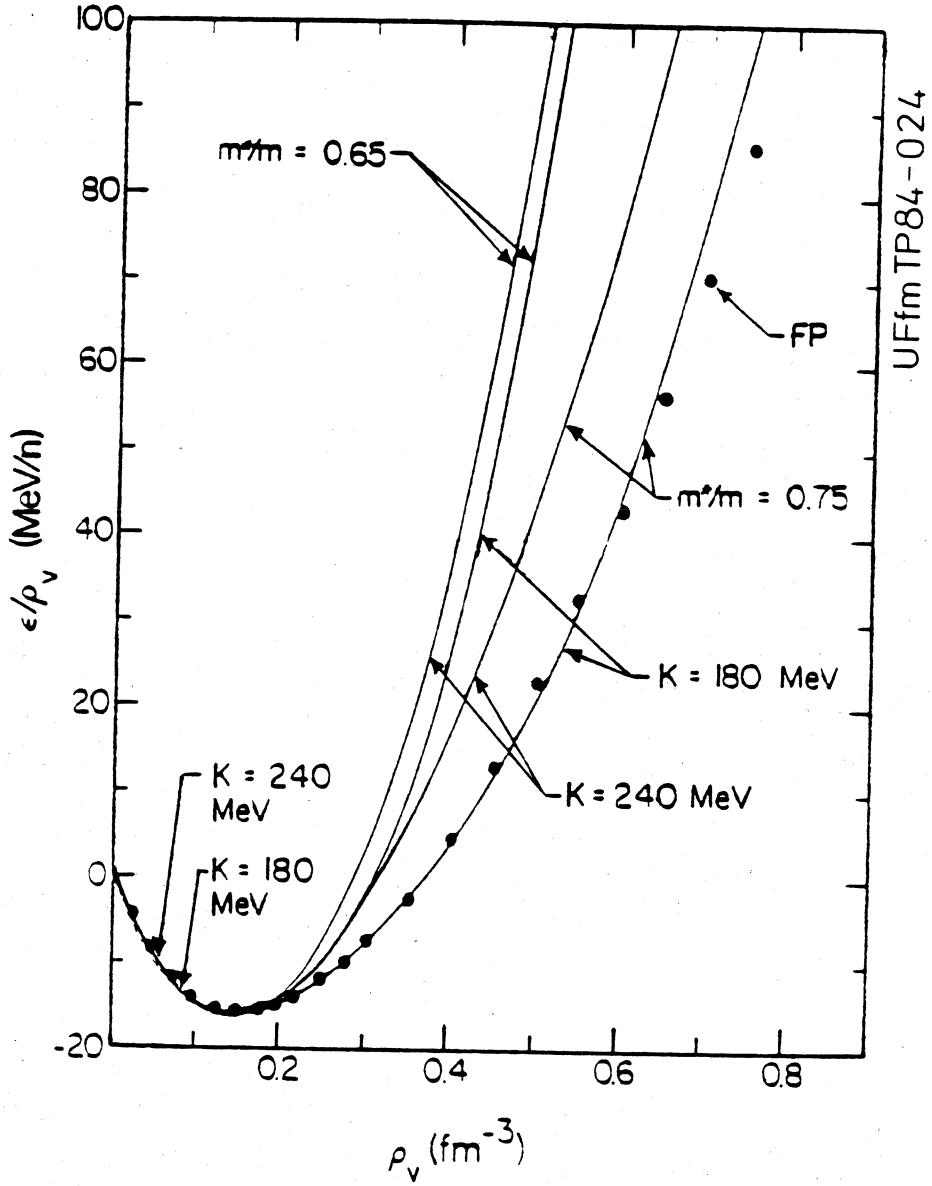
100
80
60
40
20
0
-20
0.2
0.4
0.6
0.8
ϵ/ρ_v (MeV/n)
ρ_v (fm^{-3})
m*/m = 0.65
m*/m = 0.75
FP
K = 180 MeV
K = 240 MeV
K = 240 MeV
K = 180 MeV
UFfmTP84-024

FIGURE I.2

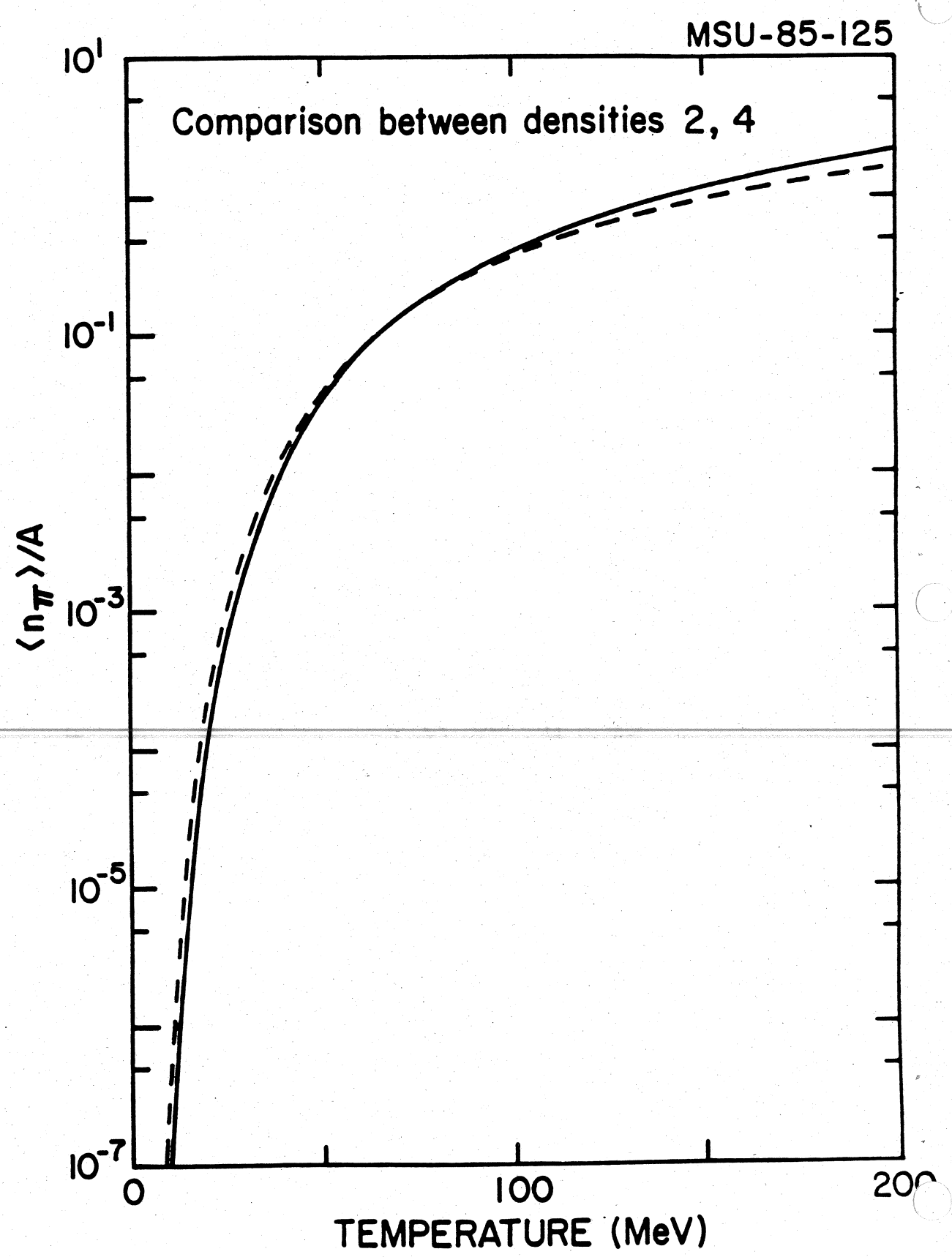
MSU-85-125
Comparison between densities 2, 4
10^{1}
10^{-1}
10^{-3}
10^{-5}
10^{-7}
$\langle n_\pi \rangle / A$
0
100
200
TEMPERATURE (MeV)

FIGURE I.3

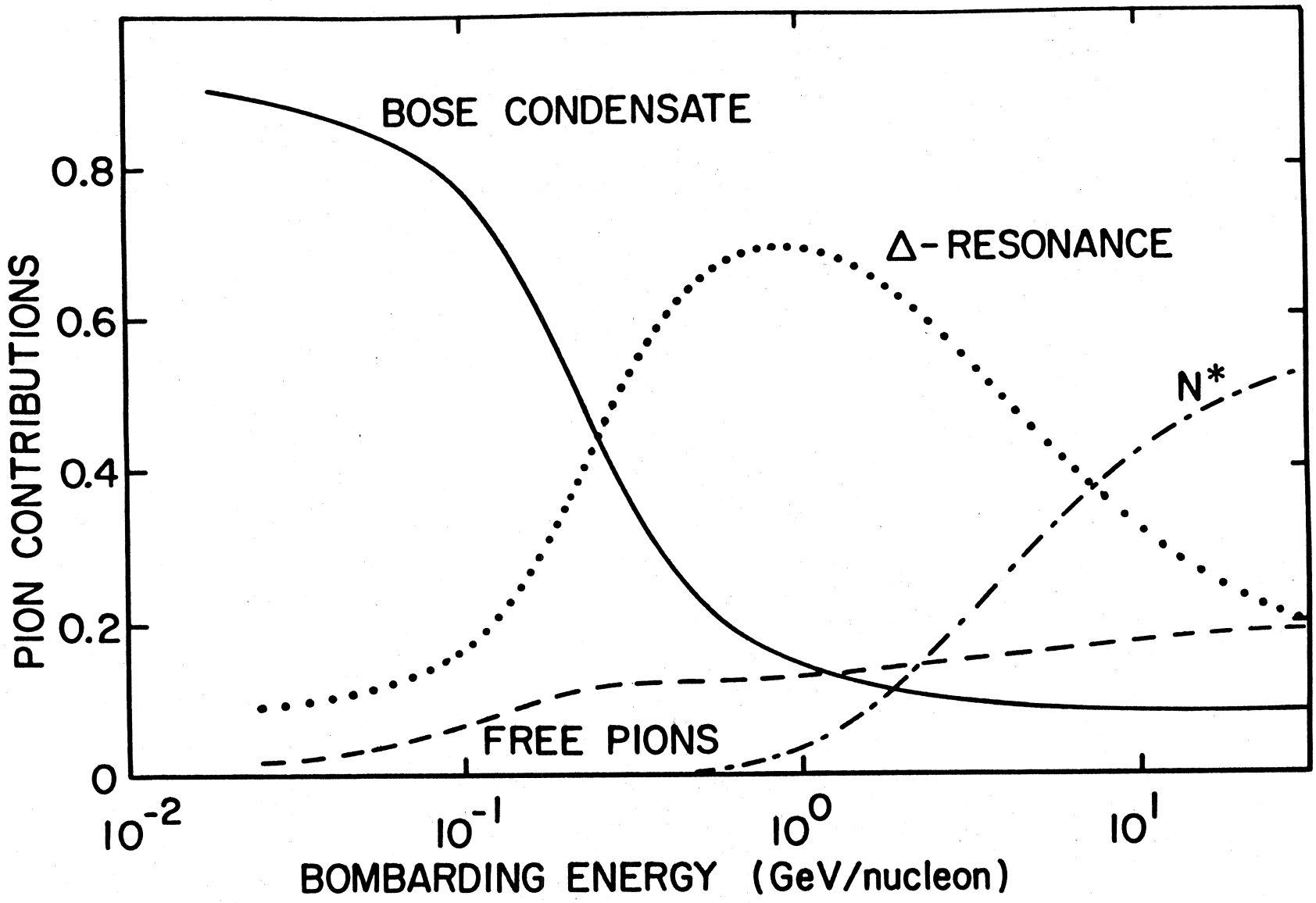
BOSE CONDENSATE
Δ-RESONANCE
N*
FREE PIONS
PION CONTRIBUTIONS
0
0.2
0.4
0.6
0.8
10^{-2}
10^{-1}
10^{0}
10^{1}
BOMBARDING ENERGY (GeV/nucleon)

FIGURE I.4

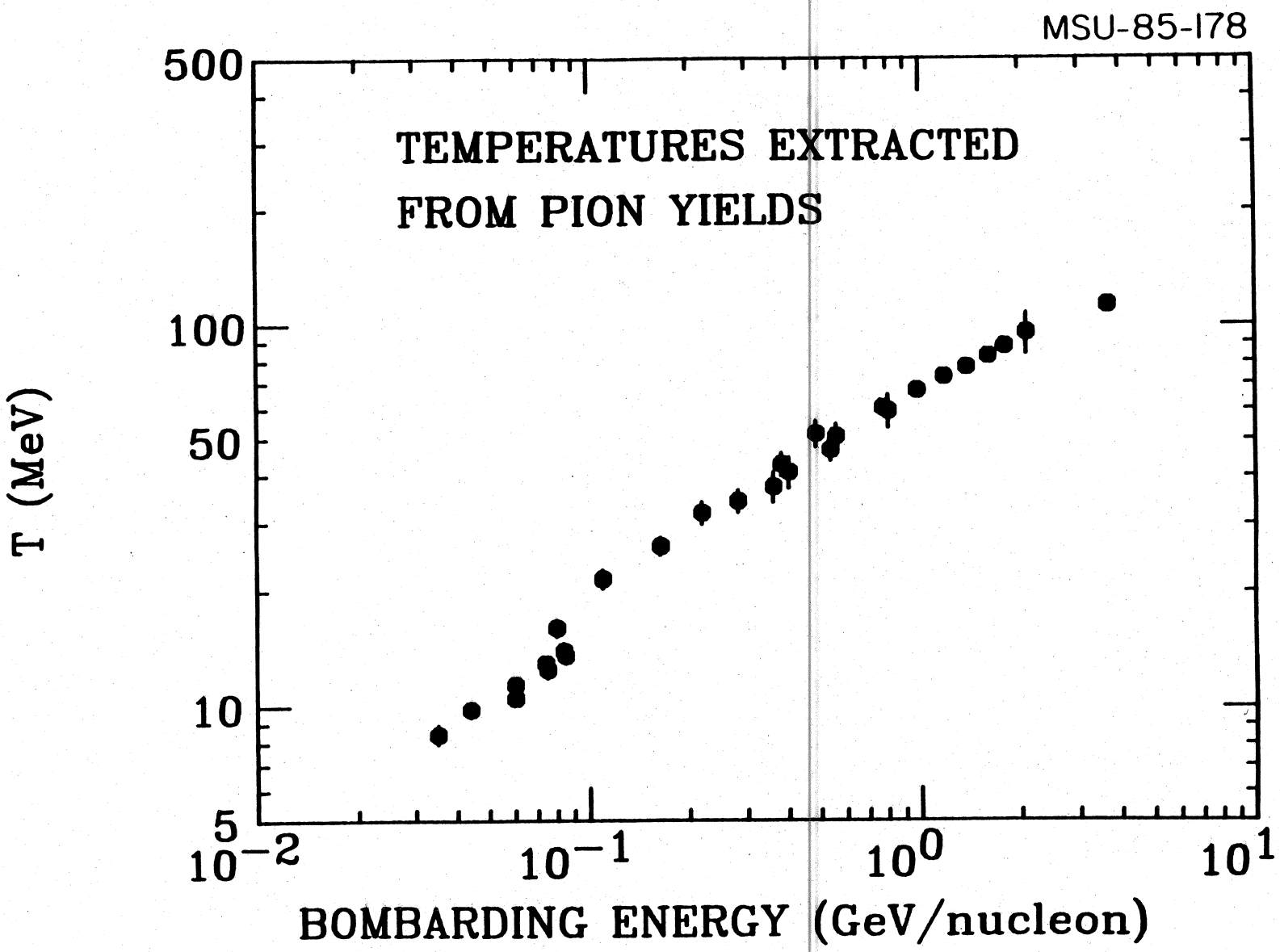
MSU-85-178
TEMPERATURES EXTRACTED
FROM PION YIELDS
T (MeV)
500
100
50
10
5
10^{-2}
10^{-1}
10^{0}
10^{1}
BOMBARDING ENERGY (GeV/nucleon)

FIGURE I.5

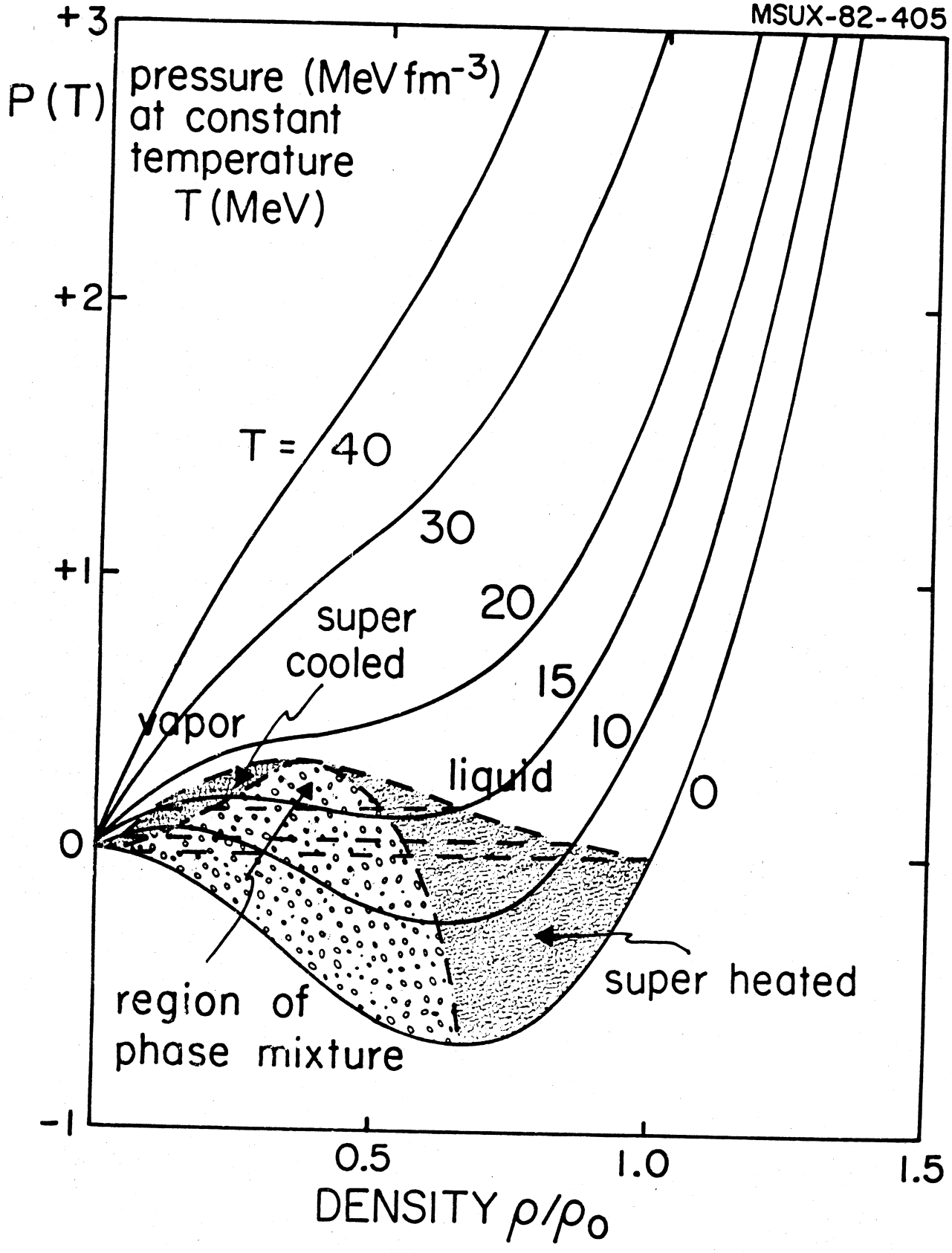
MSUX-82-405
+3
P(T)
pressure (MeV fm^{-3})
at constant
temperature
T (MeV)
+2
T = 40
30
+1
20
super
cooled
15
vapor
10
liquid
0
0
region of
phase mixture
super heated
-1
0.5
1.0
1.5
DENSITY ρ/ρ_0

FIGURE I.6

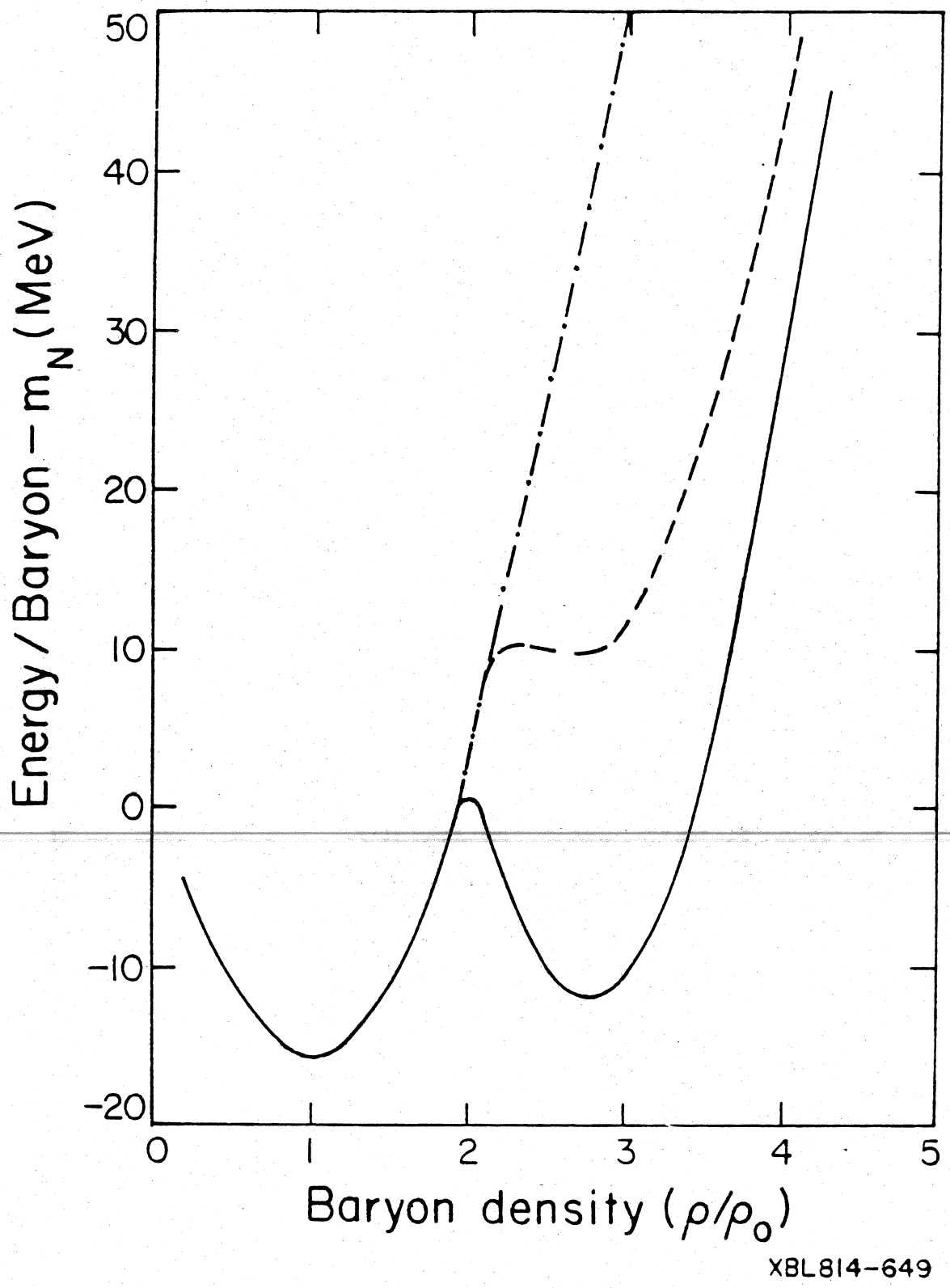
50
40
30
20
10
0
-10
-20
0
1
2
3
4
5
Energy / Baryon − m_N (MeV)
Baryon density (ρ/ρ_0)
XBL814-649

FIGURE I.7

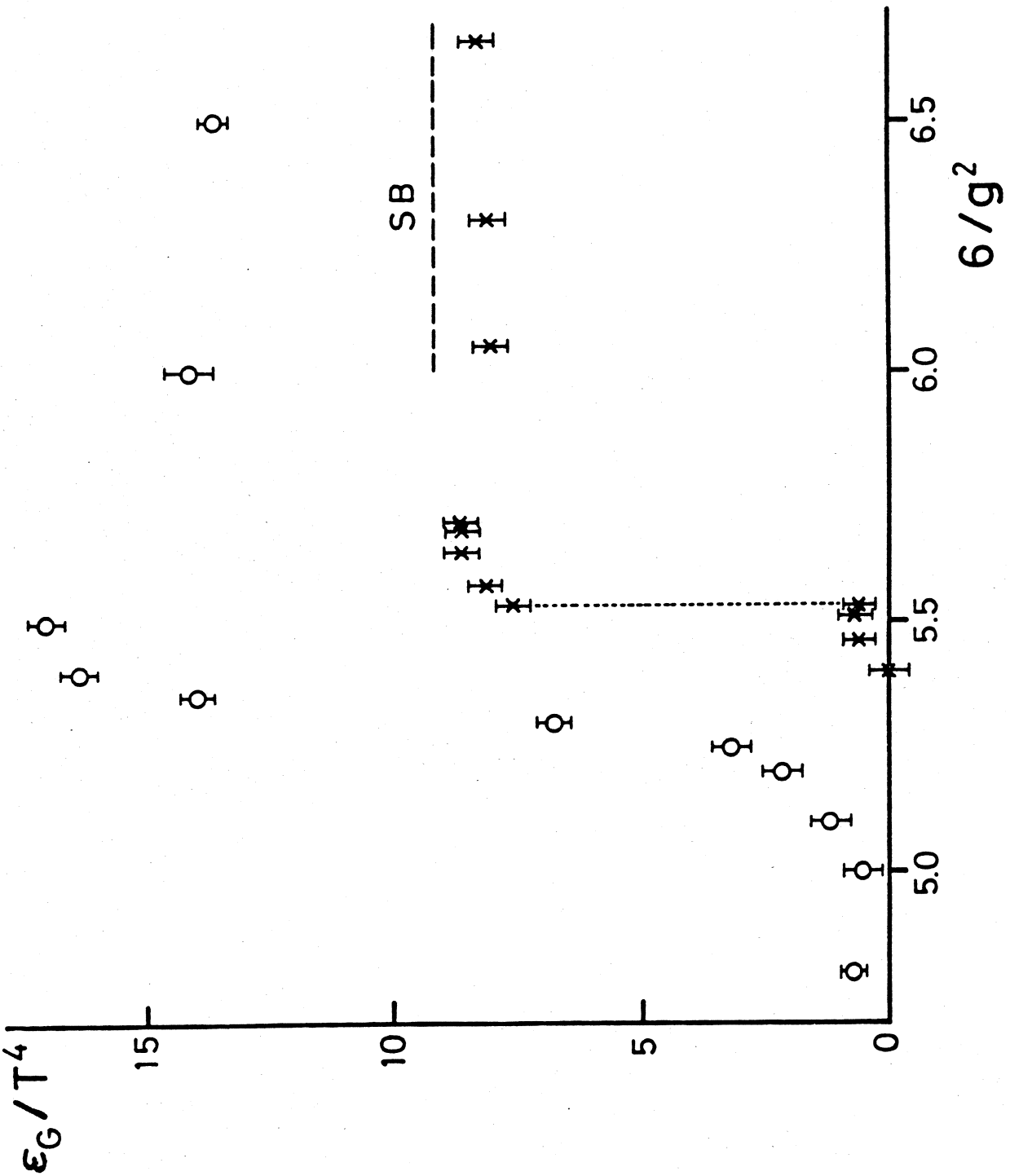

FIGURE I.8

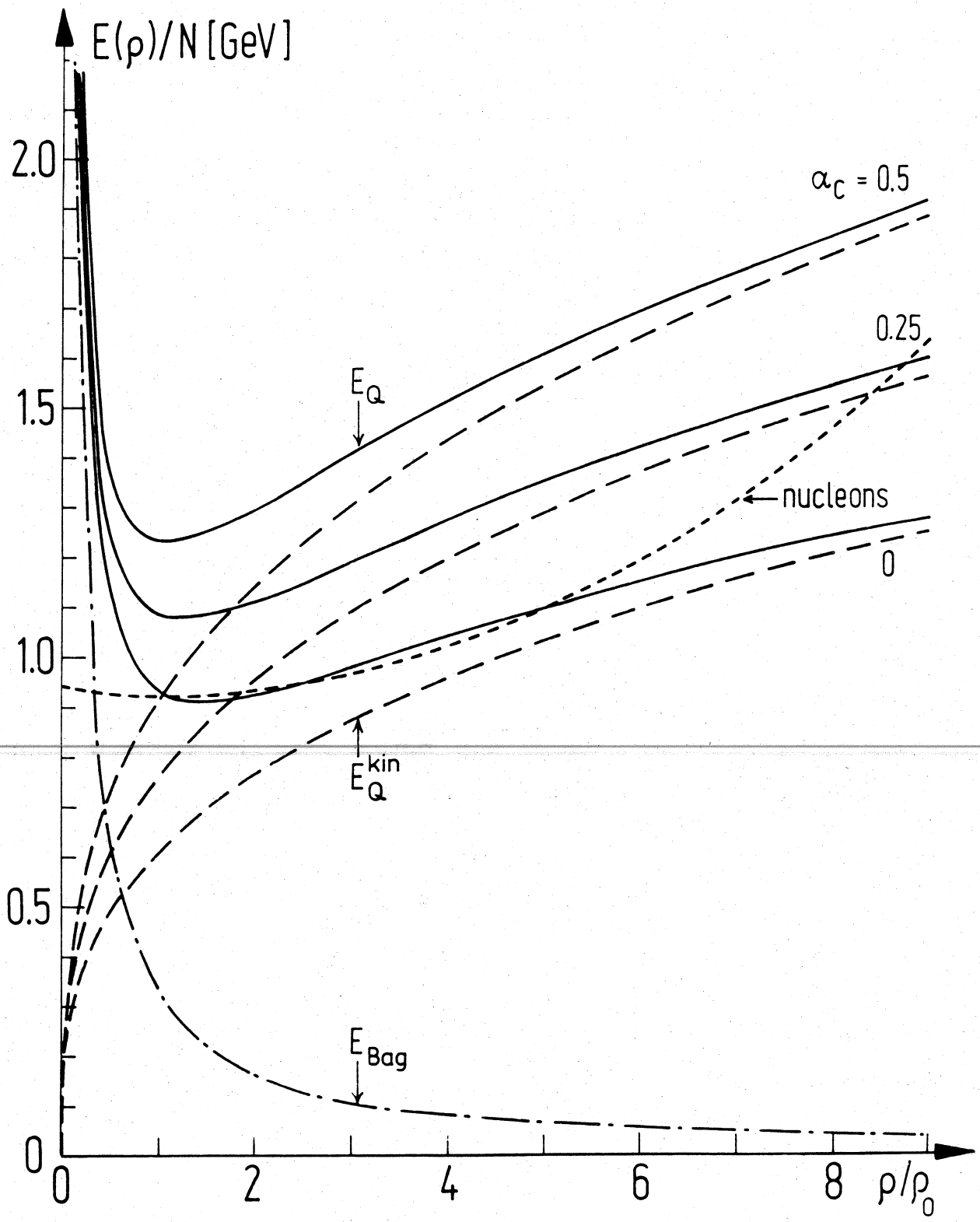
E(ρ)/N [GeV]
2.0
1.5
1.0
0.5
0
0
2
4
6
8
ρ/ρ0
αc = 0.5
0.25
0
nucleons
EQ
EQkin
EBag

FIGURE I.9

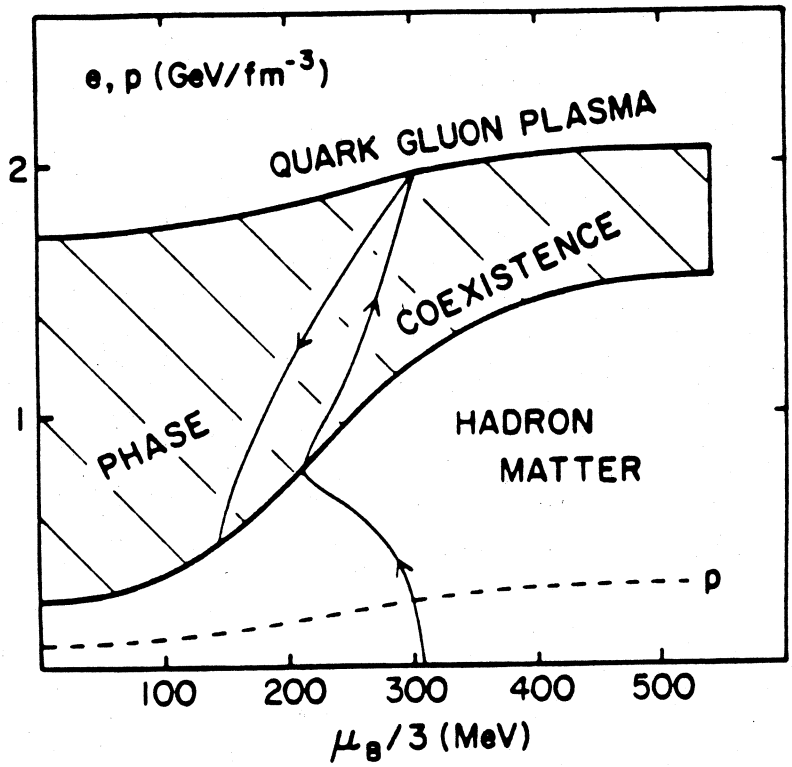
e, p (GeV/fm^{-3})
QUARK GLUON PLASMA
COEXISTENCE
PHASE
HADRON
MATTER
p
2
1
100
200
300
400
500
$\mu_B/3$ (MeV)

FIGURE I.10

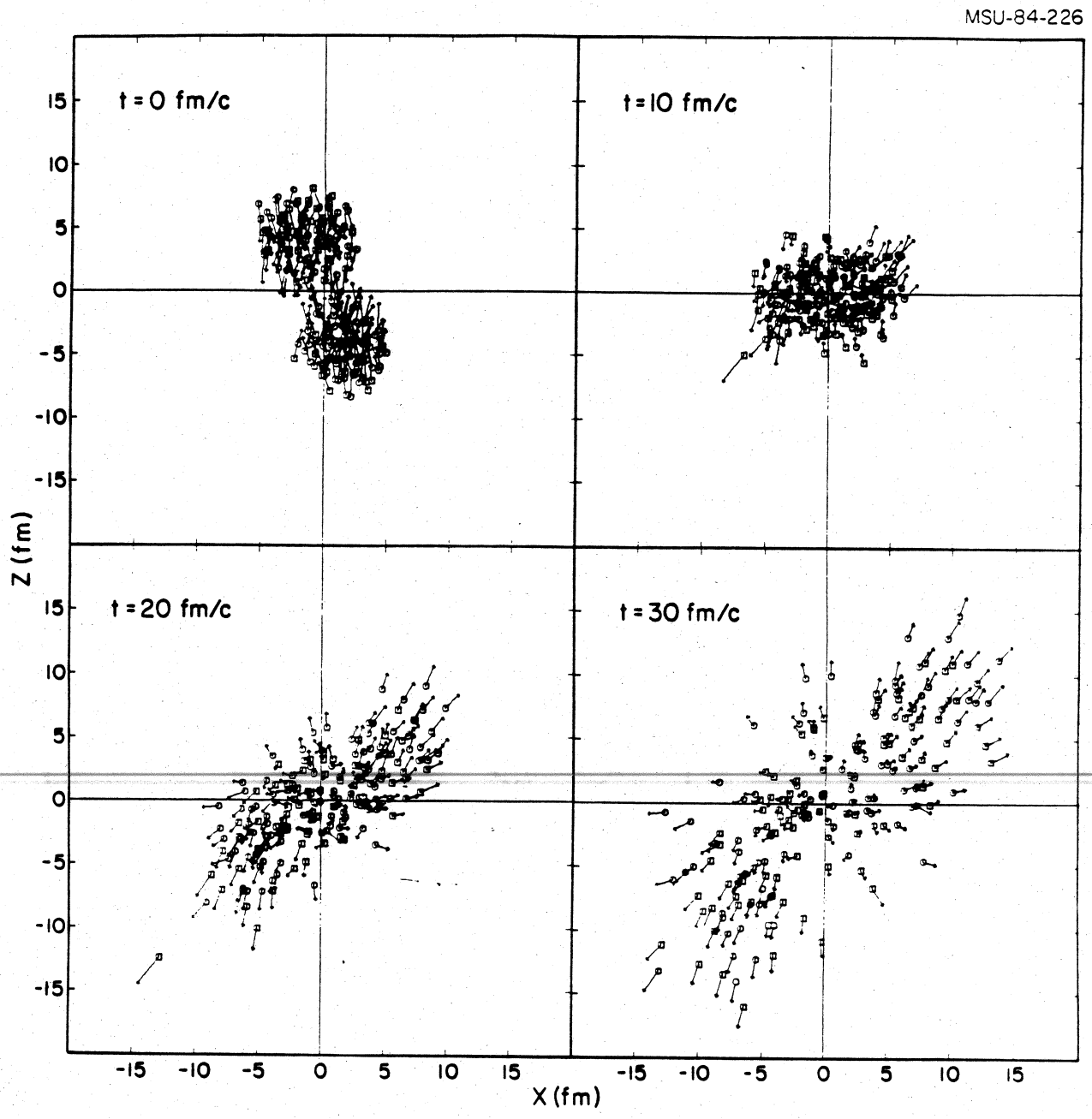

FIGURE II.1

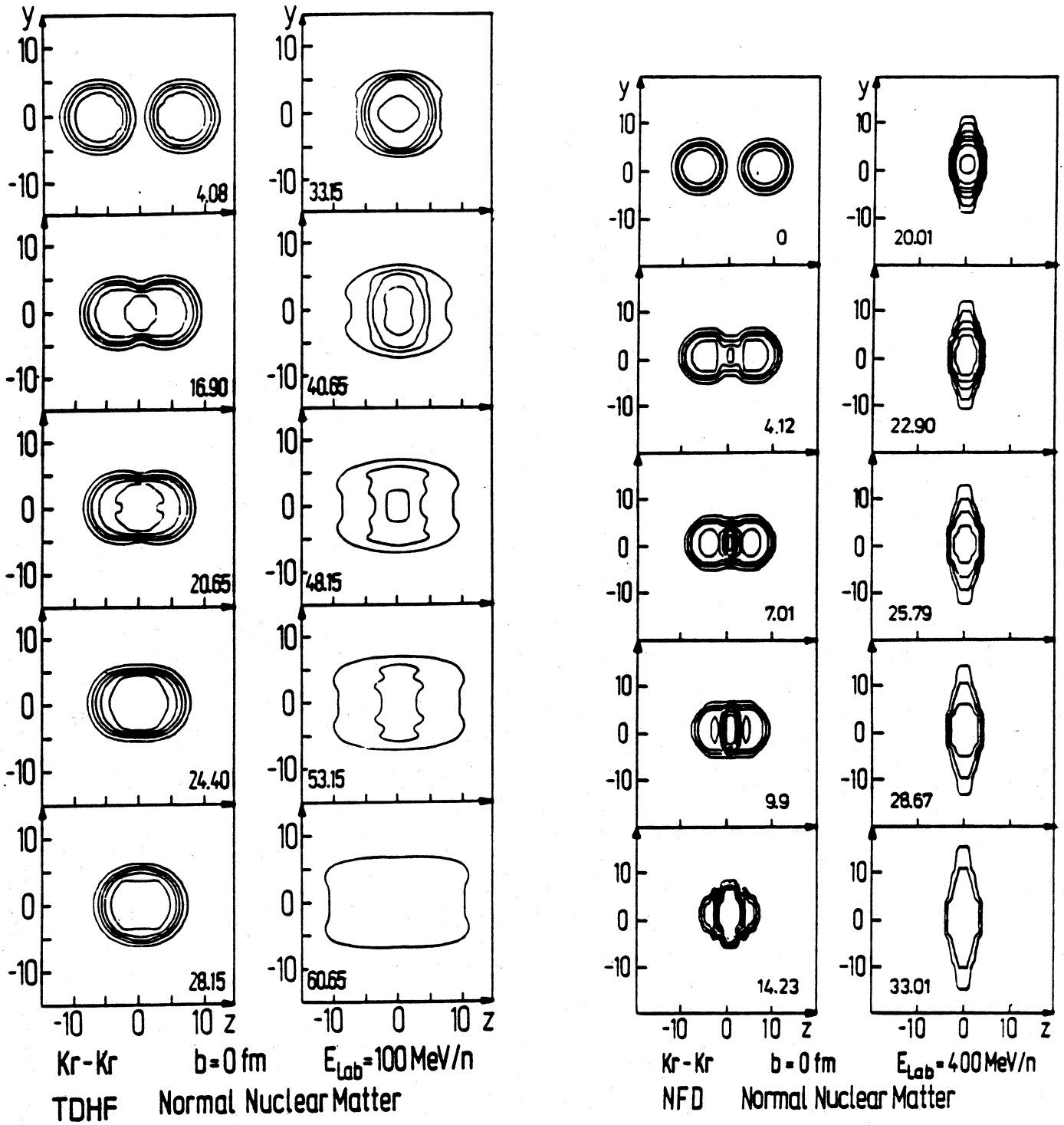
y
10
0
-10
4.08
16.90
20.65
24.40
28.15
33.15
40.65
48.15
53.15
60.65
-10 0 10 z
Kr-Kr b=0 fm E_Lab=100 MeV/n
TDHF Normal Nuclear Matter
0
4.12
7.01
9.9
14.23
20.01
22.90
25.79
28.67
33.01
Kr-Kr b=0 fm E_Lab=400 MeV/n
NFD Normal Nuclear Matter

FIGURE II.2

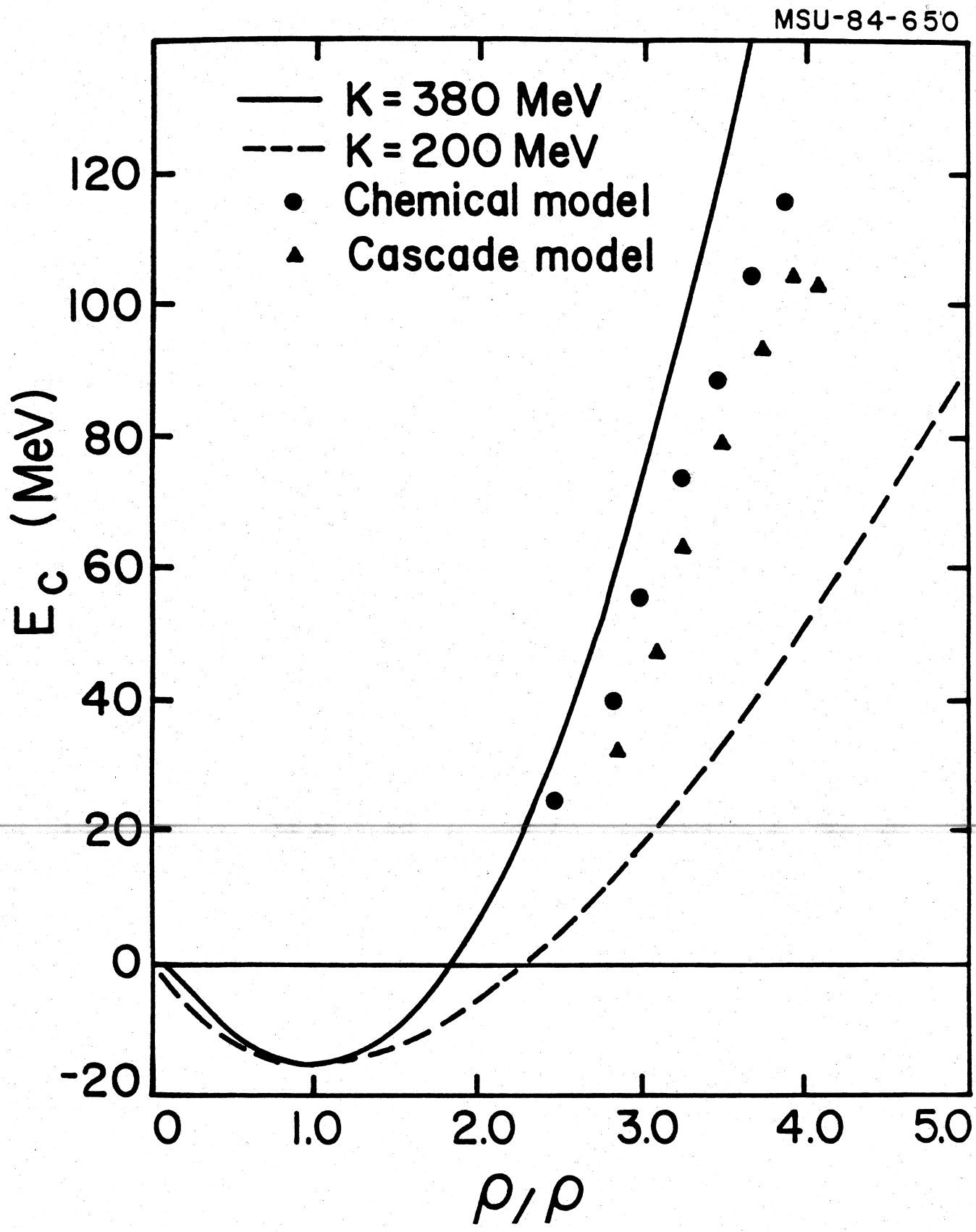
MSU-84-650
K = 380 MeV
K = 200 MeV
Chemical model
Cascade model
120
100
80
60
40
20
0
-20
E_c (MeV)
0
1.0
2.0
3.0
4.0
5.0
ρ/ρ

FIGURE II.3

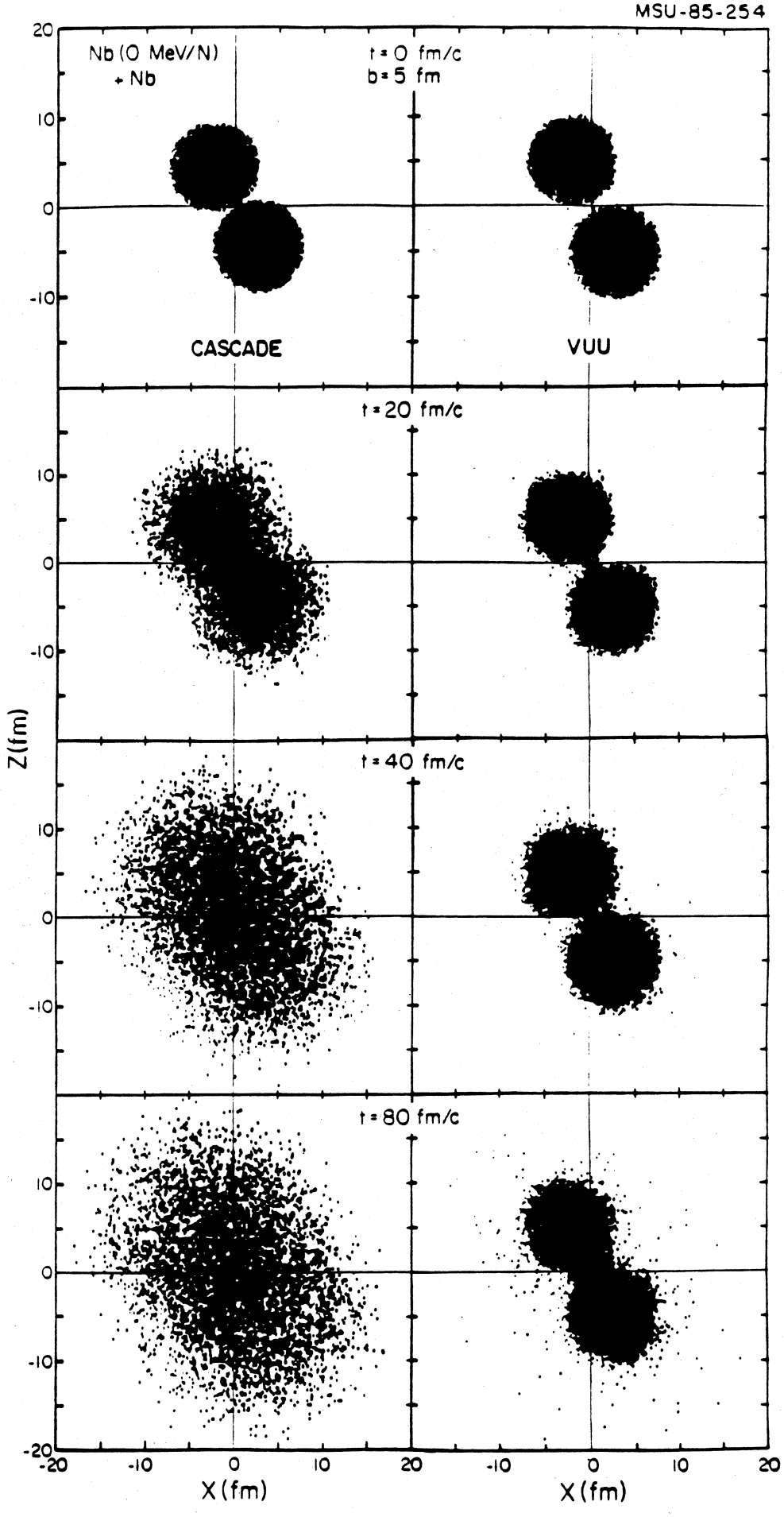
Nb (0 MeV/N)
+ Nb
t = 0 fm/c
b = 5 fm
CASCADE
VUU
t = 20 fm/c
t = 40 fm/c
t = 80 fm/c
Z(fm)
X(fm)
X(fm)

FIGURE II.4

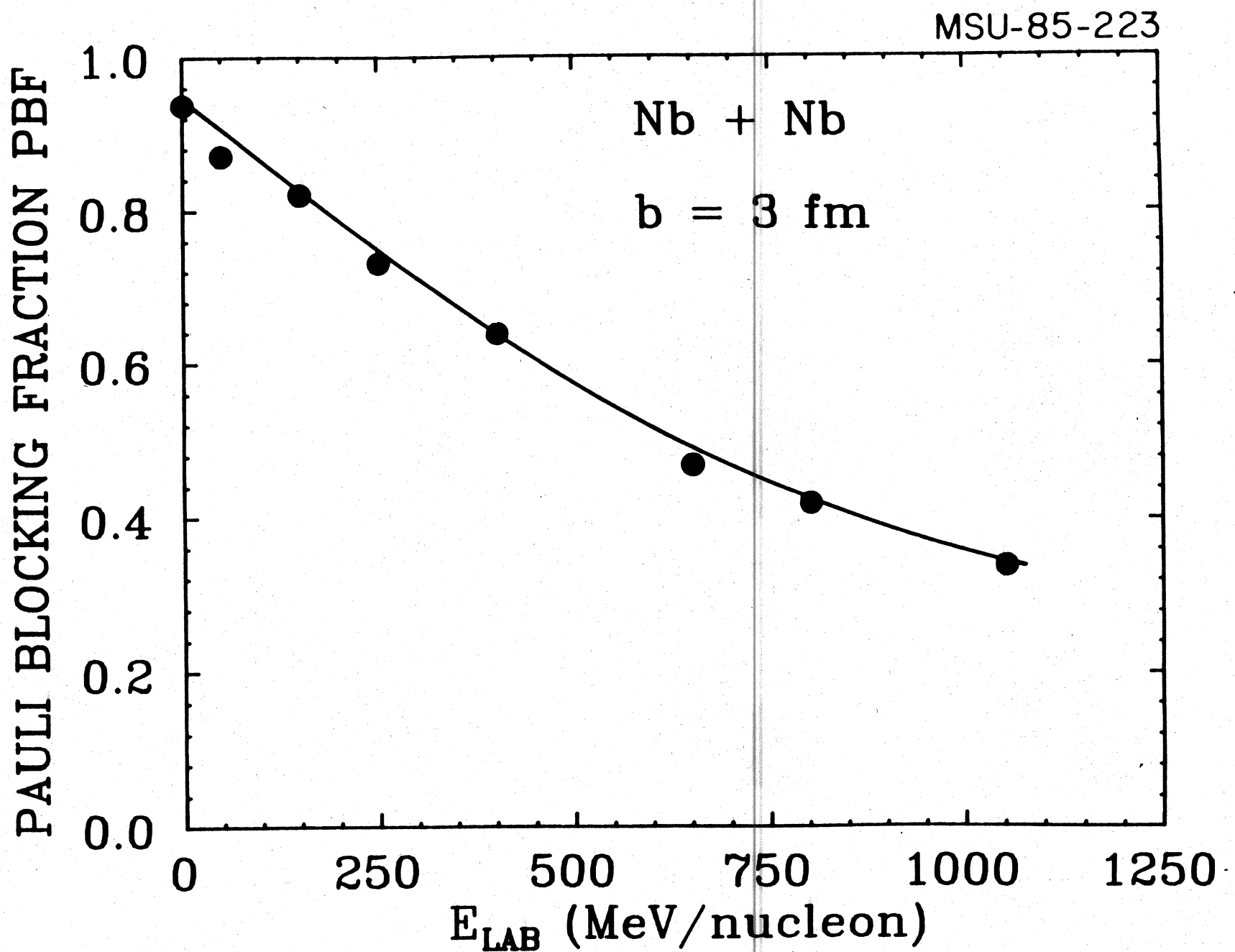
MSU-85-223
PAULI BLOCKING FRACTION PBF
1.0
0.8
0.6
0.4
0.2
0.0
Nb + Nb
b = 3 fm
0
250
500
750
1000
1250
E_LAB (MeV/nucleon)

FIGURE II.5

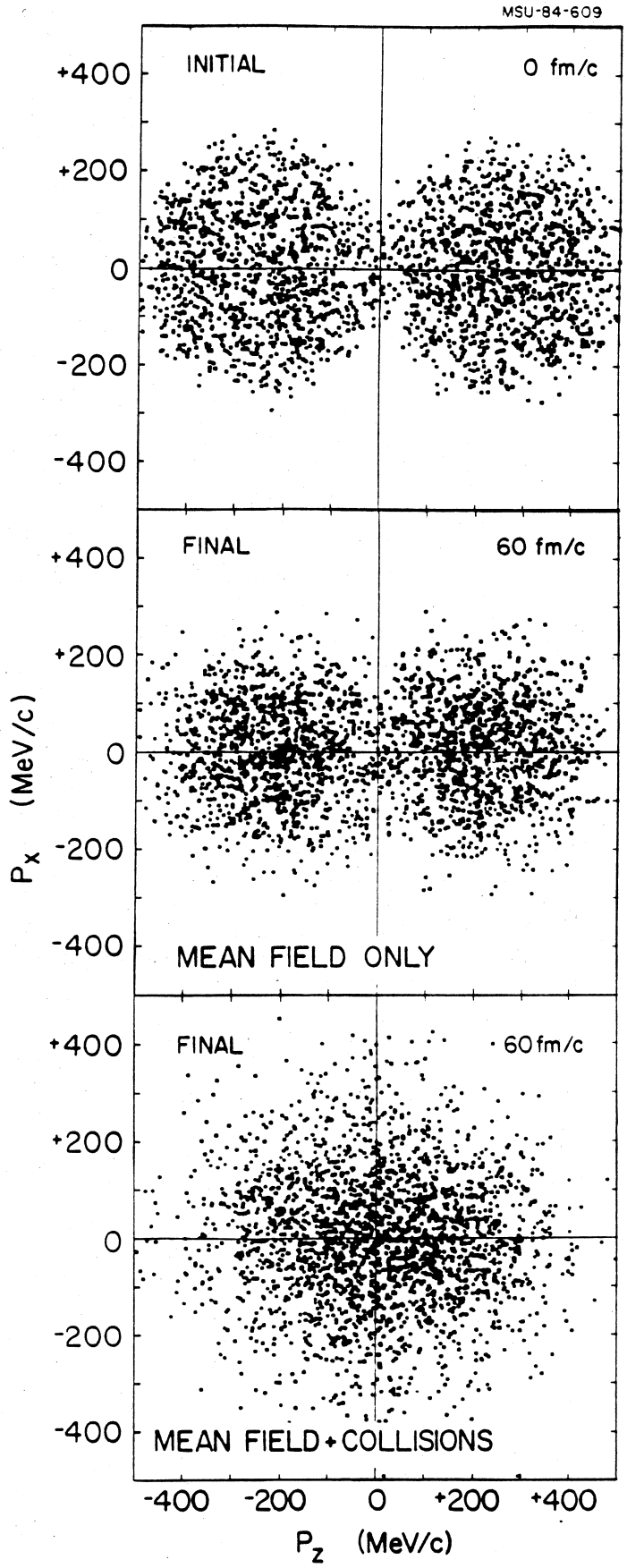
MSU-84-609
INITIAL
0 fm/c
FINAL
60 fm/c
MEAN FIELD ONLY
FINAL
60 fm/c
MEAN FIELD + COLLISIONS
+400
+200
0
-200
-400
P_x (MeV/c)
P_z (MeV/c)

FIGURE II.6

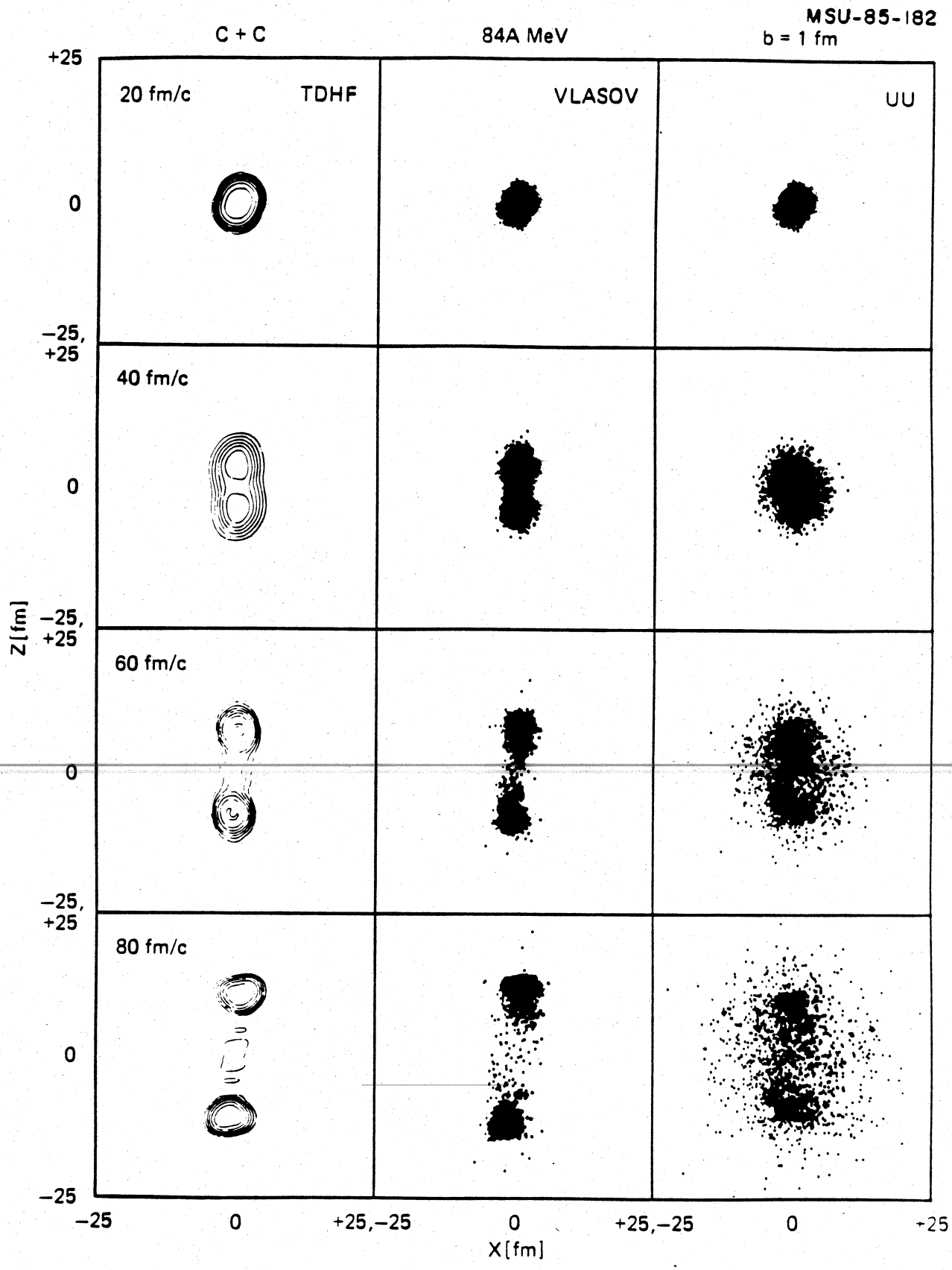
MSU-85-182
C + C
84A MeV
b = 1 fm
20 fm/c
TDHF
VLASOV
UU
40 fm/c
60 fm/c
80 fm/c
+25
0
−25,
+25
−25
Z[fm]
−25
0
+25,−25
X[fm]
+25

FIGURE II.7

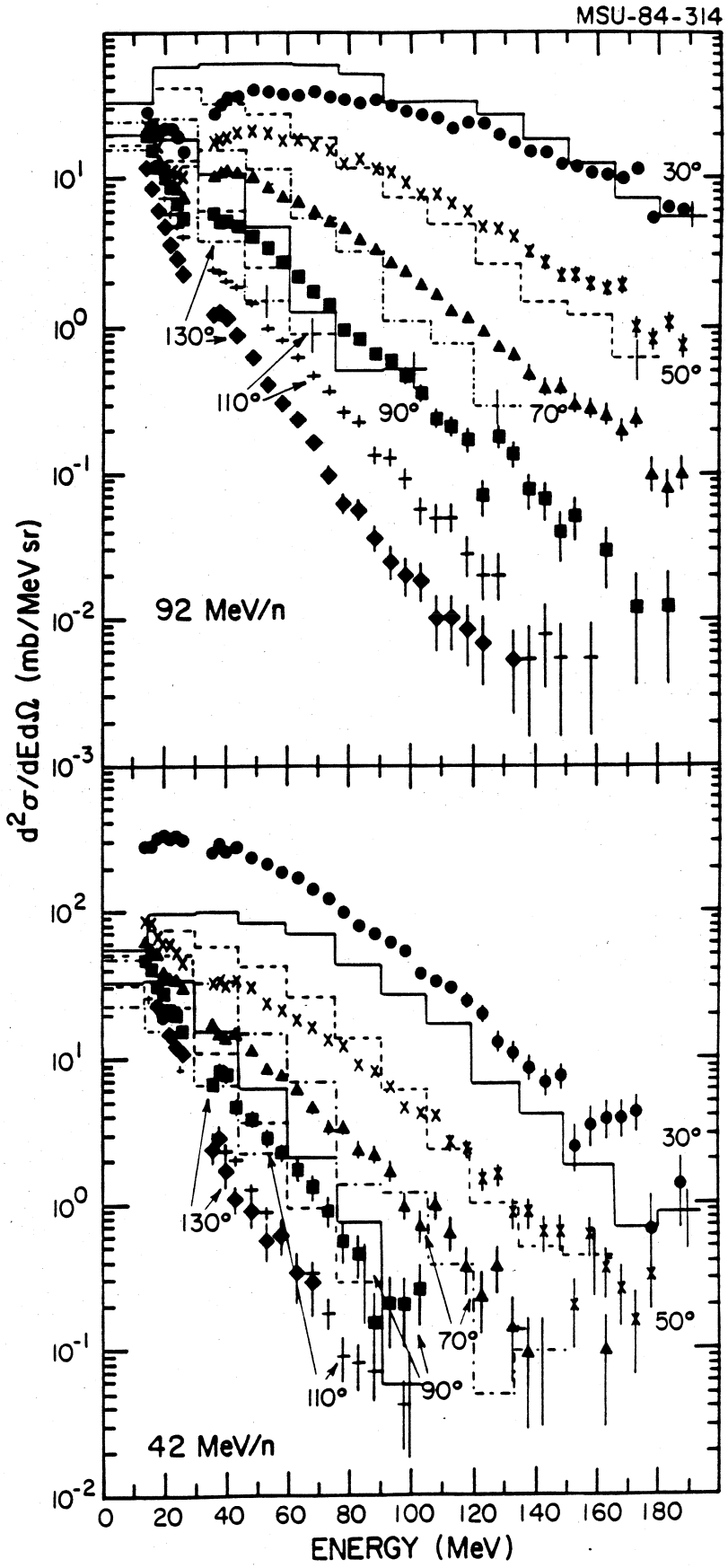
MSU-84-314
$d^2\sigma/dEd\Omega$ (mb/MeV sr)
92 MeV/n
42 MeV/n
30°
50°
70°
90°
110°
130°
ENERGY (MeV)
0
20
40
60
80
100
120
140
160
180
10^{1}
10^{0}
10^{-1}
10^{-2}
10^{-3}
10^{2}

FIGURE II.8

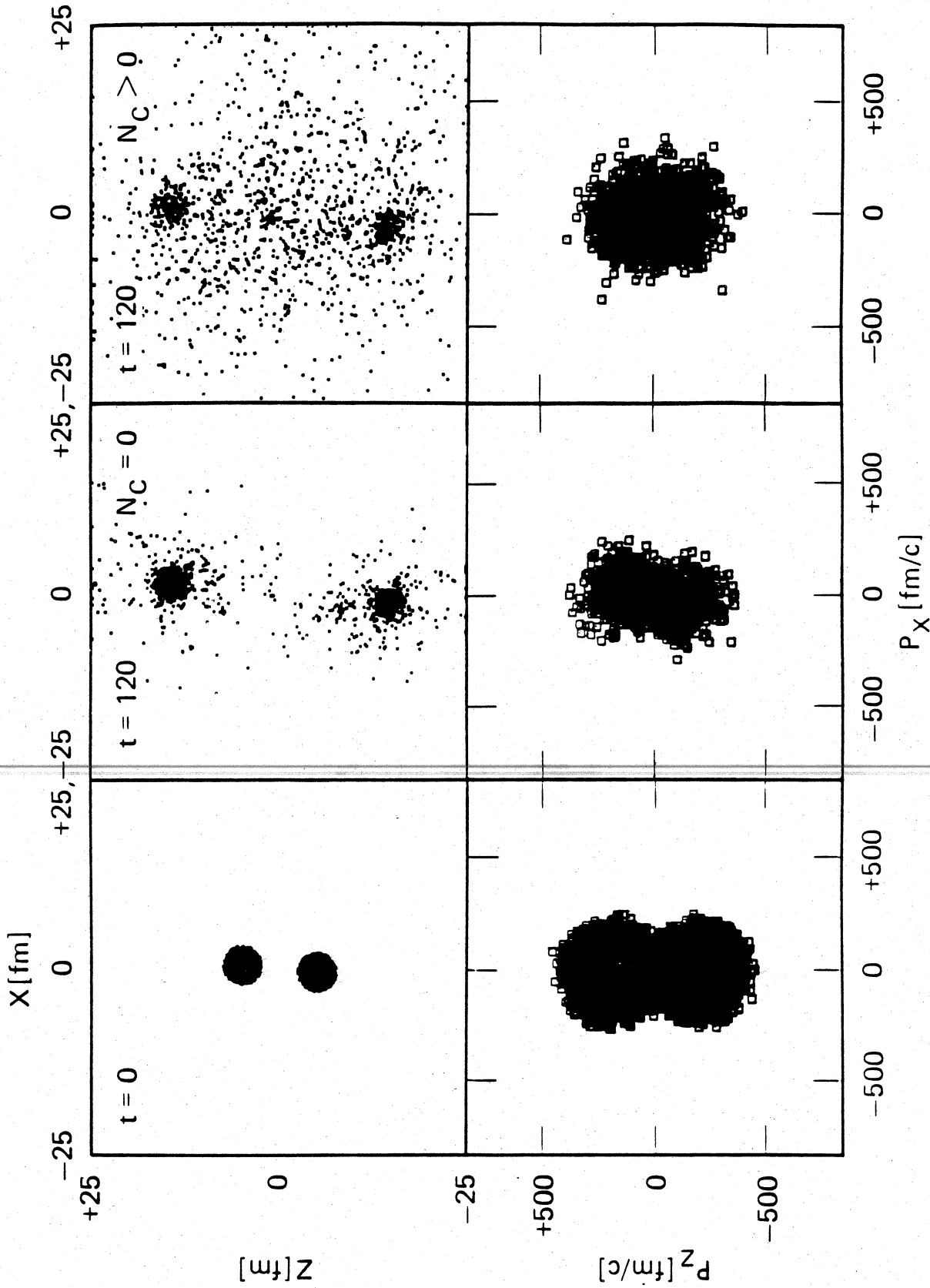

FIGURE II.9

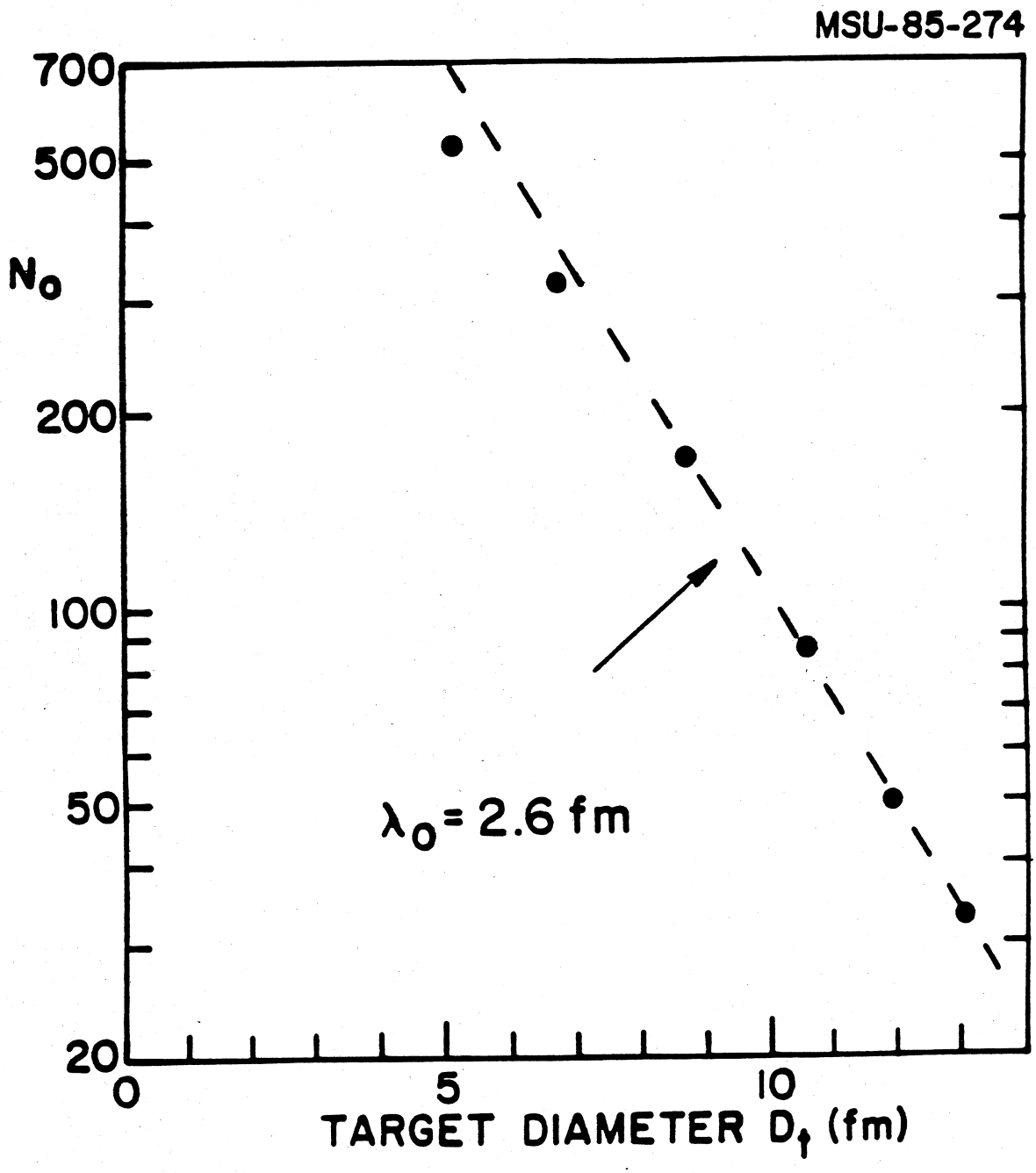
MSU-85-274
700
500
N_0
200
100
50
20
0
5
10
$\lambda_0 = 2.6$ fm
TARGET DIAMETER D_t (fm)

FIGURE II.10

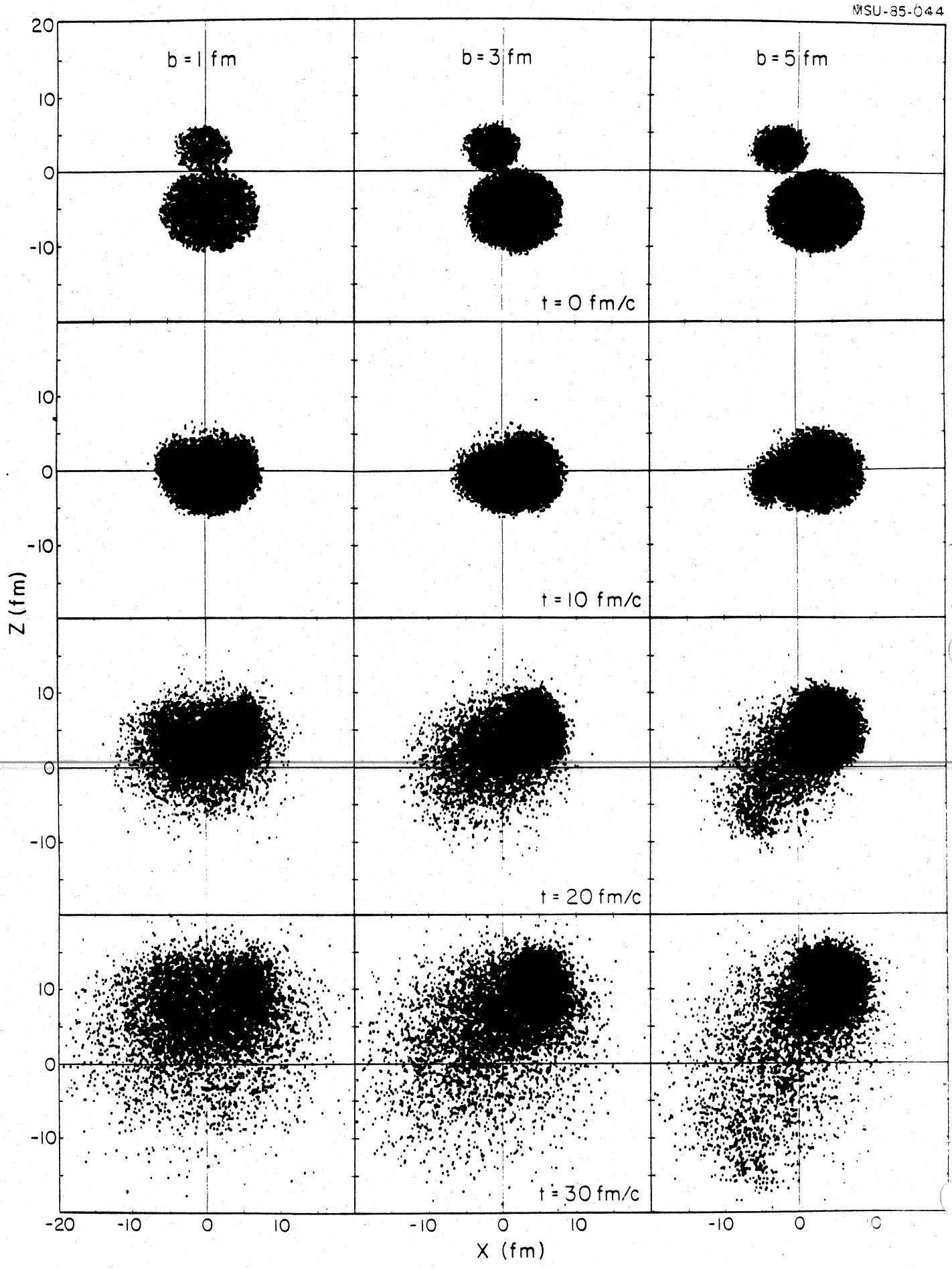
MSU-85-044
b = 1 fm
b = 3 fm
b = 5 fm
t = 0 fm/c
t = 10 fm/c
t = 20 fm/c
t = 30 fm/c
Z (fm)
X (fm)
20
10
0
-10
-20

FIGURE II.11

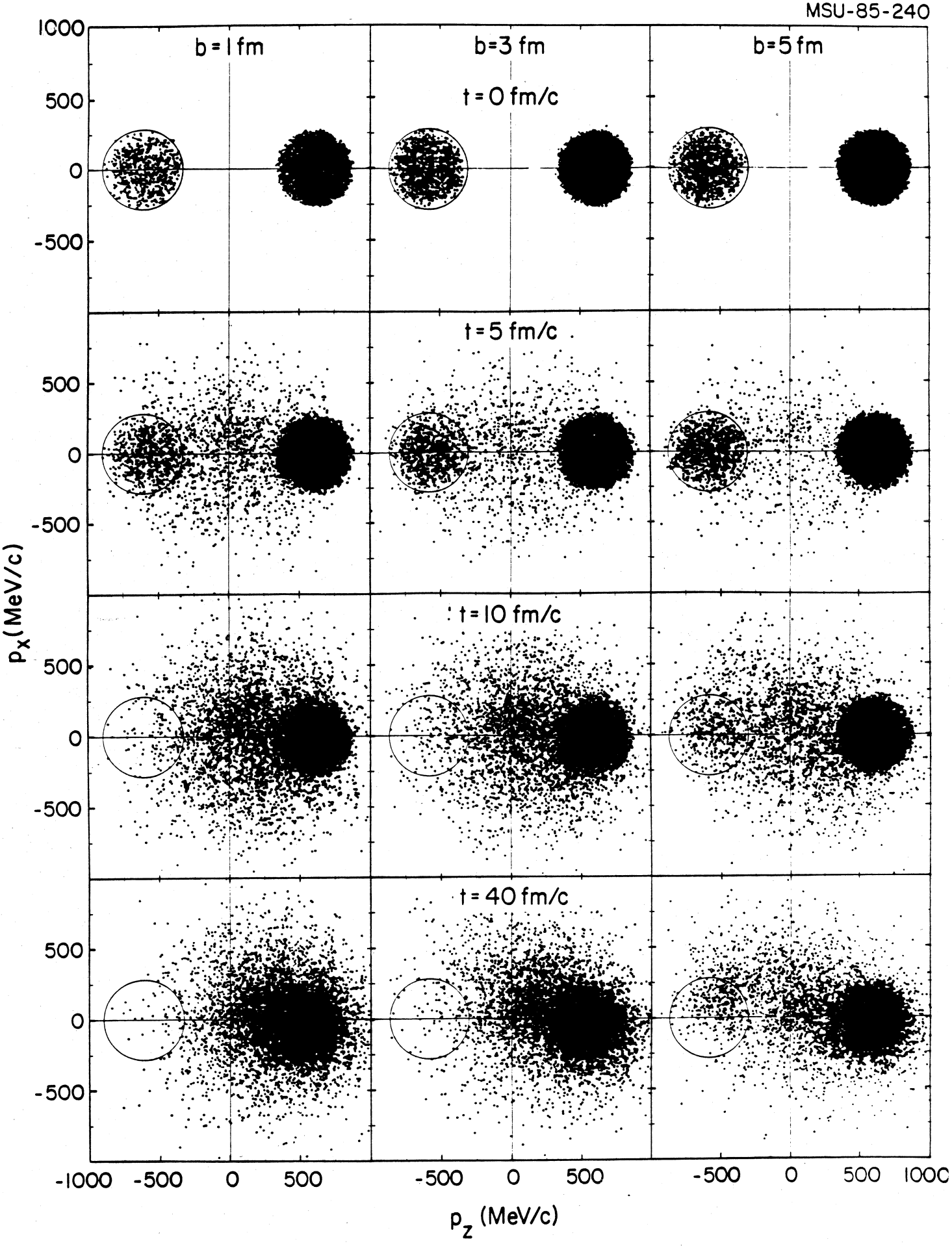
MSU-85-240
b = 1 fm
b=3 fm
b=5 fm
t = 0 fm/c
t = 5 fm/c
t = 10 fm/c
t = 40 fm/c
1000
500
0
-500
p_x(MeV/c)
-1000
-500
0
500
1000
p_z (MeV/c)

FIGURE II.12

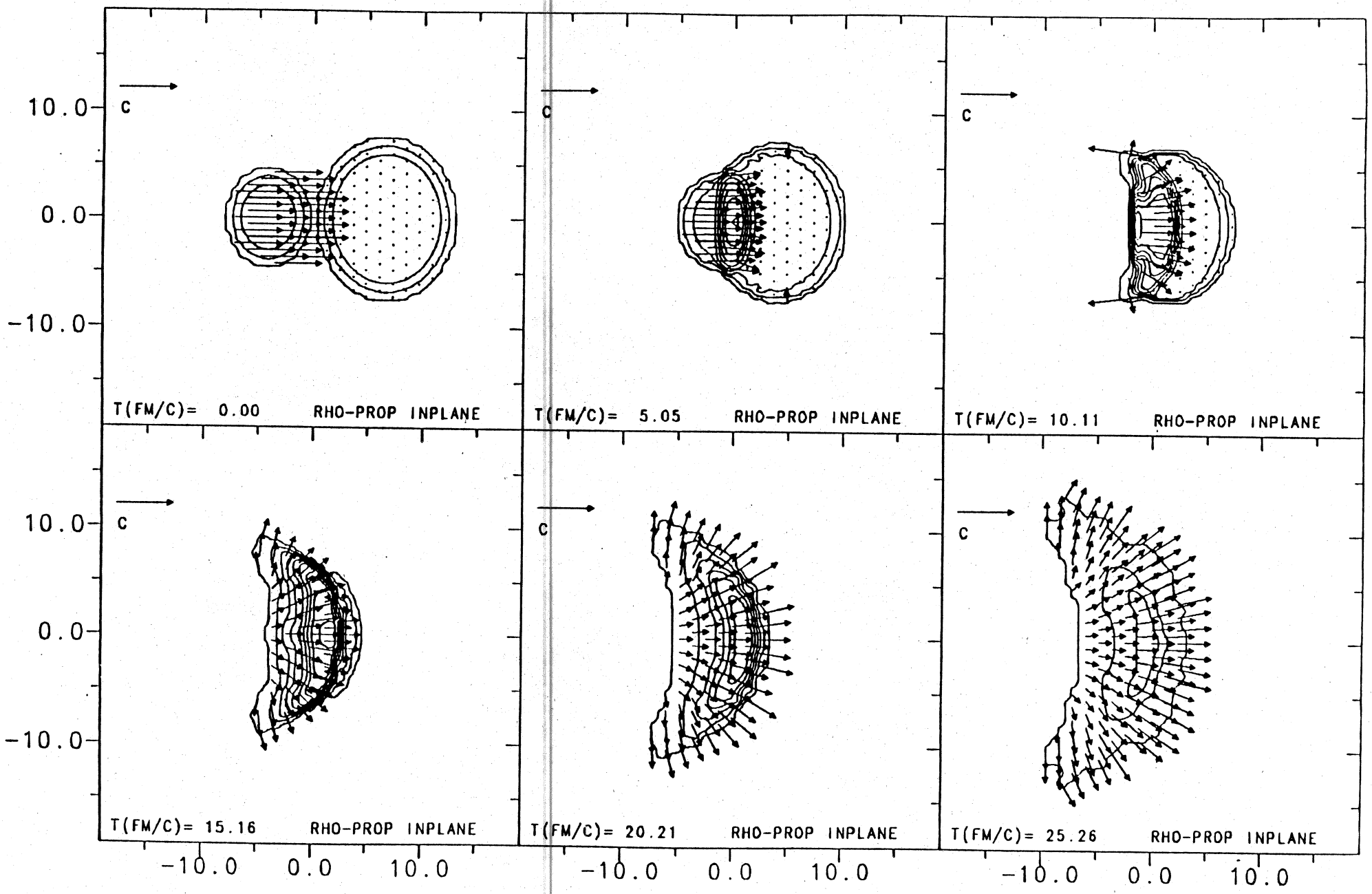

FIGURE II.13

6UUD AR->PB 800 MEV 6-COUPLE STD. EOS. DX=.6 NOPOT NOVISC B=0 CN=200 21.04.83

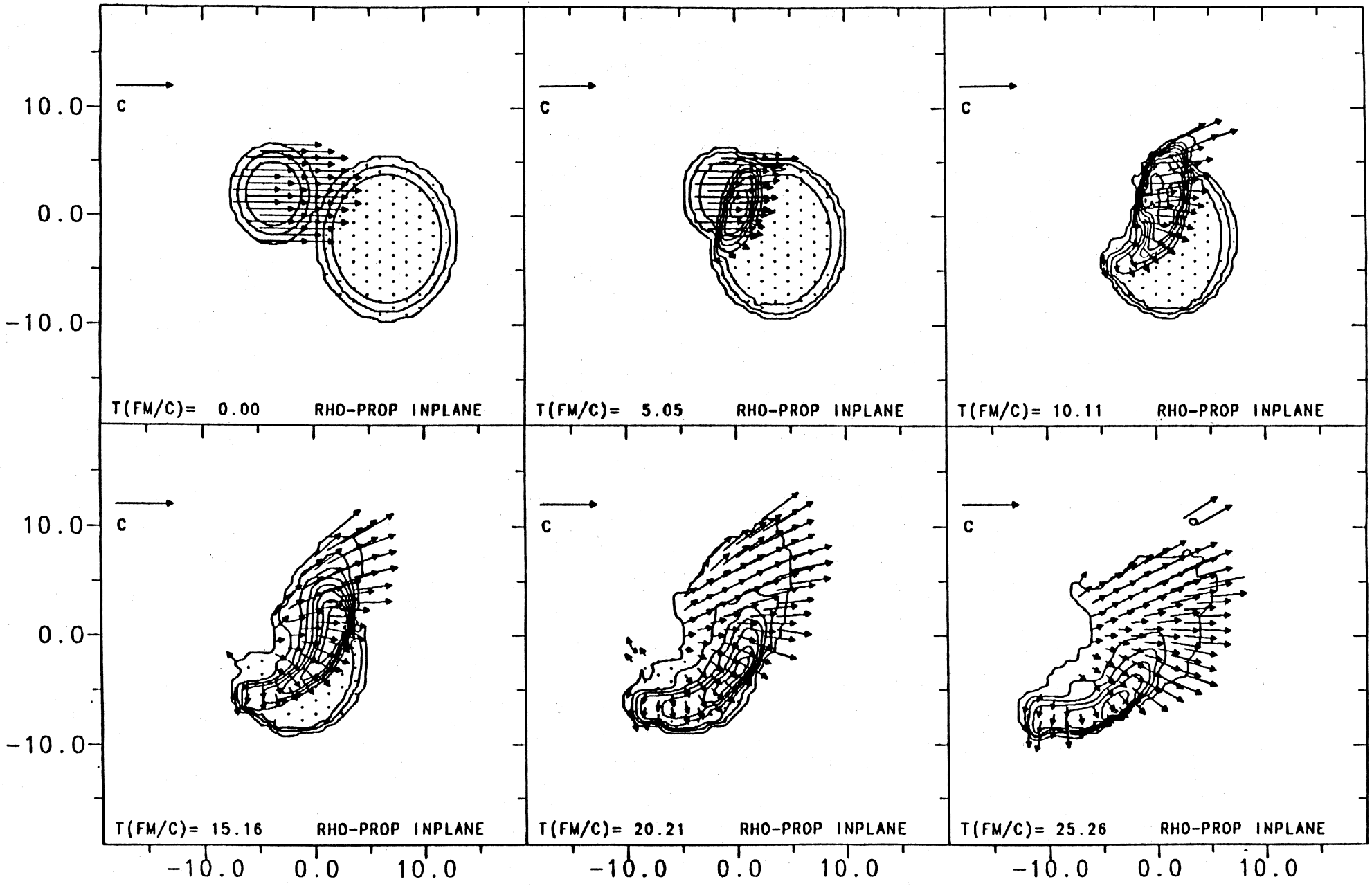

FIGURE II.14

6UUD AR->PB 800 MEV 6-COUPLE STD. EOS. DX=.6 NOPOT NOVISC B=4 CN=200 21.04.83

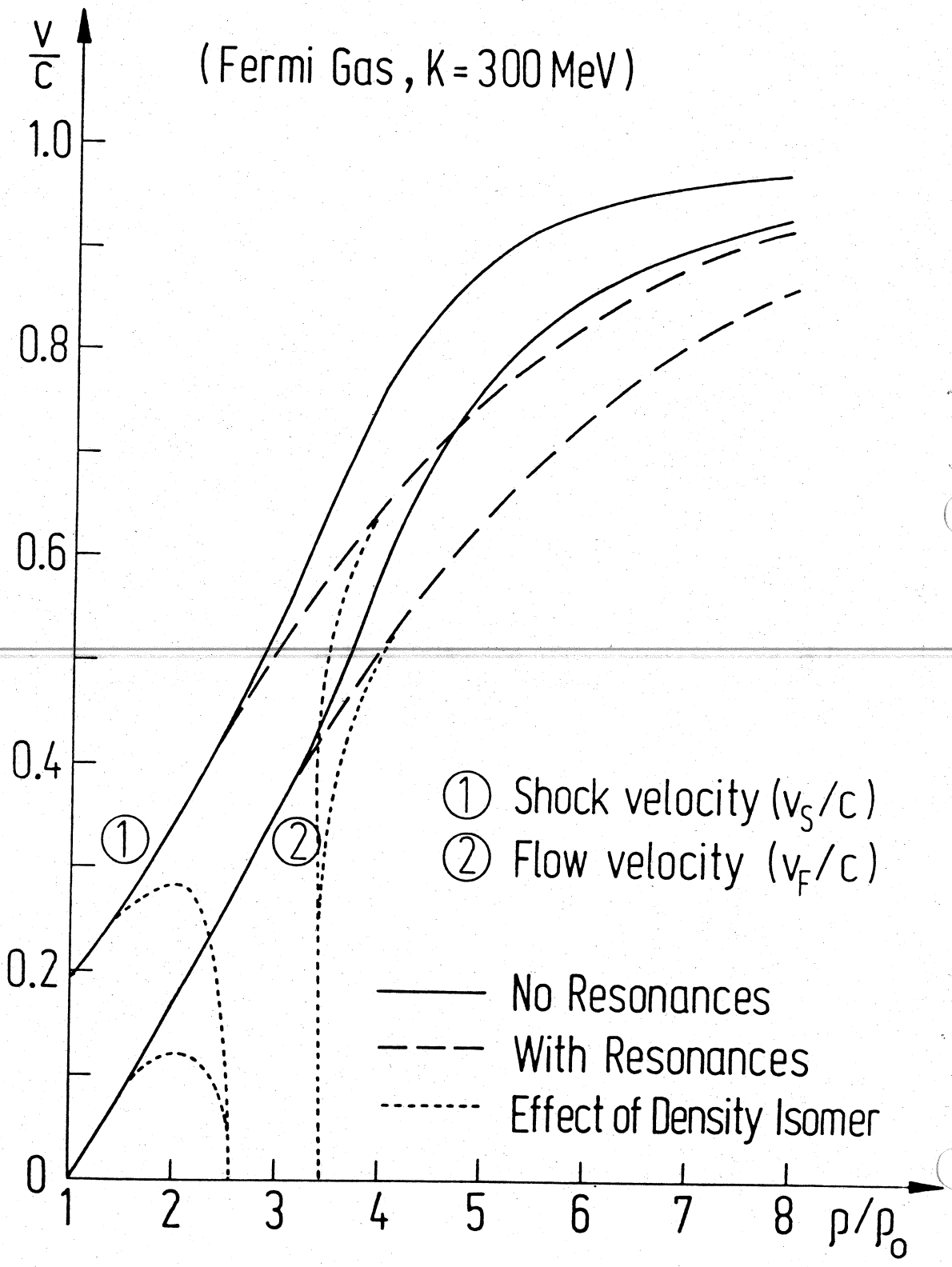
v/c
(Fermi Gas, K = 300 MeV)
1.0
0.8
0.6
0.4
0.2
0
1
2
3
4
5
6
7
8
ρ/ρ₀
① Shock velocity (v_S/c)
② Flow velocity (v_F/c)
No Resonances
With Resonances
Effect of Density Isomer

FIGURE II.15

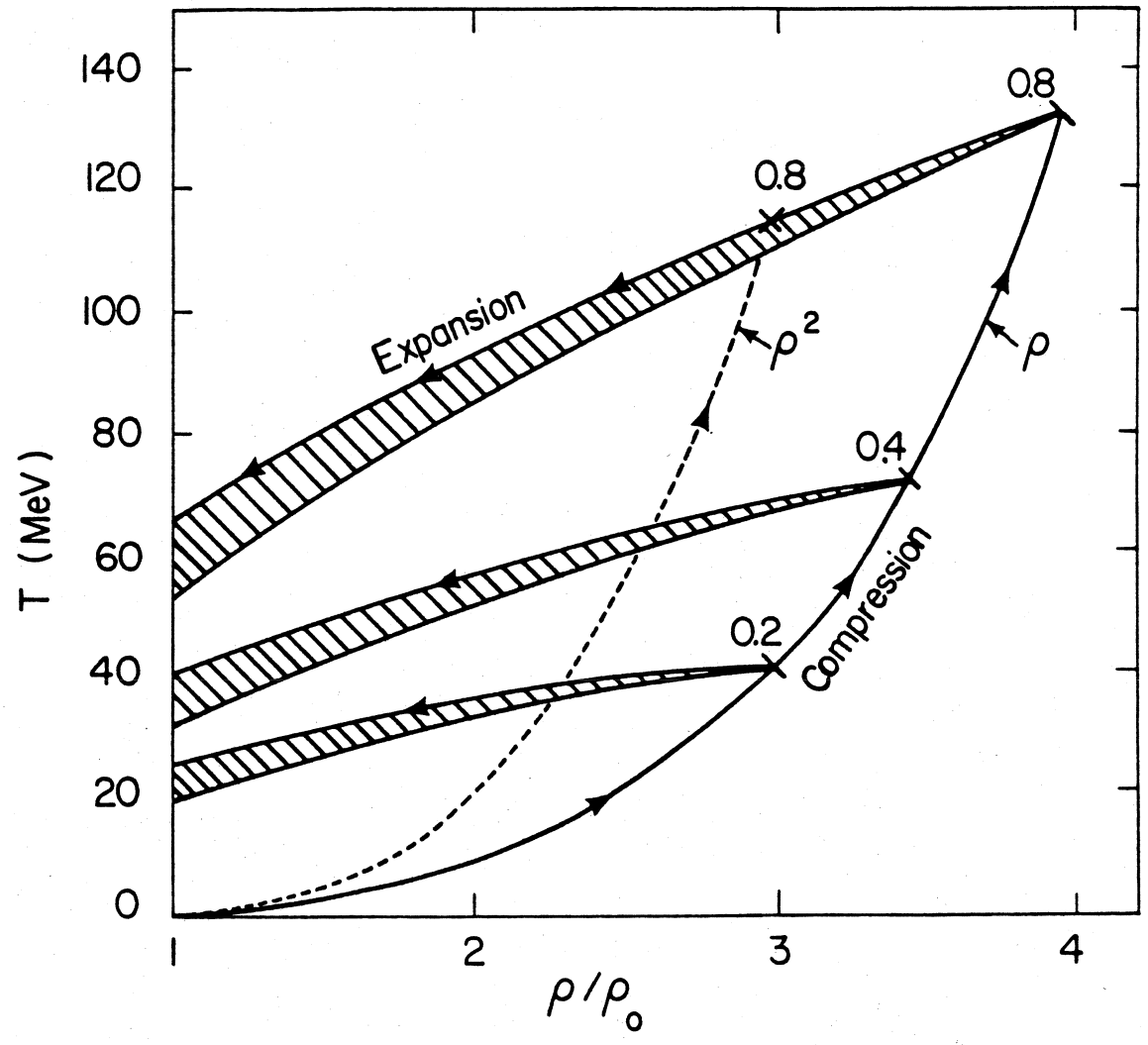

XBL 813-427

FIGURE III.1

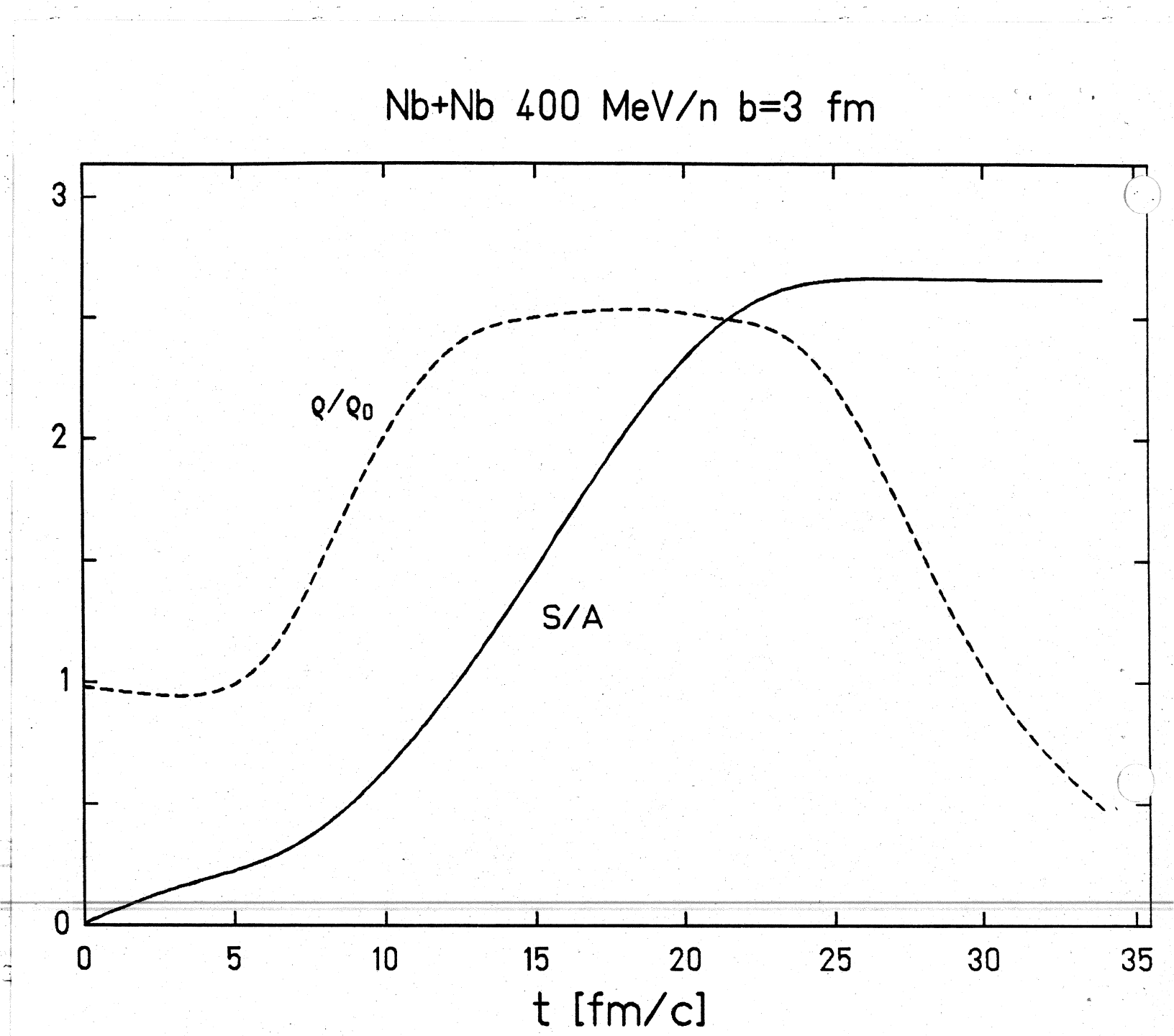

FIGURE III.2a

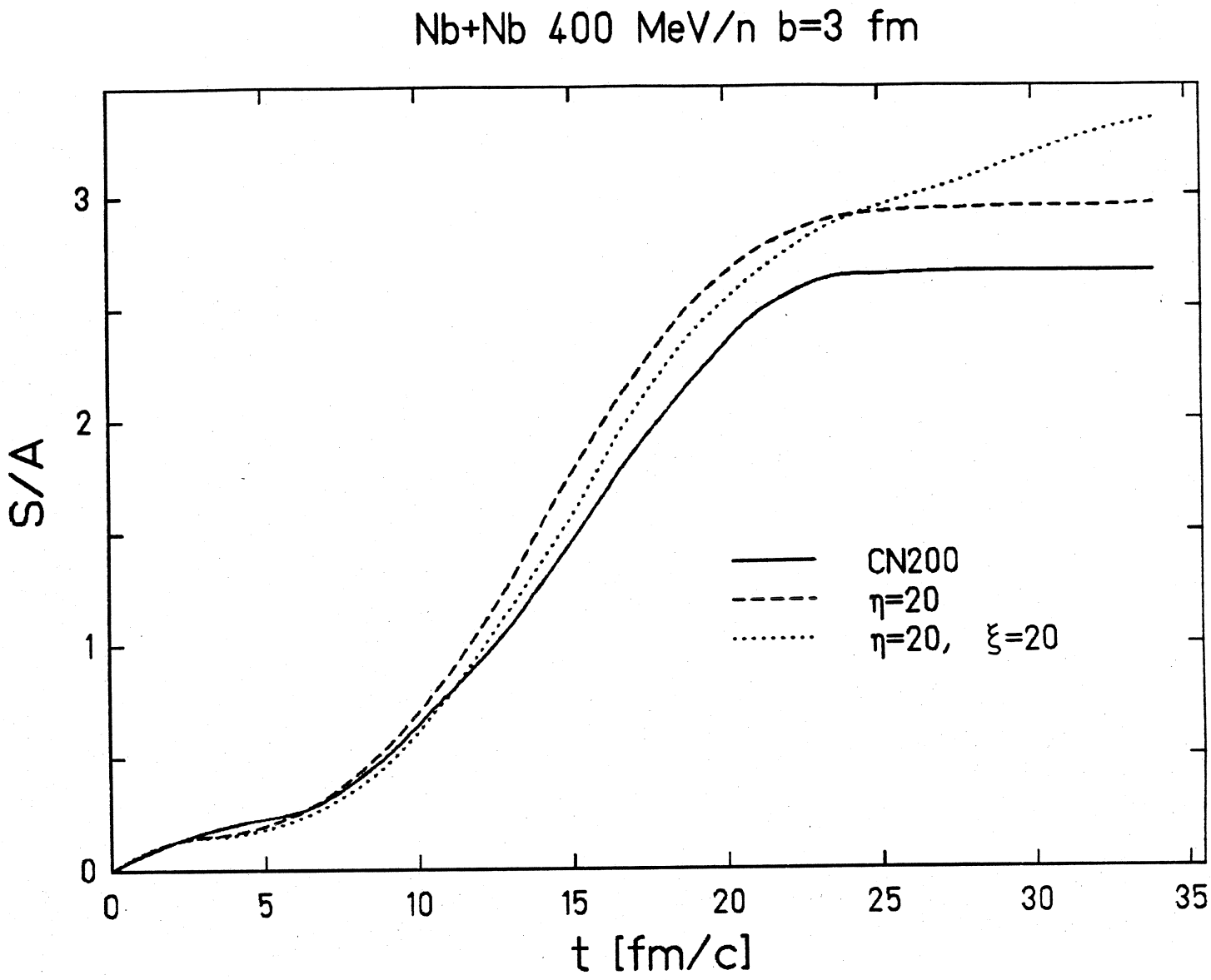

FIGURE III.2b

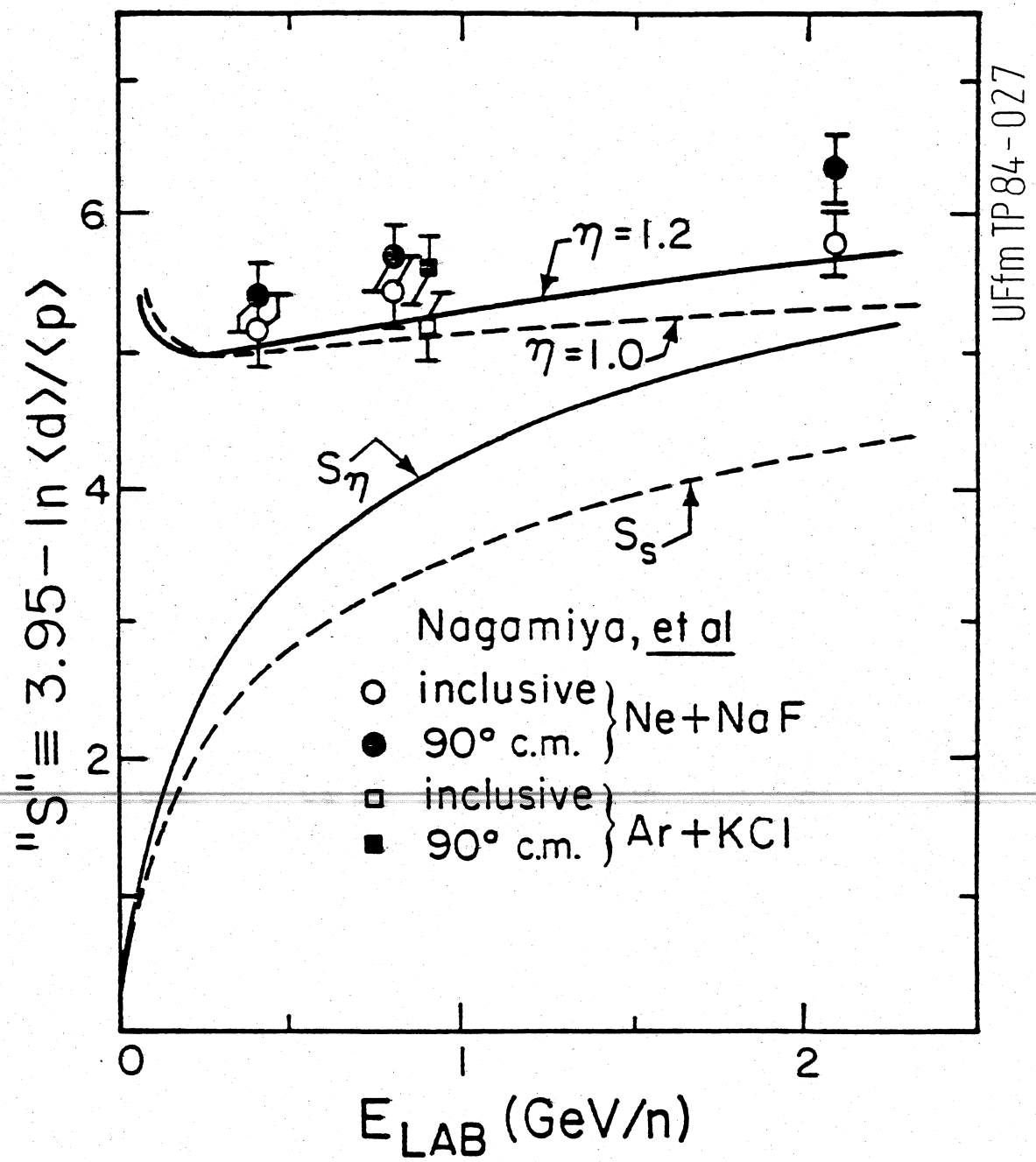
"S" ≡ 3.95 − ln ⟨d⟩/⟨p⟩
6
4
2
0
1
2
E_LAB (GeV/n)
η = 1.2
η = 1.0
S_η
S_s
Nagamiya, et al
inclusive
90° c.m.
Ne+NaF
inclusive
90° c.m.
Ar+KCl
UFfm TP 84-027

FIGURE III.3

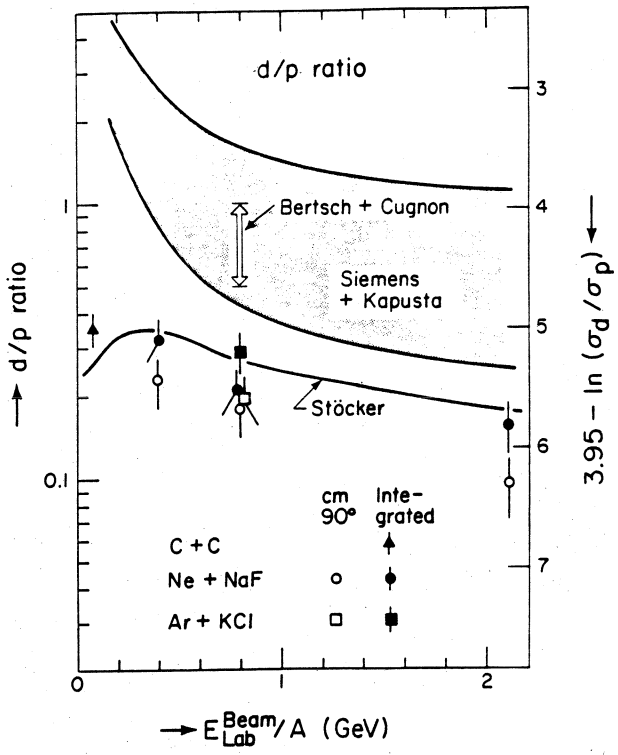
d/p ratio
Bertsch + Cugnon
Siemens
+ Kapusta
Stöcker
cm
90°
Inte-
grated
C + C
Ne + NaF
Ar + KCl
d/p ratio
3.95 − ln (σd/σp)
E Beam Lab /A (GeV)
0
1
2
0.1
1
3
4
5
6
7
XBL 822-4484

FIGURE III.4

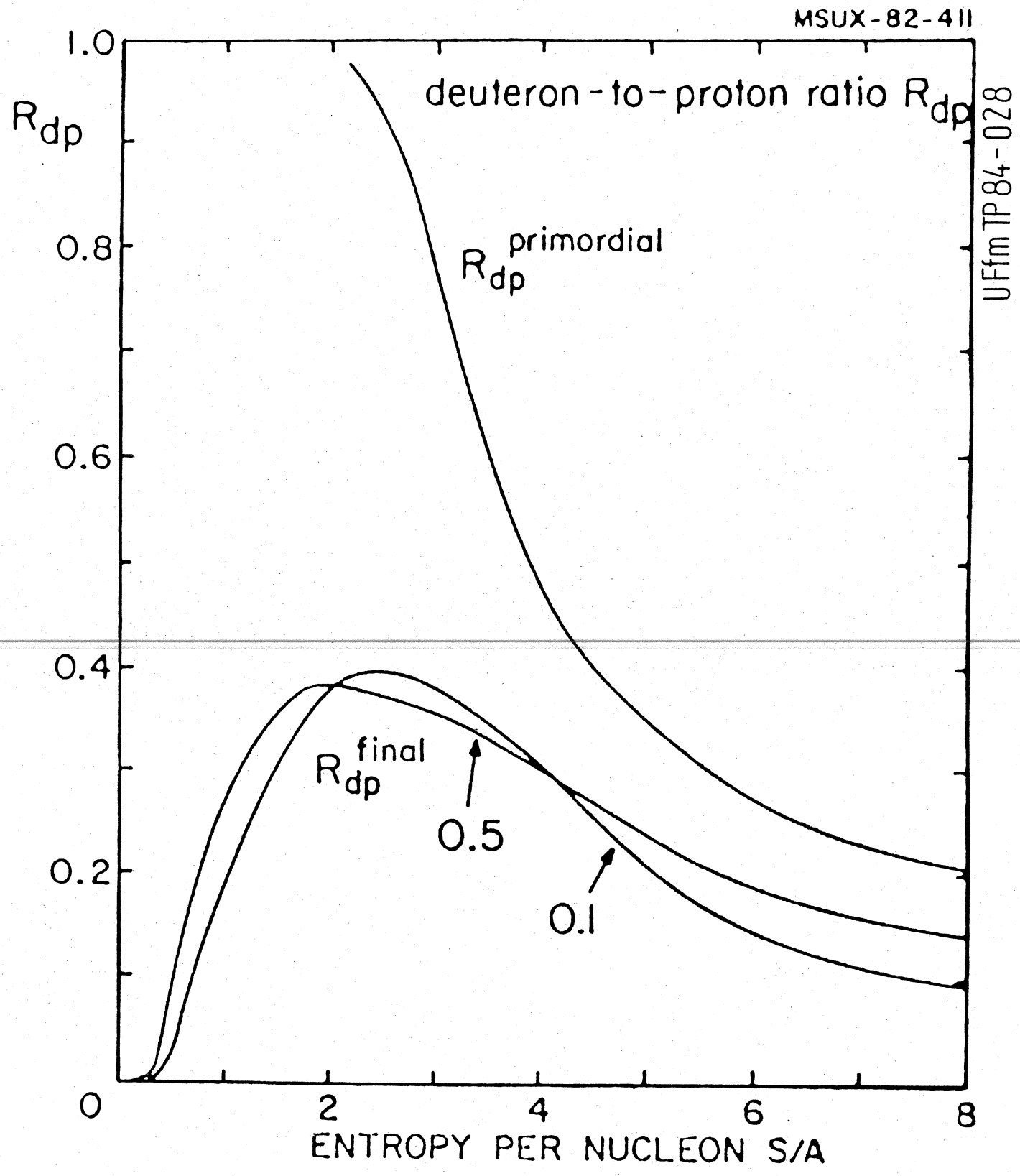
MSUX-82-411
deuteron-to-proton ratio R_{dp}
R_{dp}
$R_{dp}^{primordial}$
R_{dp}^{final}
0.5
0.1
UFfm TP84-028
1.0
0.8
0.6
0.4
0.2
0
2
4
6
8
ENTROPY PER NUCLEON S/A

FIGURE III.5

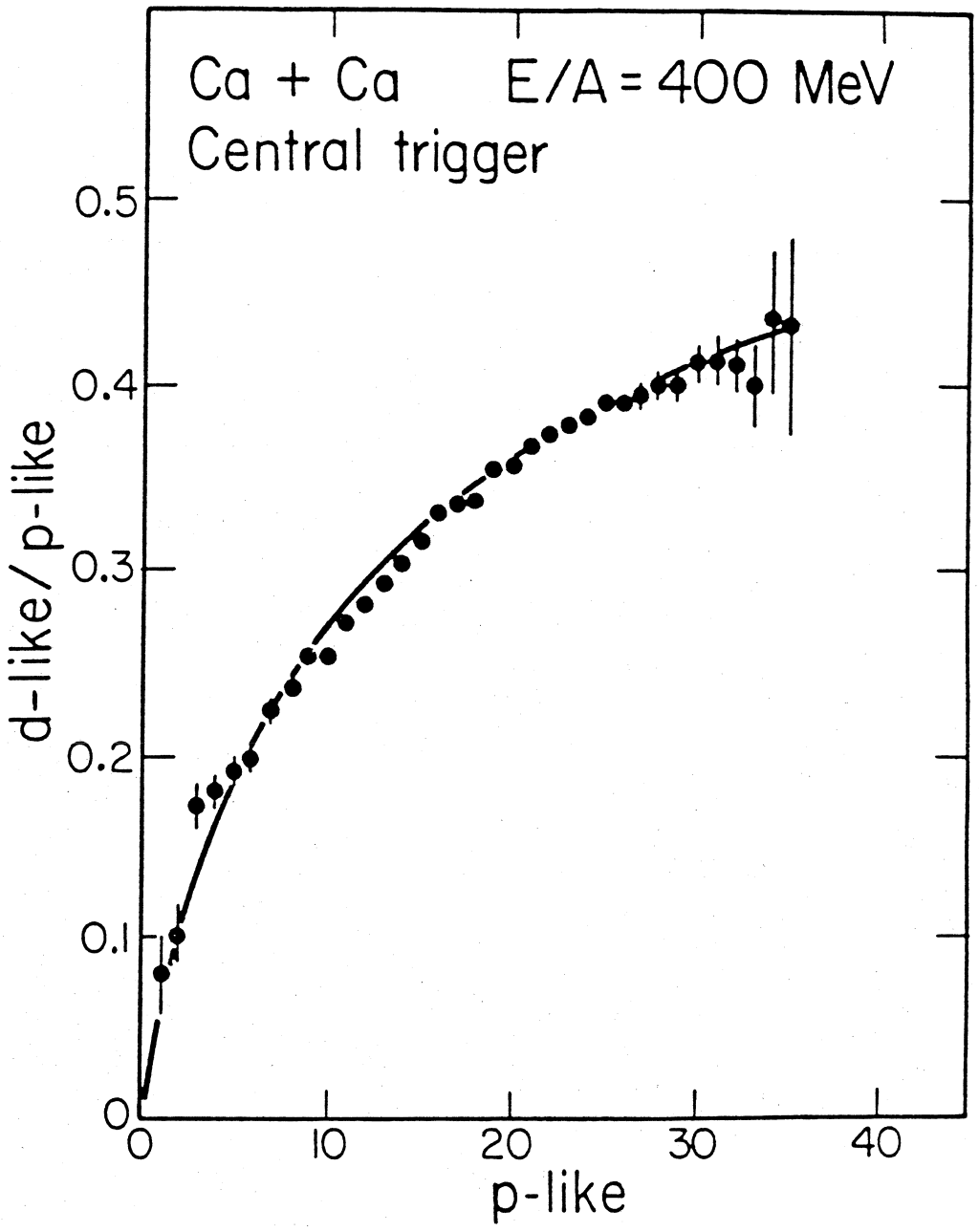

XBL 829 – 1162

FIGURE III.6

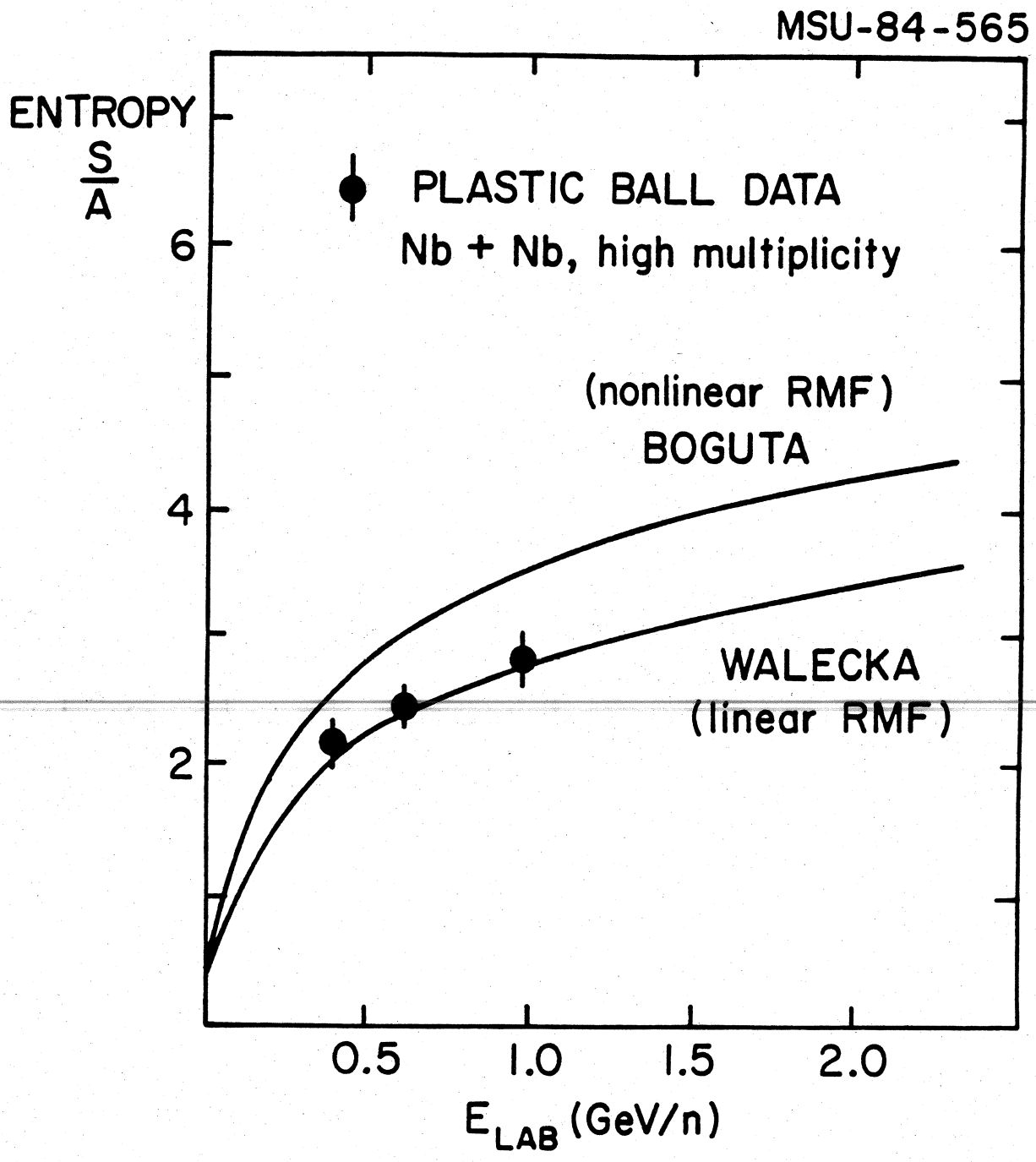
MSU-84-565
ENTROPY
S/A
PLASTIC BALL DATA
Nb + Nb, high multiplicity
(nonlinear RMF)
BOGUTA
WALECKA
(linear RMF)
6
4
2
0.5
1.0
1.5
2.0
E_LAB (GeV/n)

FIGURE III.7

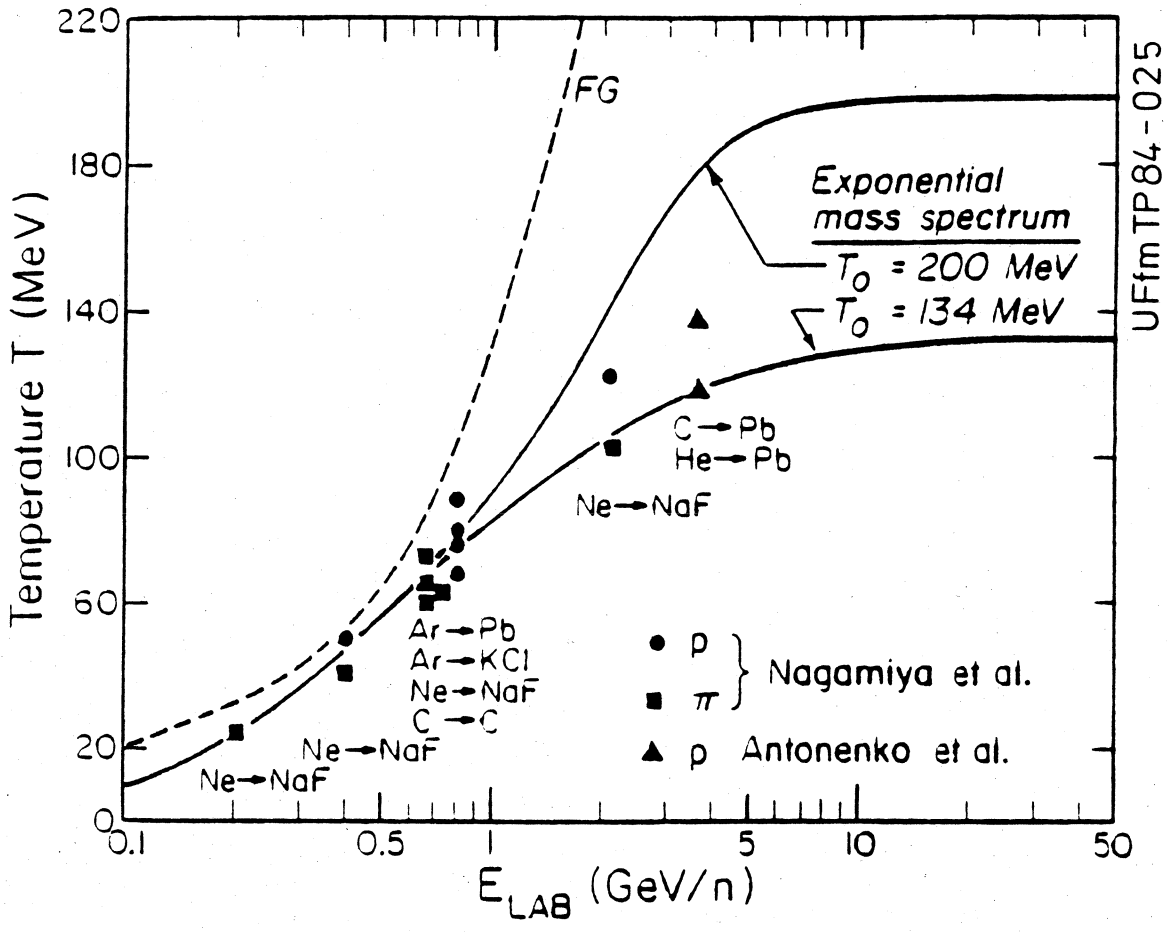
220
180
140
100
60
20
0
Temperature T (MeV)
FG
Exponential
mass spectrum
T_0 = 200 MeV
T_0 = 134 MeV
UFfm TP84-025
C → Pb
He → Pb
Ne → NaF
Ar → Pb
Ar → KCl
Ne → NaF
C → C
Ne → NaF
Ne → NaF
p
π
Nagamiya et al.
p Antonenko et al.
0.1
0.5
1
5
10
50
E_{LAB} (GeV/n)

FIGURE III.8

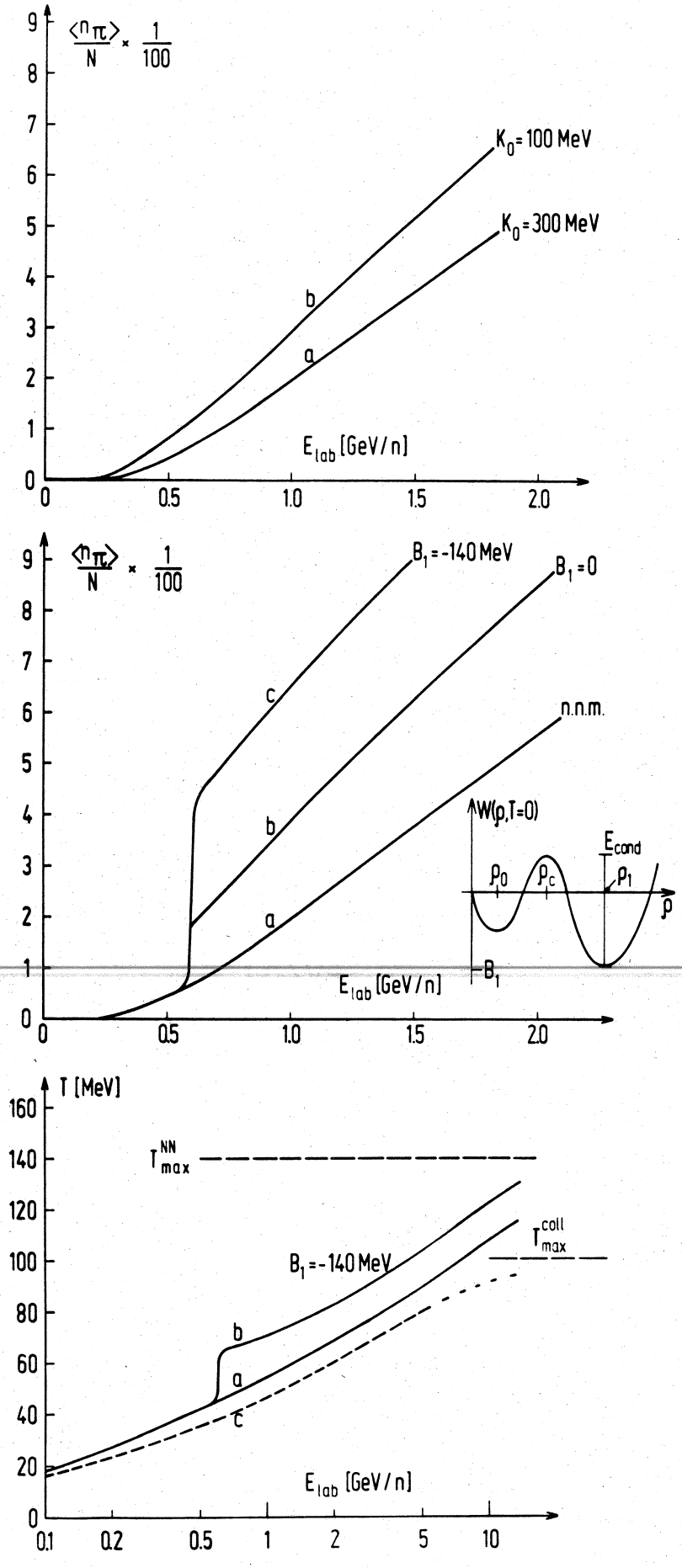
$\frac{\langle n_\pi \rangle}{N} \times \frac{1}{100}$
K_0= 100 MeV
K_0= 300 MeV
b
a
E_{lab} [GeV/n]
B_1 = -140 MeV
B_1 = 0
n.n.m.
c
b
a
W(ρ,T=0)
E_{cond}
ρ_0
ρ_c
ρ_1
ρ
$-B_1$
E_{lab} [GeV/n]
T [MeV]
T^{NN}_{max}
T^{coll}_{max}
B_1 = -140 MeV
b
a
c
E_{lab} [GeV/n]

FIGURE III.9

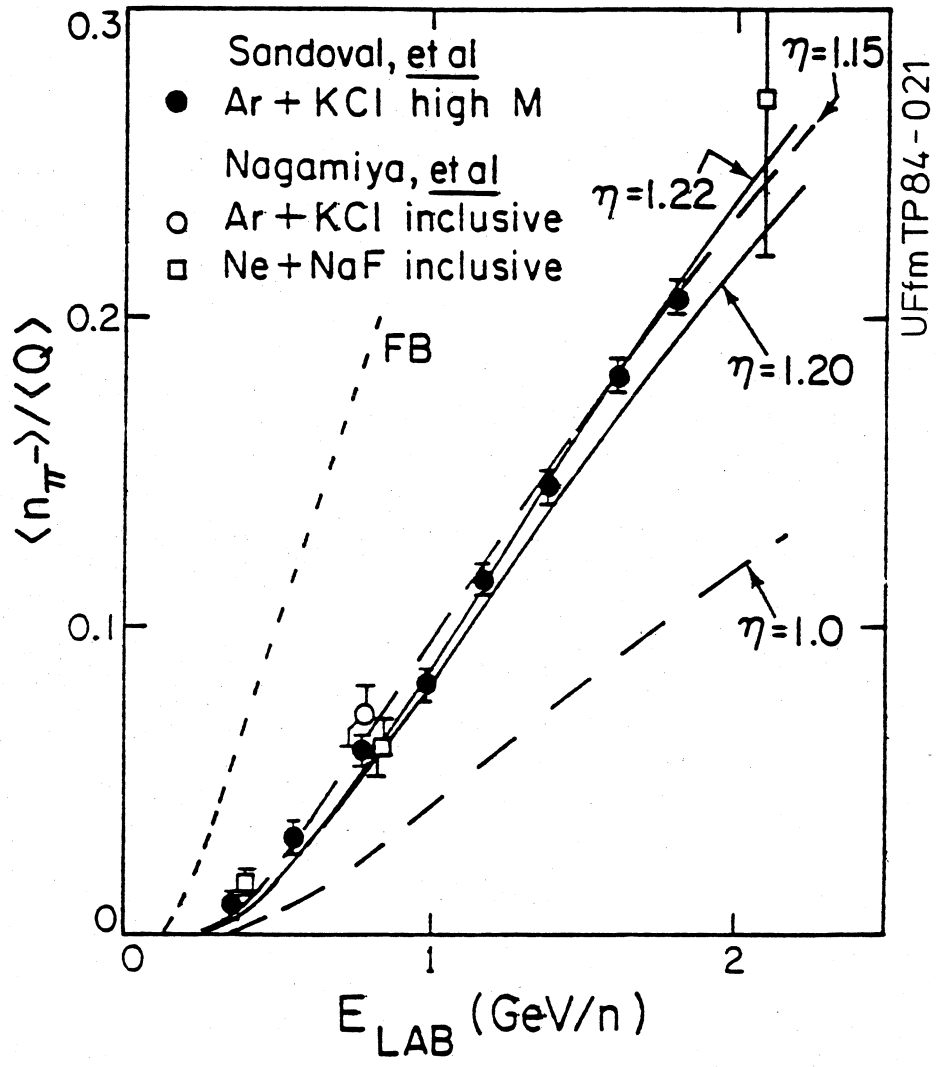

FIGURE III.10

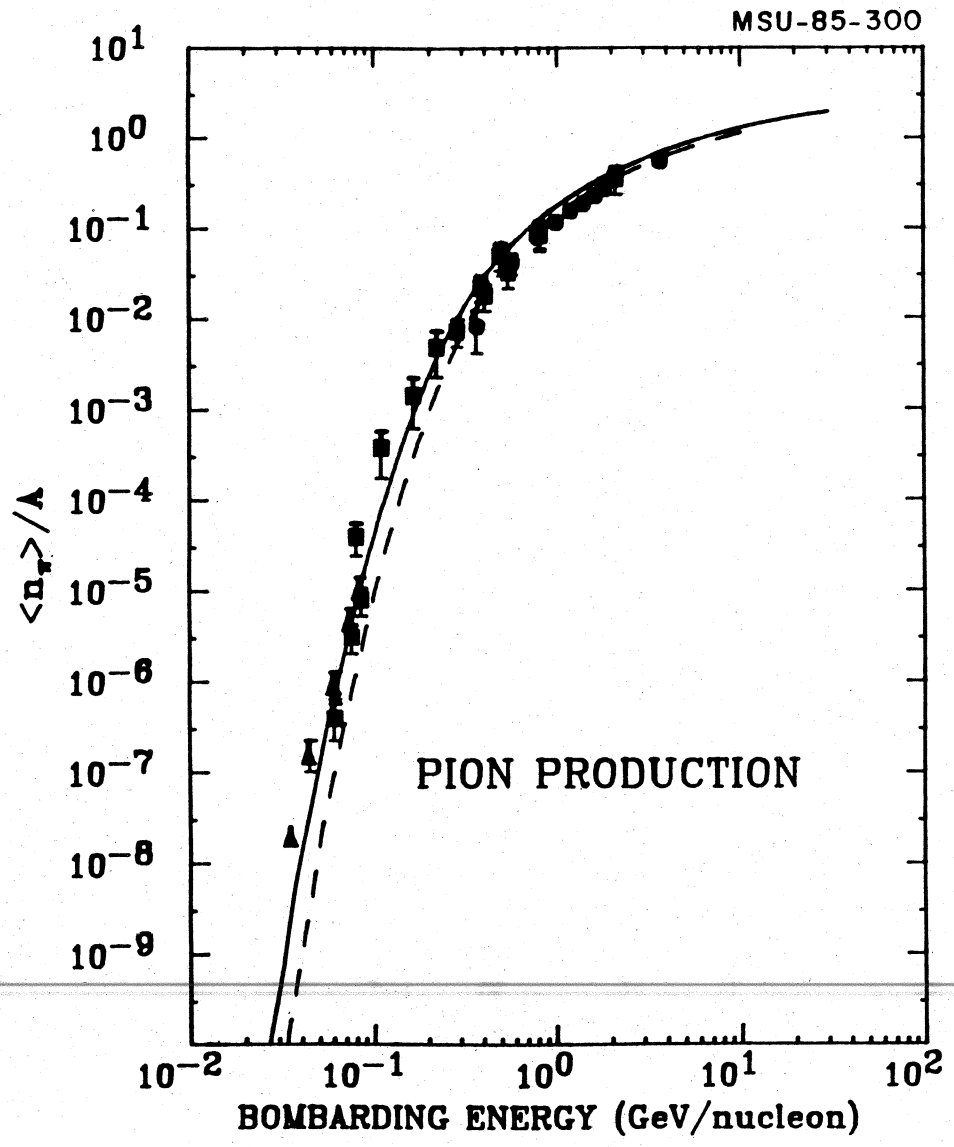

FIGURE III.11

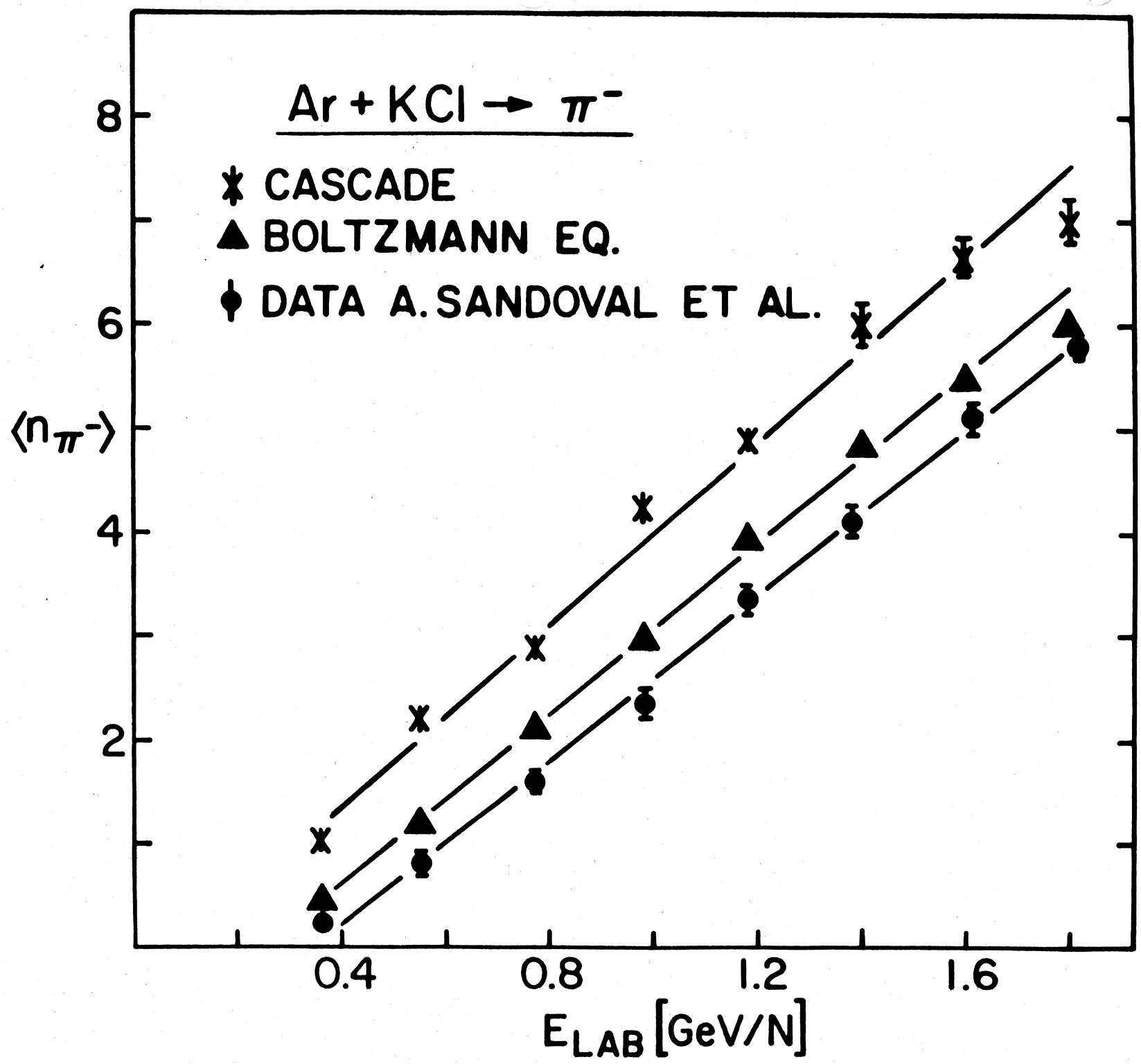

FIGURE III.12

MSU-85-244

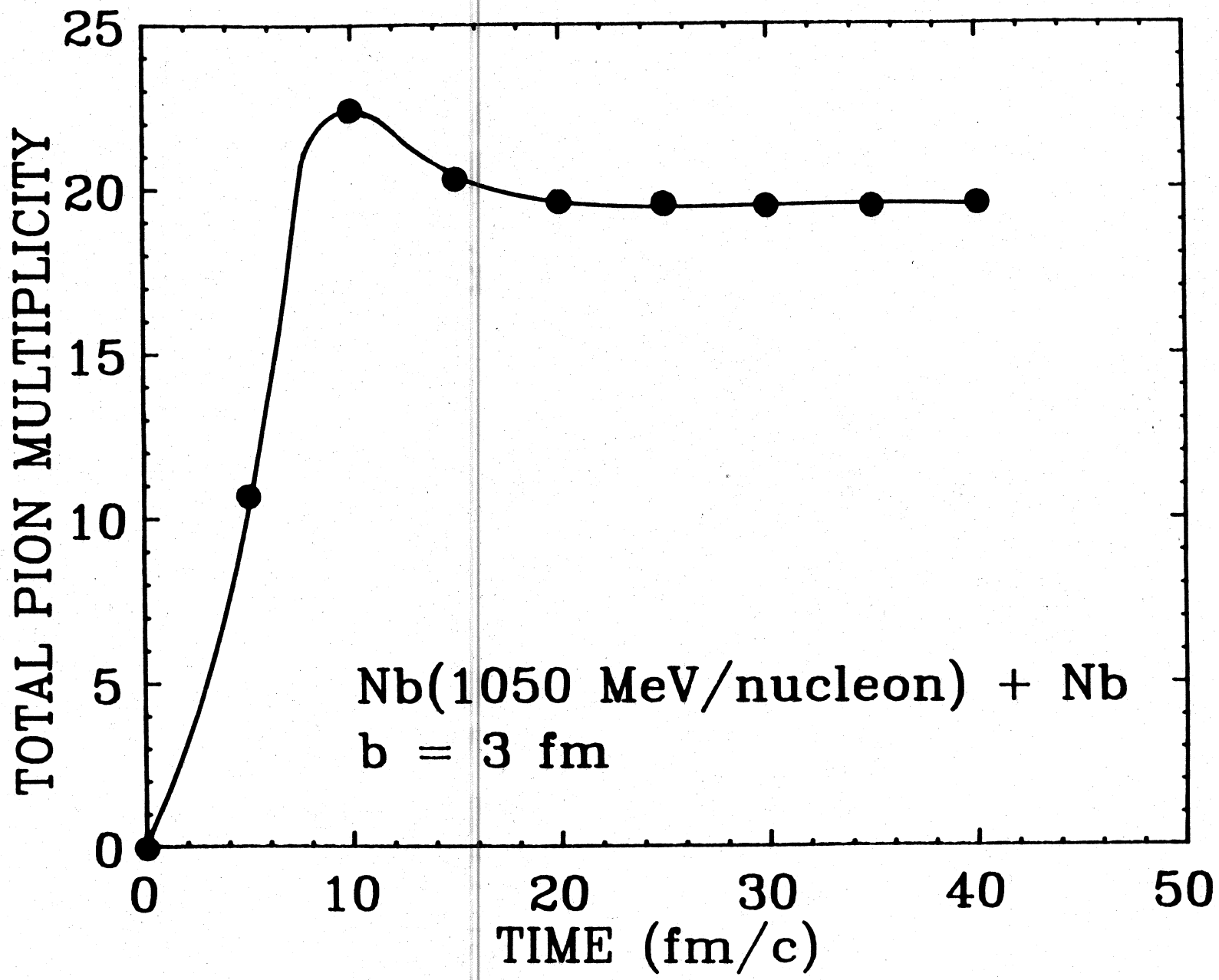

FIGURE III.13a

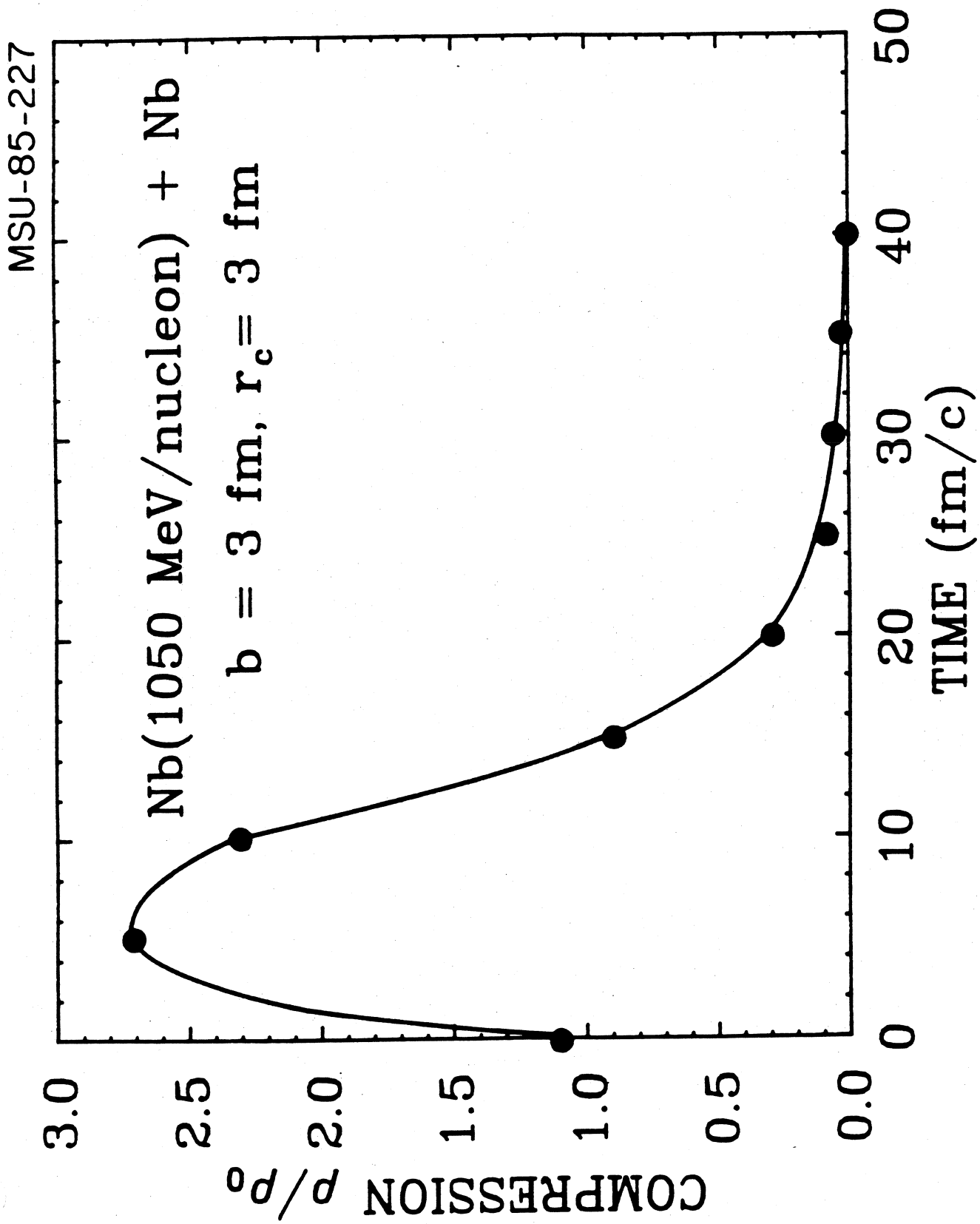

FIGURE III.13b

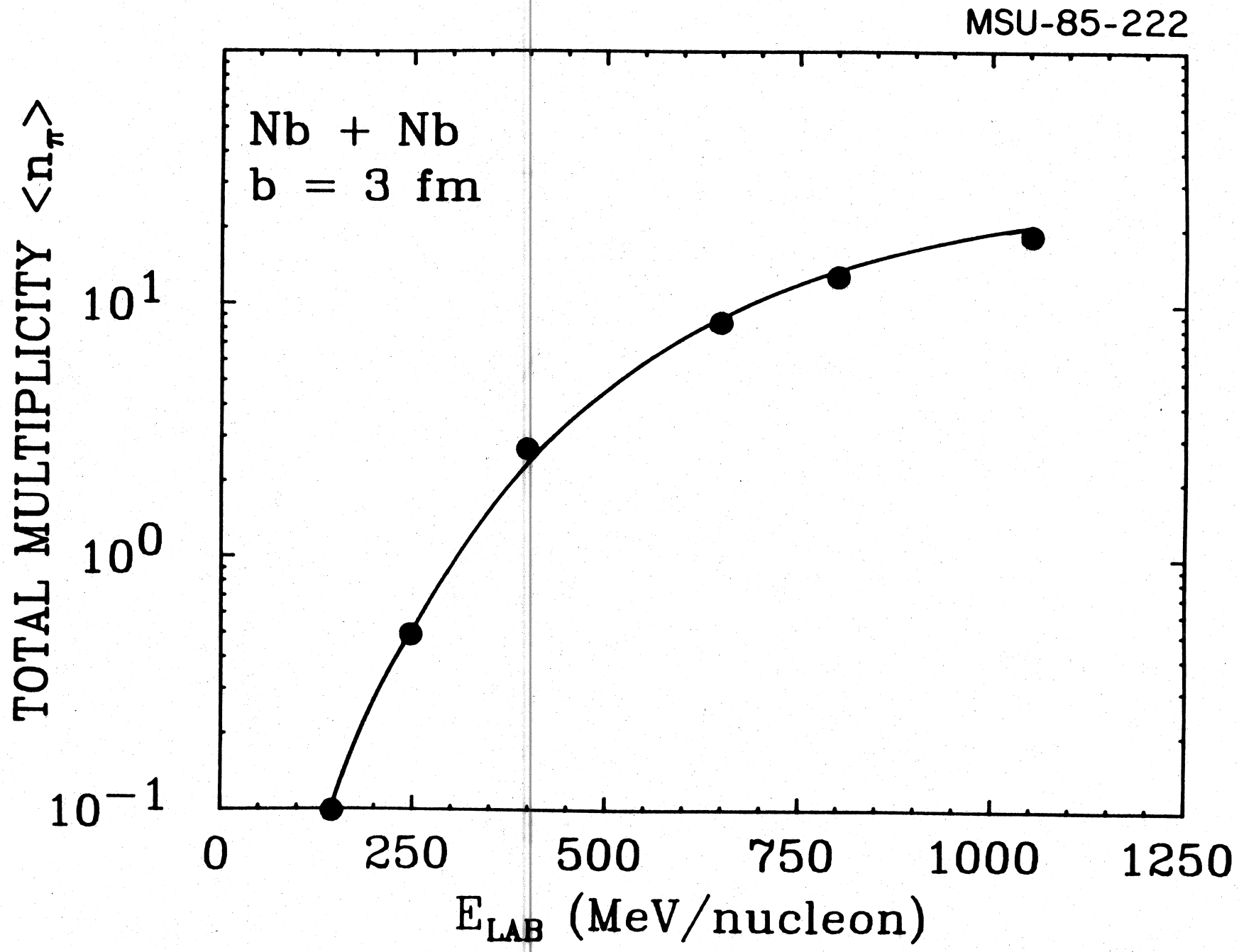

FIGURE III.14a

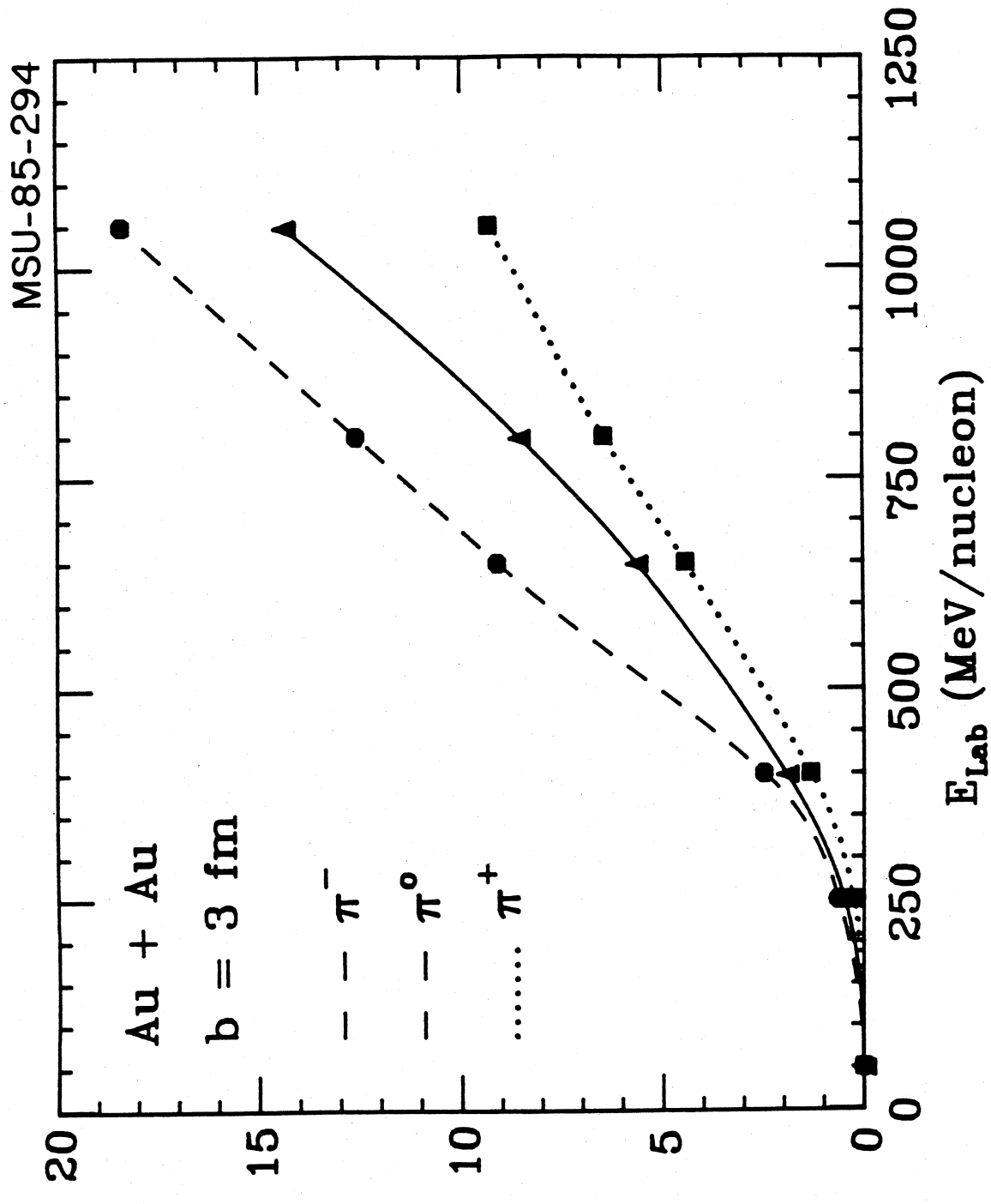

FIGURE III.14b

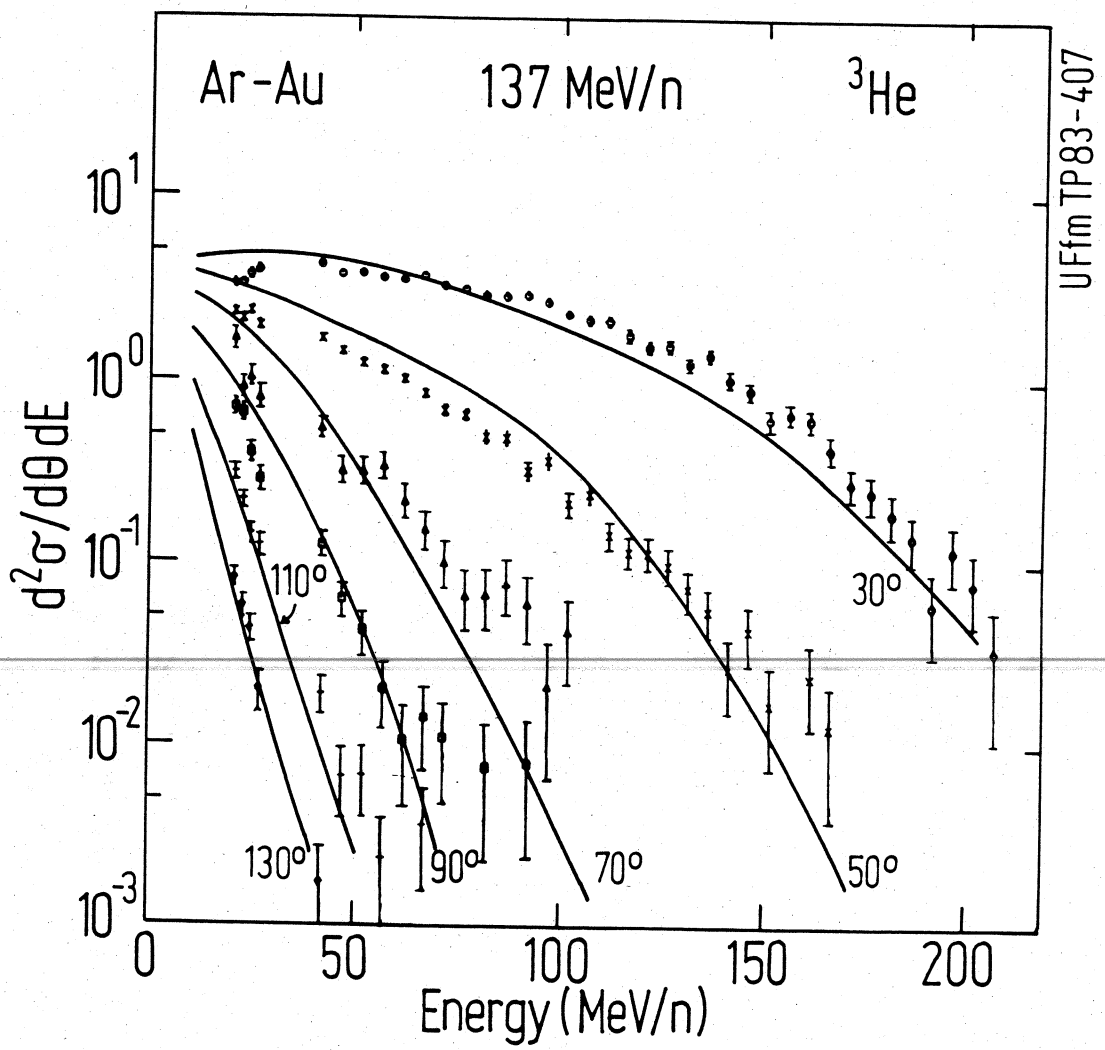

FIGURE III.15 (left)

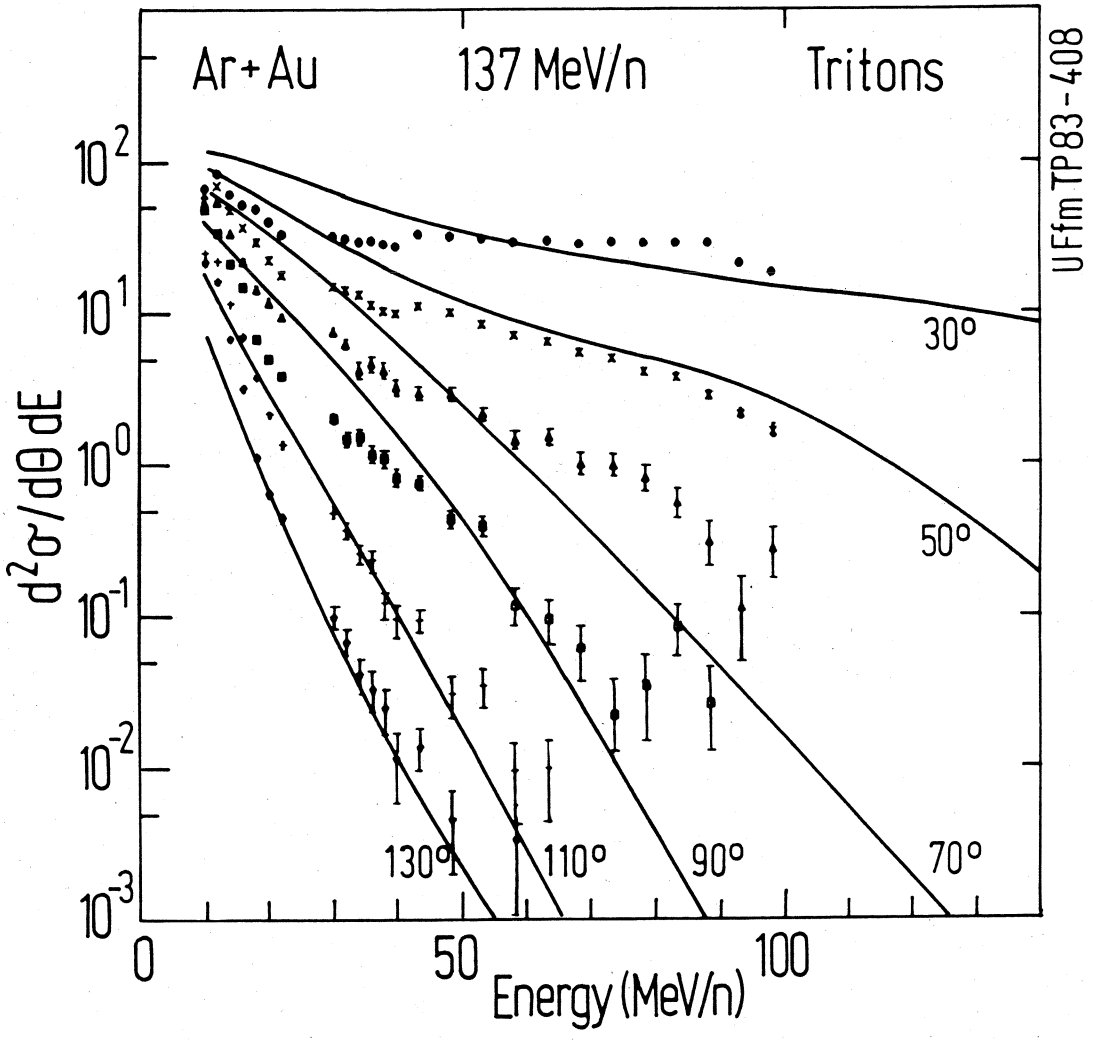

FIGURE III.15 (right)

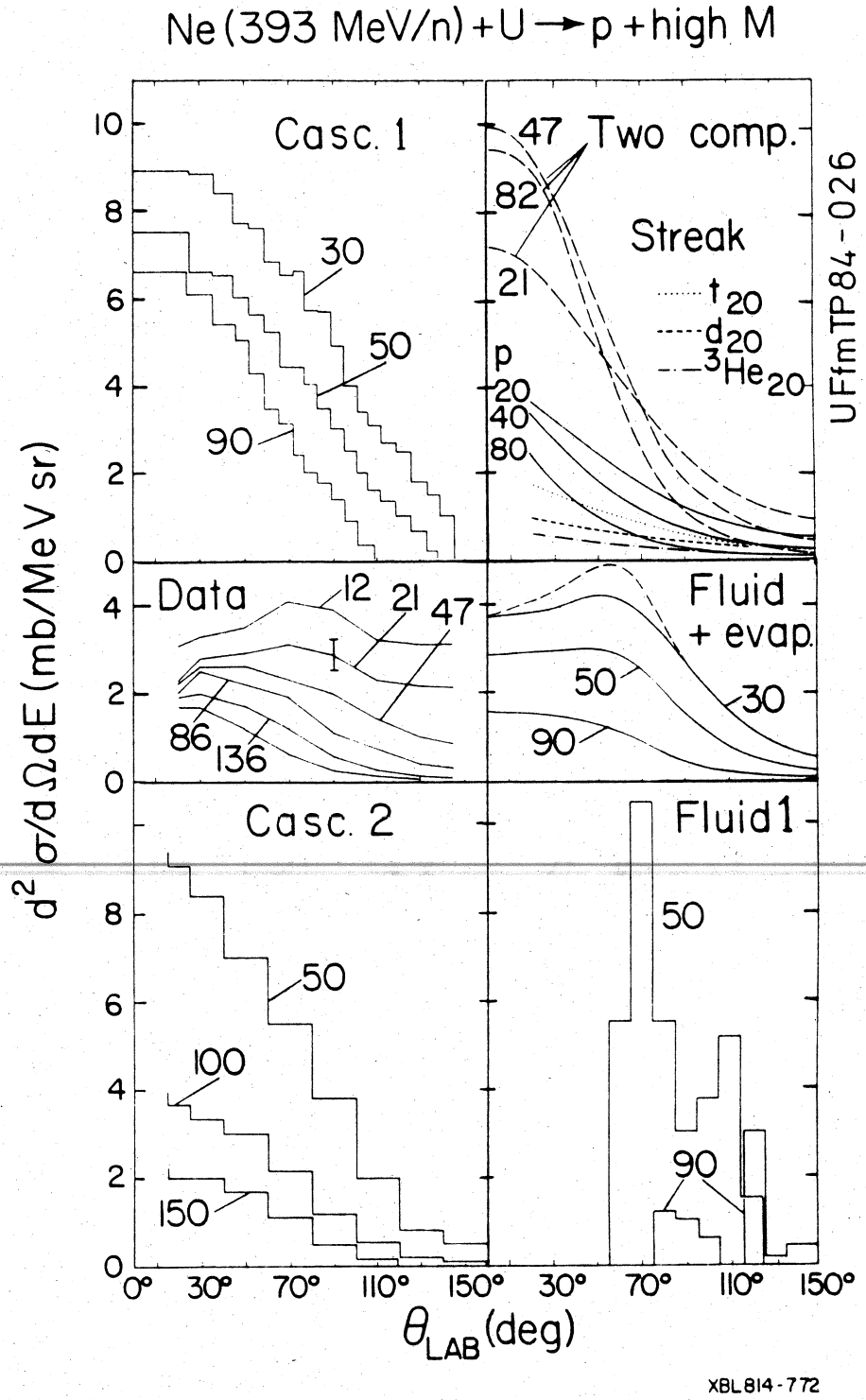

FIGURE III.16

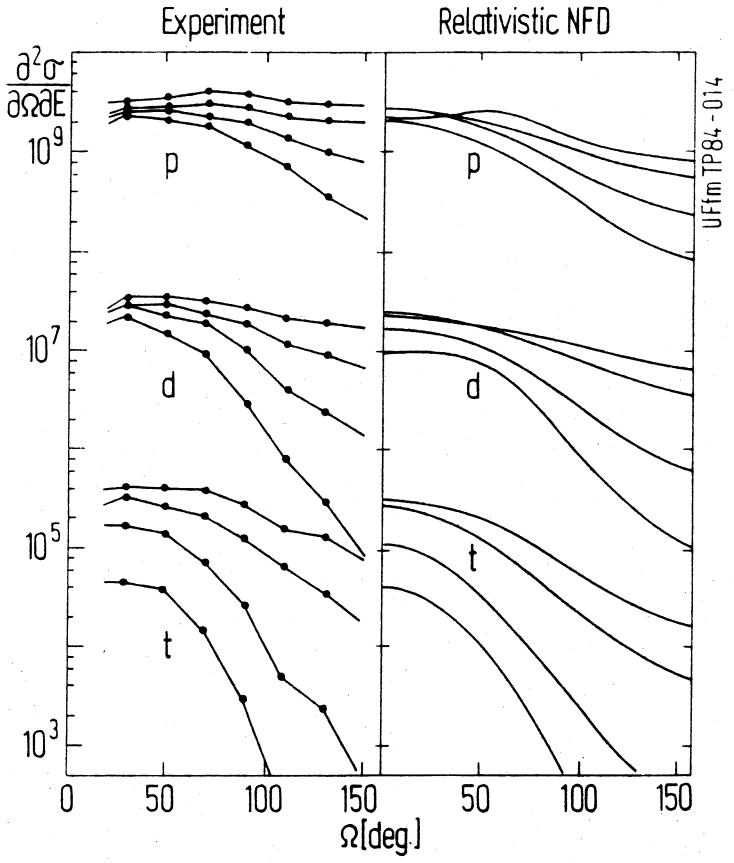

FIGURE III.17

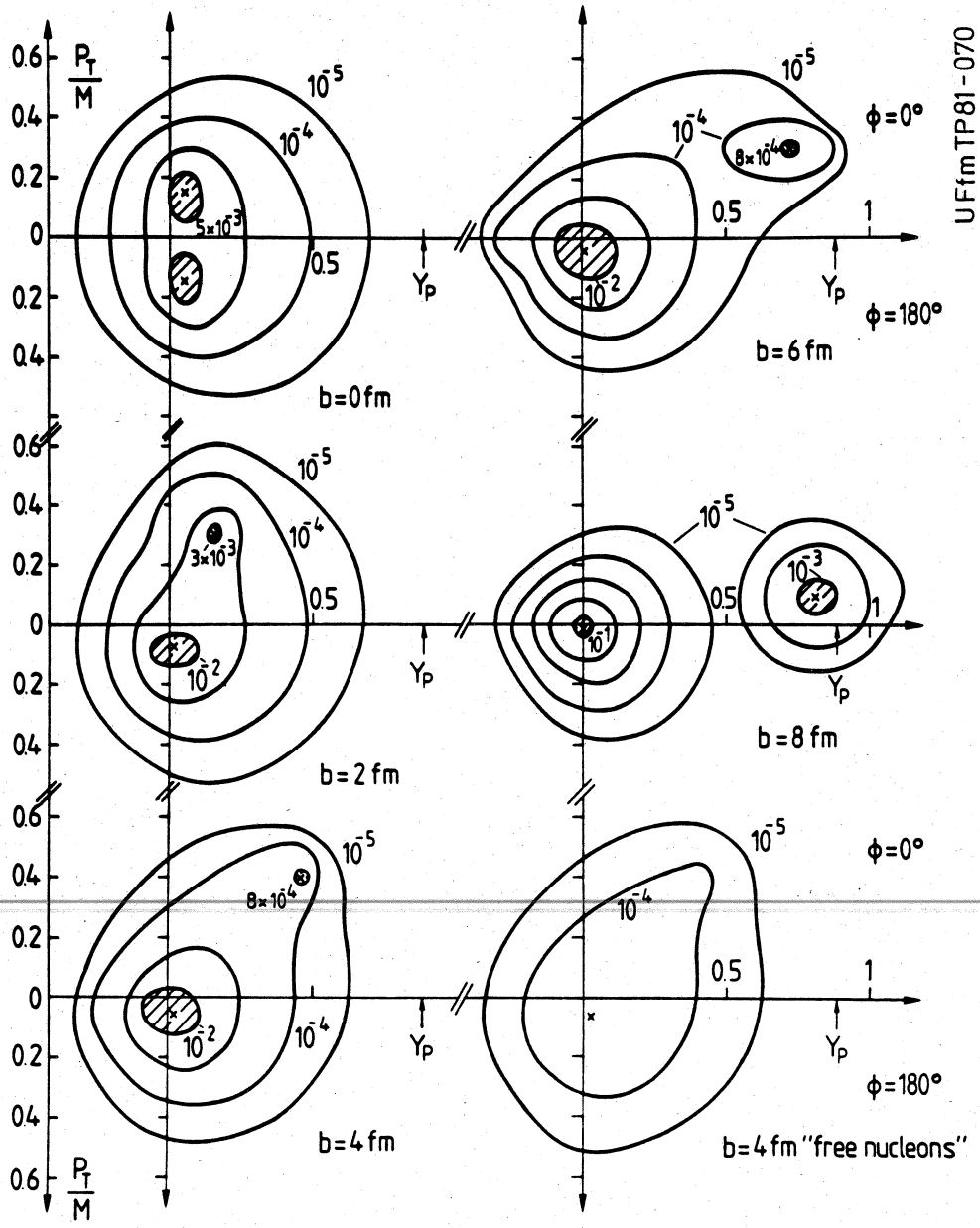

FIGURE III.18

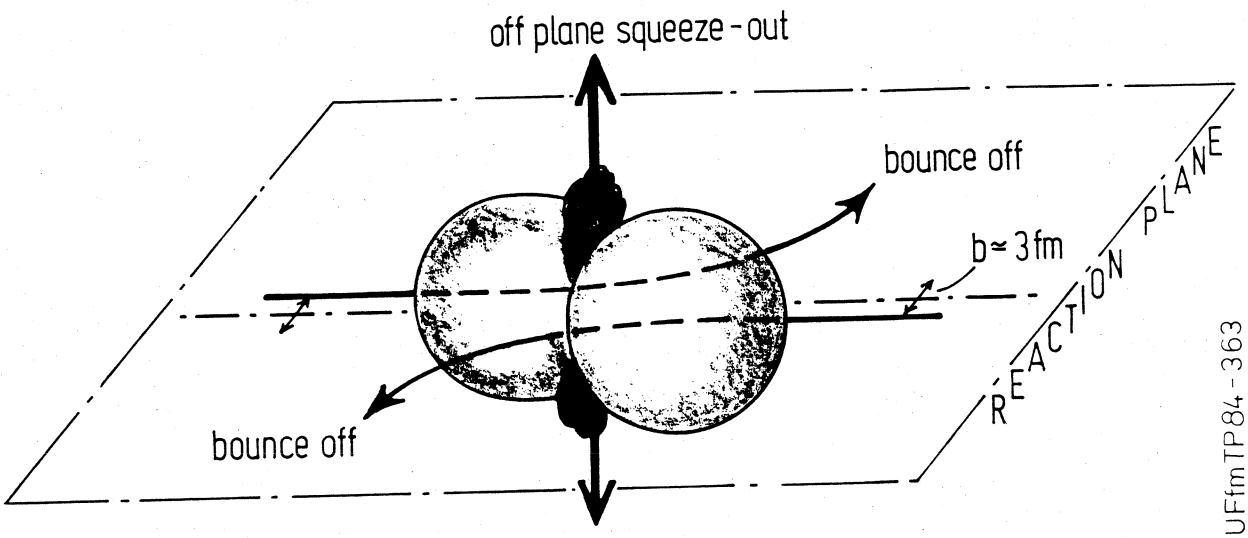

FIGURE III.19

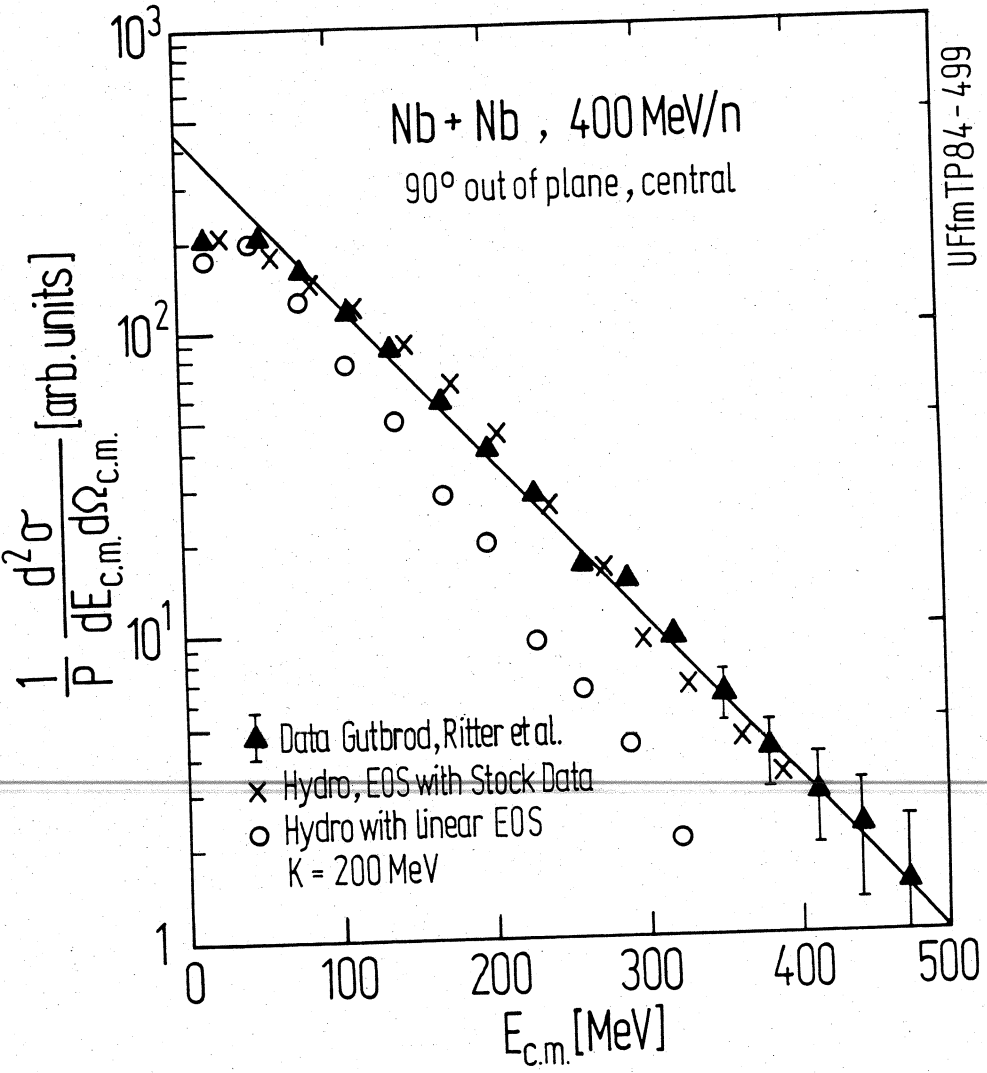

FIGURE III.20

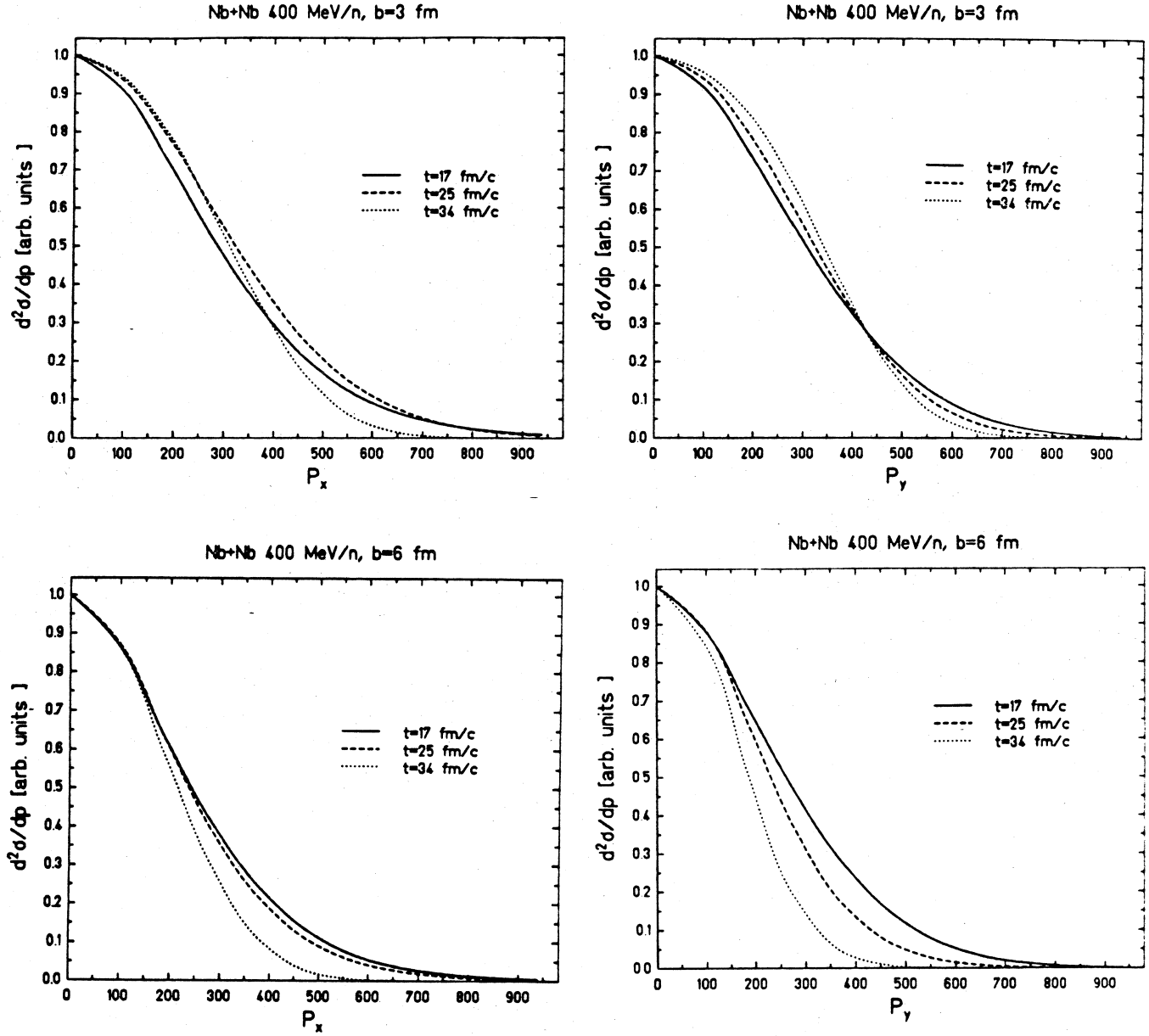

FIGURE III.21

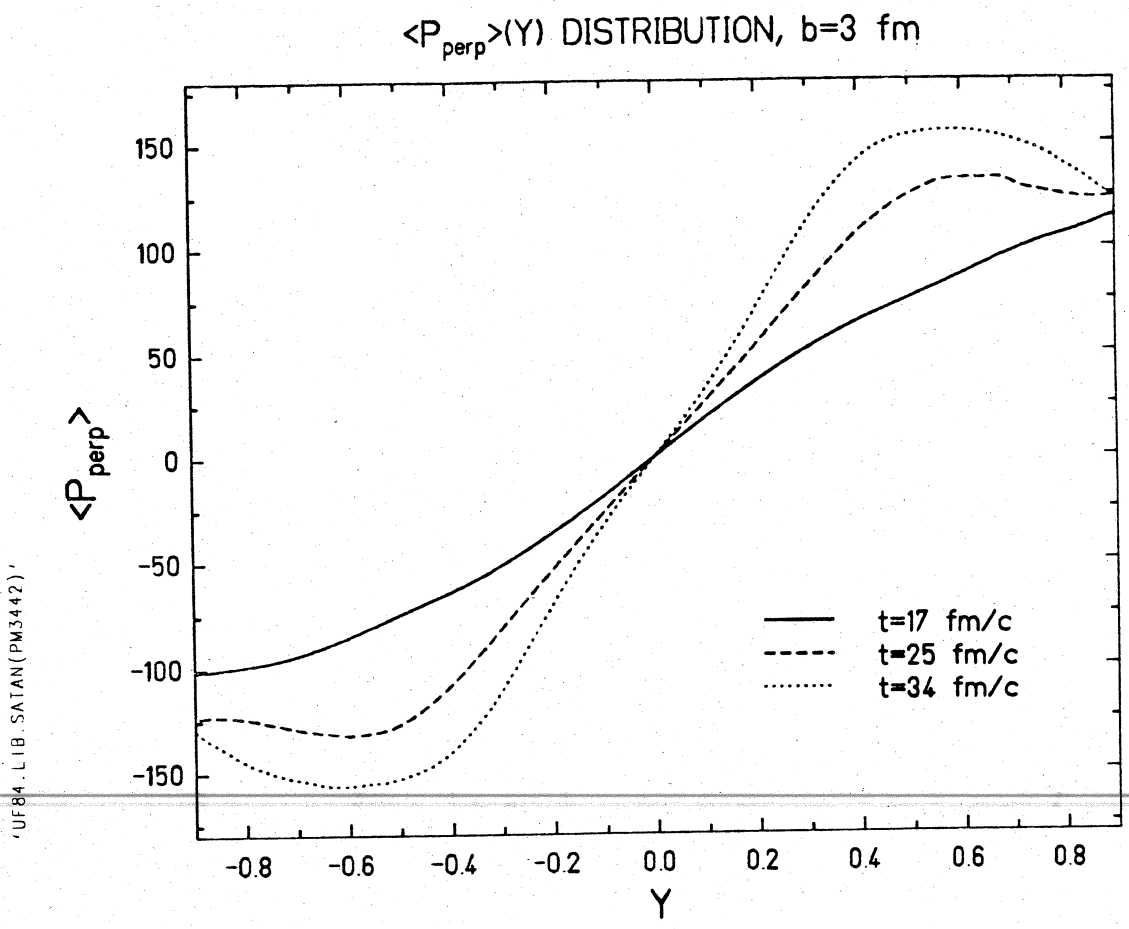

'UF84.LIB.SATAN(PM3442)'

FIGURE III.22

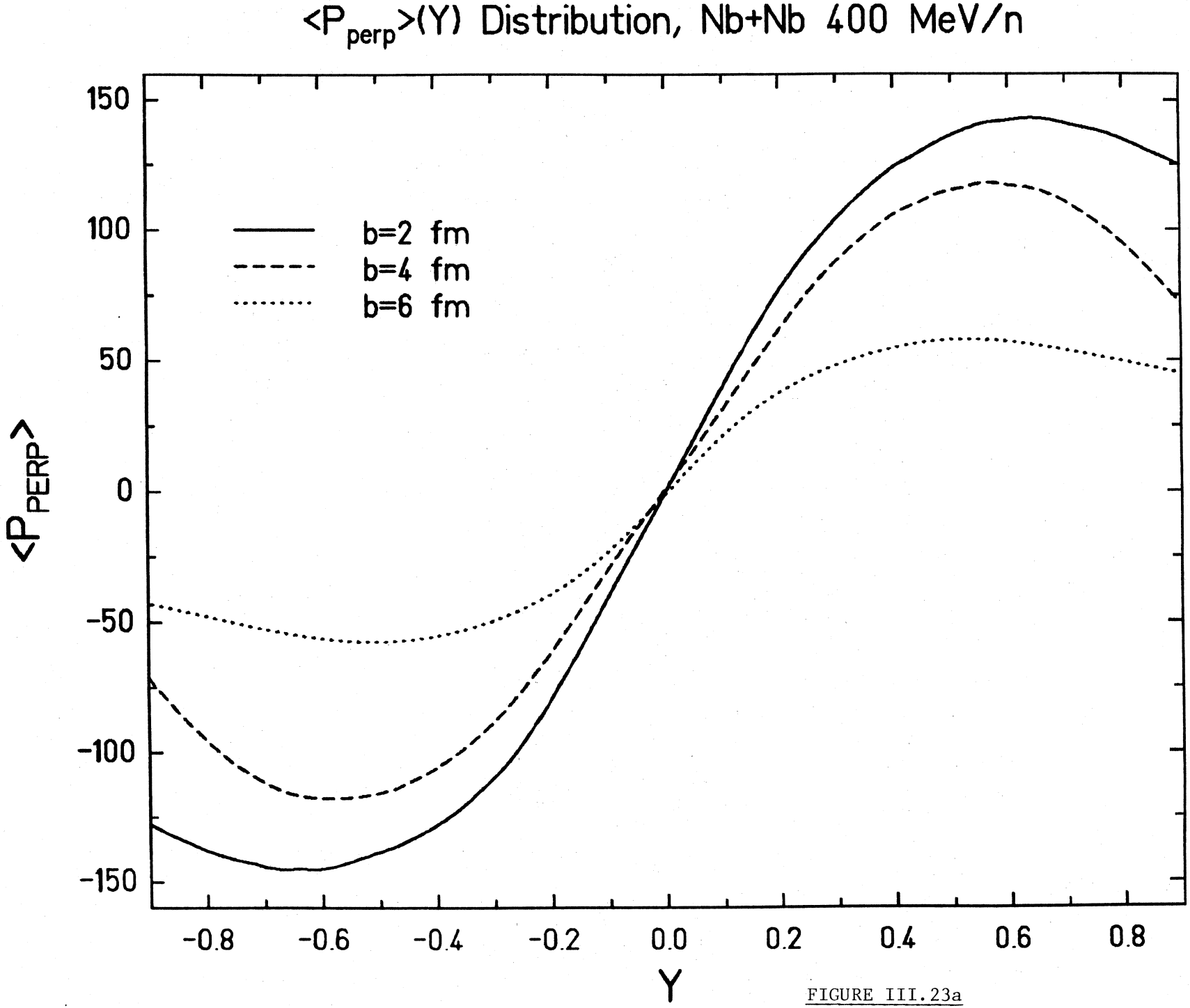

FIGURE III.23a

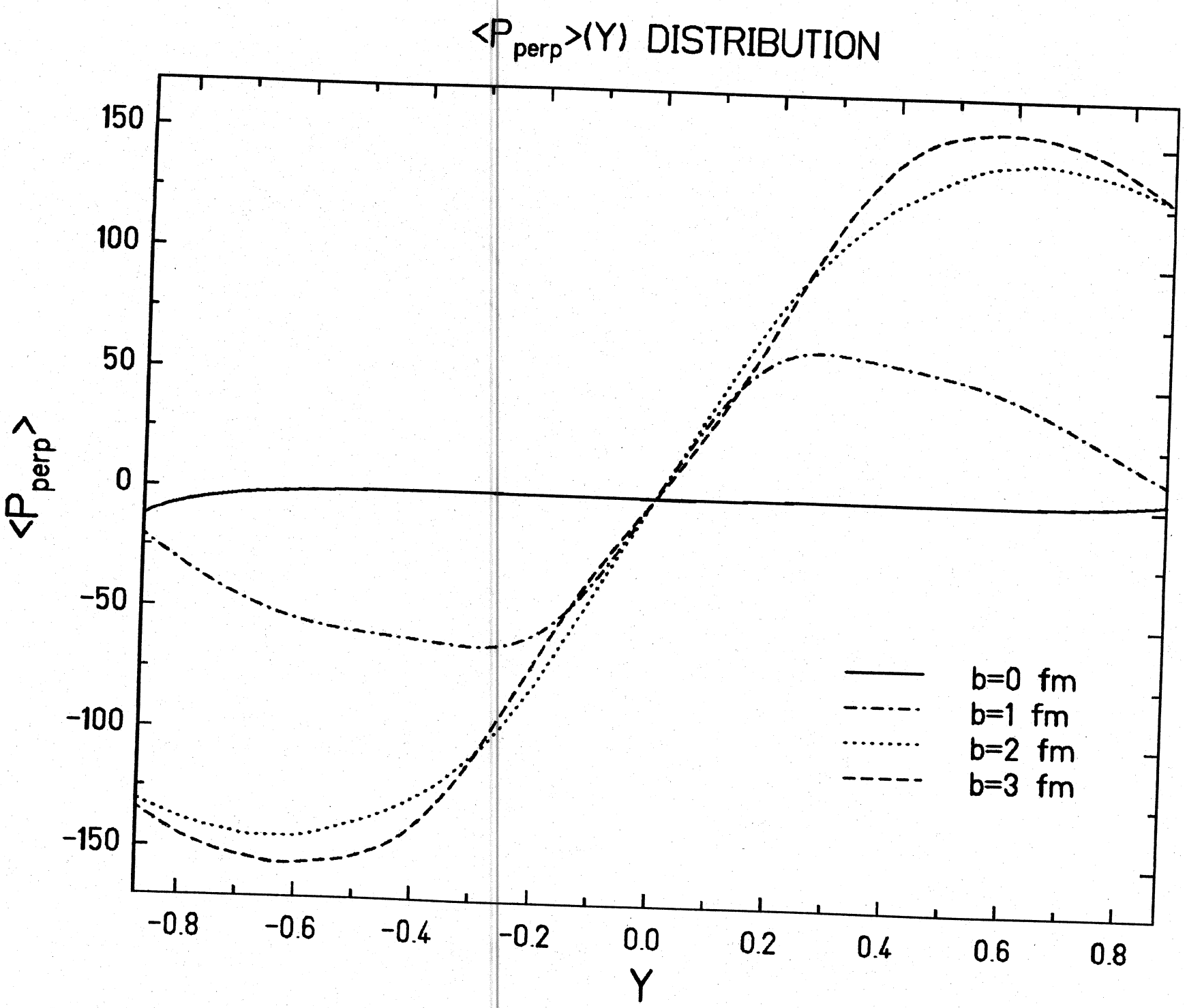
<P_perp>(Y) DISTRIBUTION
<P_perp>
150
100
50
0
-50
-100
-150
-0.8
-0.6
-0.4
-0.2
0.0
0.2
0.4
0.6
0.8
Y
b=0 fm
b=1 fm
b=2 fm
b=3 fm

FIGUR II.23b

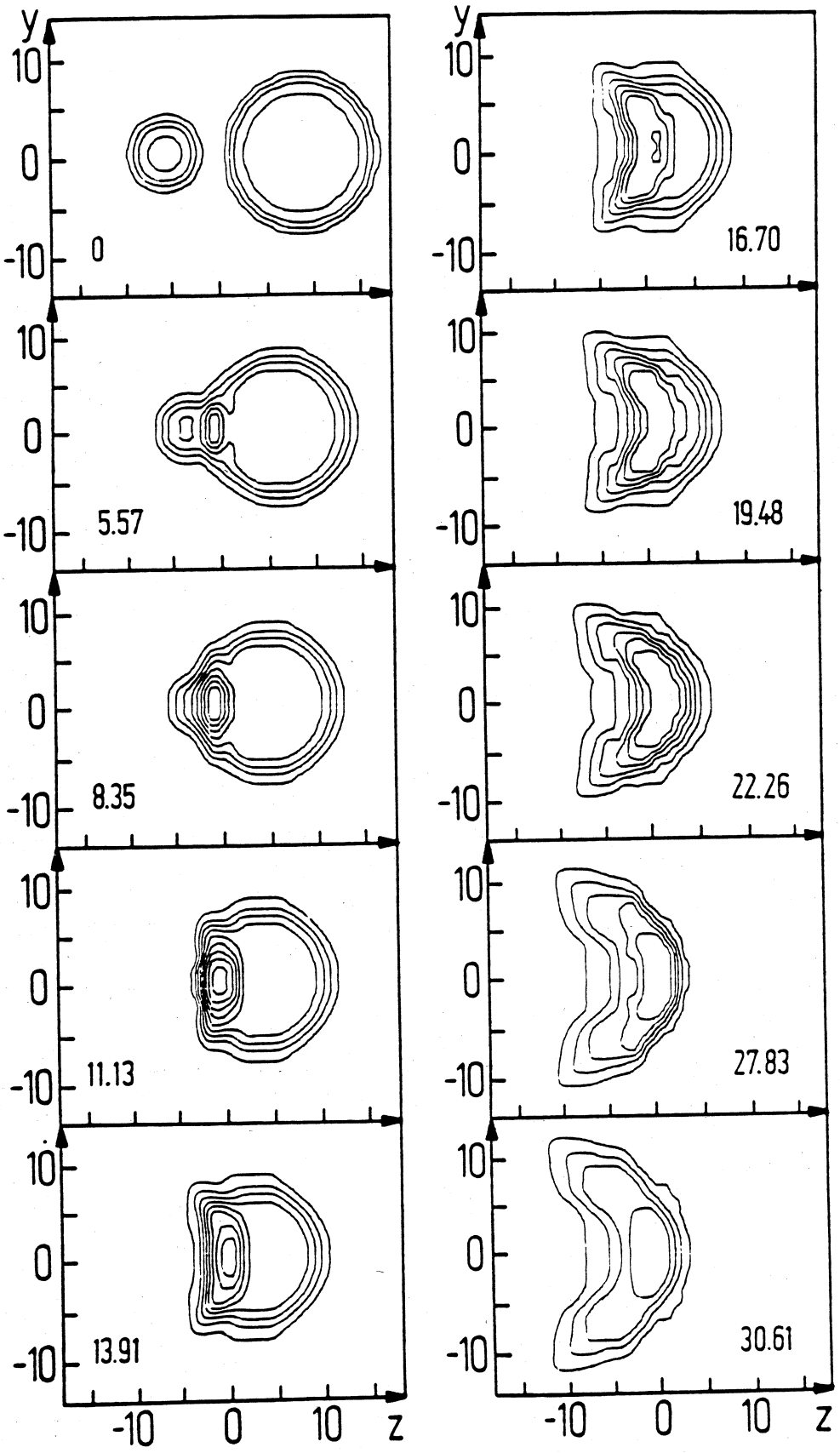

FIGURE III.24

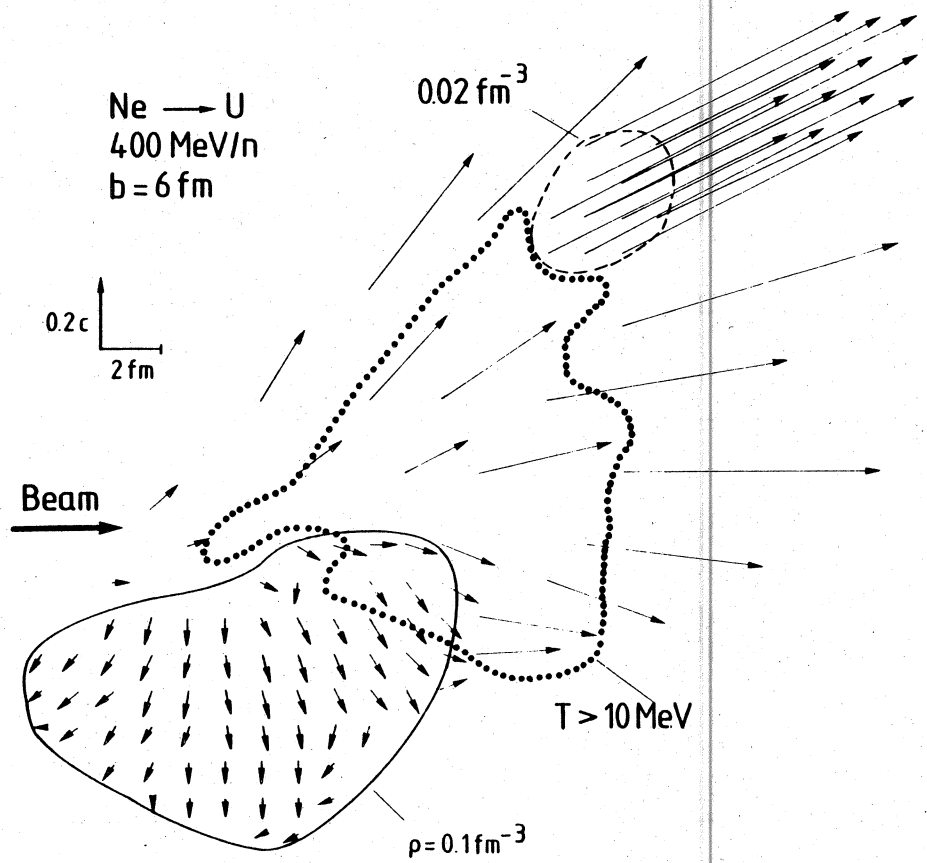

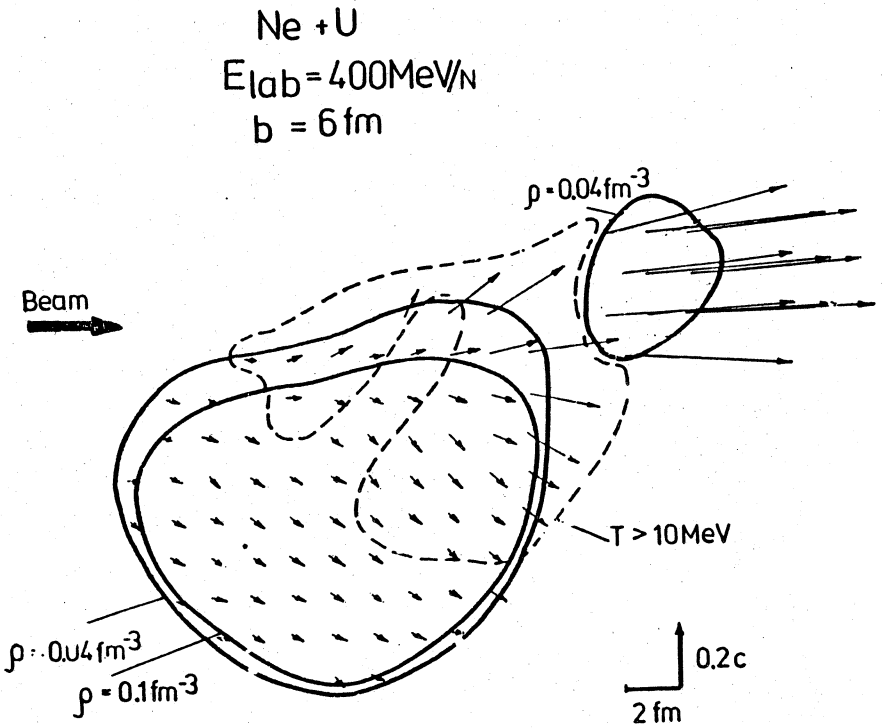

FIGURE III.25

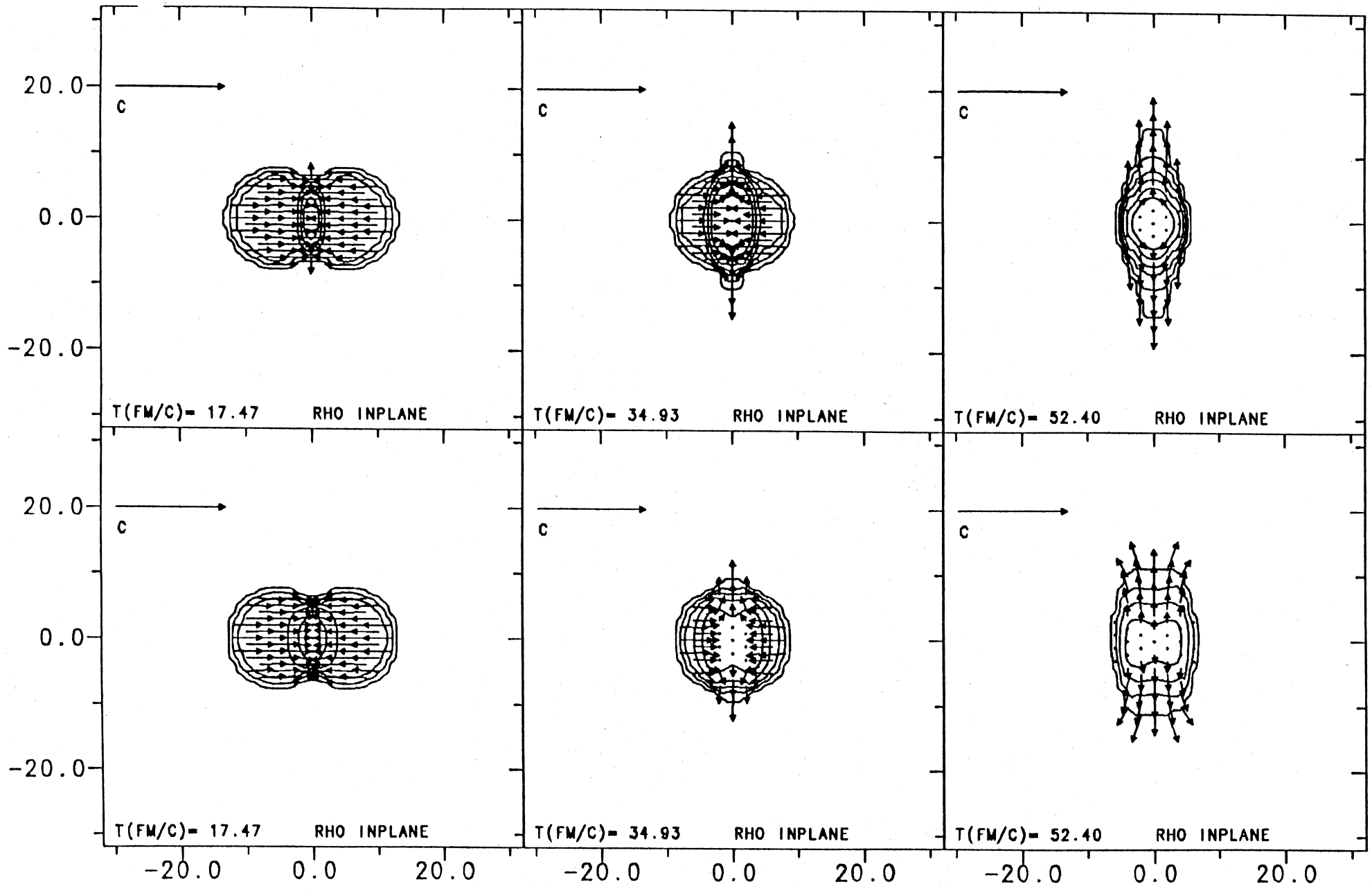

U->U E=100MEV(NR) CN=200 B=0, ETA=0, 40 PLOT BY GFHG 11.05.83

FIGURE III.26

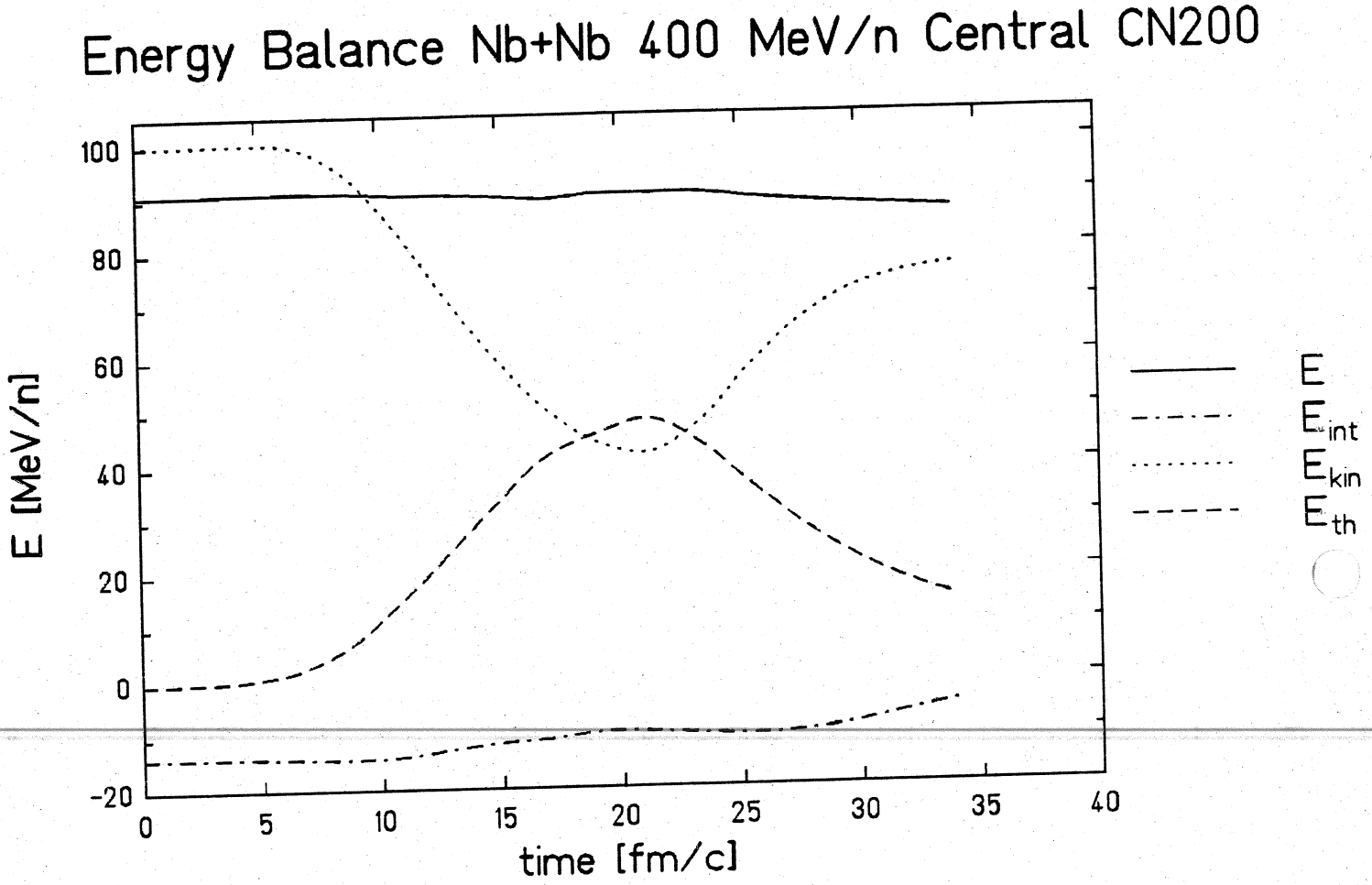

FIGURE III.27

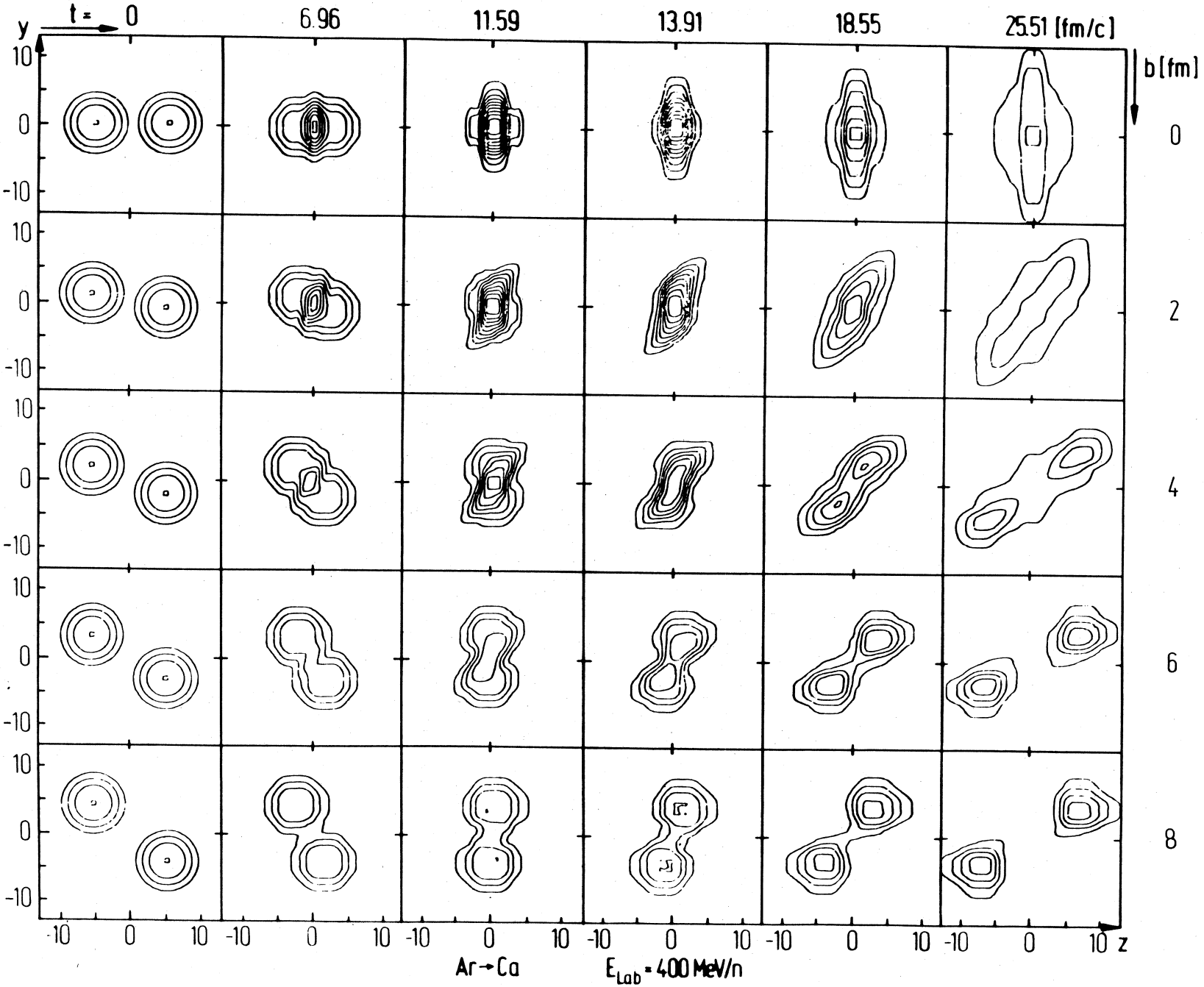

FIGURE III.28

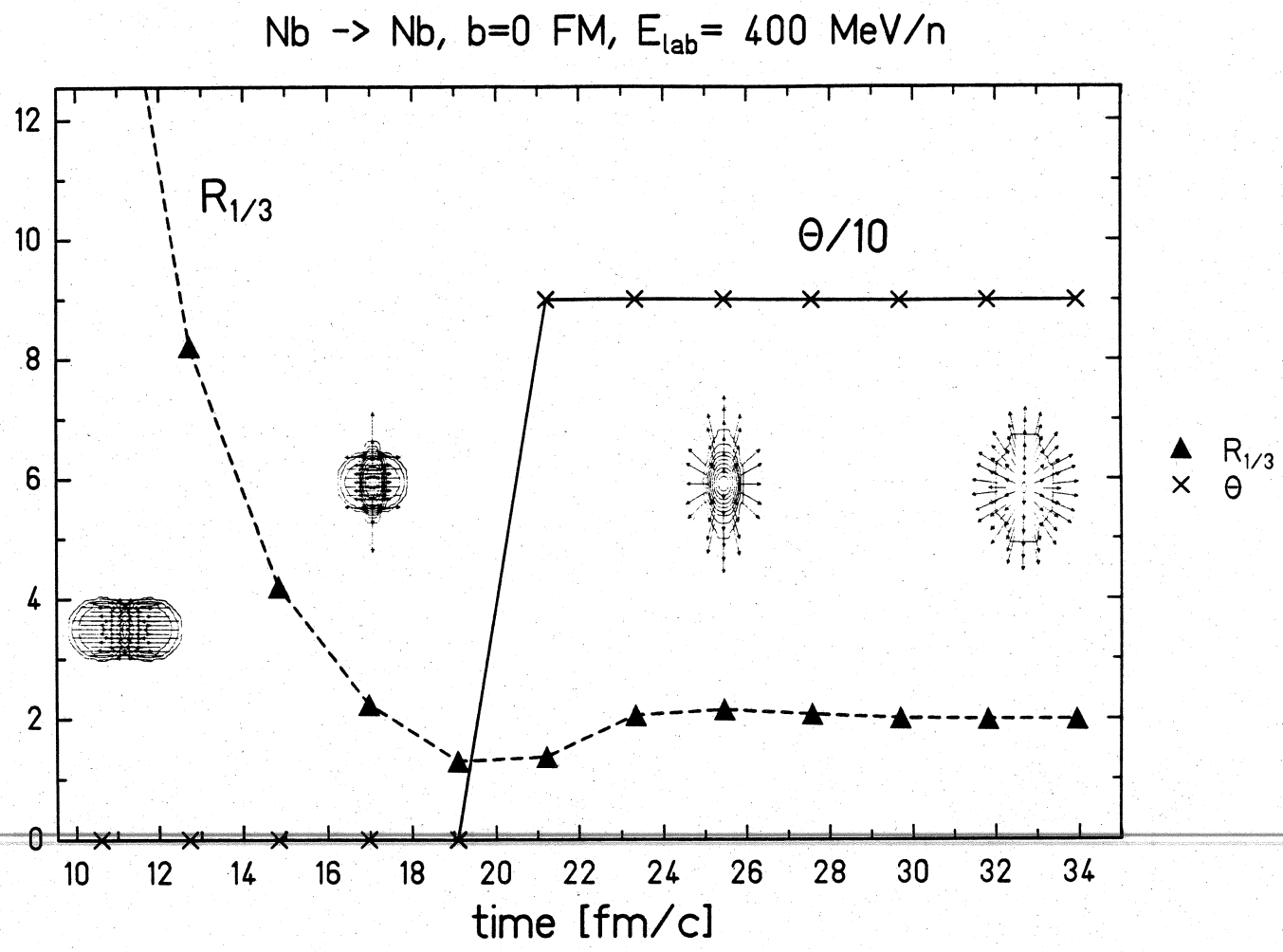

FIGURE III.29

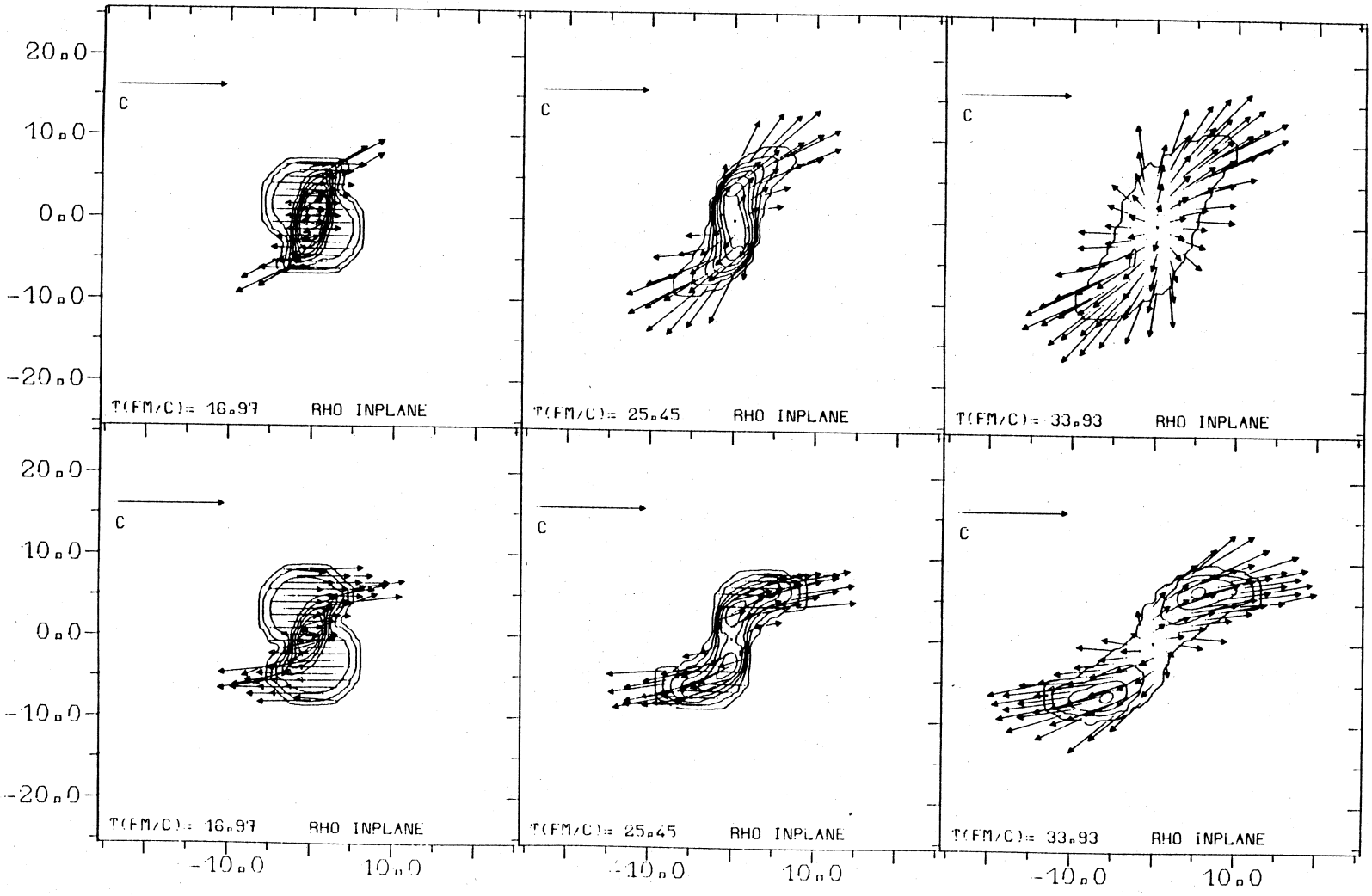

FIGURE III.30

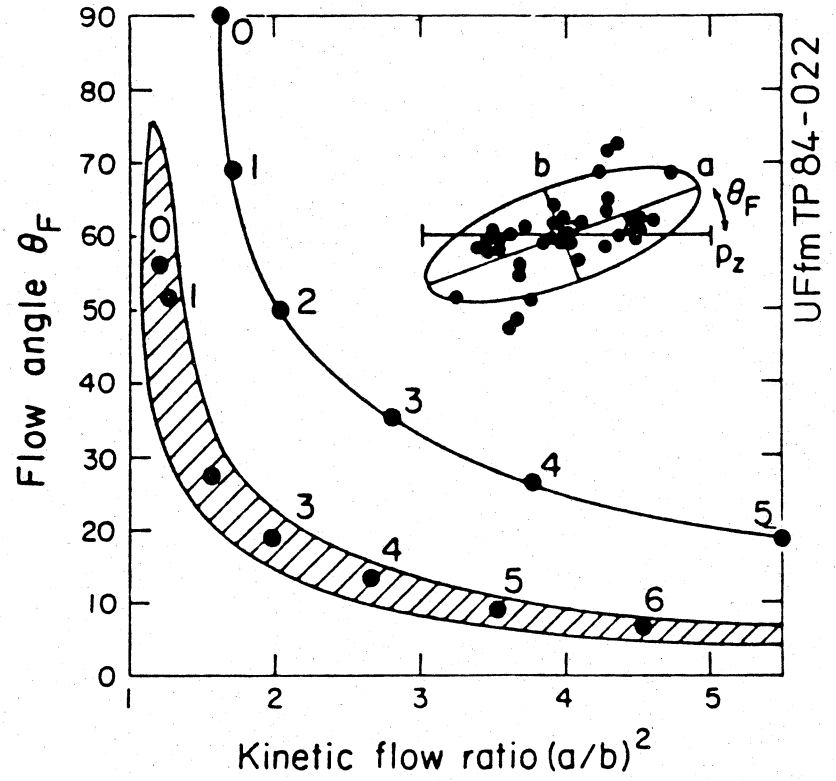

FIGURE III.31

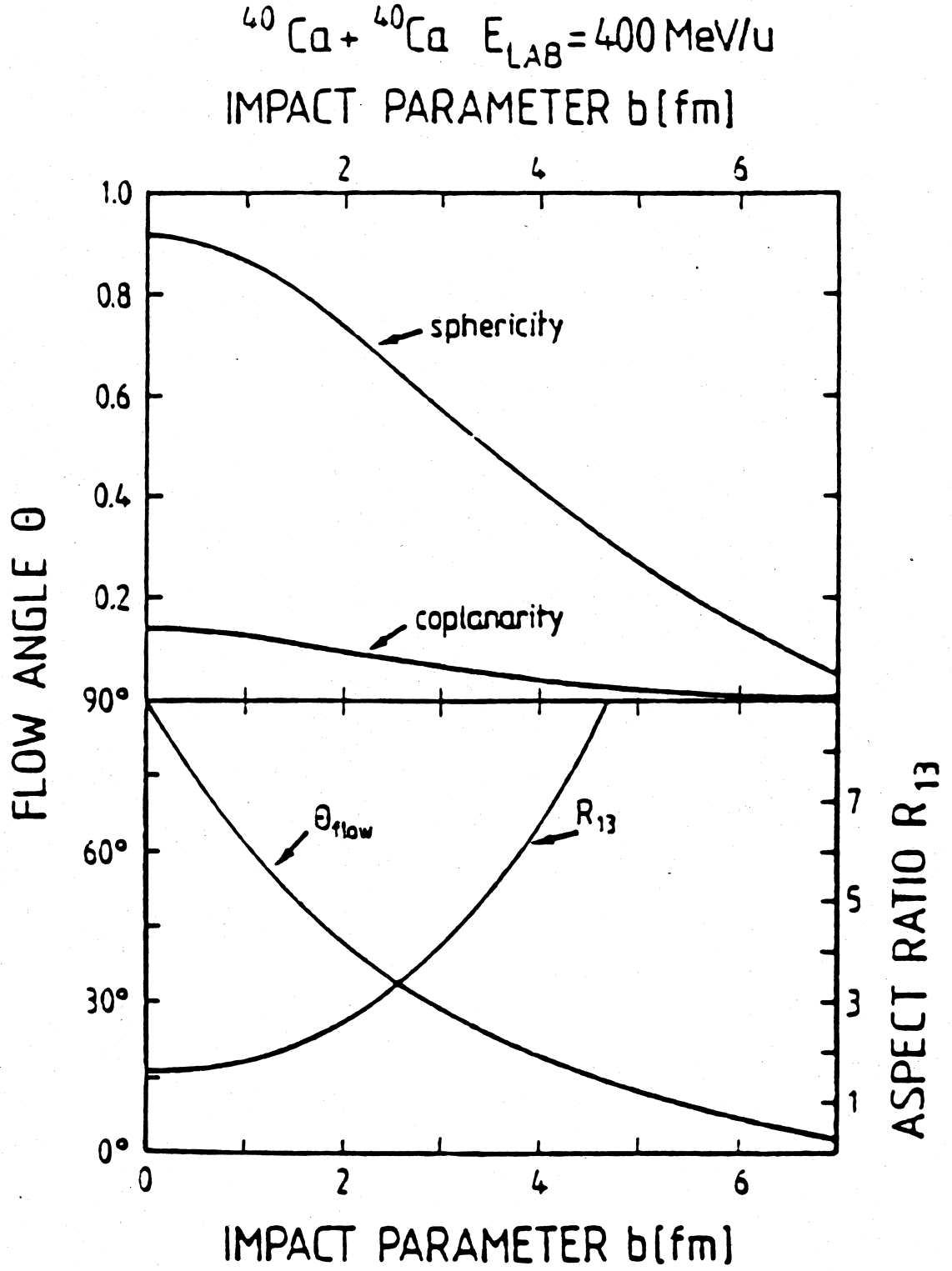

FIGURE III.32

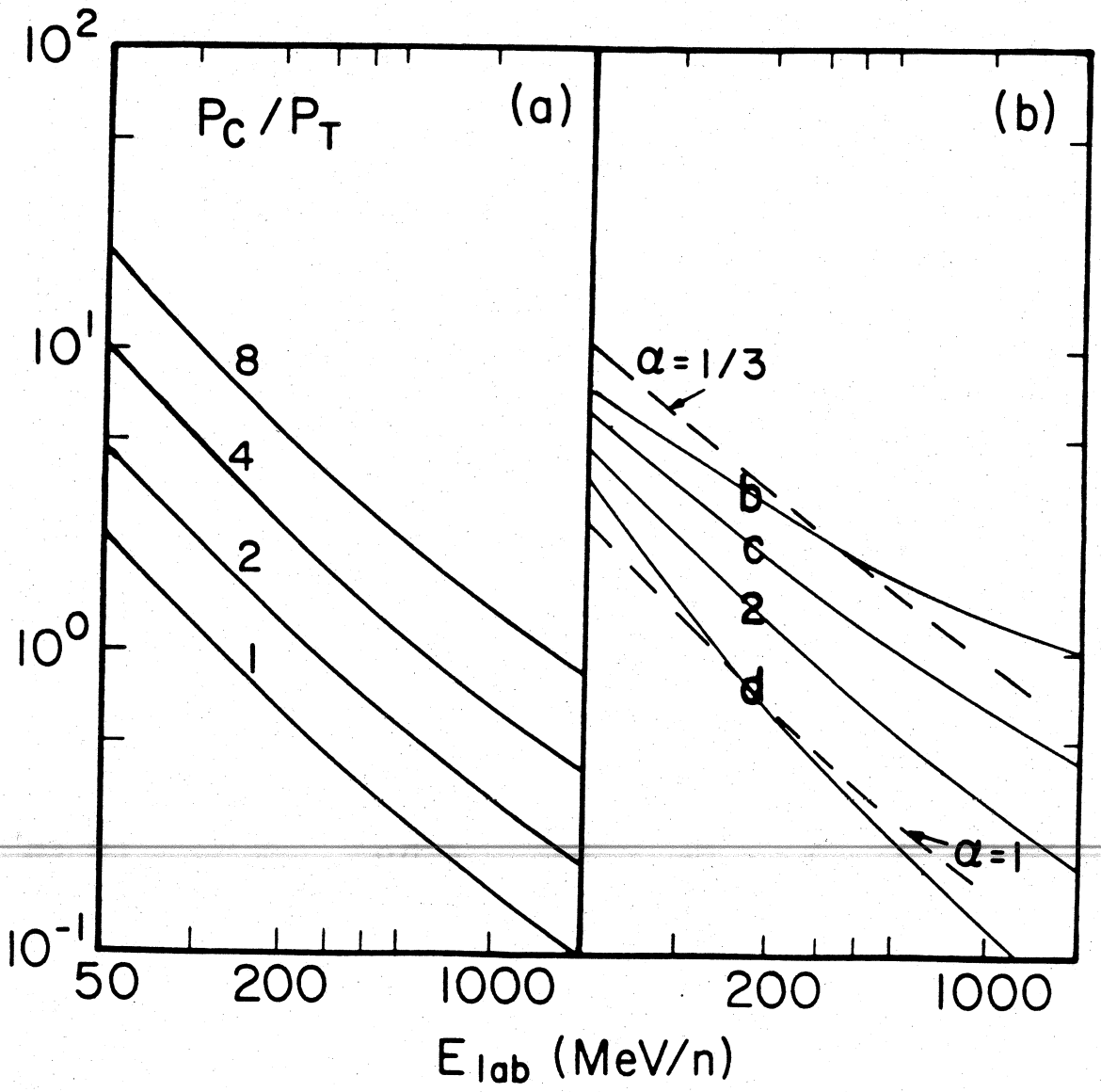

FIGURE III.33a

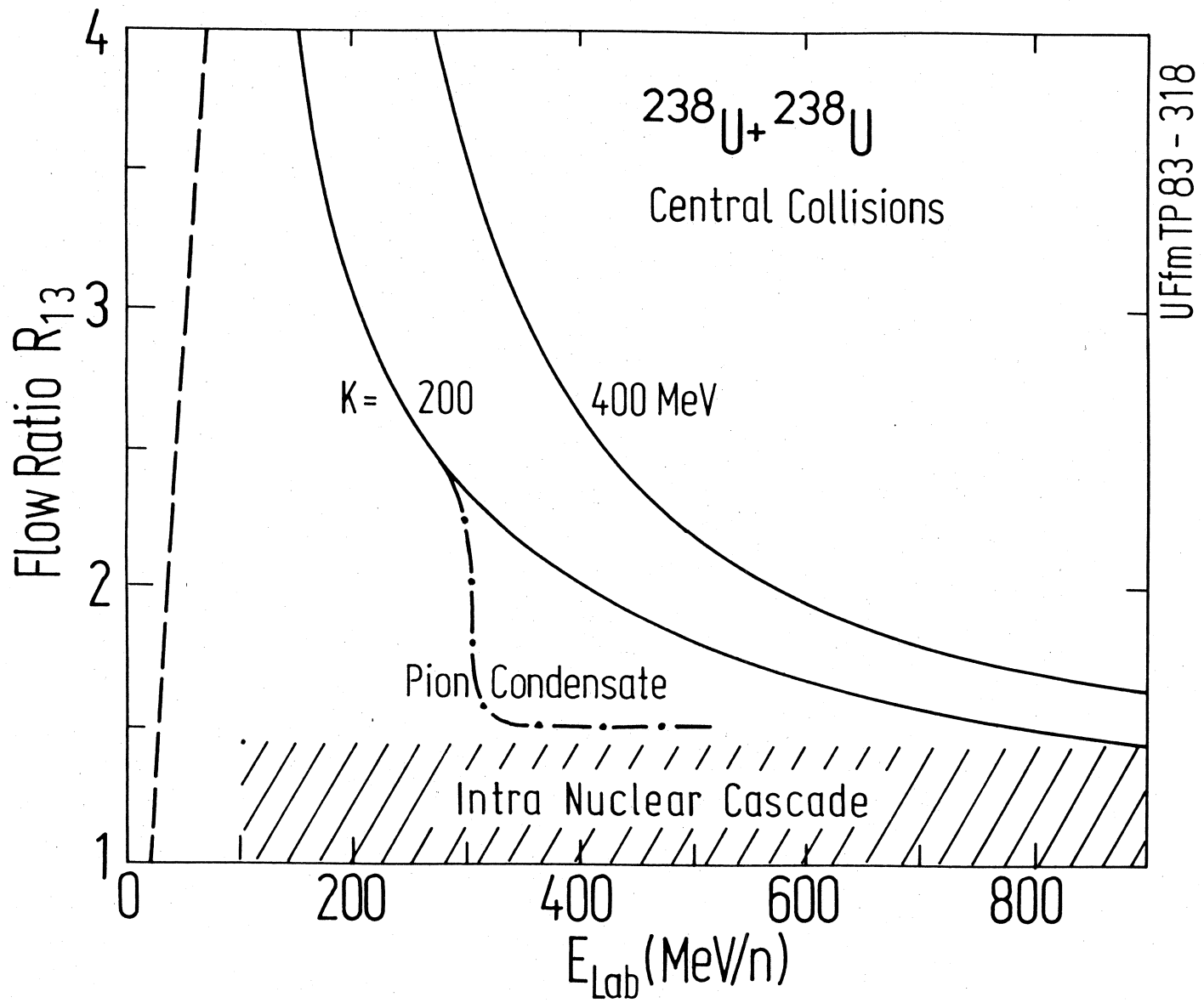

FIGURE III.33b

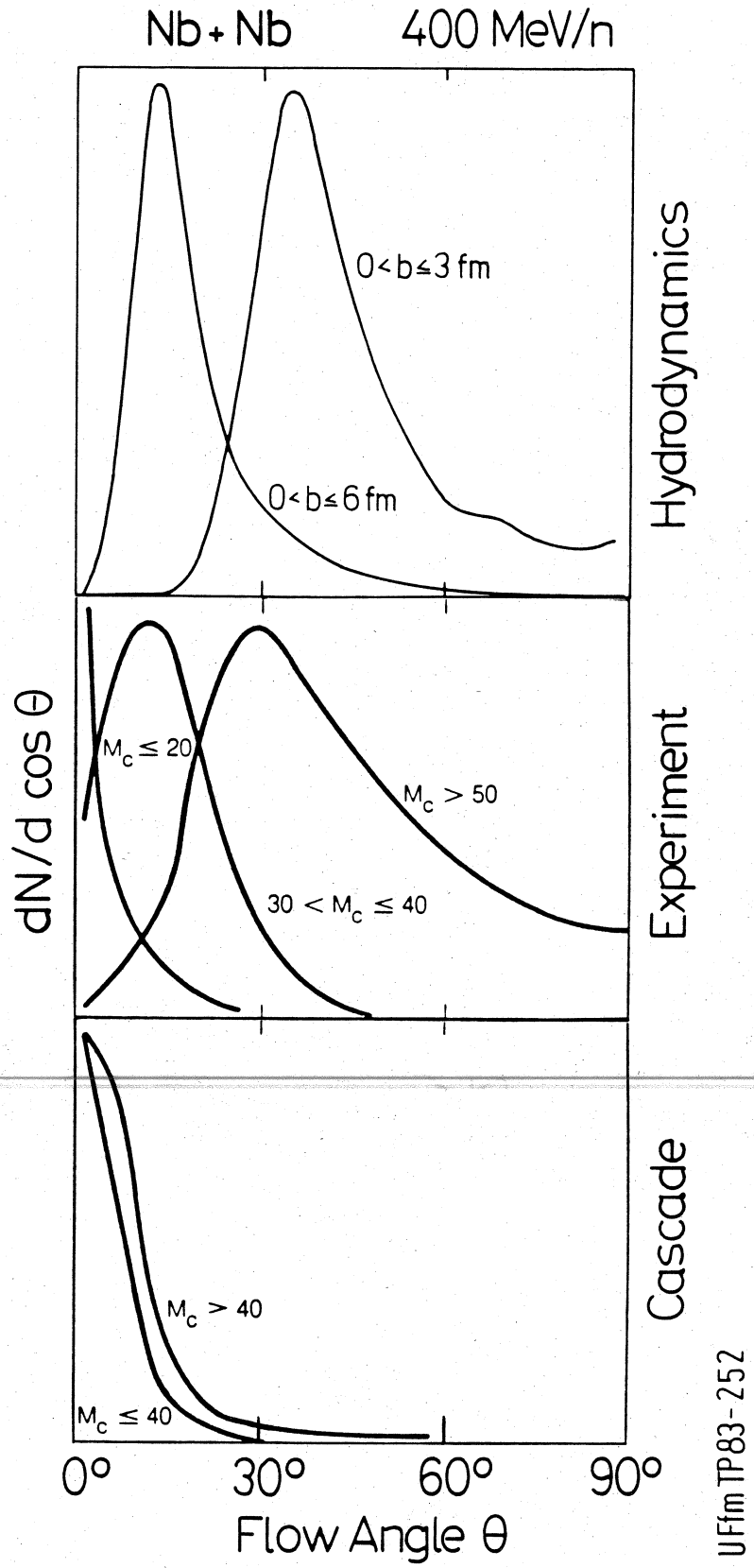

FIGURE III.34

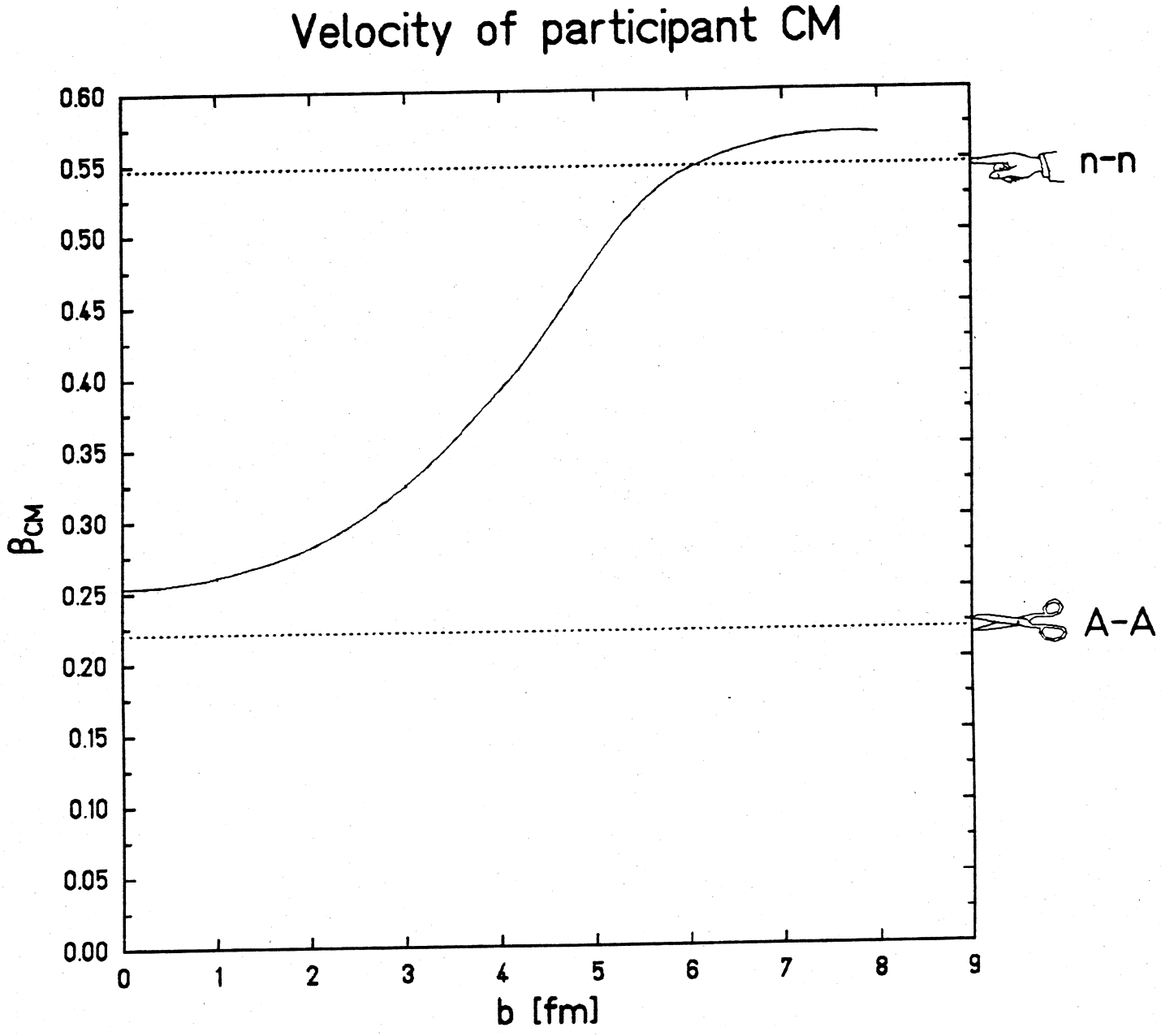

FIGURE III.35

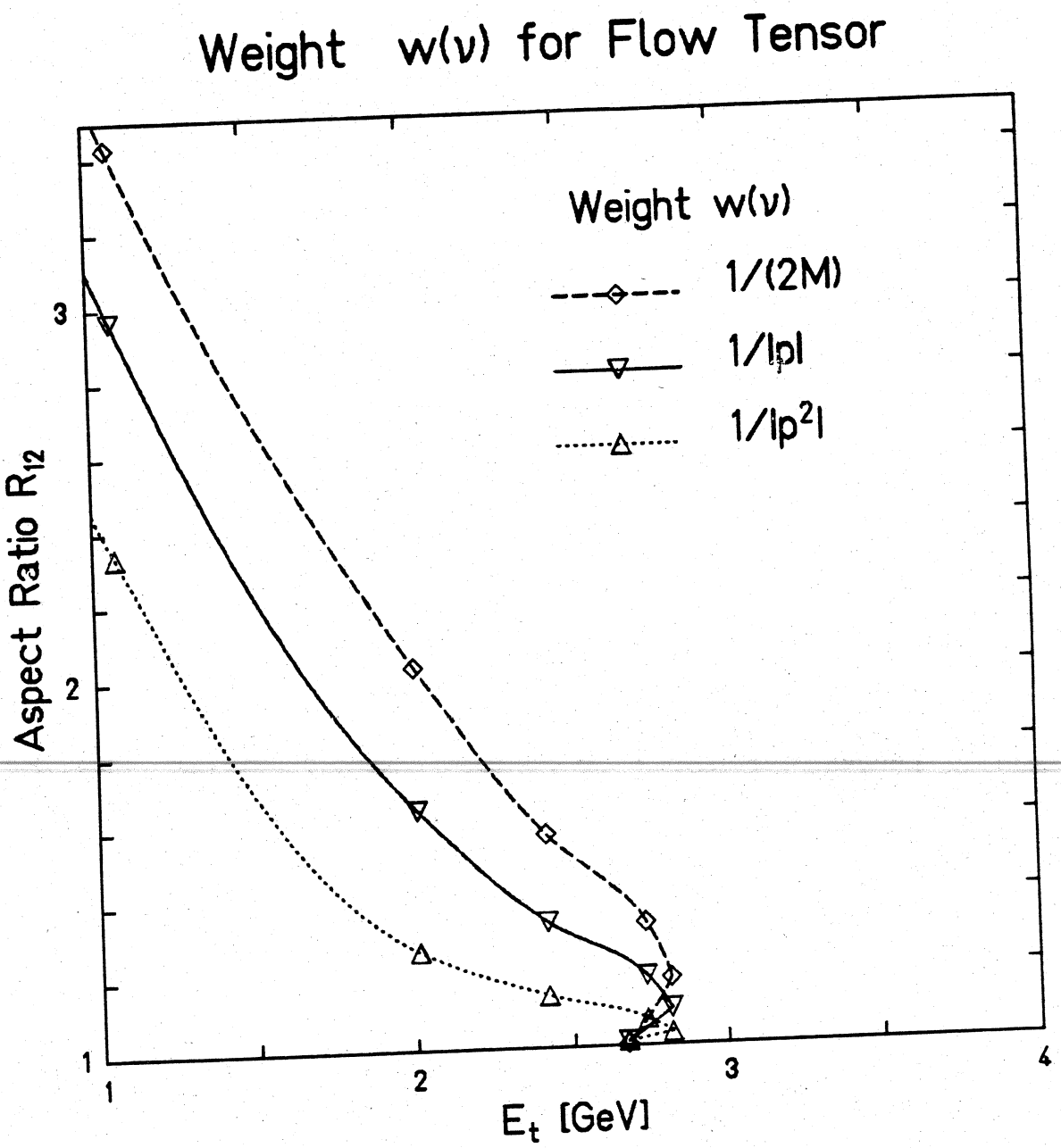

FIGURE III.36

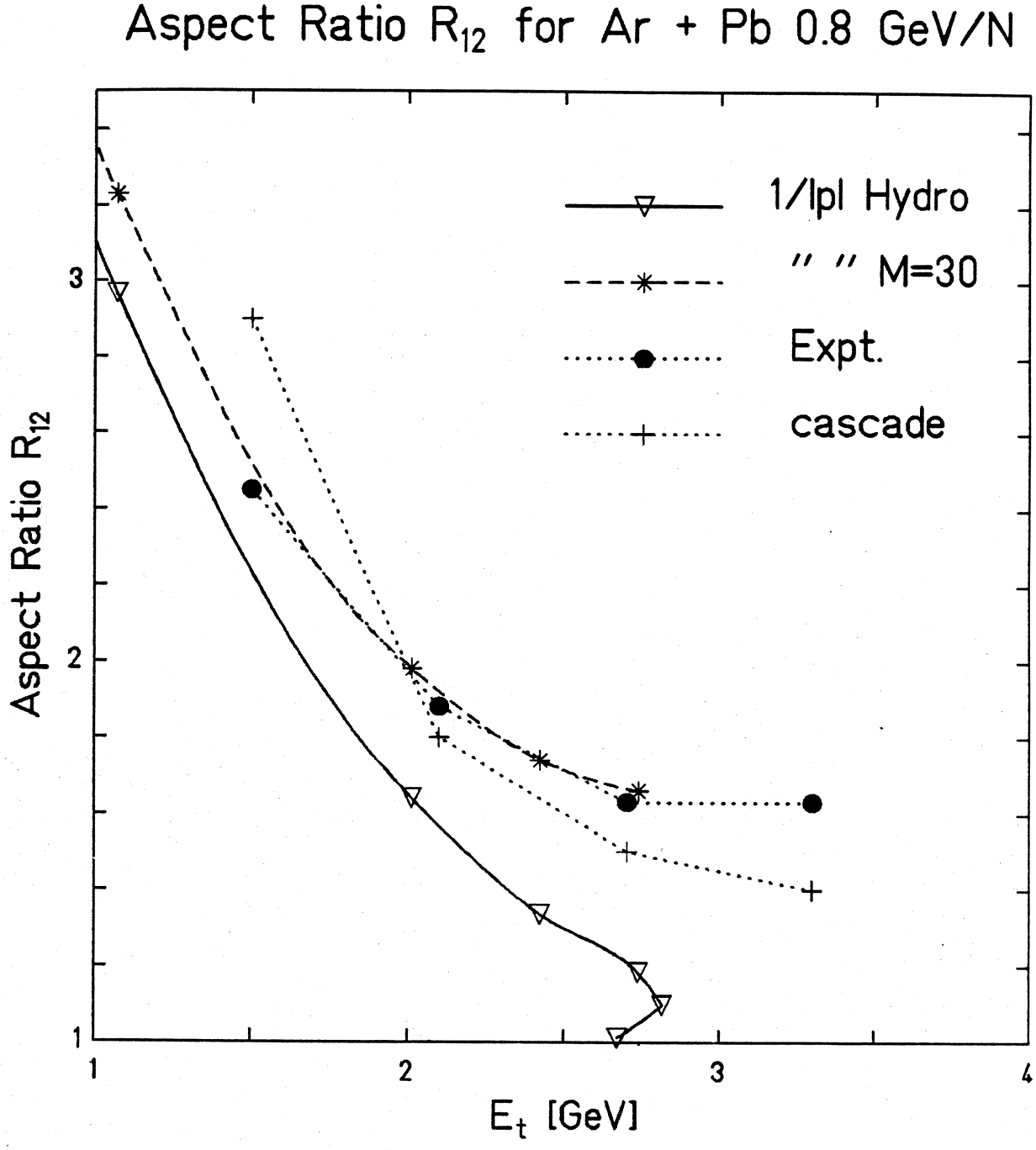

FIGURE III.37

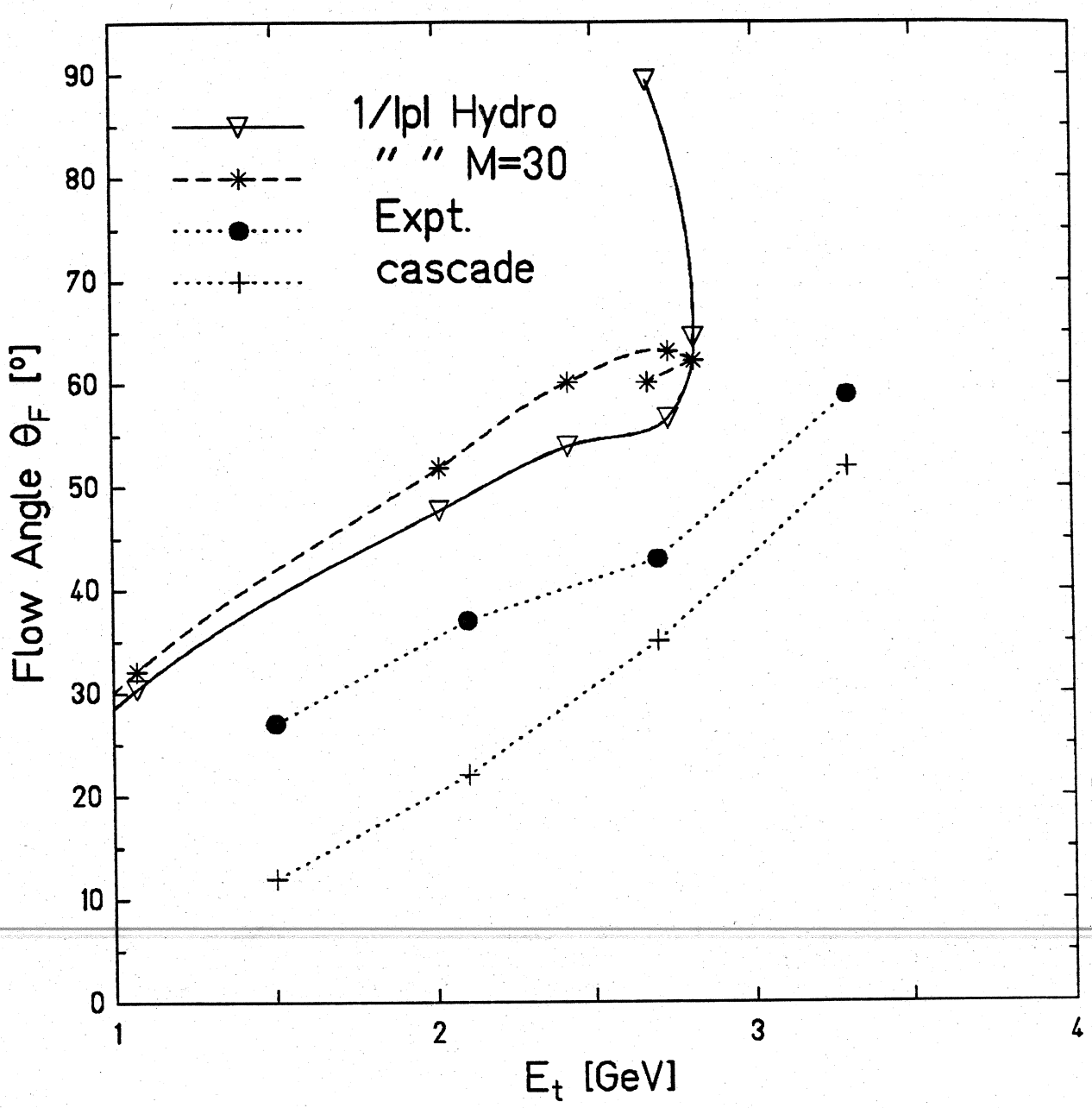

FIGURE III.38

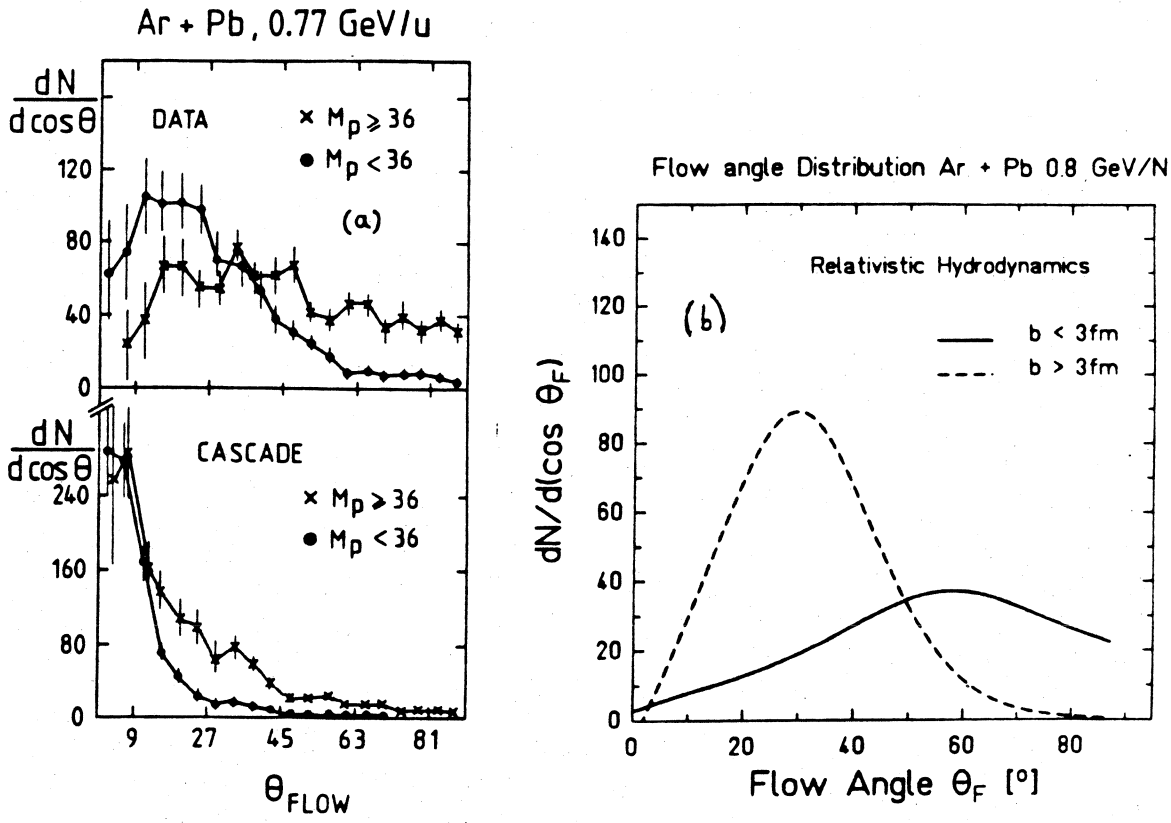

FIGURE III.39

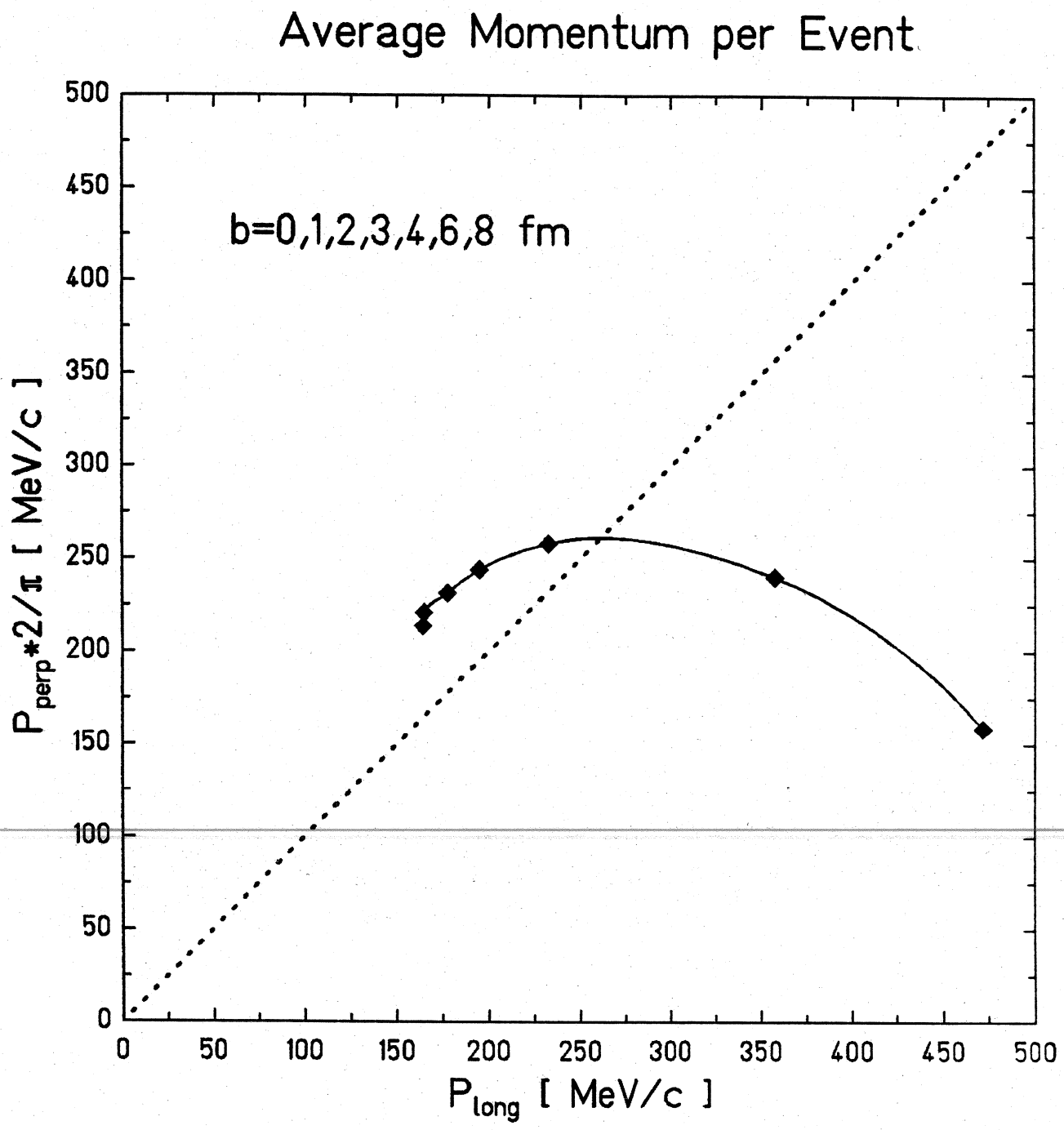

FIGURE III.40

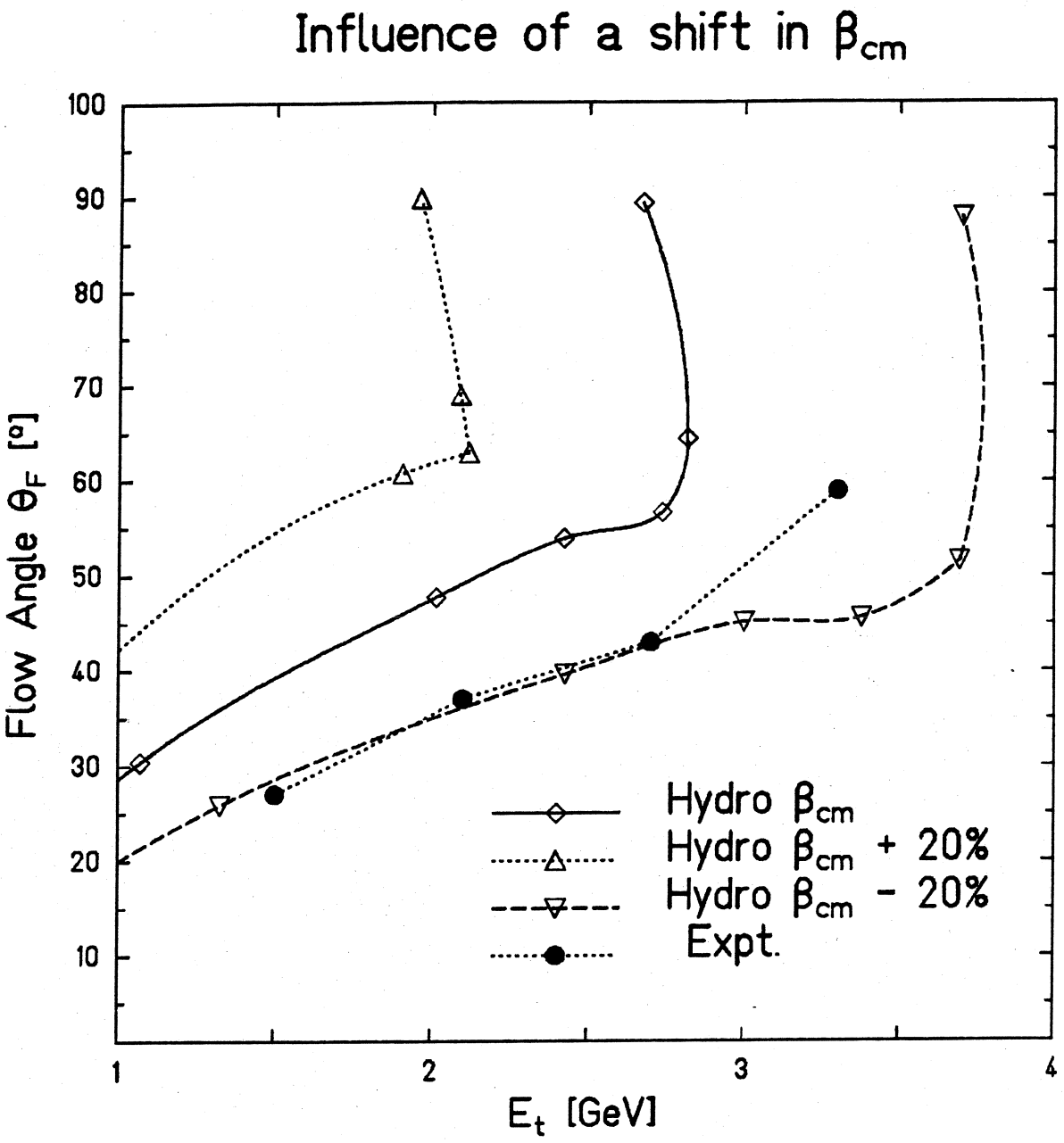

FIGURE III.41

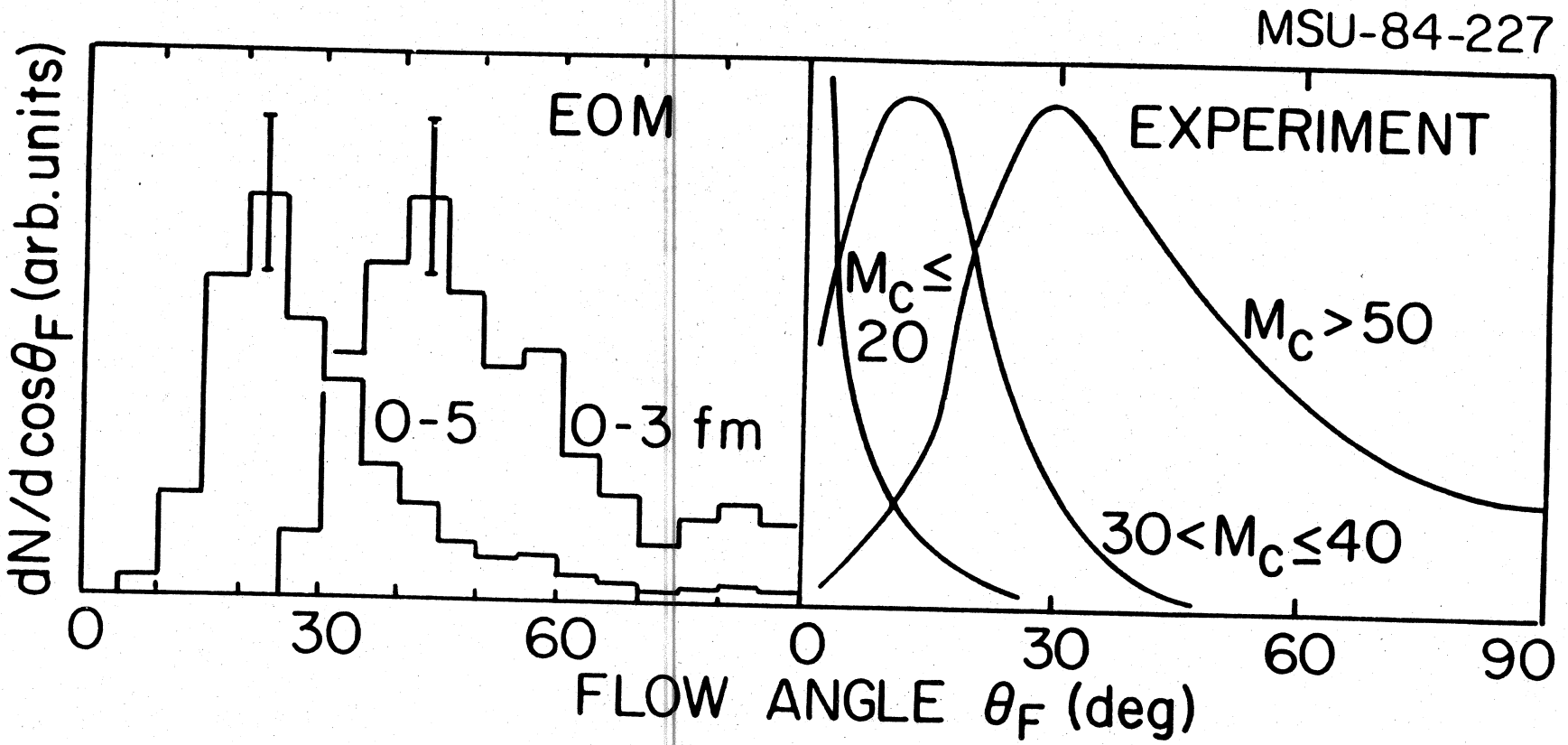

FIGURE III.42

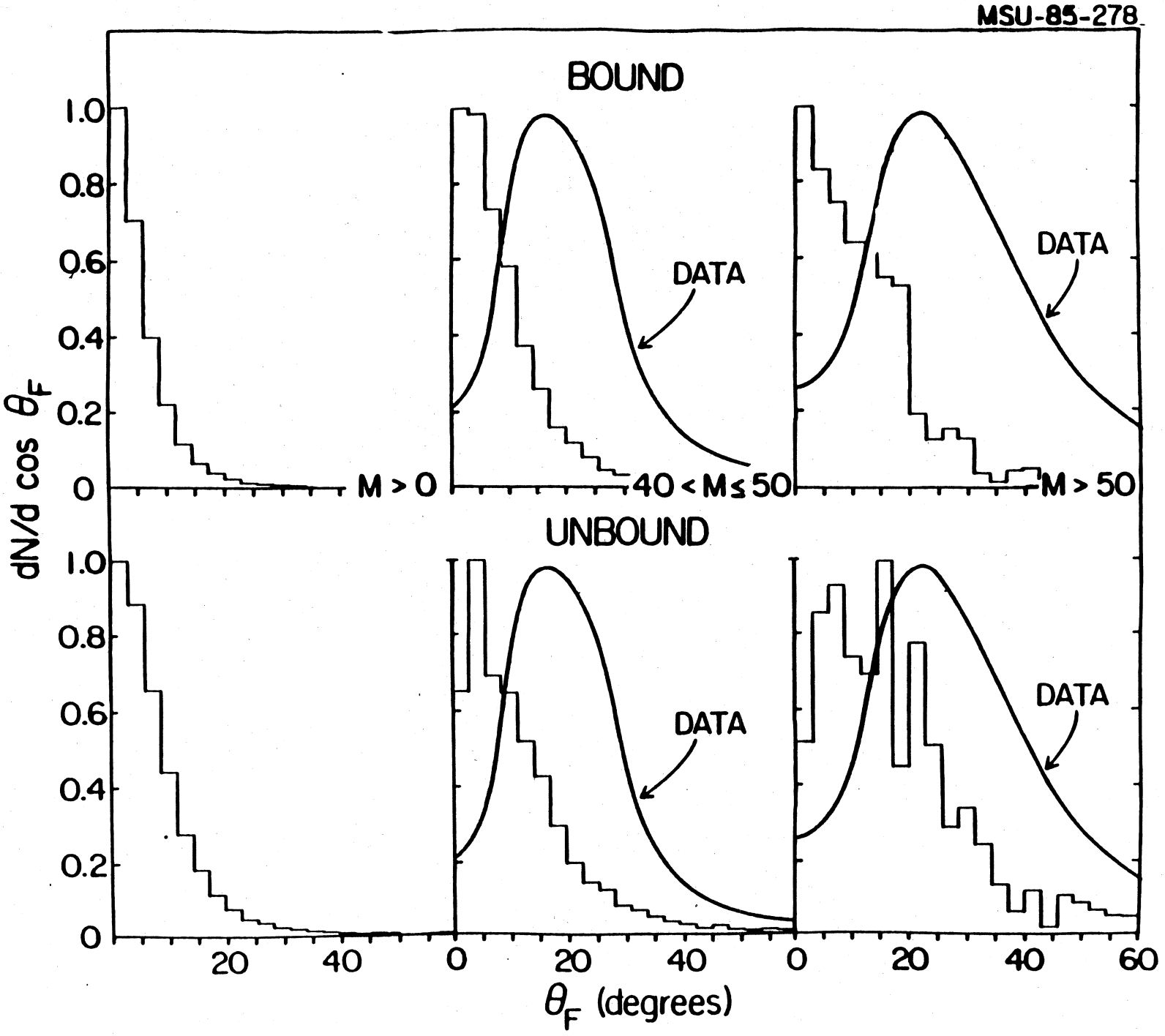

FIGURE III.43

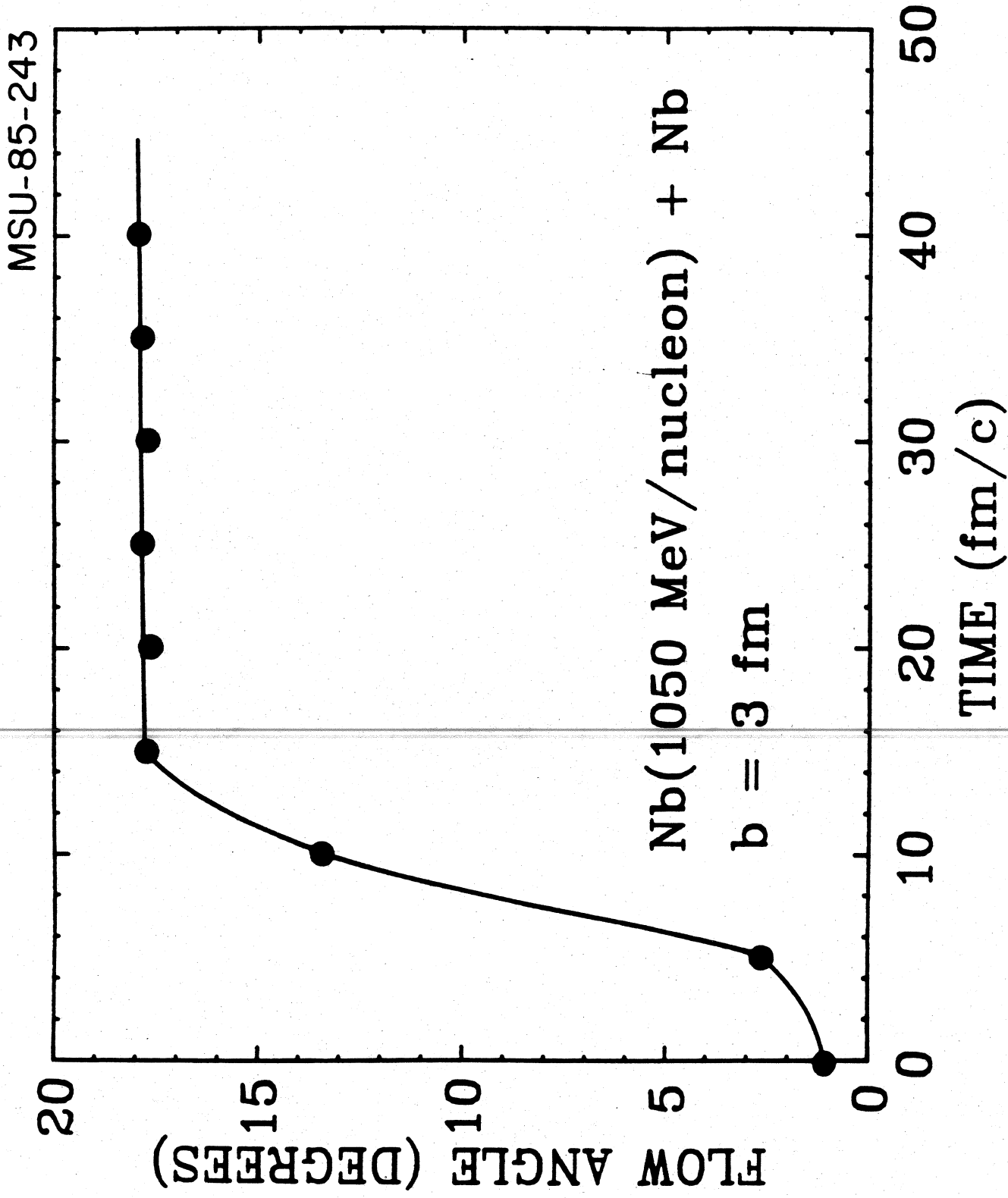

FIGURE III.44

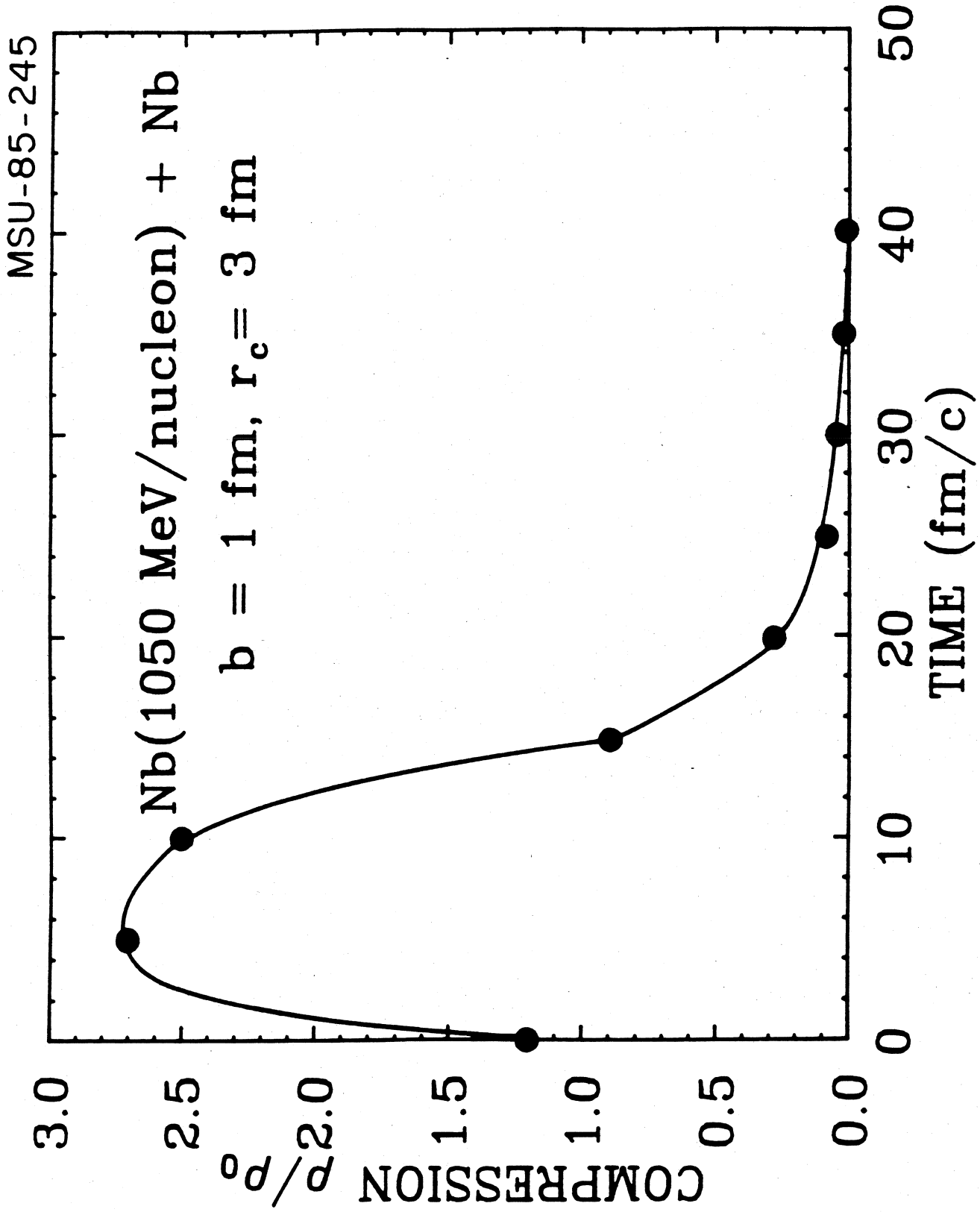

FIGURE III.45

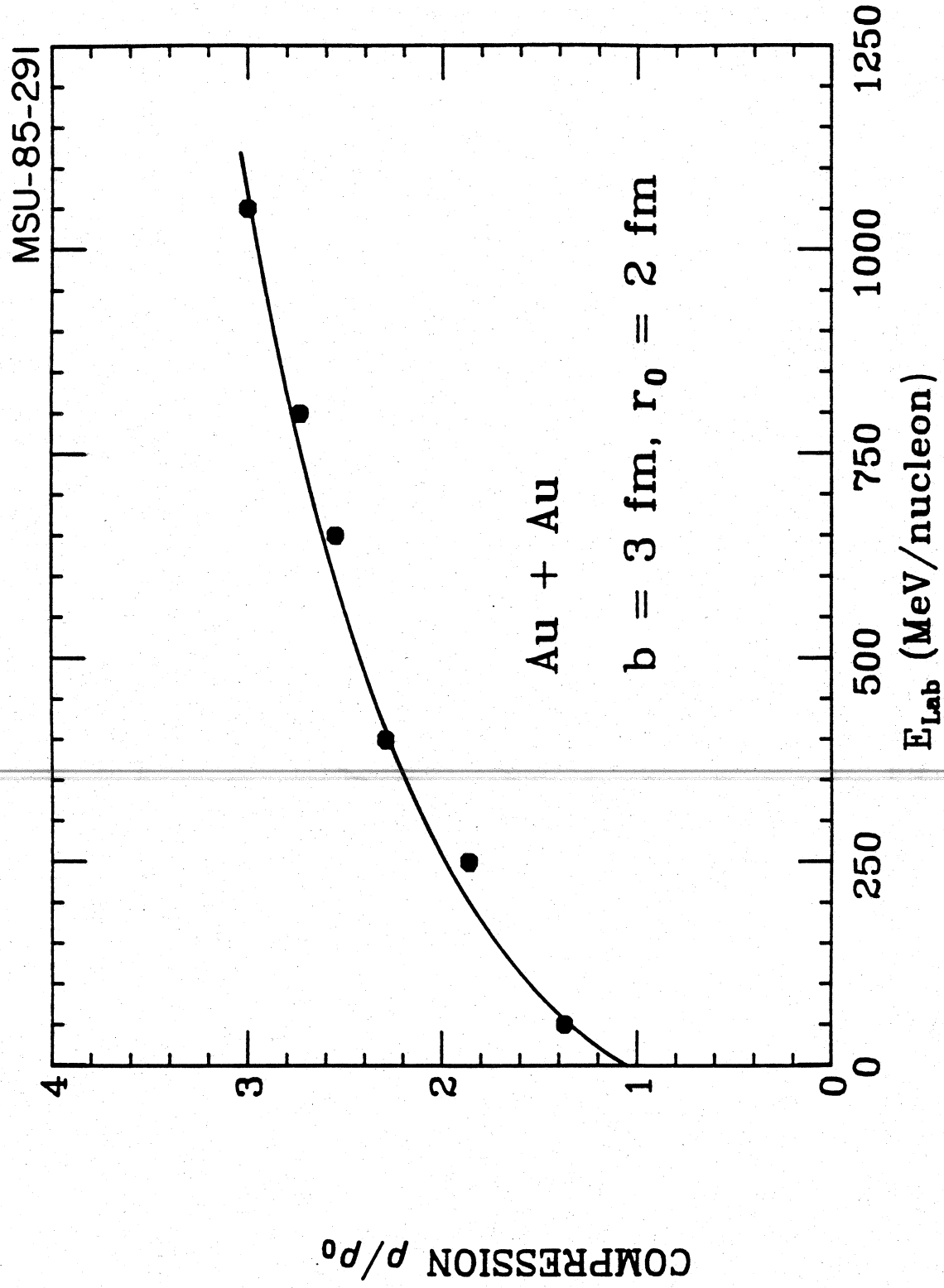

FIGURE III.46

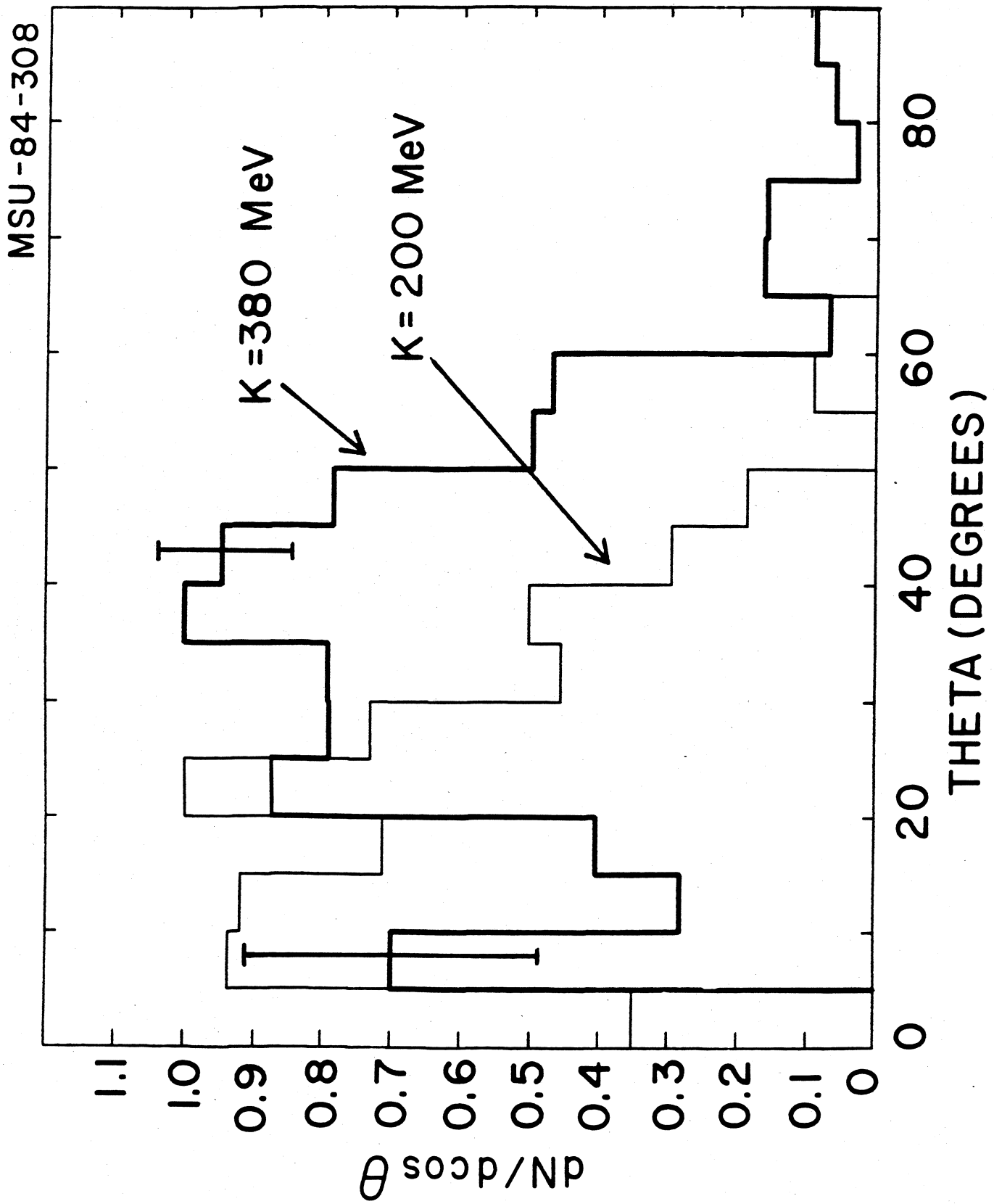

FIGURE III.47

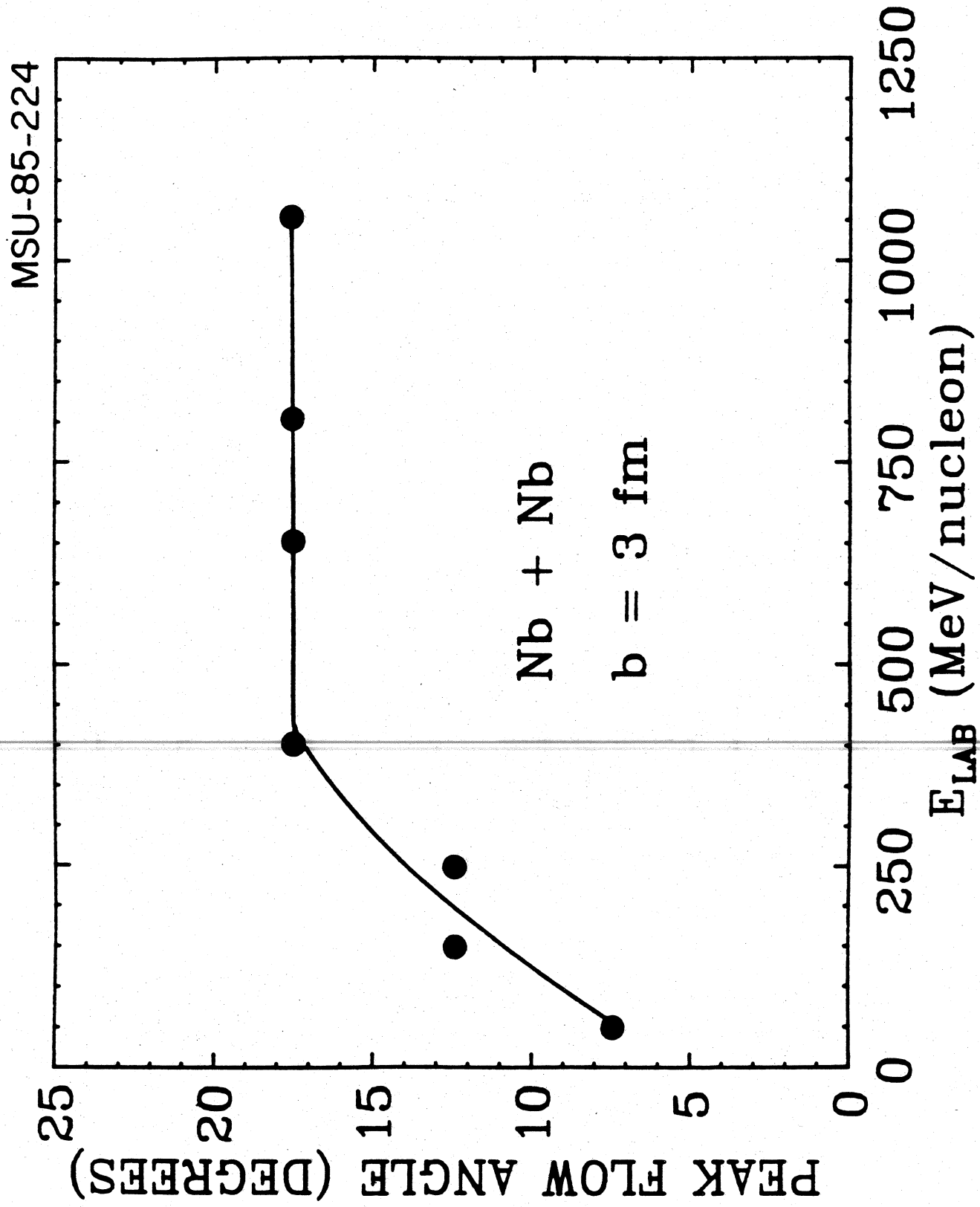

FIGURE III.48

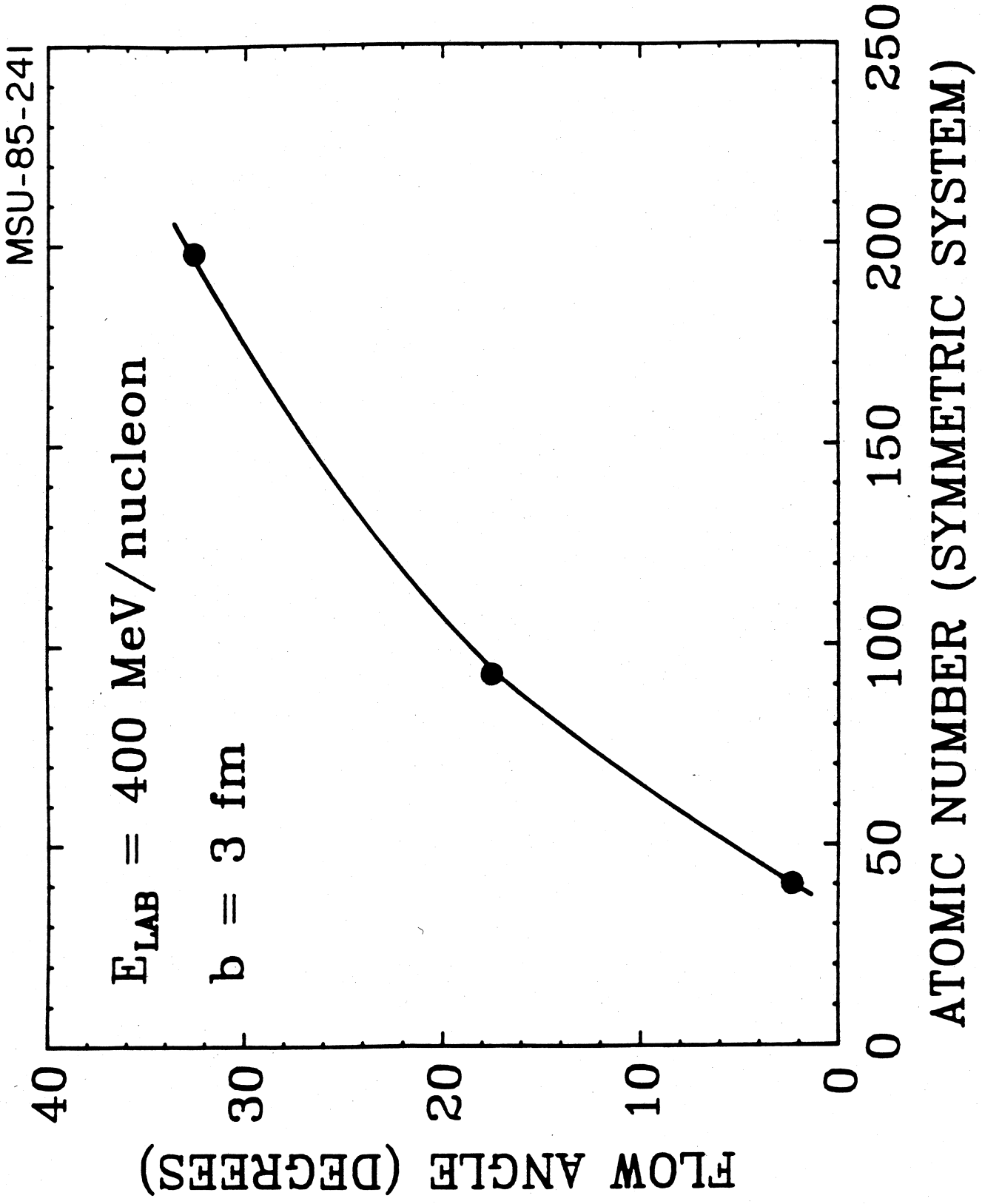

FIGURE III.49

FIGURE III.50

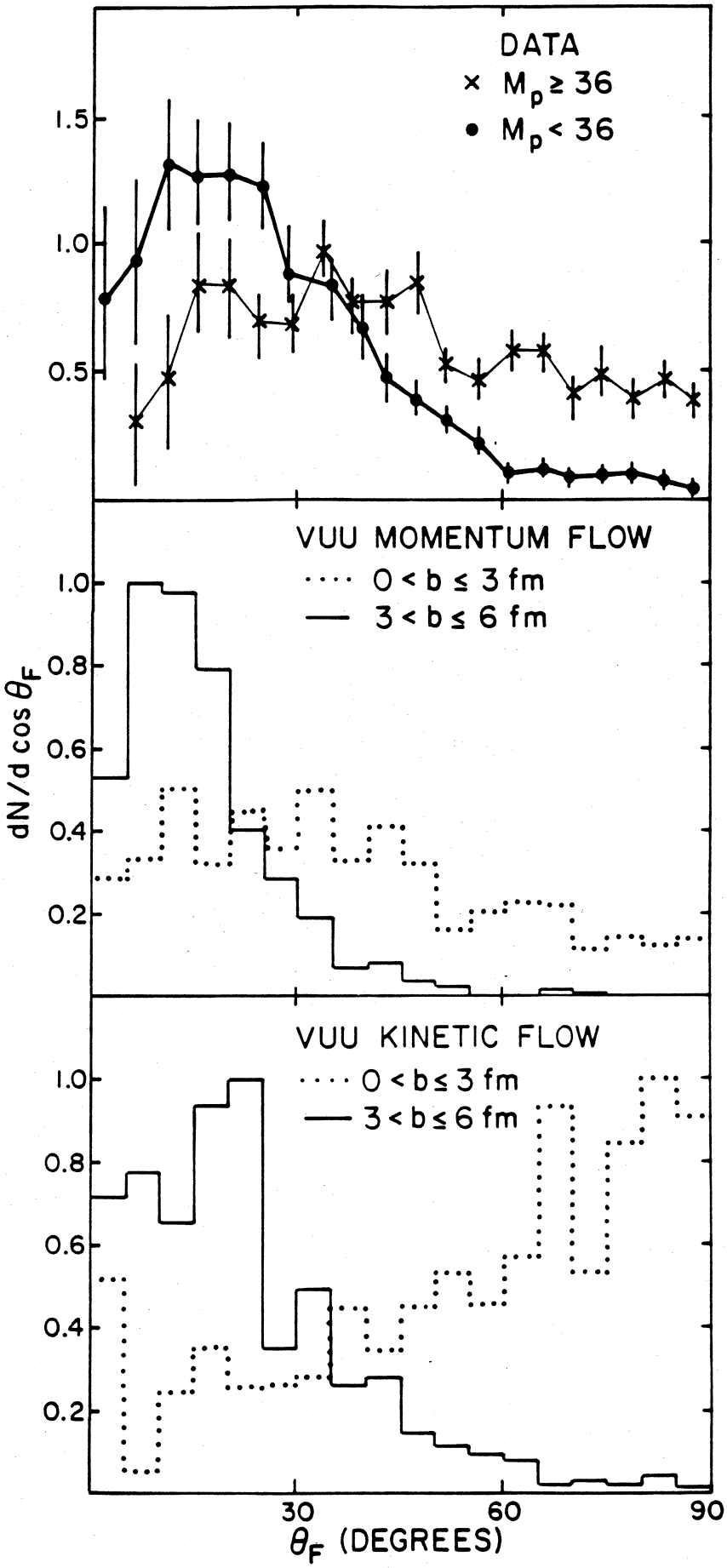

FIGURE III.51

MSU-85-239

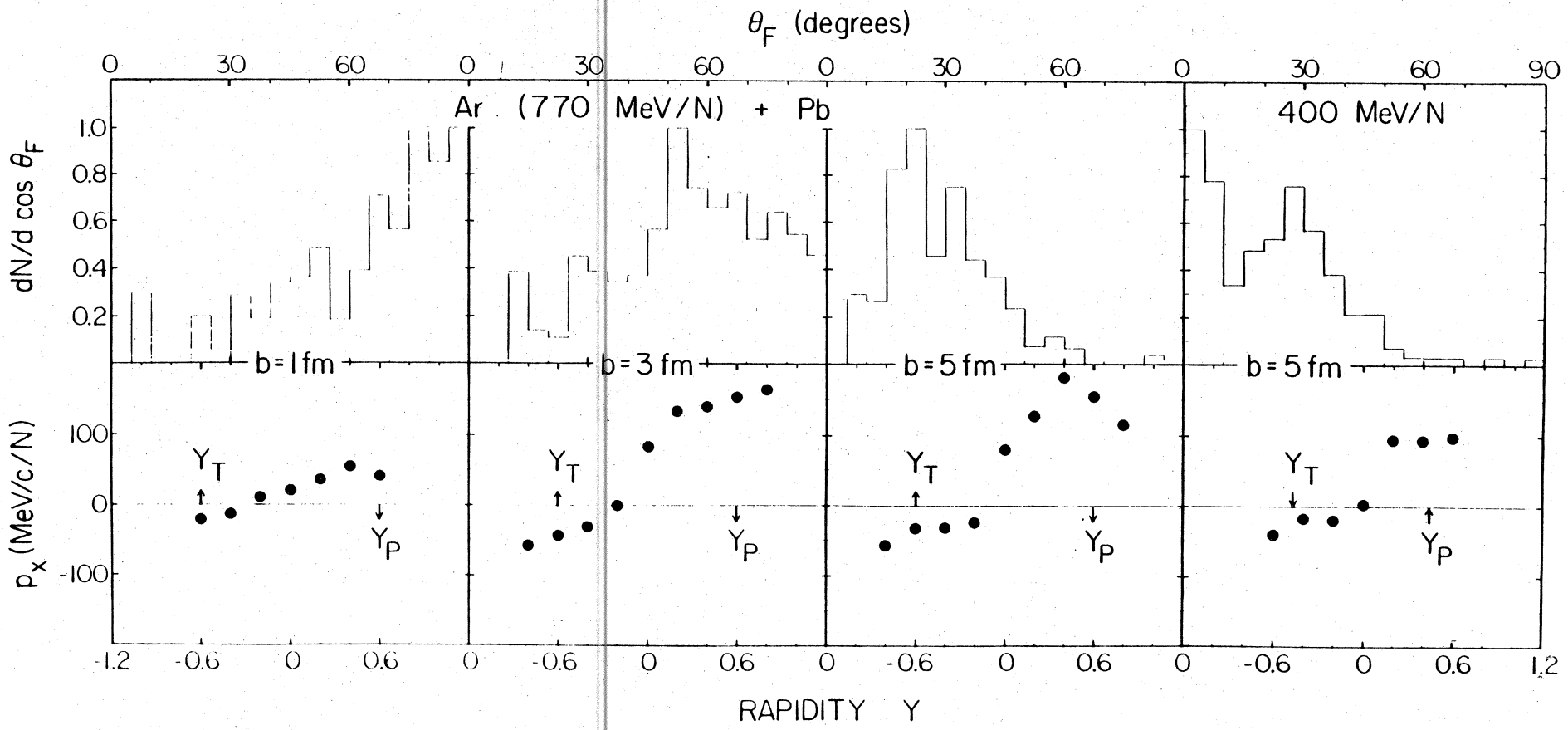

FIGURE III.52

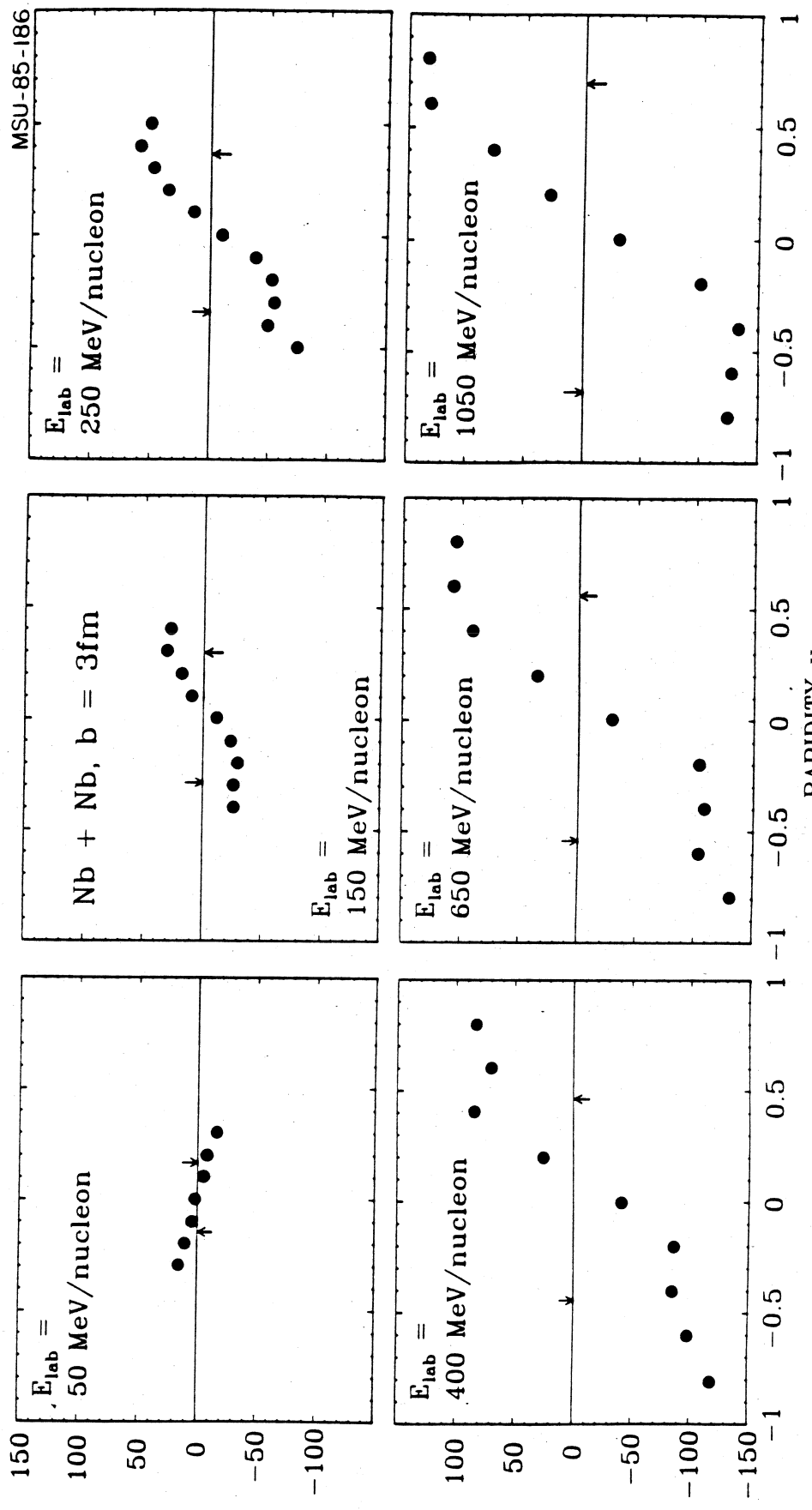

FIGURE III.53

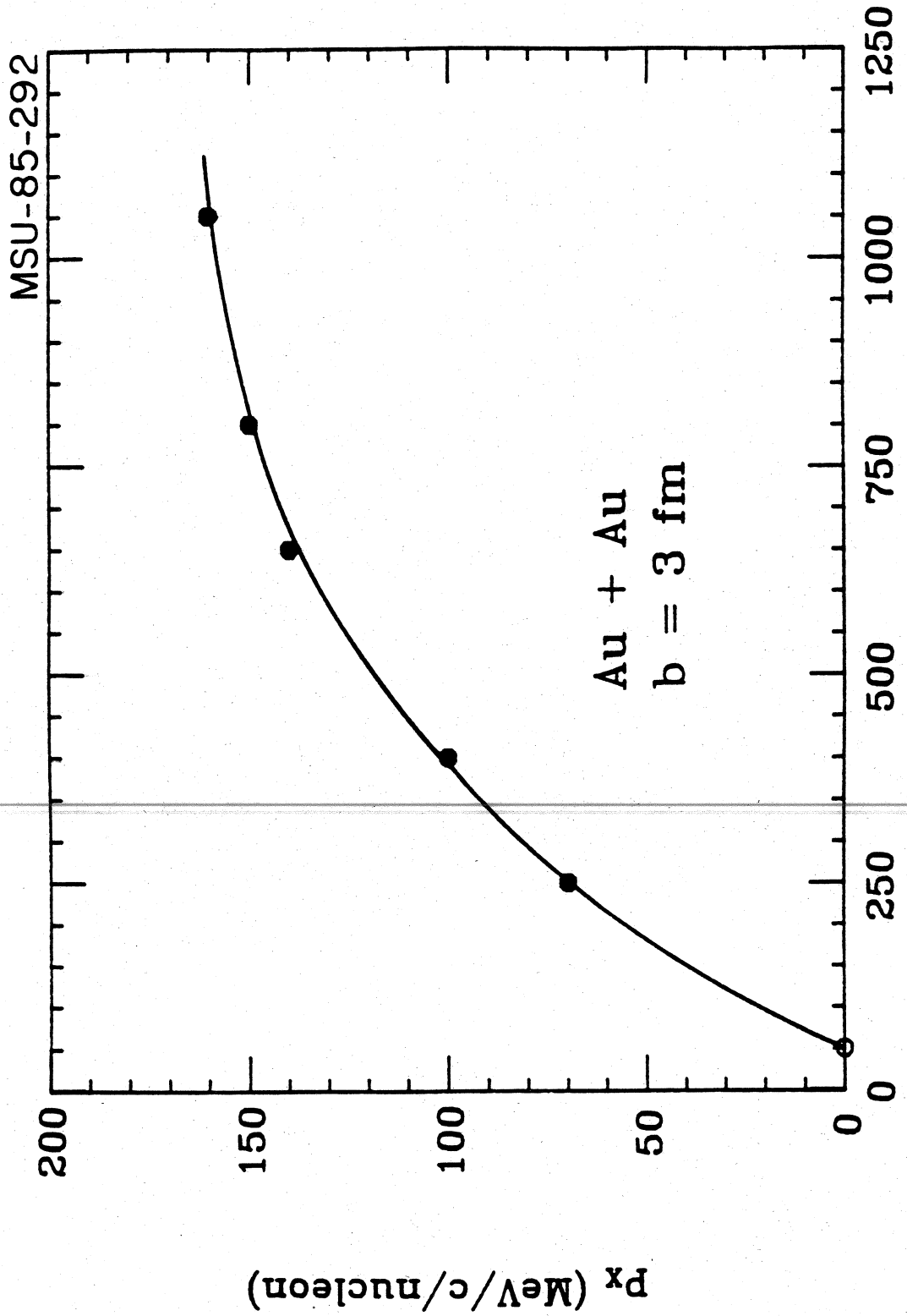

FIGURE III.54

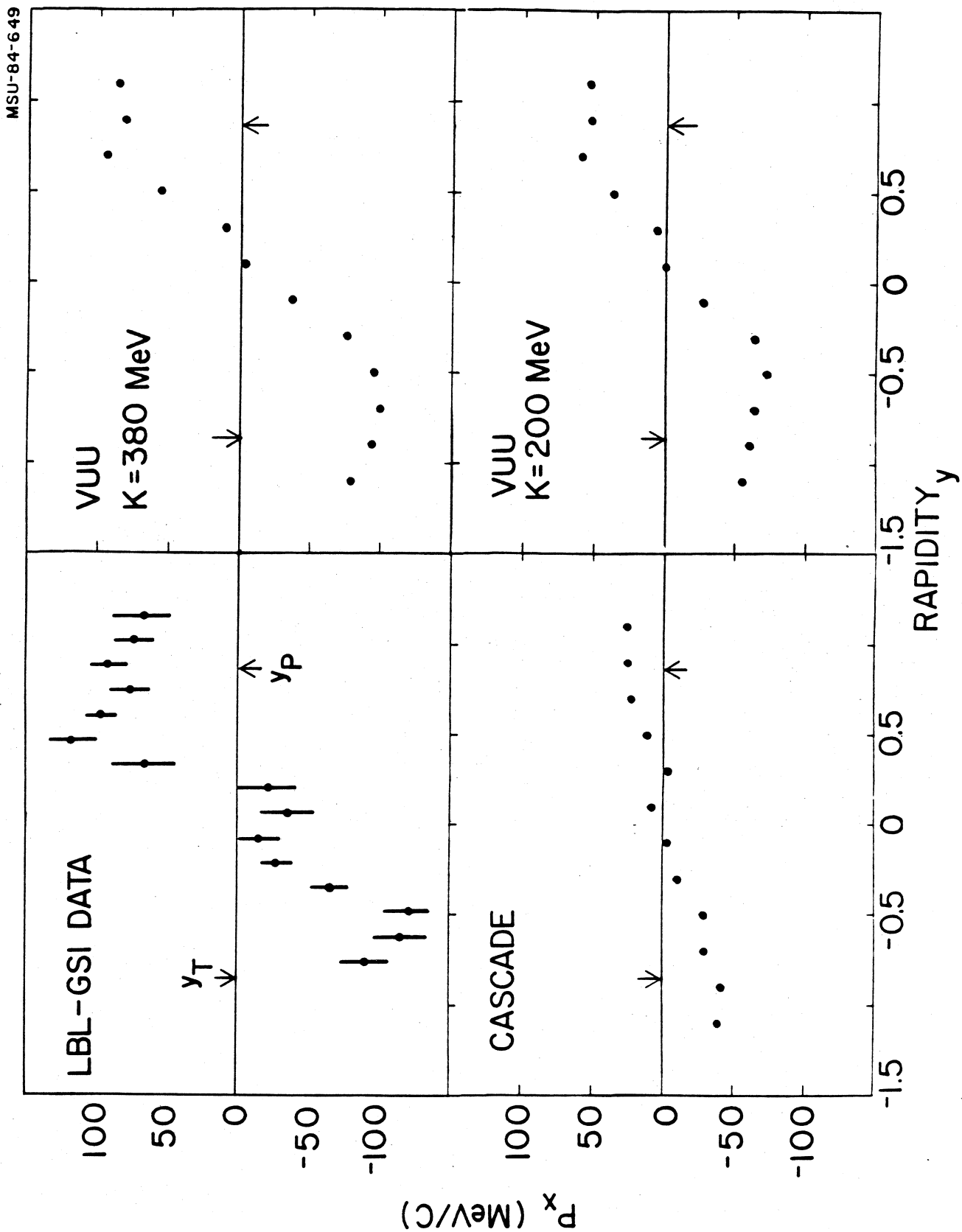

FIGURE III.55

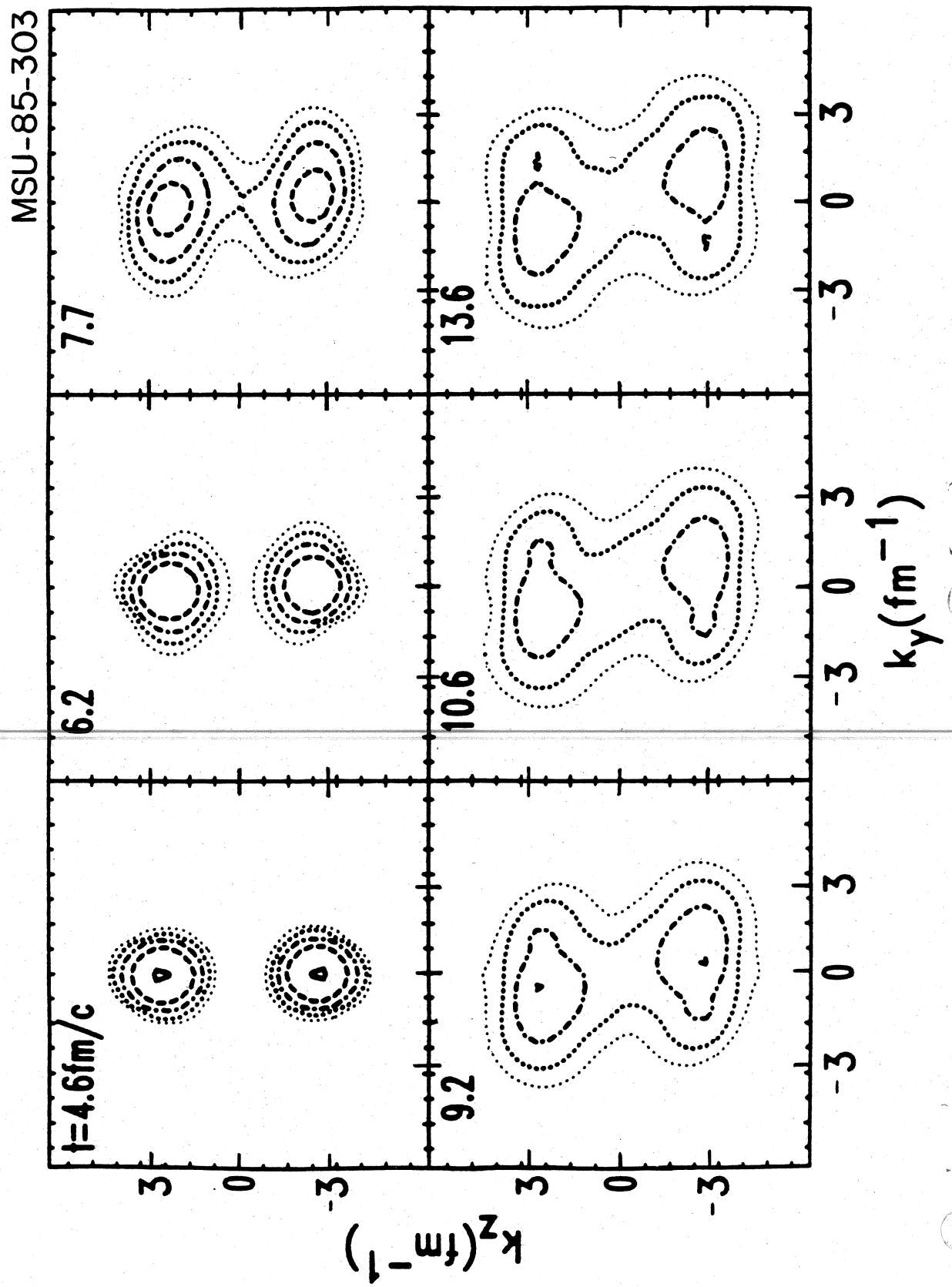

FIGURE III.56

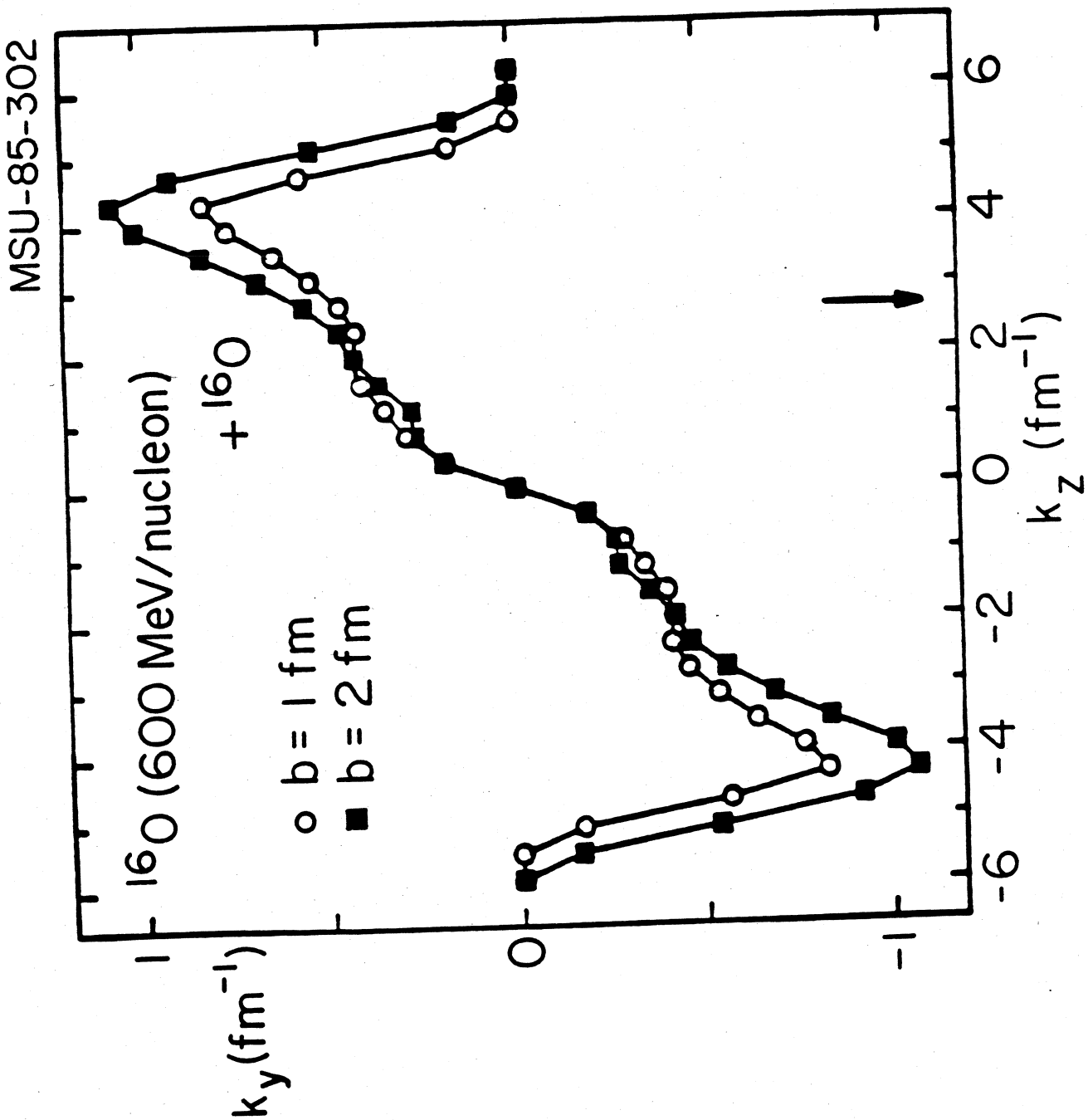

FIGURE III.57

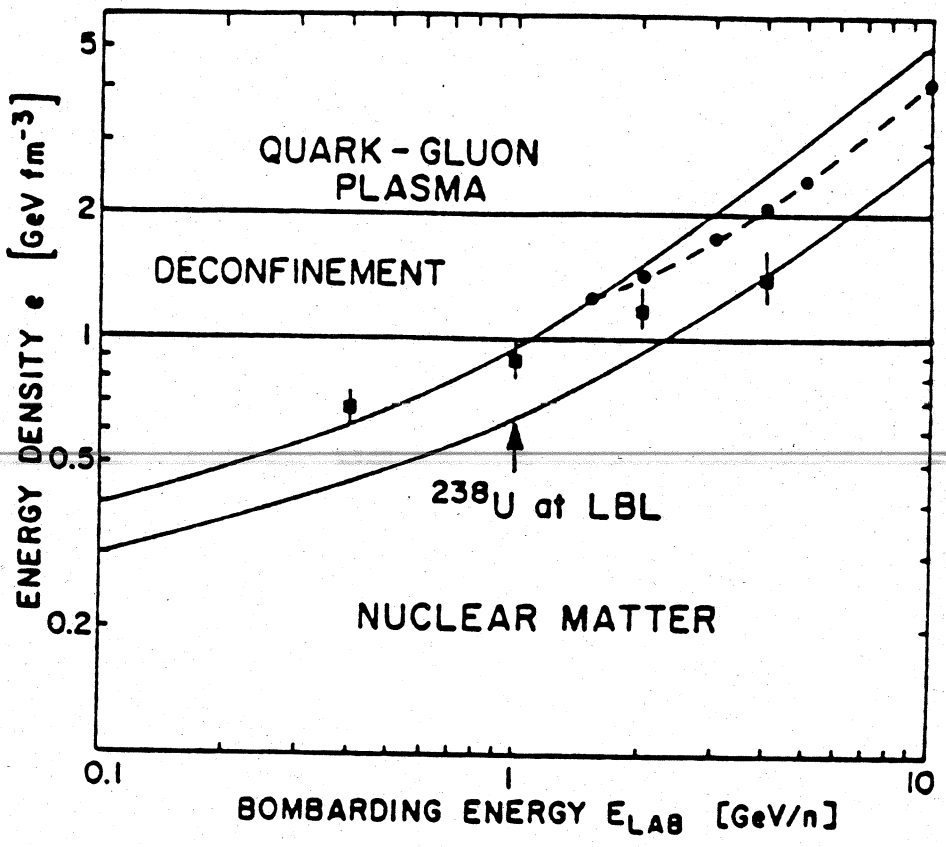
QUARK - GLUON
PLASMA
DECONFINEMENT
NUCLEAR MATTER
^{238}U at LBL
ENERGY DENSITY ε [GeV fm^{-3}]
BOMBARDING ENERGY E_{LAB} [GeV/n]
5
2
1
0.5
0.2
0.1
1
10

FIGURE IV.1

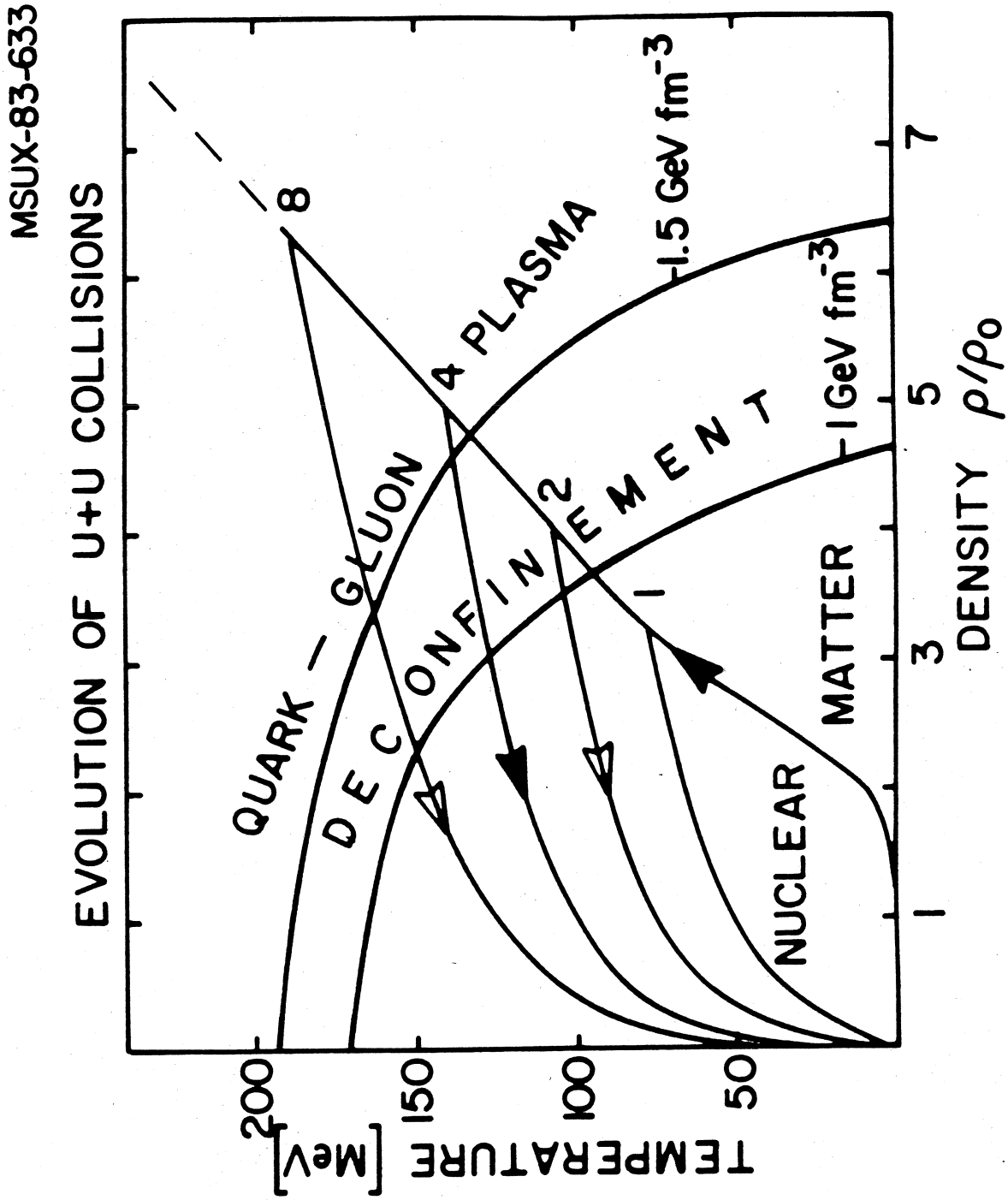
MSUX-83-633
EVOLUTION OF U+U COLLISIONS
TEMPERATURE [MeV]
200
150
100
50
DENSITY ρ/ρo
1
3
5
7
8
4
2
1
QUARK – GLUON PLASMA
DECONFINEMENT
NUCLEAR MATTER
1.5 GeV fm-3
1 GeV fm-3

FIGURE IV.2

MSU-83-635

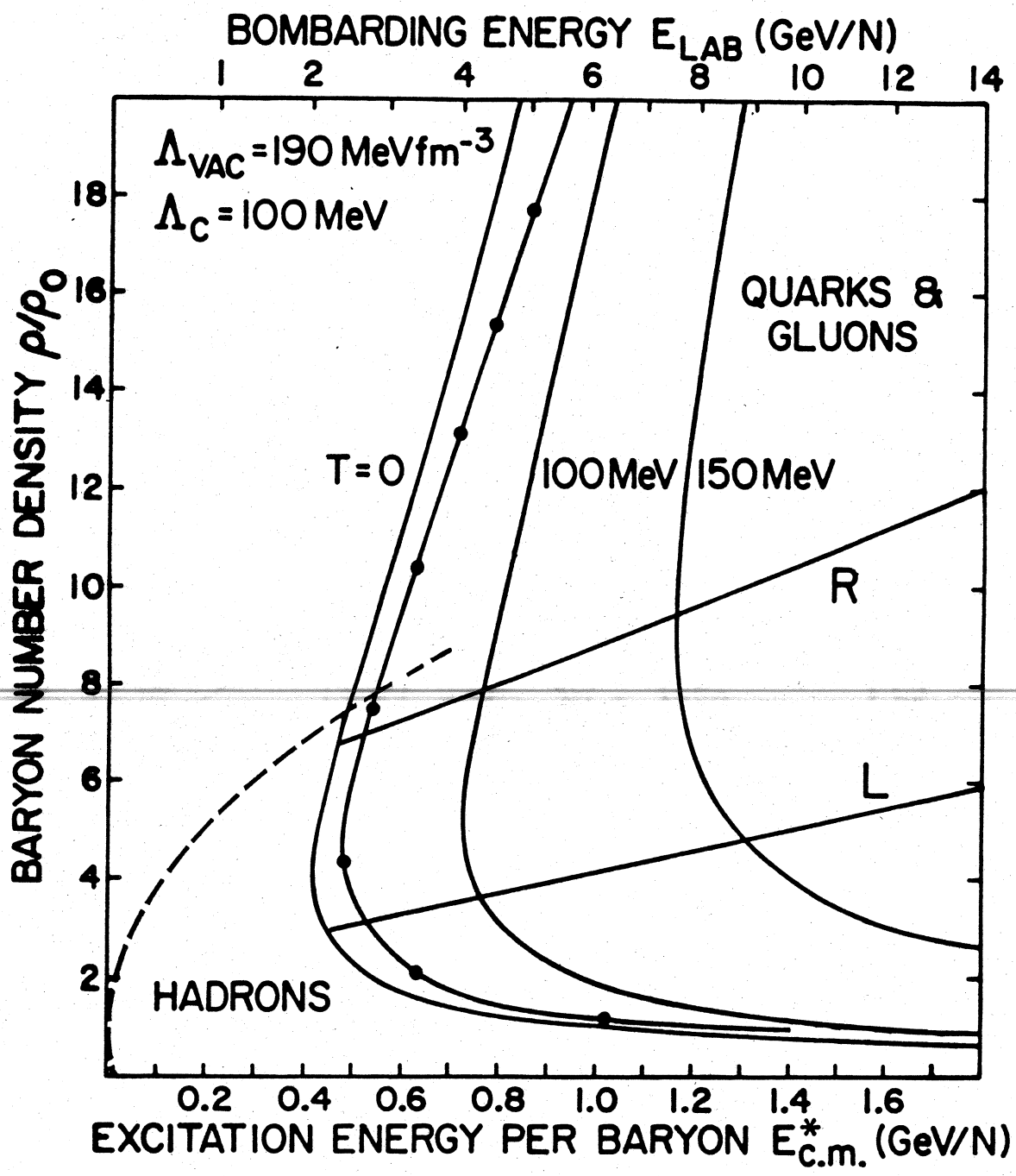

FIGURE IV.3

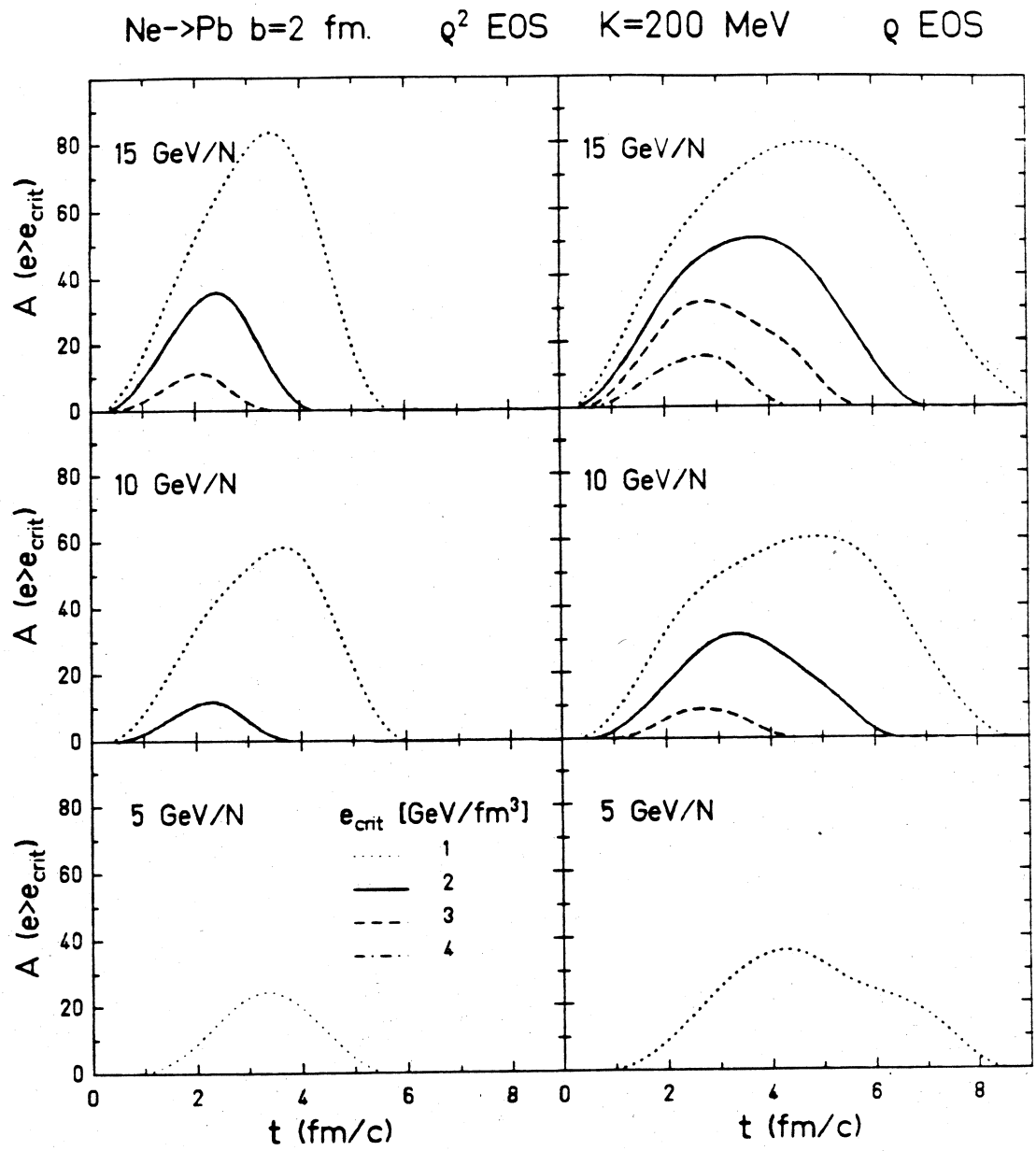
Ne->Pb b=2 fm. ρ² EOS K=200 MeV ρ EOS
15 GeV/N
15 GeV/N
10 GeV/N
10 GeV/N
5 GeV/N
5 GeV/N
A (e>e_crit)
e_crit [GeV/fm³]
1
2
3
4
t (fm/c)
t (fm/c)

FIGURE IV.4

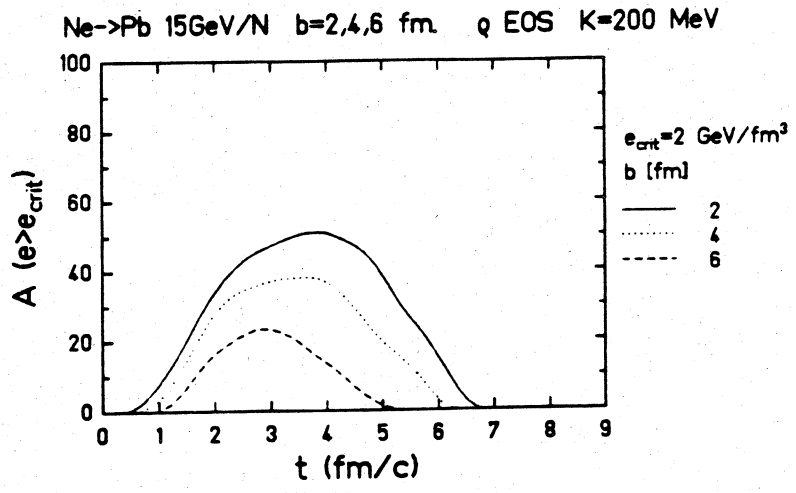

FIGURE IV.5

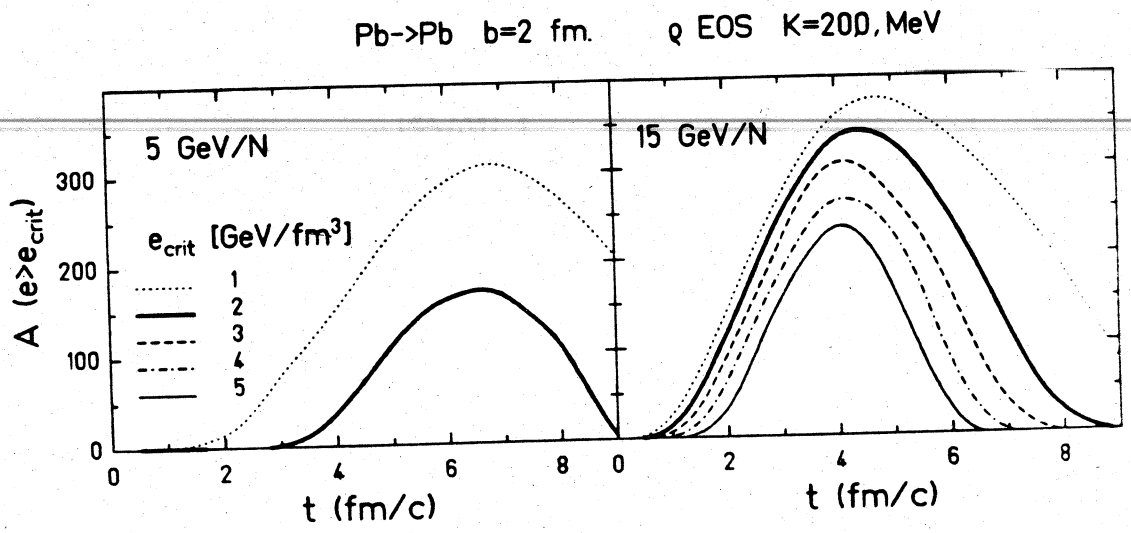

FIGURE IV.6